NIST MEASUREMENT SERVICES:
Spectral Reflectance

P. Yvonne Barnes
Edward A. Early
Albert C. Parr

Optical Technology Division
Physics Laboratory
National Institute of Standards and Technology
Gaithersburg, MD 20899-0001

March 1998

U.S. DEPARTMENT OF COMMERCE
William M. Daley, Secretary

Technology Administration
Gary R. Bachula, Acting Under Secretary for Technology

National Institute of Standards and Technology
Raymond G. Kammer, Director

National Institute of Standards and Technology Special Publication 250–48
Natl. Inst. Stand. Technol. Spec. Publ. 250–48, 153 pages (Mar. 1998)
CODEN: NSPUE2

U.S. GOVERNMENT PRINTING OFFICE
WASHINGTON: 1998

For sale by the Superintendent of Documents, U.S. Government Printing Office, Washington, DC 20402–9325

PREFACE

The calibration and related measurement services of the National Institute of Standards and Technology are intended to assist the makers and users of precision measuring instruments in achieving the highest possible levels of accuracy, quality, and productivity. NIST offers over 300 different calibrations, special tests, and measurement assurance services. These services allow customers to directly link their measurement systems to measurement systems and standards maintained by NIST. These services are offered to the public and private organizations alike. They are described in NIST Special Publication (SP) 250, NIST Calibration Services Users Guide.

The Users Guide is supplemented by a number of Special Publications (designated as the "SP250 Series") that provide detailed descriptions of the important features of specific NIST calibration services. These documents provide a description of the: (1) specifications for the services; (2) design philosophy and theory; (3) NIST measurement services; (4) NIST operational procedures; (5) assessment of the measurement uncertainty including random and systematic errors and an error budget; and (6) internal quality control procedures used by NIST. These documents will present more detail than can be given in NIST calibration reports, or than is generally allowed in articles in scientific journals. In the past, NIST has published such information in a variety of ways. This series will make this type of information more readily available to the user.

This document, SP250-48 (1998), NIST Measurement Services: Spectral Reflectance, is a revision of SP250-8 (1987). It describes the instrumentation, standards, and techniques used to measure spectral reflectance over the ultraviolet, visible, and near infrared wavelengths for Standard Reference Materials 2003, 2011, 2015, 2016, 2023, 2026, and 2044 and for Special Test 38060S. Inquiries concerning the technical content of this document or the specifications for these services should be directed to the authors or to one of the technical contacts cited in SP250.

NIST welcomes suggestions on how publications such as this might be made more useful. Suggestions are also welcome concerning the need for new calibration services, special tests, and measurement assurance programs.

Peter L.M. Heydemann
Director
Measurement Services

Katharine B. Gebbie
Director
Physics Laboratory

ABSTRACT

This document describes the instrumentation, standards, and techniques used at the National Institute of Standards and Technology to measure spectral reflectance over the ultraviolet, visible, and near infrared wavelength ranges. The organization is as follows. Part I describes the motivation for maintaining reference and transfer spectrophotometers for spectral reflectance measurements, the basics of reflection, and the standards and services that are available from NIST. Part II develops the necessary theory of reflection, beginning with basic definitions and equations and ending with the relevant measurement equations for the experiments described in this documentation. The NIST Spectral Tri-function Automated Reference Reflectometer is described in Part III. This instrument provides the basis for the development of absolute NIST standards of diffuse and specular reflectance. Part IV describes the NIST transfer spectrophotometers, high precision commercial instruments used for calibrating Standard Reference Materials such as diffuse reflectance and specular reflectance standards. The transfer instruments rely on master standards that are periodically calibrated on the high accuracy reference reflectometer described in Part III. References containing details are reproduced in the appendices.

Key words: bidirectional; diffuse reflectance; reflectance; spectrophotometer; spectrophotometry; spectral reflectance, specular reflectance

TABLE OF CONTENTS

Abstract iv

1. Introduction 1

2. Theory 4
   2.1 Basic Definitions and Equations 4
   2.2 Measurement Equations 8
      2.2.1 Bidirectional Reflectance Distribution Function 8
      2.2.2 Directional - Hemispherical Reflectance 10

3. Reference Instrument – STARR 12
   3.1 Description 12
      3.1.1 Basic Instrument 12
      3.1.2 Source System 14
      3.1.3 Goniometer 16
      3.1.4 Integrating Spheres 18
   3.2 Calibration 20
      3.2.1 Source System 20
      3.2.2 Goniometer 21
      3.2.3 Integrating Spheres 22
      3.2.4 Detectors 22
   3.3 Operation 22
      3.3.1 Source System 23
      3.3.2 Bidirectional Reflectance 23
      3.3.3 Directional - Hemispherical Reflectance 28
   3.4 Uncertainties 30
      3.4.1 Introduction 30
      3.4.2 Bidirectional Reflectance 31
      3.4.3 Directional - Hemispherical Reflectance 37

4. Transfer Instruments – Spectrophotometers 40
   4.1 Description 40
   4.2 Calibration 42
   4.3 Operation 44
   4.4 Uncertainties 45

Acknowledgments 46

References 47

Appendix A: Sample Report of Test for Bidirectional Reflectance Distribution Function
Appendix B: Sample Report of Calibration for Spectral Reflectance
Appendix C: Sample Report of Test for 0°/45° Reflectance Factor
Appendix D: Sample Report of Test for 6°/Hemispherical Reflectance
Appendix E: NIST High Accuracy Reference Reflectometer - Spectrophotometer (copy of Ref. 1)
Appendix F: Establishing a Scale of Directional - Hemispherical Reflectance Factor I: The Van den Akker Method (copy of Ref. 23)
Appendix G: Reflection Properties of Pressed Polytetrafluoroethylene Powder (copy of Ref. 26)
Appendix H: Laboratory Intercomparison Study of Pressed Polytetrafluoroethylene Powder Reflectance Standards (copy of Ref. 27)
Appendix I: 45°/0° Reflectance Factors of Pressed Polytetrafluoroethylene (PTFE) Powder (copy of Ref. 28)
Appendix J: A Wavelength Standard for the Near Infrared Based on the Reflectance of Rare-Earth Oxides (copy of Ref. 29)

LIST OF FIGURES

Figure 2.1 Geometry of incident and reflected elementary radiant beams 5
Figure 3.1 Schematics of the STARR instrument 13
Figure 3.2 Components and optical path of the STARR source 14
Figure 3.3 Goniometer system of the STARR instrument 16
Figure 3.4 Detection system on the goniometer of the STARR instrument 17
Figure 3.5 Integrating sphere of the STARR instrument 19
Figure 3.6 Sample mount of the STARR goniometer 24
Figure 3.7 Specular reflectance as a function of wavelength 27
Figure 3.8 45°/0° reflectance factor as a function of wavelength 27
Figure 3.9 BRDF as a function of reflected angle at 632.8 nm 28
Figure 3.10 6°-hemispherical reflectance factor as a function of wavelength 30
Figure 4.1 Integrating Sphere Assembly of the Lambda 19 42
Figure 4.2 Spectrum of wavelength standard 45

LIST OF TABLES

Table 1.1 Available NIST Standard Reference Materials and Calibration Services for spectral reflectance and wavelength standards 2
Table 3.1 Wavelength ranges of components used in the STARR source 15
Table 3.2 Wavelength ranges of detectors used in the STARR instrument 19
Table 3.3 Wavelengths of emission lines and absorption bands used to calibrate the wavelength scale of the STARR instrument 20
Table 3.4 Relative sensitivity coefficients for bidirectional reflectance measurements 32
Table 3.5 Relative expanded uncertainties ($k = 2$) for the bidirectional reflectance of a white PTFE plaque 33
Table 3.6 Relative combined expanded uncertainties, in percent, ($k = 2$) for the bidirectional reflectance of a white PTFE plaque 33
Table 3.7 Relative expanded uncertainties ($k = 2$) for the bidirectional reflectance of a green tile 34
Table 3.8 Relative combined expanded uncertainties, in percent, ($k = 2$) for the bidirectional reflectance of a green tile 34
Table 3.9 Relative sensitivity coefficients for 6° - hemispherical reflectance measurements 38
Table 3.10 Relative expanded uncertainties ($k = 2$) for the 6° - hemispherical reflectance of a PTFE plaque 39
Table 3.11 Relative combined expanded uncertainties ($k = 2$) for the 6° - hemispherical reflectance of a PTFE plaque 39
Table 4.1 Wavelengths of emission lines and absorption bands used to calibrate the wavelength scale of the Cary 5E transfer spectrophotometer 43
Table 4.2 Wavelengths of emission lines and absorption bands used to calibrate the wavelength scale of the Lambda 19 transfer spectrophotometer 43
Table 4.3 Standard uncertainties of spectral reflectance values for the transfer spectrophotometers in the visible wavelength region 46

1. Introduction

Spectral reflectance measurements provide important information about the optical properties of many materials. NIST strives to provide the best possible standards for diffuse and specular reflectance as well as special services and a research program to support the national requirements for these measurements. For this purpose, the Optical Technology Division of NIST maintains a primary reference laboratory for spectral reflectance with specialized instrumentation and trained personnel. This primary laboratory is responsible for realizing the absolute scales of diffuse and specular reflectance.

The Optical Technology Division has designed, built, and characterized a new high-accuracy reference instrument for reflectance, designated the Spectral Tri-function Automated Reference Reflectometer (STARR) [1]. The STARR instrument is devoted to the highest accuracy measurements such as those required for maintaining master standards. It is designed to deliver greater measurement speed and accuracy, improved mechanical stability, and higher optical throughput than the previous reference instrument. The three functional operations of the STARR instrument are absolute measurements of bidirectional, specular (regular), and directional - hemispherical reflectance.

In support of the STARR instrument, two high-precision commercial spectrophotometers with reflectometer accessories are maintained as transfer instruments and are calibrated with primary reference standards from the STARR instrument. Standards calibrated by the transfer instruments under commonly used spectral and geometrical conditions are issued as Standard Reference Materials (SRMs) [2]. Reflectance standards available as of June 1997 are listed in table 1.1. Special calibrations and tests are supplemental measurement services that are provided to the optical radiation measurement community upon request and within the guidelines outlined in the NIST Calibration Services Users Guide SP-250 [3].

In general, reflection is the process by which radiant flux (or power), incident on a stationary surface, leaves that surface from the incident side without a change in wavelength; spectral reflectance is the fraction of the incident radiant flux that is reflected as a function of wavelength. A related quantity is the reflectance factor, which is simply the ratio of the reflected radiant flux to the radiant flux that would be reflected by an ideal diffuse sample irradiated and measured in exactly the same manner.

Reflectance is often categorized as specular or diffuse. For specular reflectance, also termed regular reflectance, the angle of reflection is equal and opposite to the angle of incidence. This is what occurs ideally with mirrors. For diffuse reflectance, the radiant flux is reflected at all angles within the hemisphere bounded by the plane of the sample, except in the direction of the specular reflection angle.

There are also directions assigned to the incident and reflected radiant fluxes. If the radiant fluxes are confined within solid angles along fixed directions, the term

Table 1.1 Available NIST Standard Reference Materials* and Calibration Services for spectral reflectance and wavelength standards

SRM Number	Description			
	Specular reflectance standards			
2003	1st Surface Aluminum Mirror	5.1 mm diameter	250 nm to 2500 nm	
2011	1st Surface Gold Mirror	5.1 mm diameter	600 nm to 2500 nm	
2023	2nd Surface Aluminum Mirror	5.1 mm diameter	250 nm to 2500 nm	
2026	Black Glass (NG-9)	5.1 mm diameter	250 nm to 2500 nm	
	Diffuse reflectance standards			
2015	Opal Glass	2.5 cm x 5 cm x 0.64 cm	400 nm to 750 nm	re-certification
2016	Opal Glass	10 cm x 10 cm x 0.64 cm	400 nm to 750 nm	re-certification
2044	White Diffuser, Spectralon™	51 mm diameter	250 nm to 2500 nm	
	Wavelength standards			
1920a	Rare-Earth Mixture	51 mm diameter	740 nm to 2000 nm	
	Special test			
38060S	BRDF, Specular Reflectance, Reflectance Factor			

* NIST Special Publication 260 "NIST Standard Reference Materials Catalog 1995-96" p. 107, March 1995.

"directional" is applied to the reflectance. On the other hand, if the radiant fluxes are in all directions on the incident side of the sample, the term "hemispherical" is applied to the reflectance.

In terms of these concepts of spectral reflectance, NIST provides the following types of spectral reflectance measurements:

1. Spectral bidirectional reflectance-distribution function (BRDF), which is the ratio of the reflected radiance at a given angle to the incident irradiance from another given angle, both angles being measured in the same plane. From this, the bidirectional spectral reflectance and the bidirectional spectral reflectance factor can be calculated. Note that the widely used 45°/0° reflectance factor (where the angle of incidence is 45° and the angle of reflection is 0°) is a specific instance of the more general BRDF [4,5,6].

2. Spectral specular (regular) reflectance, which is the ratio of the reflected radiant flux to the incident radiant flux, the reflection being without diffusion in accordance with the

laws of optical reflection. While this measurement is classified separately from BRDF, it is actually another specific instance [4,5,6].

3. Spectral directional - hemispherical reflectance factor, which is the ratio of the total reflected radiant flux to that reflected by a perfectly reflecting diffuser, the angle of incidence being 6° from normal and the reflected flux being collected over the entire hemisphere [4,5,6].

Spectral reflectance measurements on submitted samples are available at cost. Preliminary discussion with NIST staff is required before submission. When high accuracy or a special geometry is required, the STARR instrument is used. The transfer instrument provides most of the measurements unless they can be performed only by the STARR instrument.

The STARR instrument can provide two conditions for spectral reflectance measurements: bidirectional and directional - hemispherical. The spectral range is 200 nm to 2500 nm and the sample size that can be accommodated is 5 cm to 30 cm, square or round. For bi-directional reflectance, the incident angle can range from 0° to 80° within the horizontal plane, while any reflected angle in that same plane greater than 5° from the incident beam can be achieved. Note that the incident and reflected angles can be adjusted to measure 45°/0° reflectance factors and specular reflectances. For directional - hemispherical reflectance, a choice of integrating spheres allows incident angles of 0° (specular component excluded) or 6° (specular component included).

The transfer spectrophotometers can provide several conditions for reflectance measurements [7,8]. The minimum sample size is 2.5 cm, round or square, while the maximum sample size is approximately 15 cm. The spectral range is 200 nm to 2500 nm. The specular reflectance of mirrors can be measured for a 6° angle of incidence only. The angle of incidence is 6° for measuring both specular reflectance and directional - hemispherical reflectance. In addition, the directional - hemispherical reflectance can be measured with the specular component either included or excluded.

2. Theory

2.1 Basic Definitions and Equations

This section is concerned with stating the basic definitions and deriving the general equations which specify reflectance in terms of the beam geometry of both the incident and reflected radiant flux. In the next section, these general equations are applied to the specific geometries used with the STARR instrument to determine the corresponding measurement equations. The approach is based upon the concepts presented in Ref. [9].

The derivation of the general equations begins by considering a relatively large area of reflecting surface irradiated by a well-collimated beam of incident radiation and examining the radiation reflected from a point well within the irradiated area. Only the geometry of this situation is considered, namely the spatial parameters of position and direction of all rays. Other radiation parameters, such as wavelength, time, polarization, and fluorescence, are not discussed in this section, although they may be important in actual measurements of reflectance. Specifically, the wavelength and polarization parameters are included in the next section.

Let radiant flux be incident on a surface from the direction (θ_i, ϕ_i), within the element of solid angle $d\omega_i$, as shown in figure 2.1. The total irradiated surface area is A_i. The portion of the incident radiant flux which strikes an element of area dA_i centered on the point (x_i, y_i) is denoted by $d\Phi_i$. The reflected radiance in the direction (θ_r, ϕ_r) at the point (x_r, y_r) which comes from $d\Phi_i$ is dL_r. In general, dL_r is directly proportional to $d\Phi_i$, so that

$$dL_r = S \cdot d\Phi_i \ . \tag{2.1}$$

The factor of proportionality S will, in general, depend upon the location of the point at which the incident flux strikes, the location of the point at which the ray of radiance dL_r emerges, and the directions, so that

$$S = S(\theta_i, \phi_i, x_i, y_i; \theta_r, \phi_r, x_r, y_r) \ . \tag{2.2}$$

This basic proportionality function S is called the bidirectional scattering-surface reflectance-distribution function (BSSRDF), and is a property of the reflecting surface.

This treatment is completely general, with no simplifying assumptions other than those of geometrical optics and ignoring all but spatial parameters. No assumption is made about the mechanism involved other than that there is some form of interaction between radiation and matter by which some of the flux incident at (x_i, y_i) emerges as reflected flux from (x_r, y_r), quantitatively expressed by the function S. To obtain more tractable expressions, some simplifying assumptions will be made that will still cover a very wide range of the cases of interest.

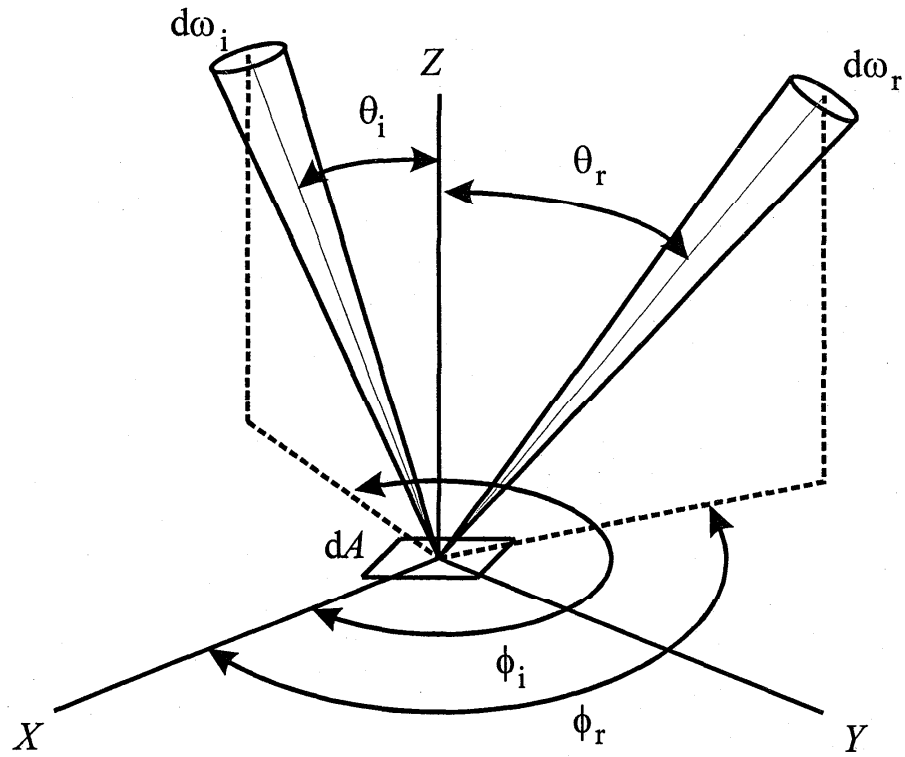

Figure 2.1. Geometry of incident and reflected elementary radiant beams.

A convenient flat surface is chosen as a reference plane to represent the reflecting surface. Then the polar angles θ are angles from the reference-plane normal, and azimuth angles ϕ are angles from an arbitrary reference direction in the reference plane, as shown in figure 2.1. Also, assume that the surface is uniformly irradiated over the entire part of the area A_i from which there is a significant contribution to the reflected flux at (x_r, y_r), so that the incident radiance depends only on direction,

$$L_i = L_i(\theta_i, \phi_i) \ . \tag{2.3}$$

The incident flux $\mathrm{d}\Phi_i$ on the element of area $\mathrm{d}A_i$ is

$$\begin{aligned} \mathrm{d}\Phi_i &= L_i \cdot \cos\theta_i \cdot \mathrm{d}\omega_i \cdot \mathrm{d}A_i \\ &= \mathrm{d}E_i \cdot \mathrm{d}A_i \end{aligned} \tag{2.4}$$

where $\mathrm{d}E_i$ is the incident irradiance and $\mathrm{d}\omega_i$ is the solid-angle element which confines the incident radiance. Summing the contributions to the reflected radiance at (x_r, y_r) from the entire incident flux in the direction (θ_i, ϕ_i) and within the solid-angle element $\mathrm{d}\omega_i$ by integrating eq (2.1) over the entire irradiated area yields

$$
\begin{aligned}
\mathrm{d}L_{\mathrm{r}}(\theta_{\mathrm{i}},\varphi_{\mathrm{i}};\theta_{\mathrm{r}},\phi_{\mathrm{r}},x_{\mathrm{r}},y_{\mathrm{r}}) &= \int \mathrm{d}L_{\mathrm{r}}(\theta_{\mathrm{i}},\varphi_{\mathrm{i}},x_{\mathrm{i}},y_{\mathrm{i}};\theta_{\mathrm{r}},\phi_{\mathrm{r}},x_{\mathrm{r}},y_{\mathrm{r}}) \\
&= \int S\cdot \mathrm{d}\Phi_{\mathrm{i}} \\
&= \mathrm{d}E_{\mathrm{i}}\cdot \int S\cdot \mathrm{d}A_{\mathrm{i}} \\
&= \mathrm{d}E_{\mathrm{i}}\cdot \int S(\theta_{\mathrm{i}},\varphi_{\mathrm{i}},x_{\mathrm{i}},y_{\mathrm{i}};\theta_{\mathrm{r}},\phi_{\mathrm{r}},x_{\mathrm{r}},y_{\mathrm{r}})\cdot \mathrm{d}A_{\mathrm{i}}
\end{aligned}
\tag{2.5}
$$

Assume further that the scattering properties of the sample are uniform and isotropic across the reference plane, so that the scattering function S does not depend on the location of the point of observation (x_r, y_r), but still depends on the distance r between (x_i, y_i) and (x_r, y_r). Equation (2.5) simplifies to

$$\mathrm{d}L_{\mathrm{r}} = \mathrm{d}E_{\mathrm{i}}\cdot f_{\mathrm{r}}(\theta_{\mathrm{i}}, \phi_{\mathrm{i}}; \theta_{\mathrm{r}}, \phi_{\mathrm{r}}) \tag{2.6}$$

where

$$f_{\mathrm{r}} = \int S(\theta_{\mathrm{i}}, \phi_{\mathrm{i}}; \theta_{\mathrm{r}}, \phi_{\mathrm{r}}; r)\cdot \mathrm{d}A_{\mathrm{i}} \tag{2.7}$$

and

$$r = [(x_{\mathrm{r}} - x_{\mathrm{i}})^2 + (y_{\mathrm{r}} - y_{\mathrm{i}})^2]^{1/2} \ . \tag{2.8}$$

Thus, for uniform irradiance over a large enough area of a uniform and isotropic surface, the basic quantity that geometrically characterizes the reflecting properties of that surface is the bidirectional reflectance-distribution function (BRDF) f_r, given by

$$f_{\mathrm{r}}(\theta_{\mathrm{i}}, \phi_{\mathrm{i}}; \theta_{\mathrm{r}}, \phi_{\mathrm{r}}) = \mathrm{d}L_{\mathrm{r}}(\theta_{\mathrm{i}}, \phi_{\mathrm{i}}; \theta_{\mathrm{r}}, \phi_{\mathrm{r}}; E_{\mathrm{i}}) \,/\, \mathrm{d}E_{\mathrm{i}}(\theta_{\mathrm{i}}, \phi_{\mathrm{i}}) \ . \tag{2.9}$$

Note that the BRDF can have any value from zero to infinity, and that real measurements involve finite, rather than infinitesimal, intervals of the parameters, yielding average values of BRDF over those intervals.

Reflectance ρ is the ratio of reflected radiant flux to incident radiant flux. From conservation of energy, it follows that reflectance may have values only in the interval from zero to one, inclusive. A general expression for reflectance can be written readily in terms of BRDF. First, the element of projected solid angle $\mathrm{d}\Omega$ is given by the product of an element of solid angle $\mathrm{d}\omega$ with the cosine of the angle θ between the normal to the surface and the direction associated with $\mathrm{d}\omega$, so that $\mathrm{d}\Omega = \cos\theta \cdot \mathrm{d}\omega$. In general, the radiant flux incident through a solid angle ω_i onto a surface element $\mathrm{d}A_i$ is

$$\mathrm{d}\Phi_{\mathrm{i}} = \mathrm{d}A \cdot \int L_{\mathrm{i}}(\theta_{\mathrm{i}}, \phi_{\mathrm{i}}) \cdot \mathrm{d}\Omega_{\mathrm{i}} \ . \tag{2.10}$$

Similarly, the flux reflected by the surface element $\mathrm{d}A$ into a solid angle ω_r is

$$\mathrm{d}\Phi_\mathrm{r} = \mathrm{d}A \cdot \int L_\mathrm{r}(\theta_\mathrm{r}, \phi_\mathrm{r}) \cdot \mathrm{d}\Omega_\mathrm{r} \,. \tag{2.11}$$

Now, the reflected radiance into the solid angle ω_r is

$$L_\mathrm{r}(\theta_\mathrm{r}, \phi_\mathrm{r}) = \int \mathrm{d}L_\mathrm{r}(\theta_\mathrm{i}, \phi_\mathrm{i}; \theta_\mathrm{r}, \phi_\mathrm{r}; E_\mathrm{i}) \tag{2.12}$$

which, using eq (2.9), gives

$$L_\mathrm{r}(\theta_\mathrm{r}, \phi_\mathrm{r}) = \int \mathrm{d}E_\mathrm{i}(\theta_\mathrm{i}, \phi_\mathrm{i}) \cdot f_\mathrm{r}(\theta_\mathrm{i}, \phi_\mathrm{i}; \theta_\mathrm{r}, \phi_\mathrm{r}) \,. \tag{2.13}$$

Expressing the incident irradiance in terms of the incident radiance in eq (2.13), eq (2.11) becomes

$$\mathrm{d}\Phi_\mathrm{r} = \mathrm{d}A \cdot \int\int f_\mathrm{r}(\theta_\mathrm{i}, \phi_\mathrm{i}; \theta_\mathrm{r}, \phi_\mathrm{r}) \cdot L_\mathrm{i}(\theta_\mathrm{i}, \phi_\mathrm{i}) \cdot \mathrm{d}\Omega_\mathrm{i} \cdot \mathrm{d}\Omega_\mathrm{r} \,. \tag{2.14}$$

The general expression for the reflectance ρ of a surface with an arbitrary configuration of beam geometry with respect to direction is obtained from the ratio of eq (2.14) to (2.10),

$$\begin{aligned} \rho(\theta_\mathrm{i},\phi_\mathrm{i};\theta_\mathrm{r},\phi_\mathrm{r};L_\mathrm{i}) &= \mathrm{d}\Phi_\mathrm{r} / \mathrm{d}\Phi_\mathrm{i} \\ &= \frac{\int\int f_\mathrm{r}(\theta_\mathrm{i},\phi_\mathrm{i};\theta_\mathrm{r},\phi_\mathrm{r}) \cdot L_\mathrm{i}(\theta_\mathrm{i},\phi_\mathrm{i}) \cdot \mathrm{d}\Omega_\mathrm{i} \cdot \mathrm{d}\Omega_\mathrm{r}}{\int L_\mathrm{i}(\theta_\mathrm{i},\phi_\mathrm{i}) \cdot \mathrm{d}\Omega_\mathrm{i}} \,. \end{aligned} \tag{2.15}$$

The only condition placed upon L_i up to this point is that it be uniform over a sufficiently large area. If it is further specified to be uniform and isotropic within the incident beam, the constant value of L_i can be brought outside the integrals in eq (2.15), leaving

$$\rho(\theta_\mathrm{i},\phi_\mathrm{i};\theta_\mathrm{r},\phi_\mathrm{r}) = (1/\Omega_\mathrm{i}) \cdot \int\int f_\mathrm{r}(\theta_\mathrm{i},\phi_\mathrm{i};\theta_\mathrm{r},\phi_\mathrm{r}) \cdot \mathrm{d}\Omega_\mathrm{i} \cdot \mathrm{d}\Omega_\mathrm{r} \tag{2.16}$$

where

$$\Omega_\mathrm{i} = \int \mathrm{d}\Omega_\mathrm{i} \,.$$

Reflectance factor R is the ratio of the radiant flux reflected by a sample surface to that reflected by an ideal perfectly diffuse standard surface irradiated in exactly the same way as the sample. For an ideal surface,

$$f_\mathrm{r}(\theta_\mathrm{i},\phi_\mathrm{i};\theta_\mathrm{r},\phi_\mathrm{r}) = 1/\pi \,, \tag{2.17}$$

so using eq (2.14) the ratio of reflected flux to ideally reflected flux is

$$\mathrm{d}\Phi_\mathrm{r} / \mathrm{d}\Phi_\mathrm{r,id} = \frac{\mathrm{d}A \cdot \int\int f_\mathrm{r}(\theta_\mathrm{i}, \phi_\mathrm{i}; \theta_\mathrm{r}, \phi_\mathrm{r}) \cdot L_\mathrm{i}(\theta_\mathrm{i}, \phi_\mathrm{i}) \cdot \mathrm{d}\Omega_\mathrm{i} \cdot \mathrm{d}\Omega_\mathrm{r}}{(\mathrm{d}A / \pi) \int L_\mathrm{i}(\theta_\mathrm{i}, \phi_\mathrm{i}) \cdot \mathrm{d}\Omega_\mathrm{i}} \ . \tag{2.18}$$

Assuming, as before, that L_i is isotropic within the full solid angle of incidence ω_i, L_i can be brought out of the integrals, leaving

$$R(\theta_\mathrm{i}, \phi_\mathrm{i}; \theta_\mathrm{r}, \phi_\mathrm{r}) = (\pi / \Omega_\mathrm{i}\Omega_\mathrm{r}) \cdot \int\int f_\mathrm{r}(\theta_\mathrm{i}, \phi_\mathrm{i}; \theta_\mathrm{r}, \phi_\mathrm{r}) \cdot \mathrm{d}\Omega_\mathrm{i} \cdot \mathrm{d}\Omega_\mathrm{r} \ . \tag{2.19}$$

2.2 Measurement Equations

2.2.1 Bidirectional Reflectance Distribution Function Measuring the BRDF of a sample is one of the primary functions of the STARR instrument. As shown in the previous section, other quantities can be calculated from the BRDF. In particular, the bidirectional reflectance $\mathrm{d}\rho$ is given by

$$\mathrm{d}\rho(\theta_\mathrm{i}, \phi_\mathrm{i}; \theta_\mathrm{r}, \phi_\mathrm{r}) = f_\mathrm{r}(\theta_\mathrm{i}, \phi_\mathrm{i}; \theta_\mathrm{r}, \phi_\mathrm{r}) \cdot \mathrm{d}\Omega_\mathrm{r} \tag{2.20}$$

and the bidirectional reflectance factor R is given by

$$R(\theta_\mathrm{i}, \phi_\mathrm{i}; \theta_\mathrm{r}, \phi_\mathrm{r}) = \pi \cdot f_\mathrm{r}(\theta_\mathrm{i}, \phi_\mathrm{i}; \theta_\mathrm{r}, \phi_\mathrm{r}) \ . \tag{2.21}$$

In addition, the BRDF as measured by the STARR instrument is also a function of wavelength λ and incident polarization σ. Therefore, these two parameters are included in f_r, yielding

$$\begin{aligned} f_\mathrm{r} &= f_\mathrm{r}(\theta_\mathrm{i}, \phi_\mathrm{i}; \theta_\mathrm{r}, \phi_\mathrm{r}; \lambda; \sigma) \\ &= \mathrm{d}L_\mathrm{r}(\theta_\mathrm{i}, \phi_\mathrm{i}; \theta_\mathrm{r}, \phi_\mathrm{r}; \lambda; \sigma) / \mathrm{d}E_\mathrm{i}(\theta_\mathrm{i}, \phi_\mathrm{i}; \lambda; \sigma) \end{aligned} \tag{2.22}$$

From eq (2.22), determining the BRDF of a sample for given values of the parameters involves measuring both the incident irradiance $\mathrm{d}E_\mathrm{i}$ and the reflected radiance $\mathrm{d}L_\mathrm{r}$. The light source generates a uniform, collimated, monochromatic, linearly polarized beam of cross-sectional area A_i. To measure the incident irradiance, the sample is removed from the beam and the detector is positioned so that the beam underfills its field stop. Therefore, all of the light in the beam is incident on the detector. To measure the reflected radiance, the sample is placed in the beam at an angle θ_i between the direction of the beam and the sample normal. The detector is then positioned a distance D from the center of the illuminated area on the sample to the aperture stop, which has circular cross-sectional area A_r. Again, the field stop of the detector is underfilled by the image of the illuminated area. The line joining the center of the illuminated area and the center of the aperture stop makes an angle θ_r with the sample normal.

The signal $S_\mathrm{i}(\lambda; \sigma)$ from the detector recorded during the measurement of the incident irradiance is given by

$$S_i(\lambda;\ \sigma) = R_i(\lambda;\ \sigma) \cdot \mathrm{d}\Phi_i(\lambda;\ \sigma)\ , \tag{2.23}$$

where $R_i(\lambda;\ \sigma)$ is the responsivity of the detector to the incident flux $\mathrm{d}\Phi_i(\lambda;\ \sigma)$. Note the explicit dependence of these values on the wavelength and polarization parameters. The incident flux in terms of irradiance $\mathrm{d}E_i(\lambda;\ \sigma)$ is given by

$$\mathrm{d}\Phi_i(\lambda;\ \sigma) = \mathrm{d}E_i(\lambda;\ \sigma) \cdot \mathrm{d}A_i\ , \tag{2.24}$$

where $\mathrm{d}A_i$ is the area of illumination. Therefore, using eqs (2.23) and (2.24), the incident irradiance is

$$\mathrm{d}E_i(\lambda;\sigma) = \frac{S_i(\lambda;\sigma)}{R_i(\lambda;\sigma)\cdot \mathrm{d}A_i}\ . \tag{2.25}$$

Likewise, the signal $S_r(\theta_i,\ \phi_i;\ \theta_r,\ \phi_r;\ \lambda;\ \sigma)$ from the detector recorded during the measurement of the reflected radiance is given by

$$S_r(\theta_i,\ \phi_i;\ \theta_r,\ \phi_r;\ \lambda;\ \sigma) = R_r(\lambda;\ \sigma) \cdot \mathrm{d}\Phi_r(\theta_i,\ \phi_i;\ \theta_r,\ \phi_r;\ \lambda;\ \sigma), \tag{2.26}$$

where $R_r(\lambda;\ \sigma)$ is the responsivity of the detector to the reflected flux $\mathrm{d}\Phi_r(\theta_i,\ \phi_i;\ \theta_r,\ \phi_r;\ \lambda;\ \sigma)$. The signal and flux now depend on the angles of reflection. The reflected flux in terms of radiance $\mathrm{d}L_r(\theta_i,\ \phi_i;\ \theta_r,\ \phi_r;\ \lambda;\ \sigma)$ is given by

$$\mathrm{d}\Phi_r(\theta_i,\ \phi_i;\ \theta_r,\ \phi_r;\ \lambda;\ \sigma) = \mathrm{d}L_r(\theta_i,\ \phi_i;\ \theta_r,\ \phi_r;\ \lambda;\ \sigma) \cdot \mathrm{d}A_i \cdot \Omega_r\ , \tag{2.27}$$

where again $\mathrm{d}A_i$ is the area of illumination and Ω_r is the solid angle from the center of that area to the aperture stop of the detector, given by

$$\Omega_r = \int \mathrm{d}\Omega_r = A_r \cdot \cos\theta_r / D^2\ . \tag{2.28}$$

Note the dependence of the reflected flux upon the angle of reflection θ_r. Combining eqs (2.26) to (2.28) yields the reflected radiance, given by

$$\mathrm{d}L_r(\theta_i,\phi_i;\theta_r,\phi_r;\lambda;\sigma) = \frac{S_r(\theta_i,\phi_i;\theta_r,\phi_r;\lambda;\sigma)}{R_r(\lambda;\sigma)\cdot \mathrm{d}A_i} \cdot \frac{D^2}{A_r \cdot \cos\theta_r}\ . \tag{2.29}$$

The BRDF is simply the ratio of eq (2.29) to eq (2.25). The area of illumination $\mathrm{d}A_i$ cancels, yielding

$$f_r(\theta_i,\phi_i;\theta_r,\phi_r;\lambda;\sigma) = \frac{S_r(\theta_i,\phi_i;\theta_r,\phi_r;\lambda;\sigma)}{S_i(\lambda;\sigma)} \cdot \frac{R_i(\lambda;\sigma)}{R_r(\lambda;\sigma)} \cdot \frac{D^2}{A_r \cdot \cos\theta_r}\ . \tag{2.30}$$

The regular reflectance $\rho(\theta_i, \phi_i; \theta_r, \phi_r; \lambda; \sigma)$, for which the special conditions $\theta_r = -\theta_i$ and $\phi_r = -\phi_i$ apply, is easily obtained from eq (2.30) by multiplying by the solid angle Ω_r, resulting in

$$\rho(\theta_i, \phi_i; -\theta_i, -\phi_i; \lambda; \sigma) = \frac{S_r(\theta_i, \phi_i; -\theta_i, -\phi_i; \lambda; \sigma)}{S_i(\lambda; \sigma)} \cdot \frac{R_i(\lambda; \sigma)}{R_r(\lambda; \sigma)} . \tag{2.31}$$

2.2.2 Directional - Hemispherical Reflectance The other primary function of the STARR instrument is to measure the directional - hemispherical reflectance of a sample. This reflectance includes both the specular and the diffuse components of the reflection. The sample to be measured is placed at a port of an integrating sphere. The incident beam strikes the sample, and the signal from a detector at another port is measured. The sphere is then rotated so that the beam strikes the sphere wall at the same angle at which it struck the sample, and again the signal is recorded. The sample is then replaced by a sample with a known reflectance, and the procedure is repeated.

In the following, the subscript x refers to the sample with the unknown reflectance, s to the sample with a known reflectance, and w to the wall of the integrating sphere. For pairs of subscripts, the first member is the object that the incident beam is striking, while the second is the sample that is at the port. For example, the subscript ws on a quantity refers to its value when the beam strikes the wall and the sample with the known reflectance is at the port. All the quantities are functions of wavelength and polarization, so this dependence is not shown explicitly in the following equations. For any of the four measurements described above, the signal S is given by

$$S = R \cdot \Phi_r , \tag{2.32}$$

where R is the responsivity of the detector and Φ_r is the reflected flux.

For the four measurements that are used to calculate the reflectance of the sample, the reflectances, in terms of the definitions from eq (2.15) and the signals from eq (2.32), are given by

$$\rho_{ws} = \frac{\Phi_{r,ws}}{\Phi_{i,ws}} = \frac{S_{ws}}{R_{ws}} \cdot \frac{1}{\Phi_{i,ws}} , \tag{2.33}$$

$$\rho_{wx} = \frac{\Phi_{r,wx}}{\Phi_{i,wx}} = \frac{S_{wx}}{R_{wx}} \cdot \frac{1}{\Phi_{i,wx}} , \tag{2.34}$$

$$\rho_{ss} = \frac{\Phi_{r,ss}}{\Phi_{i,ss}} = \frac{S_{ss}}{R_{ss}} \cdot \frac{1}{\Phi_{i,ss}} , \text{ and} \tag{2.35}$$

$$\rho_{xx} = \frac{\Phi_{r,xx}}{\Phi_{i,xx}} = \frac{S_{xx}}{R_{xx}} \cdot \frac{1}{\Phi_{i,xx}} . \tag{2.36}$$

Taking ratios for the signals measured with the samples with known and unknown reflectances, eqs (2.33) to (2.37) become

$$\frac{\rho_{xx}}{\rho_{wx}}\frac{\rho_{ws}}{\rho_{ss}} = \frac{S_{xx}}{S_{wx}}\frac{S_{ws}}{S_{ss}} \cdot \frac{R_{wx}}{R_{xx}}\frac{R_{ss}}{R_{ws}} \cdot \frac{\Phi_{i,wx}}{\Phi_{i,xx}}\frac{\Phi_{i,ss}}{\Phi_{i,ws}} \ . \tag{2.37}$$

To solve for the reflectance of the sample, ρ_{xx}, some assumptions have to be made in order to obtain this value from eq (2.37). The reflectance of the wall must remain stable during the two times when it is struck by the incident beam, so that $\rho_{wx} = \rho_{ws}$. The responsivity of the detector and integrating sphere must also remain stable over the course of the measurements, and additionally it must be independent of the sample, so that $R_{wx} = R_{xx}$ and $R_{ws} = R_{ss}$. Finally, the incident radiant flux must remain stable, both on the wall and on the sample so that $\Phi_{i,wx} = \Phi_{i,ws}$ and $\Phi_{i,xx} = \Phi_{i,ss}$, respectively. With these assumptions, which are closely realized in practice, eq (2.37) can be solved for ρ_{xx}, with the result

$$\rho_{xx} = \rho_{ss} \cdot \frac{S_{xx}}{S_{wx}}\frac{S_{ws}}{S_{ss}} \ . \tag{2.38}$$

Converting from reflectance to reflectance factor, eq (2.38) becomes

$$R_{xx} = R_{ss} \cdot \frac{S_{xx}}{S_{wx}}\frac{S_{ws}}{S_{ss}} \tag{2.39}$$

where R_{ss} and R_{xx} are the known and unknown reflectance factors, respectively.

3. Reference Instrument – STARR

3.1 Description

3.1.1 Basic Instrument The Spectral Tri-function Automated Reference Reflectometer (STARR) is designed to perform absolute spectral measurements of bidirectional, specular, and directional - hemispherical reflectance [1]. The instrument, consisting of a source, goniometer, integrating sphere, and detectors, is located on a vibration isolation table in the center of a light-tight room with black walls and ceiling and special air filters in the room ventilation system. A schematic of the instrument is shown in figure 3.1(a) with all the major components labeled. A computer is located in an adjacent room and is interfaced to the data acquisition and control electronics and devices to provide fully automatic operation of the instrument.

The source of the incident radiant flux provides a collimated, monochromatic beam of light with a known polarization over a spectral range of 200 nm to 2500 nm. The goniometer positions the sample and the detector for measurements of bidirectional reflectance. The sample holder on the goniometer centers the face of the sample on the axis of rotation, which is perpendicular to the plane of the paper in figure 3.1(a). The goniometer varies the angle of incidence from 0° to 80°, and the sample can be translated in two orthogonal directions perpendicular to the direction of the incident beam. The detector on the goniometer rotates on the same axis of rotation as the sample to measure both the incident and the reflected radiant flux, which is shown schematically in figures 3.1(b), and 3.1(c), respectively. The absolute reflectance can be calculated from the measured fluxes as detailed in the previous section. The reflected angle can have any value greater than 5° from the incident beam.

Two integrating spheres are used for directional - hemispherical reflectance measurements [10,11,12]. One sphere is used for an incident angle of 0°, while the incident angle of the other sphere is 6°. For both spheres the sample is mounted at a port opposite the entrance port of the sphere. The integrating spheres collect the reflected radiant flux over nearly the entire hemisphere, and a portion of this flux is measured by a detector attached to the sphere. The incident beam geometry for these measurements is shown in figure 3.1(d). By measuring pairs of signals, the reflectance of the sample can be calculated as detailed in the previous section.

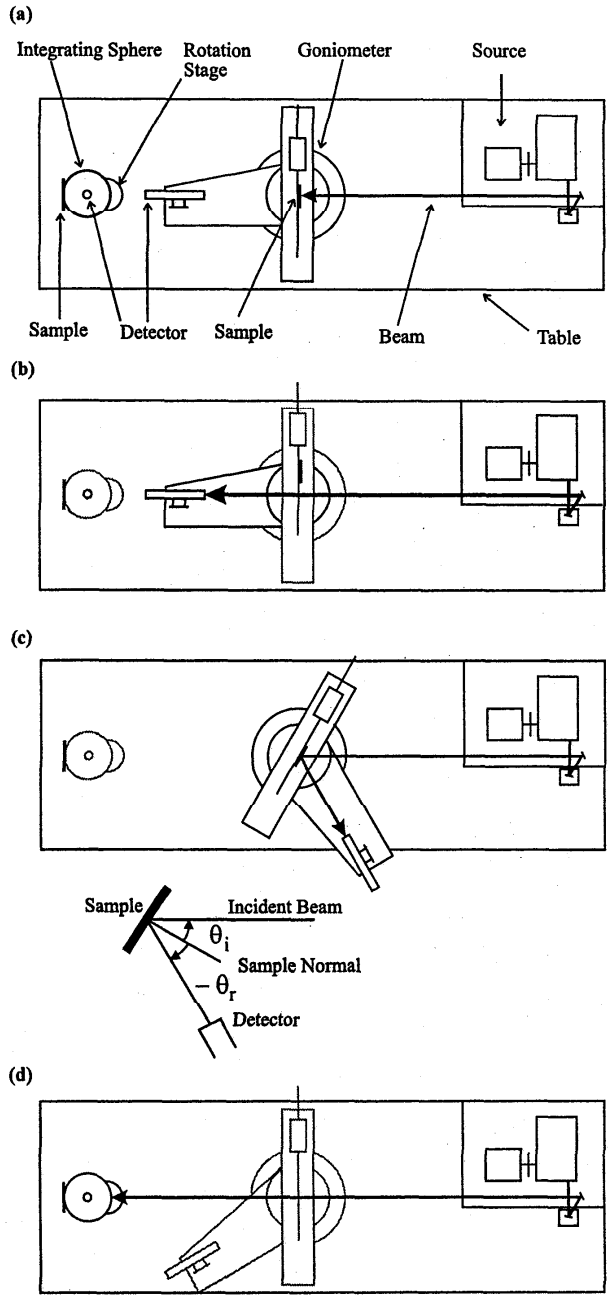

Figure 3.1. Schematics of the STARR instrument showing top views of the major components (a) and the geometrical arrangements for measuring the incident directional flux (b), the reflected directional flux (c), and the reflected hemispherical flux (d). The conventions for the incident and reflected angles are also shown in (c).

3.1.2 Source System The source system consists of an illuminator, a monochromator, a limiting aperture, a collimator, a chopper, and a polarizer. The components of the source, as well as the optical path, are shown in figure 3.2.

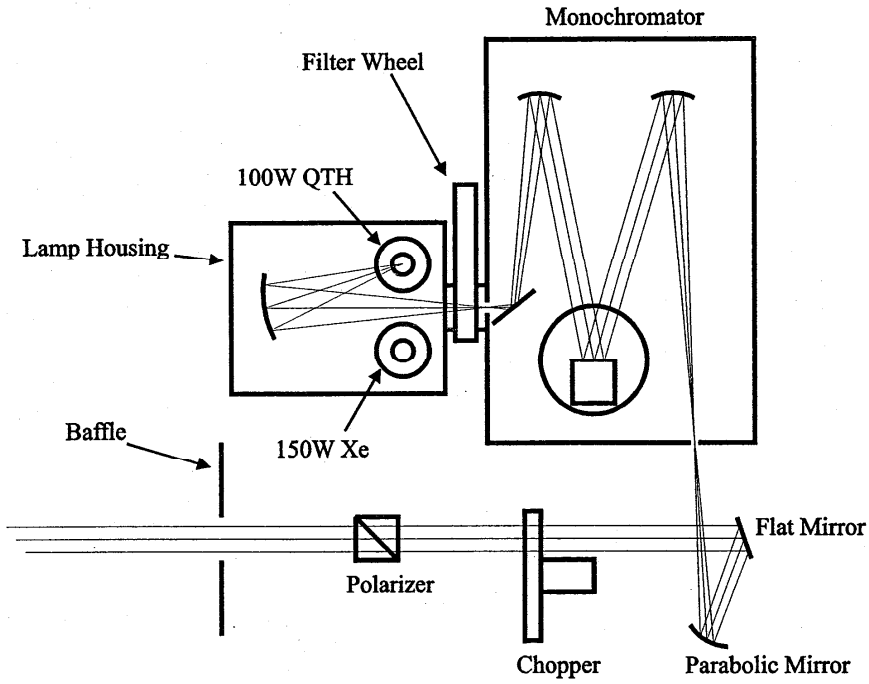

Figure 3.2. Top view of the components and optical path of the source of radiant flux for the STARR instrument.

The lamp housing contains two sources. A 150 W ultraviolet-enhanced xenon arc (Xe) lamp is used for ultraviolet wavelengths from 200 nm to 400 nm, and a 100 W quartz-tungsten-halogen (QTH) lamp is used for visible and infrared wavelengths from 400 nm to 2500 nm. Each source is operated by a separate regulated power supply used in conjunction with a light intensity controller to reduce the effects of electronic fluctuations and lamp aging. The operating conditions for each power supply are set manually. The Xe lamp is monitored by a light intensity controller equipped with a UV bandpass filter to optimize the stability in this spectral range. The QTH lamp is monitored by another light intensity controller. A concave collection mirror in the lamp housing rotates to select either of the two lamps and focuses the radiant flux from the lamp through a filter onto the entrance slit of the monochromator.

The lamp housing is attached to the monochromator with a five-position filter wheel assembly. This filter wheel contains a series of cut-on (long-pass) filters which are used for order-sorting to eliminate higher-order wavelengths from passing through the monochromator. The 1/4 m *f*/3.9 monochromator has a four-grating turret equipped with

three 600 lines/mm ruled gratings blazed at 200 nm, 400 nm, and 1000 nm, and a 150 lines/mm ruled grating blazed at 4000 nm. This last grating is not used on a regular basis, but is reserved for future upgrades into the mid-infrared spectral region. The monochromator also has an internal shutter for blocking the beam of light for dark-current measurements. The filter wheel, shutter, and grating turret are controlled by the monochromator microprocessor. The proper filter and grating for a given wavelength are automatically selected based on information stored in the monochromator non-volatile memory. The wavelength ranges covered by the various lamps, filters, and gratings are listed in table 3.1. The radiant flux exits the monochromator through a 1 mm circular aperture. The full-width-at-half-maximum spectral bandwidth is 7 nm for a 1 mm wide entrance slit and 10 nm for a 2 mm wide slit using the grating ruled at 600 lines/mm.

Table 3.1 Wavelength ranges of components used in the STARR source

Component	Wavelength range [nm]
Lamp	
Xenon arc	200 to 400
Quartz-tungsten-halogen	400 to 2500
Filter	
#1, no filter	200 to 350
#2, 309 nm cut-on	350 to 550
#3, 495 nm cut-on	550 to 900
#4, 780 nm cut-on	900 to 1600
#5, 1600 nm cut-on	1600 to 2500
Grating	
#1, 200 nm blaze	200 to 500
#2, 400 nm blaze	200 to 1600
#3, 1000 nm blaze	600 to 2500

The radiant flux exiting the monochromator passes through a baffle and is incident on a 51 mm diameter 15° off-axis parabolic mirror. The flux is collimated into a beam by this mirror and is then directed by a 51 mm diameter flat mirror through the remaining components of the source system. The collimated beam has a diameter of approximately 14 mm and a divergence of less than 1°. Both mirrors are mounted on three-axis high-resolution angular orientation holders with precision micrometers. The optical chopper is used at infrared wavelengths when a phase-locked signal is required for a sufficient signal-to-noise ratio. A Glan-Taylor polarizer is used to obtain linear polarization of the beam either perpendicular (*s*) or parallel (*p*) to the plane of incidence.

The polarizer is automated and computer controlled. The beam passes through a final baffle before exiting the source system.

3.1.3 Goniometer The goniometer used to position the sample for bidirectional reflectance measurements has four independent positioning stages. A mechanical drawing of the goniometer, showing the sample holders and detector, is shown in figure 3.3. The sample holder, designed and manufactured by NIST, is attached to a two-axis linear positioning system. This positioning system is used to center the sample in the incident beam, raster-scan the sample, and position the sample out of the path of the beam when making a measurement of the incident beam radiant flux.

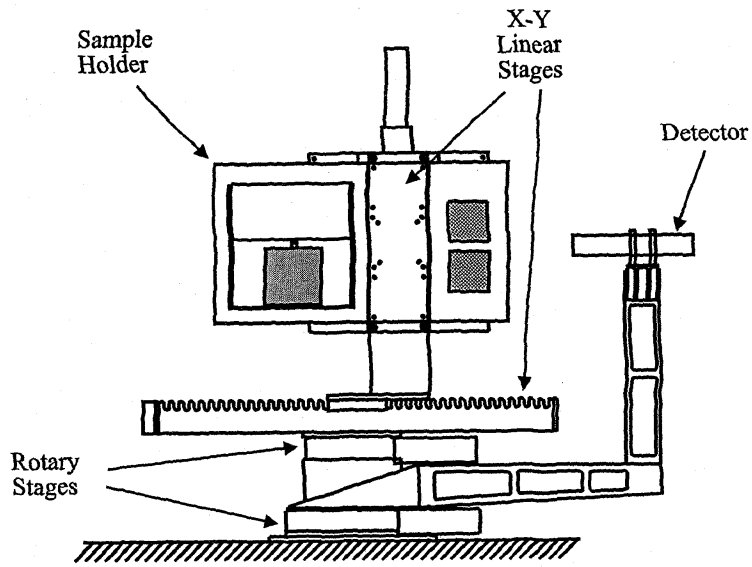

Figure 3.3. Front view of the goniometer system of the STARR instrument showing the sample holder, stages, and detector mount.

The linear positioning system is mounted on a rotation stage used to rotate the sample with respect to the incident beam. In figure 3.3, the axis of rotation is in the plane of the paper. The relatively thin profile of the sample holder and positioning system gives the goniometer a range of incident angles from 0° to 80° while maintaining mechanical rigidity. The detector system is attached to a light-weight rigid arm which is mounted on a second rotation stage. This second rotation stage is independent of and coaxial with the sample rotation stage. This allows the detector to rotate around the sample holder at a constant distance of 672.6 mm from the sample rotation axis to the solid-angle limiting aperture. These two rotation stages are precisely aligned, which was

achieved through high precision machining of a heavy-duty stainless steel chassis. The resolution and repeatability of the rotation stages are 0.001° and 0.01°, respectively. All four stages are fitted with servo motors controlled by a four-axis motion controller interfaced to the computer.

A drawing of the detector system and the optical path for reflected radiant flux is shown in figure 3.4. The detector system consists of a precision circular aperture, a fused silica lens with a focal length of 150 mm, and several stray-light reducing baffles mounted in a 51 mm diameter cylindrical housing with the detector mounted at the end. Two precision apertures, one 31.85 mm in diameter and the other 44.42 mm in diameter, can be manually interchanged. For measurements of the incident radiant flux, which is in a collimated beam, the precision aperture is underfilled and the lens converges the beam so that the detector is also underfilled. For measurements of the reflected radiant flux, the precision aperture is the aperture stop and defines the collection solid angle, and the detector is the field stop. The entire image of the incident beam upon the sample is within the field of view of the detector system for incident angles as large as 60°.

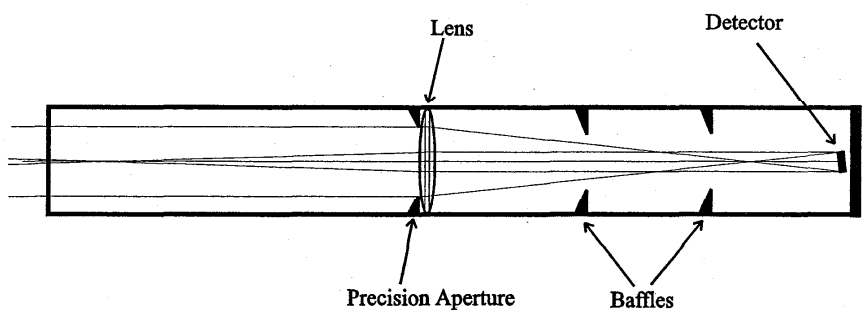

Figure 3.4. Cross-section of the detection system on the goniometer system of the STARR instrument.

Three detectors are manually interchangeable and mounted at the end of the cylindrical housing, allowing the detectors to be changed without needing to re-align the system. A uv-enhanced silicon (Si) photodiode, with dimensions 10 mm by 10 mm, is used for the spectral range of 200 nm to 1100 nm. A germanium (Ge) photodiode thermoelectrically cooled to –20 °C mounted on a 38 mm diameter integrating sphere coated with polytetrafluoroethylene (PTFE) is used for the spectral range of 800 nm to 1600 nm. The flange surrounding a 10 mm diameter entrance port of the integrating sphere fits into the end of the cylindrical housing. This same integrating sphere and thermoelectric cooling is used with an indium arsenide (InAs) photodiode for the spectral range of 1000 nm to 2500 nm.

The output current of the detector is converted to a voltage using a low-noise transimpedance amplifier. The output voltage of this amplifier is measured directly by a

seven and one-half digit digital voltmeter for the Si and Ge detectors. For the InAs detector, the incident beam is chopped and the output voltage is measured with a lock-in amplifier. The output signal of the lock-in is measured with the voltmeter.

3.1.4 Integrating Spheres Two separate integrating spheres are used to measure directional - hemispherical reflectances. Both integrating spheres are constructed of aluminum, have diameters of 30 cm, and are lined with a 10 mm thick coating of PTFE to a density of 1 g/cm^3. The spheres have 50.8 mm diameter sample ports, 38 mm diameter entrance ports, and 48 mm diameter detector ports. A cross-section of one of the spheres is shown in figure 3.5. The two spheres are identical except for a difference in the fixed angle at which the incident beam strikes the sample. In one sphere, the incident angle is 0°, so that the specular component of the reflected flux is excluded by the detector. In the other sphere most of the specular component is included in the measurement since the incident angle is 6°. Both spheres are mounted on a rotation stage so that the entrance port is centered on the incident beam and placed on the axis of rotation. Rotations of the spheres about this axis allow the incident beam to alternately strike the sample and the sphere wall.

The sample is pressed against the outside of the sample port and supported by adjustable tabs, and then secured with a spring-type clamp. The surface of the sample is located slightly inside the radius of curvature of the internal surface of the integrating sphere to allow as much of the diffusely reflected flux as possible to be included in the measurement. The incident beam has a diameter of 20 mm when it illuminates the sample. The area of the integrating sphere illuminated by the incident beam is built up so that direct reflection of the flux to the sample port is prevented.

The detector port is located 90° from the entrance and sample ports. Direct reflections from the sample to the detector are prevented by a collar, coated with PTFE, at the detector port, as shown in figure 3.5. The appropriate detector for the spectral range is mounted at the detector port. The same Si and Ge detectors that are used with the goniometer are used with the integrating spheres. For longer wavelengths, a liquid nitrogen cooled indium antinomide (InSb) detector is used for the spectral range 900 nm to 2500 nm. As with the goniometer, the output currents of the Si and Ge detectors are amplified and measured by the voltmeter. The chopper is used with the InSb detector, so the lock-in is also included in the detection circuit. A summary of the spectral ranges of the detectors used for the different reflectance configurations is given in table 3.2.

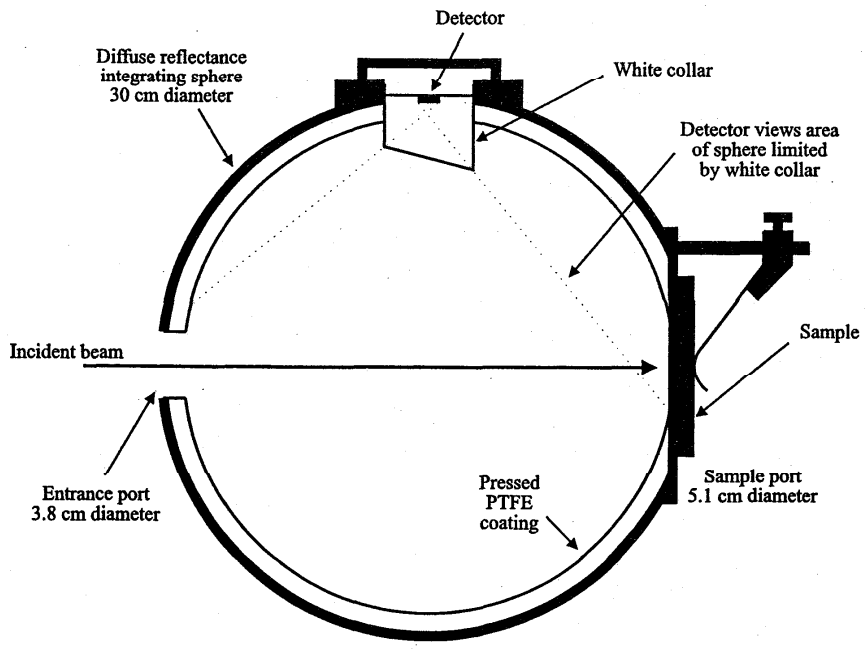

Figure 3.5. Cross-section of the integrating sphere used for 6° - hemispherical reflectance measurements with the STARR instrument.

Table 3.2 Wavelength ranges of detectors used in the STARR instrument

Detector	Wavelength range [nm]
Bidirectional reflectance	
Si	200 to 1100
Ge	800 to 1700
InAs	1200 to 2500
Directional - hemispherical reflectance	
Si	200 to 1100
Ge	800 to 1700
InSb	900 to 2500

3.2 Calibration

3.2.1 Source System Wavelength calibration consisted of comparing the wavelength indicated by the monochromator to the true wavelength. This was accomplished by measuring the emission lines of spectral line sources [13,14] and the absorption bands of some materials [15,16]. These emission lines and absorption bands are listed in table 3.3.

A low-pressure emission line lamp was mounted in place of one of the lamps in the lamp housing, and the detector on the goniometer arm, either Si or InAs, was rotated to intercept the beam emerging from the source. The monochromator was scanned through the wavelength regions of the emission lines of the lamp and the signal was recorded at small wavelength intervals. This was repeated for all the emission lamps listed in table 3.3. Likewise, the absorption band materials were mounted in the beam emerging from the source, and scans of the monochromator were performed as before.

Table 3.3 Wavelengths of emission lines and absorption bands used to calibrate the wavelength scale of the STARR instrument

Source	Wavelength [nm]
Emission lines	
Hg	253.65, 334.15, 435.83, 546.07, 1014.0, 1529.5
He	587.56, 667.81
Cd	508.58, 643.85
Absorption bands	
Polystyrene (0.6 mm)	2144
1,2,4-trichlorobenzene (0.5 mm)	1660.6, 2152.6, 2494
Didymium glass (6 mm)	1067

The indicated wavelength of the monochromator was given by the centroid of the resulting signal. The difference between the indicated wavelength and the true wavelengths of the emission lines and absorption bands was used to correct the indicated wavelength and thereby calibrate the wavelength of the monochromator. The standard uncertainty in wavelength from this calibration was 0.1 nm at ultraviolet and visible wavelengths and 0.5 nm at infrared wavelengths.

The stray radiation present in the monochromator was determined by filling the entrance slit with the light from a HeNe laser operating at 632.8 nm. The emerging beam was again incident on the Si detector, and the signal was recorded as the wavelength was scanned. The fraction of stray radiation decreased from approximately 80 x 10^{-6} at

600 nm to 0.5×10^{-6} at 400 nm. A similar level of stray radiation was found at wavelengths longer than that of the laser and using methods with filters [17,18].

The stability of the Xe source was measured with the beam emerging from the source incident on the Si detector. Signals from both the beam and background were measured at wavelengths from 200 nm to 400 nm for 30 min. The relative standard deviation of the net signal was 0.1 percent over this time. A similar measurement was performed with the QTH lamp at visible and infrared wavelengths using the Si and Ge detectors, and the relative standard deviation of the net signal varied from 0.01 percent to 0.02 percent.

3.2.2 Goniometer Calibration of the goniometer involved aligning the sample holder and incident beam with the axis of rotation. The axes of the two rotation stages were machined to be aligned by the hardware that mounts them to the optical table. Likewise, the sample holder was designed and machined so that the front surface of the sample is vertical and coplanar with the axis of rotation.

To align the horizontal position of the sample holder on the axis of rotation, an alignment jig with a cross-hair at the center was mounted in the sample holder. An alignment telescope viewed the jig, and the horizontal position of the sample holder was adjusted so that the cross-hair did not translate upon rotations of the sample holder. The center of the sample holder was positioned on the axis of rotation to within 0.1 mm.

The incident beam was centered on the axis of rotation and made normal to the sample in several steps using an alignment mirror mounted on the sample holder. For alignment in the vertical plane, the tilts and translations of the source mirrors were adjusted until the beam was retroreflected from the alignment mirror. The translations of the source mirrors in both the vertical and horizontal planes were adjusted to center the beam on the alignment mirror. Finally, the rotation of the alignment mirror was adjusted using the sample rotation stage so that the incident beam was retroreflected, which set the zero for the angle of incidence within 0.1°.

The area of the aperture stop of the detector system was determined using the NIST High Accuracy Aperture Comparator [19], and has an assigned relative standard uncertainty of 0.05 percent. The distance from the sample to the aperture stop was measured using a precision inside-micrometer. This distance was measured at five different detector arm angles at 45° intervals and varied by less than 0.1 mm.

The zero of the detector rotation stage was set by centering the detector system on the incident beam. An alignment mirror was then placed in the sample holder and rotated to retroreflect the incident beam. The sample holder was rotated in 10° steps and the detector was positioned to the appropriate angle to intercept the specular reflection of the beam. The distance from the center of the detector to the center of the reflected beam was measured for each angular setting. This procedure was repeated several times. The largest measured displacement of the beam from the detector center was 1.0 mm, corresponding to an angle of 0.1° at the distance from the sample to the receiver.

3.2.3 Integrating Spheres Calibration of the integrating spheres simply required that the incident beam be perpendicular to the entrance port of the sphere, pass through the center of this port upon rotation of the sphere, and strike the center of the sample port at the correct angle. The angle of incidence was set by designing the center of the sample port to be at an angle of either 0° or 6°, in the horizontal plane, from the diameter of the sphere passing through the center of the entrance port. The mount for the sphere was designed so that the entrance port was centered on the axis of rotation. Using translations and rotations of the sphere, the incident beam was centered on both the entrance and sample ports using cross-hairs at these ports and aligned perpendicular to the entrance port by retroreflecting the beam with a mirror over this port. The alignment was checked by rotating the sphere and verifying that the incident beam struck the correct portion of the sphere wall.

3.2.4 Detectors The linearity of the detectors was determined using a combination of multiple apertures and neutral density filters [20,21]. A double aperture mechanism consisting of two adjacent semicircular apertures, each with its own shutter, was placed in the sample holder and positioned such that both apertures were overfilled by the incident beam. The signal due to light passing through aperture "A" was measured and designated V_A. The signal due to light passing through aperture "B" was measured and designated V_B. Finally, the signal due to light passing through both apertures simultaneously was measured and designated V_{AB}. A neutral density filter was then used to attenuate the beam, and the above measurement sequence was repeated. This process continued using successively higher density filters until the attenuated beam could no longer be measured. These measurements were repeated at several wavelengths. The data were analyzed to determine at what signal level the relationship $V_A + V_B = V_{AB}$ was no longer satisfied to within the uncertainty of the measurement. For all detectors, it was found that the above relationship was satisfied until the noise floor of the detector system was reached. Therefore, the nonlinearity of the detectors was significantly less than 0.01 percent.

Since the Si detector is used without an integrating sphere, its response uniformity was measured in the NIST Detector Comparator Facility [22]. The response uniformity of the other detectors was not determined since they use an integrating sphere. The peak-to-valley nonuniformity of the Si detector was as high as 1 percent at 1000 nm and 0.6 percent at 250 nm. However, comparing the areas of the detector illuminated by the incident and reflected beams, the effect of these nonuniformities is less than 0.01 percent for the STARR instrument. The nonuniformity would contribute uncertainty only for measuring samples with a significant nonuniform spatial distribution of reflected radiant flux, which was not a measurement that the system was designed to perform.

3.3 Operation

Determining the reflectance of a sample requires several steps, namely setting up the source and detection systems, aligning the sample, and performing the measurements. Since the source system is common to both the goniometer and the integrating spheres, its setup is described first, followed by descriptions of the setup and operation for the two types of reflectance measurements. Samples are usually measured in batches, i.e. several

samples of the same type are measured in sequence. Therefore, the instrument setup is performed once prior to the batch run, and then the samples are measured. The spectral range of the measurement determines the lamp and detector combination. In some cases, more than one of either may have to be used.

3.3.1 Source System Setting up the source system first involves checking the wavelength calibration of the monochromator. As described in section 3.2 above, the wavelength is calibrated using the spectral lines of emission lamps. If there is an obvious discrepancy between this wavelength calibration and the one stored in the computer program, the new wavelength calibration is stored in memory and used in the program that operates the instrument.

The lamp appropriate for the spectral range of the measurement is turned on, the mirror in the lamp housing is turned to the appropriate position, and the lamp is allowed to warm up for at least an hour. The power to the lamp is adjusted manually to 150 W for the Xe arc lamp and 96 W for the QTH lamp. The grating is observed during the warm up period to verify that it is fully illuminated by the lamp.

3.3.2 Bidirectional Reflectance In most cases the sample, whether measuring diffuse or specular reflectance, is mounted in a holder. The sample holder attaches to the sample mount of the goniometer, shown in figure 3.6. The top bracket is attached to two parallel rails, allowing it to adjust vertically. When the sample holder is in place, the weighted top bracket pushes down on the holder and keeps it in place.

A similar holder with a glass plate, scribed with a cross-hair at the center is used to align the sample holder and the goniometer. This holder is referred to as the alignment jig. The jig is placed in the sample mount and adjusted so that the center is on the axis of rotation, shown in figure 3.6. The holder is designed so that the front of the sample, and hence the front of the glass plate of the alignment jig, is in the plane indicated in figure 3.6. With the incident beam striking the alignment jig, the two linear translation stages of the goniometer are adjusted so that the cross-hair of the jig is centered in the beam to within 0.2 mm. The absolute positions of these stages are recorded by the computer program to set the position of the center of the sample. Next, the rotation stage attached to the sample mount is adjusted so that the retroreflected beam returns to the exit slit of the monochromator to within 0.1°. The absolute position of this stage is recorded to set the position of zero rotation for the sample. The position of the alignment jig in the sample mount is indexed appropriately, the jig is removed, and a sample is put in its place. Using these techniques, the front of the sample is placed on the axis of rotation to within 0.1 mm.

The alignment procedure for the detector is as follows. Using the linear stage, the sample is translated horizontally until the incident beam is clear of the sample and falls on the detector. This position of the linear stage is also recorded by the computer. Then, the detector and front baffle tube are removed from the cylindrical housing. An alignment jig is placed over the front of the housing and the position of the housing is adjusted using tilt and translation stages and the rotation stage attached to the housing so

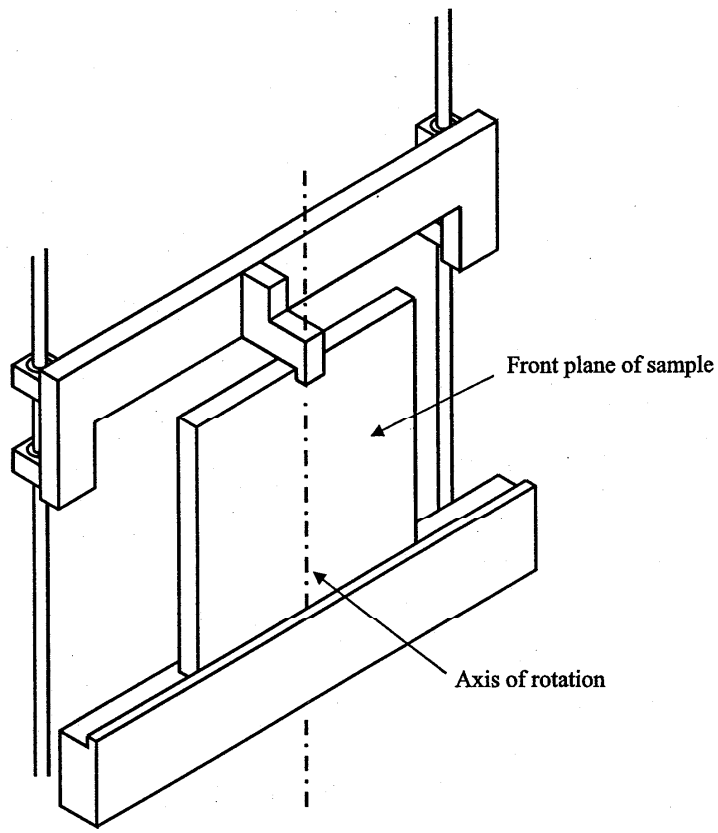

Figure 3.6. Sample mount of the STARR goniometer.

that the incident beam falls on the centers of both the alignment jig and the hole for the detector. The absolute position of the rotation stage is recorded to set the position of zero rotation for the detector. The front baffle tube and detector are reattached to the housing.

The operating parameters for the detector are determined prior to the measurements. With the incident beam falling on the detector, the signal is monitored at selected wavelengths in the spectral range of the measurement. The gain on the transimpedance amplifier is adjusted so that the maximum signal is less than 11 V. The number of power line cycles of the voltmeter, either 10 or 100, and the number of voltage readings recorded by the computer, between 3 and 20, are determined so that the standard deviation of the signal is less than 0.0002 V. The same parameters are used for all the measurements of the samples in the batch. The incident and reflected angles and wavelengths are entered in the computer program.

Since the incident beam, sample normal, and measured reflected beam are all in the same horizontal plane, the azimuth angles $\phi_i = \phi_r = 0$ are not included in the following equations. From eq (2.29), assuming the responsivity of the detector remains constant

over the time period of the measurement, the BRDF for a fixed linear polarization of the incident beam is given by

$$f_r(\theta_i;\theta_r;\lambda;\sigma)=\frac{S_r(\theta_i;\theta_r;\lambda;\sigma)}{S_i(\lambda;\sigma)}\cdot\frac{D^2}{A_r\cdot\cos\theta_r}\ , \tag{3.1}$$

where θ_i is the incident angle, θ_r is the reflected angle, λ is the wavelength, σ is the polarization, S_i is the signal from the incident radiant flux, S_r is the signal from the reflected radiant flux, D is the distance from the sample to the aperture stop, and A_r is the circular area of the aperture stop. Defining the geometrical factor by

$$\Omega_r = A_r\cdot\cos\theta_r / D^2 \tag{3.2}$$

simplifies eq (3.1) to

$$f_r(\theta_i;\theta_r;\lambda;\sigma)=\frac{S_r(\theta_i;\theta_r;\lambda;\sigma)}{S_i(\lambda;\sigma)}\cdot\frac{1}{\Omega_r}\ . \tag{3.3}$$

The BRDF of unpolarized light is given by the average of the BRDFs obtained for the two orthogonal polarizations of the incident beam, denoted by s and p, so that

$$f_r(\theta_i;\theta_r;\lambda)=\frac{1}{2}\left[f_r(\theta_i;\theta_r;\lambda;s)+f_r(\theta_i;\theta_r;\lambda;p)\right]\ . \tag{3.4}$$

Note that the reflectance ρ is given by

$$\rho=\Omega_r\cdot f_r \tag{3.5}$$

and the reflectance factor R is given by

$$R=\pi\cdot f_r\ . \tag{3.6}$$

From eqs (3.3), (3.5), and (3.6), measurements of BRDF, reflectance, and reflectance factor require measurements of the signals from the incident and reflected radiant flux. Net signals are used in all the calculations, and are the signal obtained with the shutter on the monochromator closed (i.e. no light from the source) subtracted from the signal obtained with the shutter open. For fixed incident and reflected angles, wavelength, and polarization, the following measurement sequence is performed. The sample is horizontally translated out of the path of the incident beam, the detector is rotated into the path of the incident beam, and the net incident signal S_i is measured. The sample is then translated into the incident beam and rotated to the appropriate incident angle, the detector is rotated to the appropriate reflected angle, and the net reflected signal S_r is measured. The net incident signal is measured again, and the two values are averaged to obtain the final incident signal.

The signals, together with the distance, area, and angle, are used in eq (3.3) to calculate BRDF, from which the reflectance and reflectance factor can also be calculated by using eqs (3.5) or (3.6), respectively. Equation (3.3) assumes that the source is a point, while in fact the beam has a diameter of at least 14 mm on the sample. Therefore, eq (3.3) is modified to account for the actual projected area of the incident beam on the sample for each angle of incidence.

In terms of a nested loop structure, the measurement sequence for the signals described above is the innermost loop. The next outer loop varies the reflected angles, the next loop the incident angles, the next loop the wavelengths, and the outermost loop the polarization. The spatial uniformity of BRDF can be determined for $\theta_i = 0$ by raster scanning the sample. The loop that translates the sample horizontally and vertically occurs between the loops controlling the incident and reflected angles.

The performance of the instrument is checked by measuring the BRDF of check standards similar to the type of sample under test. The number of times a check standard is measured depends upon previous experience with the samples measured in the batch. If similar samples have been measured previously, the check standard is measured only once. Otherwise, the check standard is measured both before and after the samples of the batch have been measured. The check standards are porcelain enamel on steel, a Russian opal, diffuse aluminum, and pressed PTFE.

Representative reflectances are plotted in figures 3.7 to 3.9. The specular reflectances of various mirrors as a function of wavelength are shown in figure 3.7. The 45°/0° reflectance factor of PTFE as a function of wavelength is shown in figure 3.8, while the BRDF of PTFE at 632.8 nm as a function of reflected angle is shown in figure 3.9. Appendices A, B, and C are sample reports of BRDF, specular reflectance, and 45°/0° reflectance factor measurements, respectively.

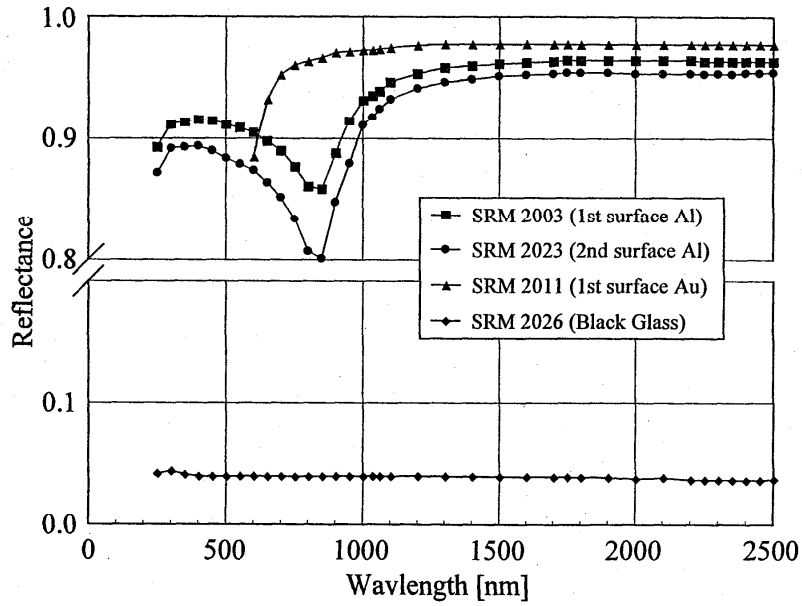

Figure 3.7. Specular reflectance as a function of wavelength for the SRMs listed in the legend. The relative expanded uncertainties of the reflectances, approximately 0.1 percent, are within the sizes of the symbols.

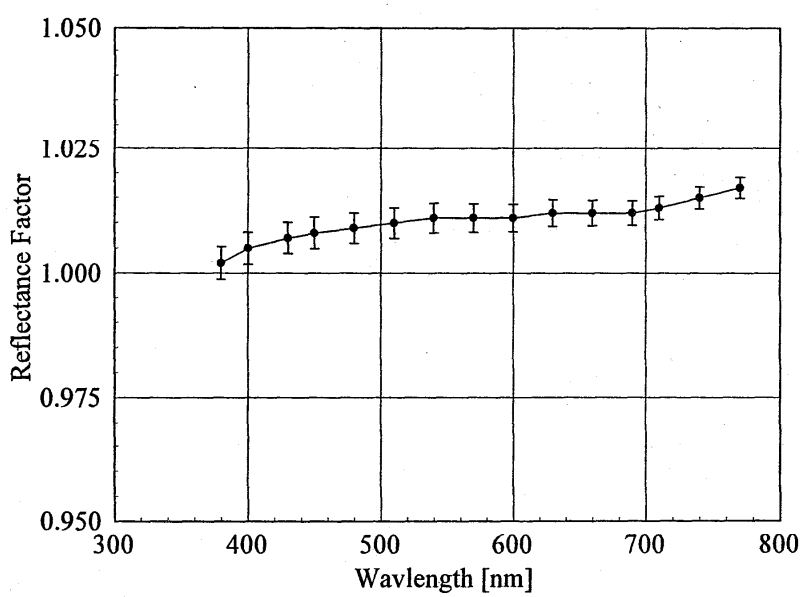

Figure 3.8. 45°/0° reflectance factor as a function of wavelength for a PTFE plaque. The vertical bars are the expanded uncertainties of the reflectance factor.

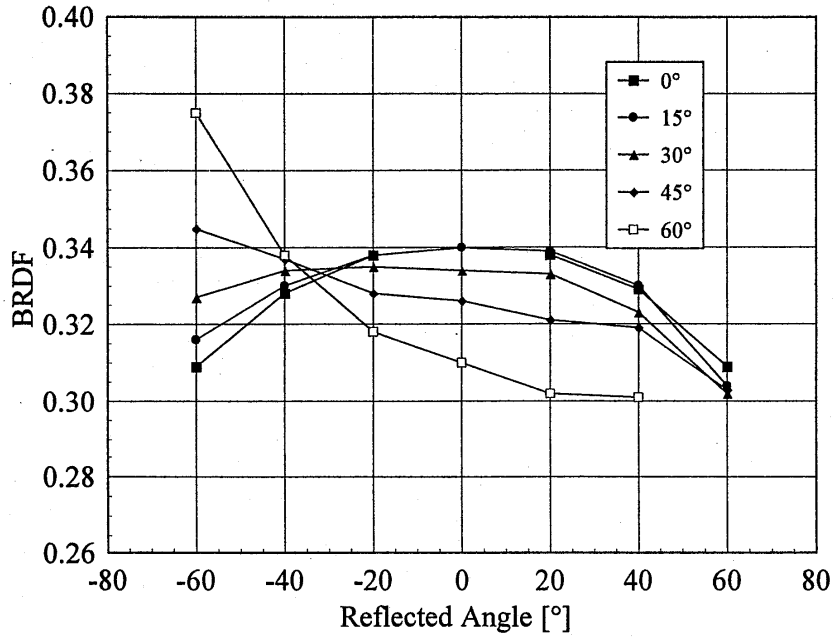

Figure 3.9. BRDF as a function of reflected angle at 632.8 nm for a PTFE plaque at the indicated incident angles. The relative expanded uncertainties of the BRDF, less than 0.2 percent, are within the sizes of the symbols.

3.3.3 Directional - Hemispherical Reflectance The sample to be measured is placed at the sample port of the integrating sphere. Three aluminum slides surrounding the sample port are adjusted to center the sample in the port, and a spring-type clamp is used to hold the sample against the port. The position of the incident beam is checked to verify that it passes through the center of the entrance port and strikes the center of the sample. The appropriate detector is attached to the detector port of the integrating sphere.

The operating parameters for the detector are determined prior to the measurements in the same manner as for the bidirectional measurements. The gain, number of power line cycles, and number of readings obtained from this procedure are then used for all the measurements of the samples in the batch.

From eq (2.39), assuming the responsivity of the detector and integrating sphere remains constant over the time period of the measurement and including the wavelength dependence, the reflectance factor of the sample R_x is given by

$$R_x(\lambda) = R_s(\lambda) \cdot \frac{S_{xx}(\lambda)}{S_{wx}(\lambda)} \frac{S_{ws}(\lambda)}{S_{ss}(\lambda)} \ . \tag{3.7}$$

where R_s is the reflectance factor of the standard, S_{xx} and S_{wx} are the signals obtained with the sample at the port and the incident beam striking the sample and wall, respectively, and S_{ss} and S_{ws} are the signals obtained with the standard at the sample port and the incident beam striking the standard and wall, respectively. The primary standard is a set of three flat PTFE samples of the same type that were calibrated for absolute spectral directional - hemispherical reflectance factor using the techniques described in Ref. [11,23,24]. Working standards of Vitrolite, Russian opal, white enamel, and a white tile were calibrated using the PTFE samples [23] and are used for measurements of similar samples.

The signals obtained with either a sample or a standard at the sample port are obtained in the same manner. At a fixed wavelength, and with no polarization of the beam, the net signal from the incident beam striking the target area of the integrating sphere wall is measured. The sphere is then rotated so that the incident beam strikes the sample at the sample port, and the net signal, S_{xx} or S_{ss}, is measured. Finally, the sphere is rotated back so that the incident beam again strikes the target area, and the net signal is measured. The two net signals obtained with the beam incident on the target area are averaged to obtain the signal S_{wx} or S_{ws}.

The signals are measured at each wavelength specified in the computer program. In general, the three PTFE standards are measured, then the sample, and finally the three PTFE standards again. The average reflectance factors and measured signals of the standards are used in eq (3.7), along with the signals obtained from the sample, to calculate the reflectance factor of the sample. Representative 6° - hemispherical reflectance factors as a function of wavelength are shown in figure 3.10, and Appendix D is a sample report of a 6° - hemispherical reflectance factor measurement.

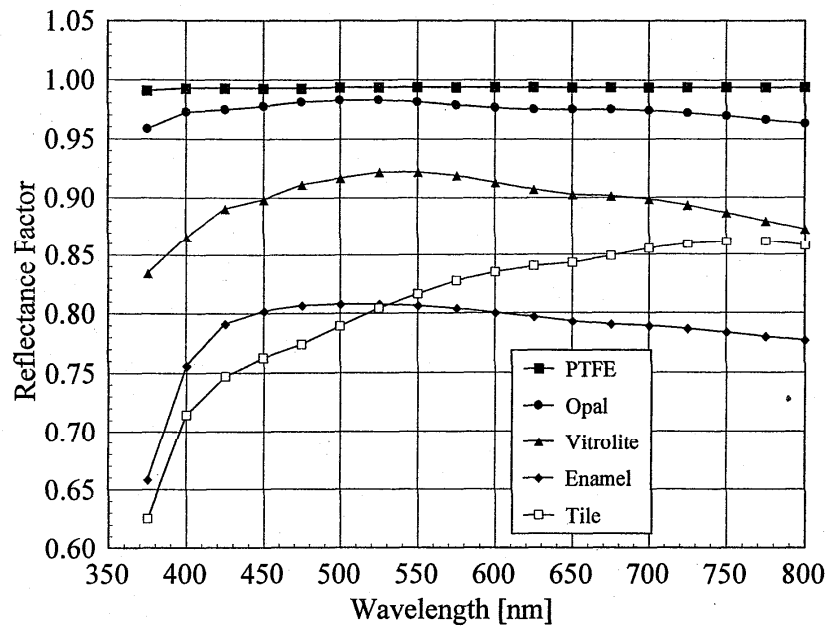

Figure 3.10. 6° - hemispherical reflectance factor as a function of wavelength for the materials listed in the legend. The relative expanded uncertainties of the relectance factor, approximately 0.3 percent, are within the sizes of the symbols.

3.4 Uncertainties

3.4.1 Introduction The approach to the uncertainty analysis follows the guidelines given in Ref. [25]. This section details the basic definitions and equations used in the uncertainty analysis, while their application to reflectance measurements are given in the following two sections.

In general, the purpose of a measurement is to determine the value of a measurand y, which is obtained from n other quantities x_i through the functional relationship f, given by

$$y = f(x_1, x_2, ..., x_i, ..., x_n) . \tag{3.8}$$

The standard uncertainty of an input quantity x_i is the estimated standard deviation associated with this quantity and is denoted by $u(x_i)$. In addition, the relative standard uncertainty is given by $u(x_i) / x_i$. The standard uncertainties may be obtained using either a Type A evaluation of uncertainty, which is based on statistical analysis, or a Type B evaluation of uncertainty, which is based on other means.

The estimated standard uncertainty in the measurand y is the combined standard uncertainty $u_c(y)$. To first order, and assuming that the standard uncertainties of each input quantity are uncorrelated, $u_c(y)$ is given by the law of propagation of uncertainty,

$$u_c^2(y) = \sum_{i=1}^{n} \left(\frac{\partial f}{\partial x_i} \right)^2 u^2(x_i) \ , \tag{3.9}$$

where $\partial f / \partial x_i$ is the sensitivity coefficient. For additive functional relationships, eq (3.9) is convenient for calculating the combined standard uncertainty. However, for multiplicative functional relationships, the relative combined standard uncertainty $u_c(y) / y$ is more convenient, and is given by

$$u_c^2(y) / y^2 = \sum_{i=1}^{n} \left(\frac{1}{y} \frac{\partial f}{\partial x_i} \right)^2 u^2(x_i) \ , \tag{3.10}$$

where $(1 / y)$ $(\partial f / \partial x_i)$ is the relative sensitivity coefficient. The expanded uncertainty U is given by $k \cdot u_c(y)$, where k is the coverage factor and is chosen on the basis of the desired level of confidence to be associated with the interval defined by U. For the purpose of this publication, $k = 2$, which defines an interval having a level of confidence of approximately 95 percent.

3.4.2 Bidirectional Reflectance Four measurement equations are relevant for determining the functional relationship of the input quantities to the measurand for bidirectional reflectance. These are stated in terms of BRDF for convenience and their extension to reflectance and reflectance factor can be easily determined from eqs (3.5) and (3.6).

The first measurement equation relates the BRDF to the signals and the geometrical quantities, and is given by eq (3.1),

$$f_r(\theta_i;\theta_r;\lambda;\sigma) = \frac{S_r(\theta_i;\theta_r;\lambda;\sigma)}{S_i(\lambda;\sigma)} \cdot \frac{D^2}{A_r \cdot \cos\theta_r} \ . \tag{3.11}$$

The second equation relates the signal from the reflected radiant flux to the incident flux, and is given by

$$S_r(\theta_i;\theta_r;\lambda;\sigma) = R(\lambda) \cdot f_r(\theta_i;\theta_r;\lambda;\sigma) \cdot \Omega_r \cdot \Phi_i(\lambda;\sigma) \ . \tag{3.12}$$

Finally, the incident beam is not monochromatic at a single wavelength λ but also has contributions from other wavelengths λ', so that $\Phi_i = \Phi_i(\lambda, \lambda')$. Therefore, the signals depend on the spectral properties of the incident flux, the BRDF, and the detector responsivity. The measurement equations for the signals from the incident and reflected fluxes are given by

$$S_{\mathrm{i}}(\lambda) = \int R(\lambda') \cdot \Phi_{\mathrm{i}}(\lambda, \lambda') \cdot \mathrm{d}\lambda' \text{ and} \tag{3.13}$$

$$S_{\mathrm{r}}(\lambda) = \int R(\lambda') \cdot f_{\mathrm{r}}(\theta_{\mathrm{i}}; \theta_{\mathrm{r}}; \lambda') \cdot \Omega_{\mathrm{r}} \cdot \Phi_{\mathrm{i}}(\lambda, \lambda') \cdot \mathrm{d}\lambda' \,, \tag{3.14}$$

where the integrals are over all wavelengths λ'.

The components of uncertainty associated with bidirectional reflectance are conveniently divided among those arising from the source, the goniometer, and the detector. These components are evaluated using eqs (3.11) to (3.14), and the relative sensitivity coefficients resulting from them are given in table 3.4. These coefficients are derived below, followed by their application to representative measurements of two types of samples, one a white PTFE plaque and the other a green tile. Note that the STARR instrument was designed to measure white samples, not colored samples. Therefore, the green tile serves to illustrate uncertainties that are nearly zero for the white plaque. The resulting relative expanded uncertainties are given in tables 3.5 and 3.7, while the relative combined expanded uncertainties are given in tables 3.6 and 3.8.

Table 3.4 Relative sensitivity coefficients for bidirectional reflectance measurements

Component of uncertainty	Relative sensitivity coefficient
Source stability, Φ_{i}	$1 / \Phi_{\mathrm{i}}$
Wavelength, λ	$(1 / f_{\mathrm{r}}) \cdot (\partial f_{\mathrm{r}} / \partial \lambda)$
Stray light, $S_{\mathrm{sl}}(\lambda)$	$(q_{\mathrm{r}}(\lambda) - q_{\mathrm{i}}(\lambda)) / (1 + q_{\mathrm{r}}(\lambda))$
Angle of incidence, θ_{i}	$(1 / f_{\mathrm{r}}) \cdot (\partial f_{\mathrm{r}} / \partial \theta_{\mathrm{i}})$
Angle of reflection, θ_{r}	$\tan \theta_{\mathrm{r}}$
Aperture area, A_{r}	$1 / A_{\mathrm{r}}$
Distance, D	$2 / D$
Signal, incident, S_{i}	$1 / S_{\mathrm{i}}$
Signal, reflected, S_{r}	$1 / S_{\mathrm{r}}$

Table 3.5 Relative expanded uncertainties ($k = 2$) for the bidirectional reflectance of a white PTFE plaque

Component of uncertainty	Type	Relative expanded uncertainty [%]					
		Wavelength [nm]					
		200	400	800	1200	1600	
Source stability	A	0.20	0.20	0.04	0.04	0.04	
Wavelength	B	0.04	<0.01	<0.01	<0.01	<0.01	
Stray-light	B	<0.01	<0.01	<0.01	<0.01	<0.01	
Signal, incident	A	0.18	0.06	0.06	0.02	<0.01	
Signal, reflected	A	1.66	0.22	0.16	0.06	0.22	
		Angle [°]					
		0	15	30	45	60	75
Angle of reflection	B	0	0.08	0.16	0.28	0.48	1.04
Aperture area	B	0.10					
Distance	B	0.06					

Table 3.6 Relative combined expanded uncertainties, in percent, ($k = 2$) for the bidirectional reflectance of a white PTFE plaque

Angle of reflection [°]	Wavelength [nm]				
	200	400	800	1200	1600
0	1.69	0.32	0.21	0.14	0.25
15	1.69	0.34	0.23	0.16	0.26
30	1.69	0.36	0.26	0.21	0.30
45	1.71	0.43	0.35	0.31	0.38
60	1.75	0.58	0.52	0.50	0.54
75	1.98	1.09	1.06	1.05	1.07

Table 3.7 Relative expanded uncertainties ($k = 2$) for the bidirectional reflectance of a green tile

Component of uncertainty	Type	Relative expanded uncertainty [%]					
		Wavelength [nm]					
		400	500	600	700		
Source stability	A	0.20	0.02	0.02	0.04		
Wavelength	B	0.16	0.36	0.22	0.18		
Stray-light	B	3.66	0.16	<0.01	<0.01		
Signal, incident	A	0.88	0.02	<0.01	0.32		
Signal, reflected	A	2.72	1.32	1.96	1.36		
		Angle [°]					
		0	15	30	45	60	75
Angle of reflection	B	0	0.08	0.16	0.28	0.48	1.04
Aperture area	B	0.10					
Distance	B	0.06					

Table 3.8 Relative combined expanded uncertainties, in percent, ($k = 2$) for the bidirectional reflectance of a green tile

Angle of reflection [deg]	Wavelength [nm]			
	400	500	600	700
0	4.65	1.38	1.98	1.41
15	4.65	1.38	1.98	1.42
30	4.66	1.39	1.98	1.42
45	4.66	1.41	2.00	1.44
60	4.68	1.46	2.03	1.49
75	4.77	1.73	2.23	1.76

The three components of uncertainty arising from the source are an uncertainty from the stability of the source, an uncertainty in wavelength, and an uncertainty from stray light. From the measurements detailed in section 3.2.1, the flux in the beam emerging from the source had a standard deviation that depends on wavelength. Using

eq (3.14), the relative sensitivity coefficient of the reflected signal due to the incident flux is $1 / \Phi_i$. The expanded relative standard uncertainty in BRDF due to instability of the source is given in tables 3.5 and 3.7 at selected wavelengths.

The maximum error in wavelength is 0.1 nm for wavelengths shorter than 1000 nm, and 0.5 nm for longer wavelengths. The uncertainty in BRDF due to these uncertainties in wavelength is determined by the dependence of $f_r(\theta_i;\ \theta_r;\ \lambda;\ \sigma)$ on wavelength, with a relative sensitivity coefficient of $(1 / f_r)\ (\partial f_r / \partial \lambda)$. For example, the BRDF of a white sample is virtually independent of wavelength, therefore the relative sensitivity coefficient is nearly zero. In contrast, the BRDF of a colored sample changes rapidly at certain wavelengths, and therefore the relative sensitivity coefficient is finite at those wavelengths. The relative expanded uncertainties in BRDF due to errors in wavelength, assuming a rectangular probability distribution, are given in tables 3.5 and 3.7 at selected wavelengths.

The spectral dependencies of the measured signals are given by eqs (3.13) and (3.14). Ideally, the signals are due only to radiant flux within the bandwidth of the source, either 7 nm or 10 nm about the wavelength setting of the monochromator. However, because of stray light in the source, there is radiant flux at other wavelengths, which contributes to the measured signal. An equation for estimating the uncertainty due to stray light and a method for calculating this contribution are given below.

Let $S_i(\lambda)$ be the measured signal from the incident flux at wavelength setting λ of the monochromator. This signal is the sum of the signal $S_{i,bw}(\lambda)$ due to light within the bandwidth $\Delta\lambda$ and the signal $S_{i,sl}(\lambda)$ due to stray light. Let $q_i(\lambda) = S_{sl}(\lambda) / S_{bw}(\lambda)$ be the ratio of the signal due to stray light to the signal due to flux within the bandwidth. Then,

$$S_i(\lambda) = S_{i,bw}(\lambda)\cdot[1 + q_i(\lambda)]\ . \tag{3.15}$$

Similarly, the measured signal from the reflected flux is given by

$$S_r(\lambda) = S_{r,bw}(\lambda)\cdot[1 + q_r(\lambda)]\ . \tag{3.16}$$

Using eqs (3.15) and (3.16) for the measured signals and eq (3.11) for the dependence of BRDF on the signals, and showing only the wavelength dependence explicitly, the relative change in $f_r(\lambda)$ due to stray light is given by

$$\frac{\Delta f_r(\lambda)}{f_r(\lambda)} = \frac{q_r(\lambda) - q_i(\lambda)}{1 + q_i(\lambda)} \tag{3.17}$$

To estimate the signals due to flux within the bandwidth and due to stray light, eqs (3.13) and (3.14) are expanded in terms of the two contributions to the measured signal, so that

$$S_{\mathrm{i,bw}}(\lambda) = \int_{\lambda-\Delta\lambda}^{\lambda+\Delta\lambda} R(\lambda')\cdot\Phi_{\mathrm{i}}(\lambda,\lambda')\cdot\mathrm{d}\lambda' \text{ and} \tag{3.18}$$

$$S_{\mathrm{i,sl}}(\lambda) = \int_{0}^{\lambda-\Delta\lambda} R(\lambda')\cdot\Phi_{\mathrm{i}}(\lambda,\lambda')\cdot\mathrm{d}\lambda' + \int_{\lambda+\Delta\lambda}^{\infty} R(\lambda')\cdot\Phi_{\mathrm{i}}(\lambda,\lambda')\cdot\mathrm{d}\lambda' \,. \tag{3.19}$$

$$S_{\mathrm{r,bw}}(\lambda) = \int_{\lambda-\Delta\lambda}^{\lambda+\Delta\lambda} R(\lambda')\cdot f_{\mathrm{r}}(\lambda')\cdot\Omega_{\mathrm{r}}\cdot\Phi_{\mathrm{i}}(\lambda,\lambda')\cdot\mathrm{d}\lambda' \text{ and} \tag{3.20}$$

$$S_{\mathrm{r,sl}}(\lambda) = \int_{0}^{\lambda-\Delta\lambda} R(\lambda')\cdot f_{\mathrm{r}}(\lambda')\cdot\Omega_{\mathrm{r}}\cdot\Phi_{\mathrm{i}}(\lambda,\lambda')\cdot\mathrm{d}\lambda' + \int_{\lambda+\Delta\lambda}^{\infty} R(\lambda')\cdot f_{\mathrm{r}}(\lambda')\cdot\Omega_{\mathrm{r}}\cdot\Phi_{\mathrm{i}}(\lambda,\lambda')\cdot\mathrm{d}\lambda' \tag{3.21}$$

Additionally, the incident flux $\Phi_{\mathrm{i}}(\lambda, \lambda')$ is the product of the flux $\Phi_{\mathrm{s}}(\lambda)$ of the lamp and the slit-scattering function $z(\lambda, \lambda')$ of the monochromator and the other optics, so that

$$\Phi_{\mathrm{i}}(\lambda, \lambda') = \Phi_{\mathrm{s}}(\lambda)\cdot z(\lambda, \lambda') \,. \tag{3.22}$$

For purposes of estimating the contribution of stray light to the measured signal, the slit-scattering function is assumed to have the form

$$z(\lambda,\lambda') = \begin{cases} 1 & \text{for} \quad \lambda-\Delta\lambda \le \lambda' \le \lambda+\Delta\lambda \\ 0 & \text{for} \quad \lambda' < \lambda_{\mathrm{cut-on}} \\ 10^{-5} & \text{otherwise} \end{cases} \tag{3.23}$$

where $\lambda_{\mathrm{cut\text{-}on}}$ is the cut-on wavelength of the appropriate order-sorting filter. The actual BRDF is assumed to be given by the measured BRDF.

The ratio $q_{\mathrm{i}}(\lambda)$ for the incident beam can be calculated using the responsivities of the detectors, the relative spectral output of the sources, and eqs (3.18), (3.19), (3.22), and (3.23). Since the corresponding ratio for the reflected beam, $q_{\mathrm{r}}(\lambda)$, depends on the BRDF of the sample, from eqs (3.20) and (3.21), these were calculated for the two examples of a white PTFE plaque and a green tile. The corresponding expanded relative standard uncertainties using eq (3.17) are given at selected wavelengths in tables 3.5 and 3.7. Note that if $f_{\mathrm{r}}(\lambda)$ does not depend on wavelength, $q_{\mathrm{i}}(\lambda) = q_{\mathrm{r}}(\lambda)$ and the uncertainty due to stray light is zero. This situation is closely approximated by the white PTFE plaque.

The components of uncertainty arising from the goniometer are errors in the incident and reflected angles. The zero angle of incidence was determined to within 0.1° from the retroreflected beam and to within 0.1° from differences between the alignment mirror and the sample surface. The resolution and repeatability of the incident angle are

0.001° and 0.01°, respectively. Assuming a rectangular probability distribution for these errors, the combined standard uncertainty in the angle of incidence is 0.08°. Since the uncertainty in BRDF due to an uncertainty in incidence angle θ_i depends upon the properties of the sample, the relative sensitivity coefficient is given by $(1 / f_r) \cdot (\partial f_r / \partial \theta_i)$. This uncertainty is not included in the tables 3.5 and 3.7 since the dependence of BRDF on the angle of incidence was not determined for these samples.

As detailed in section 3.2.2., the angle of reflection is determined to within 0.1°. Differences between the alignment mirror and the sample surface are also within 0.1°. Again assuming a rectangular probability distribution for these errors, the combined standard uncertainty in reflected angle is 0.08°. Using eq (3.11), the relative sensitivity coefficient due to the angle of reflection is $\tan\theta_r$. The resulting relative expanded uncertainties at selected angles of reflection are given in tables 3.5 and 3.7.

The components of uncertainty arising from the detector are uncertainties in the aperture area, distance from aperture to sample, and noise in the signal. The relative expanded uncertainty in the aperture area A_r is taken to be 0.10 percent, while the relative sensitivity coefficient calculated from eq (3.11) is $1 / A_r$.

For the distance, the sample holder is aligned on the axis of rotation of the goniometer to within 0.1 mm, as detailed in section 3.2.2; the distance from the sample to the aperture is measured to within 0.1 mm, again as detailed in section 3.2.2; and the sample is placed in the sample holder to within 0.1 mm. Assuming rectangular probability distributions for all of these errors, the combined standard uncertainty in the distance is 0.1 mm. Using eq (3.11), the relative sensitivity coefficient due to the distance is $2 / D$, which results in a relative expanded uncertainty of 0.06 percent at a distance of 650 mm.

Again using eq (3.11), the relative sensitivity coefficients due to the signals are $1/ S_i$ and $1 / S_r$ for the signals from the incident and reflected flux, respectively. The standard deviations of the mean for the net signals are propagated through to the final signals to obtain the expanded relative standard uncertainties. These are listed at selected wavelengths in tables 3.5 and 3.7. Note that the relative expanded uncertainties in the reflected signals are greater than those from the incident signals since the fluxes are significantly smaller in the former case than in the later. The relative combined expanded uncertainties given in tables 3.6 and 3.8 are obtained from the root-sum-square of the uncertainties listed in tables 3.5 and 3.7, respectively.

3.4.3 Directional - Hemispherical Reflectance Only two measurement equations are needed for determining the functional relationship of the input quantities to the measurand for direction-hemispherical reflectance. They are analogous to eqs (3.11) and (3.12). The first relates the reflectance factor of the sample, R_x, to the signals and the reflectance factor of the standard, R_s, and is given by eq (3.7), which is repeated here

$$R_x(\lambda) = R_s(\lambda) \cdot \frac{S_{xx}(\lambda)}{S_{wx}(\lambda)} \frac{S_{ws}(\lambda)}{S_{ss}(\lambda)} \quad , \tag{3.24}$$

The second equation relates any signal $S(\lambda)$ from the reflected flux in the integrating sphere to the incident flux $\Phi(\lambda)$, and is given by

$$S(\lambda) = \Re(\lambda) \cdot R(\lambda) \cdot \Phi(\lambda) \ , \tag{3.25}$$

where $\Re(\lambda)$ is the responsivity of the integrating sphere and detector and $R(\lambda)$ is the reflectance factor . Since the reflectance factor of a sample is always determined relative to that of a standard with nearly the same reflectance factor, there is no uncertainty associated with stray light, as detailed in the previous section. Therefore, the analogues to eqs (3.13) and (3.14) are not included in the measurement equations for directional - hemispherical reflectance factor.

The components of uncertainty associated with directional - hemispherical reflectance are conveniently divided among those arising from the source (stability and wavelength), the detector (signals), and the standard (reflectance). These components are evaluated using eqs (3.24) and (3.25), and the relative sensitivity coefficients resulting from them are given in table 3.9. These coefficients are derived similarly to those listed in table 3.4, so the derivation will not be repeated below. There is a factor of 2 associated with the coefficient for the source stability since there are two ratios of signals in eq (3.24). The resulting expanded relative standard uncertainties for a representative PTFE plaque are given in table 3.10 and the expanded combined relative uncertainties are given in table 3.11.

Table 3.9 Relative sensitivity coefficients for directional - hemispherical reflectance measurements

Component of uncertainty	Relative sensitivity coefficient
Source stability, Φ_i	$2 / \Phi_i$
Wavelength, λ	$(1 / \rho_x) \cdot (\partial\rho_x / \partial\lambda)$
Signal, wall and standard, S_{ws}	$1 / S_{ws}$
Signal, wall and unknown, S_{wx}	$1 / S_{wx}$
Signal, standard, S_{ss}	$1 / S_{ss}$
Signal, unknown, S_{xx}	$1 / S_{xx}$
Reflectance of standard, ρ_s	$1 / \rho_s$

Table 3.10 Relative expanded uncertainties (k = 2) for the 6° - hemispherical reflectance of a PTFE plaque

Component of uncertainty	Type	Relative expanded uncertainty [%]				
		Wavelength [nm]				
		200	*400*	*800*	*1200*	*1600*
Source stability	A	0.40	0.40	0.08	0.08	0.08
Wavelength	B	0.04	<0.01	<0.01	<0.01	<0.01
Signals	A	0.50	0.30	0.12	0.06	0.08
Standard	B			0.18		

Table 3.11 Relative combined expanded uncertainties (k = 2) for the 6° - hemispherical reflectance of a PTFE plaque

Wavelength [nm]	Relative combined expanded uncertainty [%]
200	0.67
400	0.53
800	0.23
1200	0.21
1600	0.21

4. Transfer Instrument – Spectrophotometers

4.1 Description

Two commercial spectrophotometers, a Varian-Cary 5E and a Perkin-Elmer Lambda 19,[†] are used as transfer instruments and are calibrated with primary reference standards from the STARR instrument. The reflectance standards issued as SRMs are calibrated on these transfer spectrophotometers. Since these are commercial instruments, the descriptions will be limited to the features that are pertinent for understanding their operation. Additional details can be found in the users' manuals [7,8].

Both transfer spectrophotometers are double beam instruments with transmittance and reflectance capabilities. They are equipped with microprocessors with programmable features under external computer control. Both use a double monochromator with order-sorting filters for wavelength selection, and are purged with purified nitrogen gas. The Varian-Cary 5E, hereafter referred to as the Cary 5E, is equipped with a Diffuse Reflectance Attachment (DRA), while the Perkin-Elmer Lambda 19, hereafter referred to as the Lambda 19, is equipped with an Integrating Sphere Assembly (ISA).

The spectral wavelength range of the instruments is 200 nm to 2500 nm. This range is conveniently divided into three regions, the ultraviolet (200 nm to 400 nm), the visible (400 nm to 700 nm), and the near-infrared (700 nm to 2500 nm). The sources, order-sorting filters, gratings, and detectors are automatically controlled so that continuous spectral scans can be made through the full wavelength range of the instrument. A deuterium lamp is the source for the ultraviolet wavelength range, while a quartz-tungsten-halogen lamp is used at other wavelengths. One grating is used for the ultraviolet and visible ranges, while the other grating is used for the near-infrared range. Likewise, a photomultiplier tube (PMT) detector is used for the ultraviolet and visible ranges while a lead sulfide (PbS) detector is used for the near-infrared range. The spectral bandwidth in the ultraviolet and visible ranges is adjustable from 0.1 nm to 3.8 nm (3.0 nm) on the Cary 5E (Lambda 19), and in the near-infrared range is adjustable from 1.0 nm to 14.3 nm (20 nm) on the Cary 5E (Lambda 19).

The integrating sphere of the DRA on the Cary 5E has a diameter of 110 mm. The PMT is mounted above the sphere and views the sphere interior through an elliptical aperture. The PbS detector port is adjacent to the PMT port. Baffles attached to the top of the sphere interior block first reflections from the sample to the detectors. The sphere interior and baffles are coated with pressed PTFE powder.

The reference beam enters the sphere through a port 22 mm high by 12 mm wide located 90° from the sample port. The reference beam target area is located on the

[†] Certain commercial equipment, instruments, or materials are identified in this paper in order to specify the experimental procedure adequately. Such identification is not intended to imply recommendation or endorsement by the National Institute of Standards and Technology, nor is it intended to imply that the materials or equipment identified are necessarily the best available for the purpose.

opposite side of the sphere. The sample beam is nearly collimated and enters the sphere through a rectangular port approximately 30 mm high by 20 mm wide. The sample port is opposite this entrance port and is 22.5 mm in diameter. An image of the exit slit of the monochromator is formed at the sample plane. The width of this image may vary, depending on the bandwidth setting. The image height is about 15 mm at the maximum exit slit height. The image height can be decreased by reducing the exit slit to one-third of its maximum height.

The section of the sphere at the sample port can be turned in the plane of this port. In one position of this section the sample plane is tilted so that the sample beam is incident at 6° from the normal. This angle allows the specular component of the reflected sample beam to be trapped in the sphere. In the other position, this section is turned 180°. In this configuration the sample beam is normal to the sample plane and the specular component returns along the axis of the sample beam and passes back out of the sphere through the sample beam entrance port. This allows only the diffuse component of the reflected beam to be measured.

The ISA on the Lambda 19 was custom-designed for high precision by the NIST staff. A top view diagram of the ISA is shown in figure 4.1. The integrating sphere of the ISA has a diameter of 220 mm. The PMT is mounted above the sphere and views the sphere interior through an circular aperture. The PbS detector port is adjacent to the PMT port, and each port is symmetrically placed with respect to the sample and reference ports. There are appropriate baffles designed to block the first sample reflection to the detectors. The sphere interior and baffles are fabricated from Spectralon™.

There are two entrance ports, one for the reference beam and the other for the sample beam. The sample beam enters the sphere through a port with a diameter of 22 mm located nearly opposite to the 22 mm diameter sample port. The ports for the reference beam and reference sample are similar. The incidence angle of the center of the beams is 6°. The removable reference sample is freshly prepared high purity PTFE. The centers of all the ports except those of the detectors lie along the horizontal great circle of the sphere. The integrating sphere design accommodates not only measurements for which the specular beam is included in the measurement result, but also measurements for which the specular beam is excluded from the result. This is achieved by removing a set of plugs on the integrating sphere so that the specular component of the beam exits the sphere through these ports. These plugs were machined to complete the spherical shape of the wall.

The sphere wall is brought to a knife edge at the sample and reference ports to completely collect the hemispherically scattered light from the sample and the reference. Since Spectralon™ is a volume diffuser and will transmit light to a depth of several millimeters, the outer sphere shell directly behind the Spectralon™ wall was painted with $BaSO_4$ around the sample and reference ports to attempt to achieve the highest possible reflectance.

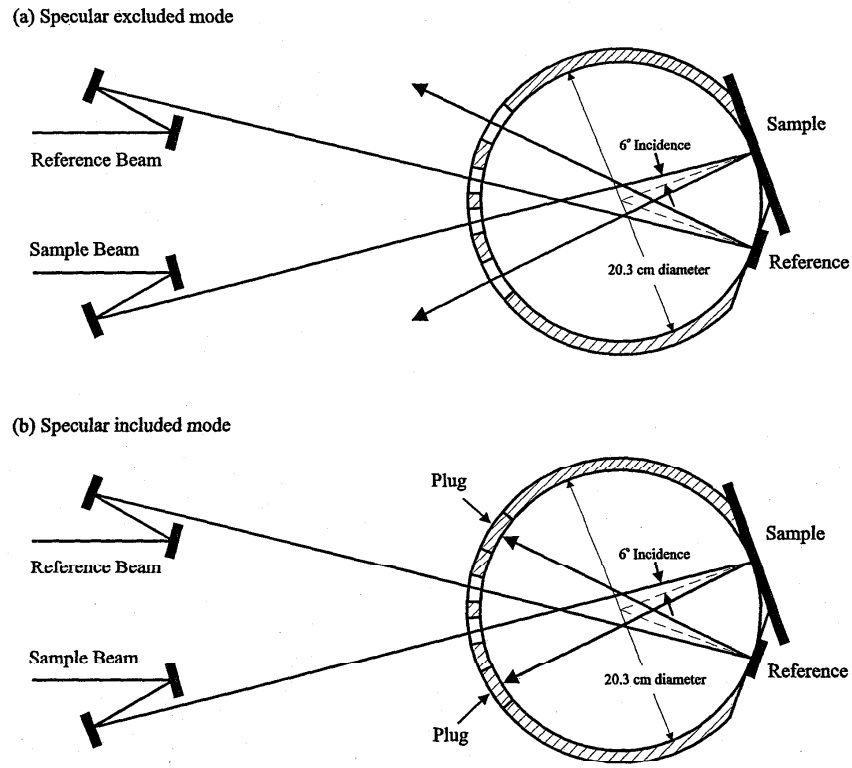

Figure 4.1. Top view of the Integrating Sphere Assembly of the Perkin-Elmer Lambda 19 transfer spectrophotometer configured for reflectance operating in the specular excluded (a) and specular included (b) modes.

4.2 Calibration

While emission lamps can be placed in the source compartment of the Cary 5E, the same is not true of the Lambda 19. Therefore, both emission lines and absorption bands are used to calibrate the wavelength scales of the Cary 5E, while only absorption bands and the emission lines of deuterium are used for the Lambda 19. The lines and bands used for the Cary 5E are listed in table 4.1, while those for the Lambda 19 are listed in table 4.2. The maximum error in the wavelength scale is 0.1 nm in the ultraviolet and visible wavelength ranges and 0.5 nm in the near-infrared for both instruments. The deuterium lamp is used to check the wavelength scales on a routine basis.

Table 4.1 Wavelengths of emission lines and absorption bands used to calibrate the wavelength scale of the Cary 5E transfer spectrophotometer

Source	Wavelength [nm]
Emission lines	
Hg	253.65, 334.15, 435.83, 546.07, 1014.0, 1529.5
D_2	486.0, 656.10, 1312.2[(a)], 1968.3[(a)], 2624.4[(a)]
Ne	703.24
Xe	881.94, 979.97
Kr	1816.73
Absorption bands	
1,2,4-trichlorobenzene (0.5 mm)	2152.6
Holmium oxide (SRM 2034)	241.0, 249.8, 278.1, 287.0, 333.5, 345.5, 361.4, 385.4, 416.1, 451.3, 467.8, 485.3, 536.5, 640.5
Rare-Earth oxide (SRM 1920)	799.0, 886.7, 1132.4, 1260.8, 1535.4, 1682.2, 1757.8, 1847.0, 1932.5, 1970.8

[(a)]These wavelengths are the 2nd, 3rd, and 4th order lines of the 656.1 nm line.

Table 4.2 Wavelengths of emission lines and absorption bands used to calibrate the wavelength scale of the Lambda 19 transfer spectrophotometer

Source	Wavelength [nm]
Emission lines	
D_2	486.0, 656.10, 1312.2[(a)], 1968.3[(a)], 2624.4[(a)]
Absorption bands	
Didymium glass	1067.0
Holmium oxide (SRM 2034)	241.0, 249.8, 278.1, 287.0, 333.5, 345.5, 361.4, 385.4, 416.1, 451.3, 467.8, 485.3, 536.5, 640.5
Rare-Earth oxide (SRM 1920)	799.0, 886.7, 1132.4, 1260.8, 1535.4, 1682.2, 1757.8, 1847.0, 1932.5, 1970.8

[(a)]These wavelengths are the 2nd, 3rd, and 4th order lines of the 656.1 nm line.

The presence of stray light in the transfer spectrophotometers sample beam was checked using a number of solutions and glass filters that have sharp cut-off absorption features in different spectral regions. The techniques for measuring stray radiation are described in ASTM and other publications [17,18]. The level of stray radiation was checked for spectral bandwidths of 1.0 nm and 3.6 nm. The results of these measurements indicate that the level of stray light is not significant for the transfer spectrophotometers, especially since samples are always calibrated using a reference with the same spectral characteristics.

The linearity of the detectors on both instruments was determined with a set of transmittance standards [21]. These transmittance standards were calibrated on the NIST reference transmittance spectrophotometer at 546 nm and 770 nm. The measured transmittances and resulting differences with the transmittances of the standards are used to correct for the non-linearity of the detectors.

4.3 Operation

The SRMs listed in table 1.1 are calibrated on the transfer spectrophotometers using master standards as a means for transferring the absolute reflectance scale from the fundamental measurements of these quantities on the STARR. Pressed PTFE powder is preferred as a master standard for diffuse reflectance (SRMs 2015, 2016, and 2044) because the absolute reflectance of this material is well documented [26,27,28]. Other transfer standards used are master first surface aluminum and gold mirrors, second surface aluminum mirrors, and Black Glass for calibrating SRMs 2003, 2011, 2023, and 2026. The wavelength SRM 1920a is also calibrated on the Cary 5E as described in Ref. [29], and the reflectance of this standard as a function of wavelength is shown in figure 4.2.

The instrument parameters are set after a 2 h warm up period. The wavelength calibration is checked during this time by running the instrument test procedure with the deuterium emission lines. Data for determining the reflectance of a sample are recorded in the following sequence. Prior to beginning a measurement, a sample of PTFE is placed at the sample port and a spectral scan is performed. The resulting signals from this scan are used to adjust the fluxes in the reference and sample beams so that they are nearly equal. Then a master standard, either for specular or directional - hemispherical reflectance, is placed at the sample port. A spectral scan of the master standard is performed, recording the signals as a function of wavelength for both the reference and the sample beams. In the notation of section 2.2.2, now including the wavelength dependence, these are the signals $S_{ws}(\lambda)$ and $S_{ss}(\lambda)$, respectively. The sample to be calibrated is then placed at the sample port, and another spectral scan is performed. This yields the signals $S_{wx}(\lambda)$ and $S_{xx}(\lambda)$. If additional samples are to be calibrated, they are measured in turn. The master standard is measured again, then background measurements are made by placing a large black cavity at the sample port and performing a spectral scan.

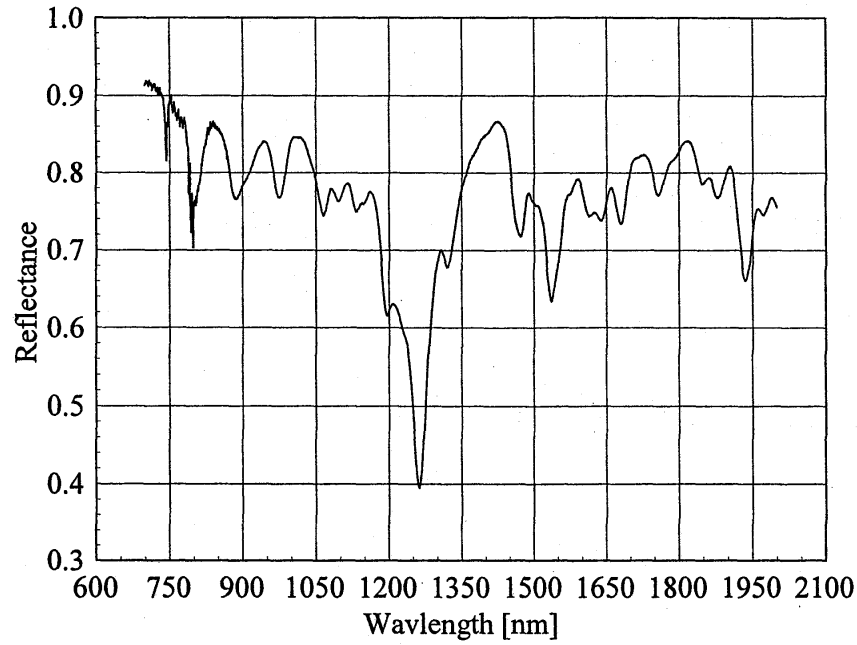

Figure 4.2. Reflectance as a function of wavelength for the rare-earth mixture wavelength standard SRM 1920a.

The corrected, net signals are calculated in two steps. First, the net signals are obtained by subtracting the background signals. Then, the signals from the master standards are corrected for nonlinearity of the detector and for drift in the instrument by linearly interpolating these signals to the time when the sample to be calibrated was measured. The reflectance or reflectance factor of the sample is calculated from eq (2.38) or (2.39) using the corrected, net signals and the known reflectance or reflectance factor of the master standard. Note that eqs (2.38) and (2.39) are valid for the both the double-beam transfer spectrophotometers and the single-beam STARR instrument.

4.4 Uncertainties

The expanded uncertainty (k = 2) in diffuse and specular reflectance obtained through these measurements and data reduction procedures is generally 0.003. The components of uncertainty arise from the source stability and wavelength, non-linearity and noise in the detector, and reflectance of the master standard. The standard uncertainties associated with these components in the visible wavelength region are given in table 4.3, along with the expanded uncertainty of the reflectance.

There are some sample-related features that can cause errors that are not corrected for in the data reduction. Examples of such error sources are large sample nonuniformity, surface characteristics such as parallel grooves, surface waves and dimples that scatter the specular component, and thin coatings that cause interference effects. If any of these

features, or others that could affect the measurements, are observed on the sample, a note is made in the calibration report.

Table 4.3 Standard uncertainties of spectral reflectance values for the transfer spectrophotometers in the visible wavelength region

Component of uncertainty	Standard uncertainty
Source stability	0.5×10^{-3}
Wavelength	0.2×10^{-5}
Detector linearity	0.7×10^{-3}
Signal noise	0.8×10^{-3}
Reflectance of standard	0.5×10^{-3}
Combined Standard Uncertainty	1.3×10^{-3}
Expanded Uncertainty ($k = 2$)	2.6×10^{-3}

Acknowledgments

The success of the Measurement Services and Standard Reference Materials for spectral reflectance detailed in this Special Publication benefited from the efforts of Robert D. Saunders, James E. Proctor, Jack J. Hsia, and Thomas A. Germer, who helped with the design, construction, and characterization of the STARR instrument.

References

[1] James E. Proctor and P. Yvonne Barnes, "NIST High Accuracy Reference Reflectometer-Spectrophotometer," J. Res. Natl. Inst. Stand. Technol. **101**, 619 (1996).

[2] Standard References Materials Catalog 1995 - 1996, NIST Special Publication 260.

[3] NIST Calibration Services Users Guide, NIST Special Publication 250.

[4] F. A. Jenkins and H. E. White, Fundamentals of Optics, 3rd Edition, McGraw-Hill, NY (1957) p. 521.

[5] ASTM Compilation, ASTM Standard on Color and Appearance Measurements, 5th Edition (1996).

[6] International Commission on Illumination, International Lighting Vocabulary, Publication CIE No. 17.4 (1987).

[7] Perkin-Elmer Reference Guide to the Lambda 19 UV-VIS-NIR Spectrophotometer.

[8] Varian-Cary 5E UV-VIS-NIR Spectrophotometer's Reference Guide.

[9] F. E. Nicodemus, J. C. Richmond, J. J. Hsia, I. W. Ginsburg, and T. Limperis, "Geometrical Considerations and Nomenclature for Reflectance," U.S. NBS Monograph 160 (1977).

[10] W. H. Venable, Jr., J. J. Hsia, and V. R. Weidner, "Development of a NIST Reference Spectrophotometer for Diffuse Transmittance and Reflectance," National Bureau of Standards (U.S.) Tech Note 594-11 (1976).

[11] G. Goebel, B. Caldwell, and H. K. Hammond III, "Use of an Auxillary Sphere with Spectrophotometer to Obtain Absolute Reflectance," J. Opt. Soc. Am. **56**, 783 (1966).

[12] J. A. Van den Akker, L. R. Dearth, and W. W. Shillcox, "Evaluation of Absolute Reflectance for Standardization Purposes," J. Opt. Soc. Am. **56**, 250 (1966).

[13] Craig J. Sansonetti, Marc L. Salit, and Joseph Reader, "Wavelengths of Spectral Lines in Mercury Lamps," Appl. Opt. **35**, 74 (1996).

[14] CRC Handbook of Chemistry and Physics, 3rd Edition, CRC Press, Inc. (1982).

[15] W. H. Venable, Jr. and K. L. Eckerle, "Standard Reference Materials: Didymium Glass Filters for Calibrating the Wavelength Scale of Spectrophotometers - SRM 2009, 2010, 2013, and 2014," U.S. NBS Special Publication 260-66 (1979).

[16] Devinder Gupta, Lan Wang, Leonard H. Hanssen, Jack J. Hsia, and Raju U. Datla, "Standard Reference Materials: Polystyrene Films for Calibrating the Wavelength Scale of Infrared Spectrophotometers - SRM 1021," NIST Special Publication 260-122 (1995).

[17] American Society for Testing and Materials, "Standard Test Method for Estimating Stray Radiant Power Ratio of Spectrophotometers by the Opaque Film Method, ASTM E387-84," Annual Book of ASTM Standards, Section 14.01, 469 (1985).

[18] K. D. Mielenz, V. R. Weidner, and R. W. Burke, "Heterochromatic Stray Light in UV Absorption Spectrometry: A New Test Method, " Appl. Opt. **21**, 3354 (1982).

[19] J. B. Fowler and G. Deszi, "High Accuracy Measurement of Aperture Area Relative to a Standard Known Aperture," J. Res. Natl. Inst. Stand. Technol. **100**, 277 (1995).

[20] K. D. Mielenz and K. L. Eckerle, "Spectrophotometer Linearity Testing using the Double-Aperture Method," Appl. Opt. **11**, 2294 (1972).

[21] K. L. Eckerle, V. R. Weidner, J. J. Hsia, and K. Kafadar, "Measurement Assurance Program Transmittance Standards for Spectrophotometric Linearity Testing: Preparation and Calibration," J. Res. Natl. Bur. Stand. (U.S.) **88**, 25 (1983).

[22] C. L. Cromer, G. P. Eppledauer, J. E. Hardis, T. C. Larason, and A. C. Parr, "National Institute of Standards and Technology Detector-Based Photometric Scale," Appl. Opt. 32, 2936 (1993).

[23] W. H. Venable, Jr., J. J. Hsia, and V. R. Weidner, "Establishing a Scale of Directional - Hemispherical Reflectance Factor I: The Van den Akker Method," J. Res. Natl. Bur. Stand. **82**, 29 (1977).

[24] W. Budde, W. Erb, and J. J. Hsia, "International Intercomparison of Absolute Reflectance Scale," Color Research and Application **7**, 24 (1982).

[25] Barry N. Taylor and Chris E. Kuyatt, "Guidelines for Evaluating and Expressing the Uncertainty of NIST Measurement Results," NIST Technical Note 1297 (1994).

[26] V. R. Weidner and J. J. Hsia, "Reflection Properties of Pressed Polytetrafluoroethylene Powder," J. Opt. Soc. Am. **71**, 856 (1981).

[27] V. R. Weidner, J. J. Hsia, and B. Adams, "Laboratory Intercomparison Study of Pressed Polytetrafluoroethylene Powder Reflectance Standards," Appl. Opt. **24**, 2225 (1985).

[28] P. Yvonne Barnes and Jack J. Hsia, "45°/0° Reflectance Factors of Pressed Polytetrafluoroethylene (PTFE) Powder," NIST Tech Note 1413 (1995).

[29] Victor R. Weidner, Patricia Y. Barnes, and Kenneth L. Eckerle, "A Wavelength Standard for the Near Infrared Based on the Reflectance of Rare-Earth Oxides," J. Res. Natl. Bur. Stand. **91**, 243, (1986).

Appendix A

REPORT OF TEST

38060S Bidirectional Reflectance Distribution Function (BRDF)
of
One White Target

Submitted by:

Any Company
Attn: Yura Customer
Any Street
Any Town, Any State Zip Code-0000

(See your Contract No. 000000-000 Dated Month Day, Year)

1. Description of Test Item

The test item submitted was an encased white target, 50.8 mm by 50.8 mm and identified by the letter "A".

2. Description of Test

Bidirectional Reflectance Distribution Function (BRDF) measurements as a function of wavelength were made using the NIST Spectral Tri-function Automated Reference Reflectometer (STARR). The collimated light beam (< 1° divergence) was centered on the sample in the plane of incidence. The reported results are the averaged values from measurements made at two orthogonal polarizations. The measurements were made at each specified wavelength for the geometrical conditions illustrated in Figure 1. The spectral bandpass was 10 nm. A quartz-tungsten-halogen lamp was used as the source and a silicon photodiode was used as the detector. The average projected solid angle of the limiting aperture of the detector was determined for each viewing angle by measuring the distance between the limiting aperture and the specimen plane, and the diameter of the aperture.

Laboratory Environment:
Temperature: 21°C ± 0.6 °C
Relative Humidity: 35% ± 0.6%

Test Date: Month Day, Year
NIST Test No.: Division Number/Test Folder Number-Year

Since the illuminated area of the specimen is not a point source, the average projected solid ai of the illuminated area was determined for computing the BRDF values. The circular rece aperture subtended a half angle of approximately 1.4° at the center of the sample. When the l beam is incident on the test specimen at an angle of 60°, the major and minor axes of the illumin area are 28 mm and 14 mm. When the light beam is incident on the test specimen at an angle c (normal incidence), the illuminated area has a diameter of 14 mm. The distance from the cente the illuminated area to the center of the limiting aperture of the detector is approximately 673 r The diameter of the limiting aperture is 31.85 mm.

3. Results

The BRDF of the test item is computed from the ratio of the signal from the reflected flux to signal from the incident flux, divided by the projected solid angle and the cosine of the angl reflection. The BRDF values for both polarizations are averaged to obtain the reported values. results of the data reduction are listed in Tables 1 and 2. The expanded uncertainty (k=2) for BRDF values listed in Tables 1 and 2 is 0.004.

4. General Information

1) The encased test samples were measured in the "as received condition" and the front sur alignment was at the encasement.

2) Spatial uniformity was not assessed.

3) This test report may not be reproduced except in full without the written consent of Laboratory.

Prepared by:

P. Yvonne Barnes
Optical Technology Division
Physics Laboratory

Approved by:

Robert D. Saunders
For the Director,
National Institute of
Standards and Technology

TABLE 1

White Target A

ANGLE OF INCIDENCE: 0°

WAVELENGTH: 800 nm

ANGLE OF VIEWING [degrees]	BRDF
60	------
40	0.300
20	0.300
0	0.310
-20	0.320
-40	0.340
-60	0.400

TABLE 2

White Target A

ANGLE OF INCIDENCE: 45°

ANGLE OF VIEWING: 0°

Wavelength [nm]	BRDF
400	0.323
500	0.323
600	0.323
700	0.323
800	0.323
900	0.323
1000	0.323

Appendix B

REPORT OF CALIBRATION

38060S Spectral Reflectance
of a
First Surface Aluminum Mirror SRM 2003
Series D

Submitted by:

Any Company
Attn: Yura Customer
Any Street
Any Town, Any State Zip Code-0000

(Purchase Order No. 00-0000-00 dated Month Day, Year)

1. Description of Calibration Item

Standard Reference Material (SRM) 2003 consists of a low thermal expansion glass substrate, 5.1 cm in diameter and 0.9 cm thick, onto which aluminum has been vacuum deposited. SRM 2003 is supplied with a threaded protective aluminum container fitted with a Teflon insert. The insert has been constructed so that it does not impinge upon the calibrated surface. The top or lid of the container bears a label that identifies the type of SRM and the Series Number. The SRM is placed face down in the bottom half of its container.

2. Description of Calibration

The reflectance measurements as a function of wavelength were made using the NIST Spectral Tri-function Automated Reference Reflectometer (STARR). The nearly collimated light beam illuminated an area of approximately 14 mm in diameter and was centered on the sample in the plane of incidence. Measurements were made using a 6°/6° geometry. Measurements were made with light polarized parallel and perpendicular to the plane of incidence. The reported results are the averaged values of measurements made at the two polarizations.

Laboratory Environment:
Temperature: 23°C ± 0.6°C
Humidity: 50% ± 0.6%

SRM 2003 was calibrated over the wavelength range of 250 nm to 2500 nm as follows: 50 ı intervals over the range of 250 nm to 1000 nm, 100 nm intervals over the range of 1000 nm 1300 nm, and 200 nm intervals over the range of 1300 nm to 2500 nm. The spectral bandpass v approximately 10 nm.

The following sources and detectors were used: a xenon arc lamp and a silicon photodiode detec over the range of 250 nm to 400 nm, a tungsten source and a silicon photodiode detector over t range of 450 nm to 1100 nm, and a quartz-tungsten-halogen lamp and an indium-aresenide detec over the range of 1100 nm to 2500 nm.

3. Results

The reflectances are listed in Table 1. The expanded uncertainties (k=2) of the reflectances a 0.005 for wavelengths shorter than 350 nm, 0.003 for wavelengths from 400 nm to 2000 nm, a 0.005 for wavelengths longer than 2000 nm. The expanded uncertainties include increased randc noise at wavelengths below 350 nm and above 2000 nm. Contributors to the Type A uncertainty a spatial uniformity over an area with diameter 20 mm and surface conditions, source stability, a: signals. Contributors to the Type B uncertainty are the receiver system non-linearity and no uniformity, scattered flux, angular setting, and view factor uncertainties.

4. General Information

1) SRM 2003 is not durable. Airborne particulates, aromatics, laboratory conditions, and improp handling may adversely affect the surface conditions. If the delicate aluminum surface becom contaminated it cannot be restored to its original reflectance by cleaning.

2) It is strongly recommended that a face mask be worn to prevent fogging or contaminating tl mirror with vapors or particles from the mouth or nose. It is further recommended that a fingers/thumbs be covered with a lint-free glove i.e., nylon or latex types to prevent late fingerprints on mirror surfaces. If and only if dust must be removed, be extremely careful wh using a very clean air bulb and use it so that no condensation is generated by a high velocity a flow over the mirror's calibrated surface.

3) The data in Table 1 are valid for a 6° angle of incidence only.

4) This report may not be reproduced except in full, without written permission from this Laboratory.

REPORT OF CALIBRATION
Any Company
38060S Spectral Reflectance of a First Surface Aluminum Mirror

Prepared by:

P. Yvonne Barnes
Optical Technology Division
Physics Laboratory
(301) 975-2345

Approved by:

Robert D. Saunders
For the Director,
National Institute of
Standards and Technology
(301) 975-2355

References

[1] Linford, R.M.F., Strouse, E.A., *Optical Coatings for Space Laser Communications System*, SPIE, Vol. 150, Laser and Fiber Optics Communications, pp 55 - 61, (1978)

[2] Hass, G., *Filmed Surface for Optics*, JOSA, Vol. 45, No. 11, pp 1070 - 1073 (1957).

[3] Hass, G., Hunter, W.R., Tousey, R., Influence of Purity, Substrate Temperature, and Aging Conditions on the Extreme Ultraviolet, JOSA, Vol. 49, No. 6, pp 593 - 602 (1959).

[4] Hass, G., Tousey, R., *Reflecting Coatings for the Extreme Ultraviolet*, JOSA, Vol. 49, No. 6, pp 593 - 602 (1959).

[5] Hass, G., Waylonis, J.E., *Optical Constants and Reflectance and Transmittance of Evaporated Aluminum in the Visible and Ultraviolet*, JOSA, Vol. 51, No. 7, pp 719 - 722 (1961).

[6] Bennett, H.E., Silver, M., Ashley, *Infrared Reflectance of Aluminum Evaporated in Ultraviolet*, JOSA, Vol. 51, No. E.J., 7, pp 719 - 722 (1961).

[7] Hass, G., *Reflectance and Preparation of Front Surface Mirrors for Use at Various Angles of Incidence from the Ultraviolet to the far Infrared*, JOSA, Vol. 72, No. 1, pp 27 -39 (1982).

[8] Taylor, B.N., and Kuyatt, C.E., *Guidelines for Evaluating and Expressing the Uncertainty of the NIST Measurement Results*, NIST Technical Note 1297 (1994)

[9] Taylor, B., *Guidelines for the Use of the International System of Units (SI),* NIST Technical Note 811 (1995).

Table 1

First Surface Aluminum Mirror, SRM 2003, Series D

Wavelength [nm]	Reflectance
250	0.883
300	0.901
350	0.904
400	0.903
450	0.899
500	0.899
550	0.898
600	0.895
650	0.882
700	0.870
750	0.854
800	0.855
850	0.887
900	0.916
950	0.924
1000	0.934
1100	0.955
1200	0.962
1300	0.965
1500	0.966
1700	0.967
1900	0.967
2100	0.967
2300	0.967
2500	0.967

REPORT OF TEST

38060S 45°/0° Reflectance Factor

of a

White Diffuser Tablet

Submitted by:

Any Company
Attn: Yura Customer
Any Street
Any Town, Any State Zip Code-0000

(Reference Purchase Order Number: 00-0000-00 dated Month Day, Year)

1. Description of Test Item

The test item submitted was a plaque of pressed polytetrafluoroethylene.

2. Description of Test

The reflectance factor measurements as a function of wavelength were made using the NIST Spectral Tri-function Automated Reference Reflectometer (STARR). The nearly collimated light beam was centered on the sample in the plane of incidence. The reported results are the averaged values from measurements made at two orthogonal polarizations. The spectral bandpass was 10 nm. A quartz-tungsten-halogen lamp was used as the source and a silicon photodiode was used as the detector. The average projected solid angle of the limiting aperture of the detector was determined by measuring the distance between the limiting aperture and the specimen plane, and the diameter of the aperture.

Laboratory Environment:
Temperature: 21 °C ± 0.6 °C
Relative Humidity: 49 % ± 0.6 %

Since the illuminated area of the specimen is not a point source, the average projected solid angle of the illuminated area was determined for computing the reflectance factors. The circular receiver aperture subtended a half angle of approximately 1.4° at the center of the sample. When the light beam is incident on the test specimen at an angle of 45°, the major and minor axes of the illuminated area are 19.8 mm and 14 mm. When the light beam is incident on the test specimen at an angle of 0° (normal incidence), the illuminated area has a diameter of 14 mm. The distance from the center of the illuminated area to the center of the limiting aperture of the detector is approximately 673 mm. The diameter of the limiting aperture is 31.85 mm.

3. Results

The results of the data reduction are listed in Table 1. The expanded uncertainty (k=2) for the values listed in Table 1 is 0.004.

4. General Information

1) The reflectance factor of the sample is the ratio of the reflectance of the sample to the reflectance of a perfect Lambertian diffuser under the same measurement conditions. The 45°/ 0° reflectance factor is the reflectance factor for 45° incidence and 0° viewing.

2) The test samples were measured in the "as received condition".

3) Spatial uniformity was not assessed.

4) The test report may not be reproduced except in full without the written consent of this Laboratory.

Prepared by:

P. Yvonne Barnes
Optical Technology Division
Physics Laboratory
(301) 975-2345

Approved by:

Robert D. Saunders
For the Director,
National Institute of
Standards and Technology
(301) 975-2355

Table 1

REPORT OF TEST
Any Company
38060S 45°/0° Reflectance Factor

Reflectance factor R as a function of wavelength λ
for 45° incident angle and 0° viewing angle
of the pressed PTFE plaque

[nm]	R(45°/0°)		[nm]	R(45°/0°)		[nm]	R(45°/0°)
380	1.011		525	1.015		670	1.015
385	1.011		530	1.015		675	1.015
390	1.011		535	1.015		680	1.015
395	1.011		540	1.015		685	1.015
400	1.011		545	1.015		690	1.015
405	1.011		550	1.015		695	1.015
410	1.011		555	1.015		700	1.015
415	1.011		560	1.015		705	1.015
420	1.012		565	1.015		710	1.015
425	1.012		570	1.015		715	1.015
430	1.012		575	1.015		720	1.015
435	1.012		580	1.015		725	1.015
440	1.012		585	1.015		730	1.015
445	1.012		590	1.015		735	1.015
450	1.012		595	1.015		740	1.015
455	1.012		600	1.015		745	1.015
460	1.012		605	1.015		750	1.015
465	1.012		610	1.015		755	1.015
470	1.012		615	1.015		760	1.015
475	1.012		620	1.015		765	1.015
480	1.012		625	1.015		770	1.015
485	1.012		630	1.015		775	1.015
490	1.012		635	1.015		780	1.015
495	1.012		640	1.015			
500	1.012		645	1.015			
505	1.012		650	1.015			
510	1.015		655	1.015			
515	1.015		660	1.015			
520	1.015		665	1.015			

Test Date: Month Day, Year
NIST Test No.: Division Number/Test Folder Number-Year

REPORT OF TEST

38060S 6°/Hemispherical Reflectance Factor
of
One White Diffuser Plate and
One Aluminum Diffuser Plate

Submitted by:

Any Company
Attn: Yura Customer
Any Street
Any Town, Any State Zip Code-0000

(Reference Purchase Order Number: 00-0000-00 Dated Month Day, Year)

1. Description of Test Items

The materials submitted for this test are identified as follows:

1. White Diffuser plate (7.6 cm by 12.7 cm)
2. Aluminum Diffuser (7.6 cm by 12.7 cm)

2. Description of Test

The reflectance factor measurements as a function of wavelength were made using the NIST Spectral Tri-function Automated Reference Reflectometer (STARR). Three specimens of freshly pressed polytetrafluoroethylene (PTFE) powders were prepared and then measured before and after the test specimens. Measurements were made at the twelve specified wavelengths, with the specular beam included in the measurement of 6°/hemispherical reflectance factor. The sample beam illuminated an area with diameter 20 mm in the center of the specimen. The spectral bandwidth was 10 nm.

Laboratory Environment:
Temperature: 23 °C ± 0.6 °C
Relative Humidity: 40% ± 0.6%

3. Results of Test

The average of the PTFE measurements and the absolute reflectance factor (relative to that of a perfect diffuser) of the PTFE was used to adjust the measured reflectance factor of the test items to the absolute reflectance scale. The results of the data reduction are listed in Tables 1 and 2.

The expanded uncertainty (k=2) for the 6°/hemispherical reflectance factor values listed in Tables 1 and 2 are as follows: 0.005 for the measurements at 230 nm and 252 nm, 0.003 for the measurements from 273.5 nm to 400 nm. The factors that contribute to this uncertainty are the variation in reflectance factor of freshly pressed PTFE specimens, the increased random noise at the shortest wavelengths, and random noise in the measurements.

4. General Information

1) The test samples were measured in the "as received condition".

2) The test report may not be reproduced except in full without the written consent of this Laboratory.

Prepared by:

P. Yvonne Barnes
Optical Technology Division
Physics Laboratory

Approved by:

Robert D. Saunders
For the Director
National Institute of
Standards and Technology

Table 1

6°/Hemispherical Reflectance Factor
Specimen: WHITE DIFFUSER PLATE

Wavelength [nm]	Reflectance Factor
230	0.885
252	0.921
273.5	0.942
283	0.947
292.2	0.958
301.9	0.966
312.5	0.969
331.2	0.977
339.8	0.979
350	0.983
375	0.983
400	0.990
425	0.990

Table 2

6°/Hemispherical Reflectance Factor
Specimen: ALUMINUM DIFFUSER

Wavelength [nm]	Reflectance Factor
230	0.409
252	0.442
273.5	0.468
283	0.475
292.2	0.482
301.9	0.489
312.5	0.496
331.2	0.507
339.8	0.511
350	0.516
375	0.526
400	0.530
425	0.533

Appendix E

Volume 101, Number 5, September–October 1996
Journal of Research of the National Institute of Standards and Technology

[J. Res. Natl. Inst. Stand. Technol. **101**, 619 (1996)]

NIST High Accuracy Reference Reflectometer-Spectrophotometer

Volume 101 | Number 5 | September–October 1996

James E. Proctor and P. Yvonne Barnes

National Institute of Standards and Technology,
Gaithersburg, MD 20899-0001

A new reflectometer spectrophotometer has been designed and constructed using state-of-the-art technology to enhance optical properties of materials measurements over the ultraviolet, visible, and near-infrared (UV-Vis-NIR) wavelength range (200 nm to 2500 nm). The instrument, Spectral Tri-function Automated Reference Reflectometer (STARR), is capable of measuring specular and diffuse reflectance, bidirectional reflectance distribution function (*BRDF*) of diffuse samples, and both diffuse and non-diffuse transmittance. Samples up to 30 cm by 30 cm can be measured. The instrument and its characterization are described.

Key words: bidirectional; diffuse; hemispherical; monochromator; reflectance; reflectometer; scatter; spectrophotometer; specular.

Accepted: April 2, 1996

1. Introduction

The Optical Technology Division of the Physics Laboratory at the National Institute of Standards and Technology has designed and constructed a new reflectometer-spectrophotometer to replace the previous generation Reference Reflectance Instrument (RRI) [1]. The new instrument, the Spectral Tri-function Automated Reference Reflectometer (STARR), delivers higher accuracy, greater speed of measurement, and greater functionality than the previous instrument. The STARR is capable of measuring spectral reflectance (specular and diffuse) at incidence angles up to 80° from sample normal, and observation angles from within 5° of the incident beam to 80° from sample normal. Spectral transmittance can be measured for incident and observation angles up to 80° from sample normal. The receiver (detector system) has an aperture stop, the area of which has been accurately measured, which remains at a fixed distance from the illuminated spot on the sample for all observation angles. This allows the STARR to make high accuracy bidirectional reflectance distribution function (*BRDF*) [2] measurements. In all operating modes, a sample up to 30 cm by 30 cm can be raster-scanned to measure sample spatial uniformity.

The key improvements over the RRI include greater mechanical stability, higher precision positioning, higher source system throughput, improved detector performance, larger sample holder, sample raster-scanning capability, increased measurement speed, and improved air filtering for a cleaner laboratory environment.

2. Reflectometer Design

Two major problems with the previous instrument (RRI) were poor mechanical stability and low signal levels in the ultraviolet (UV) spectral region. To ensure exceptional mechanical stability, heavy duty precision linear and rotary stages were used in the new design. All components of the STARR are mounted on a 3.6 m by 1.2 m by 0.3 m thick vibration isolated optical table.

This table is located in the center of a light-tight room with black walls and ceiling. Special air filters have been incorporated into the room ventilation system to provide a clean environment. This room also houses all of the STARR electronic components. The instrument is fully automated and is controlled by a computer in an adjacent room. Figure 1 shows the source optics and monochromator mounted at one end of the optical table, the reflectometer-spectrophotometer near the center of the table, and a hemispherical reflectometer located at the far end of the optical table. This hemispherical reflectometer attachment, which is currently under development, will be used for measuring directional-hemispherical reflectance factor, and will not be discussed further in this paper.

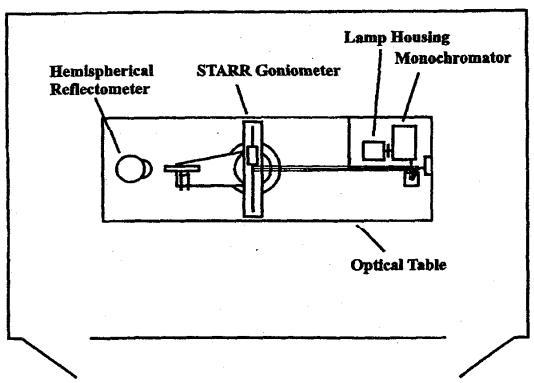

Fig. 1. Top view of the Spectral Tri-function Automated Reference Reflectometer (STARR) facility.

The STARR goniometer has four independent positioning stages. The sample holder, shown in Fig. 2, is attached to a two axis linear positioning system which gives the range of motion needed to raster-scan the entire 30 cm by 30 cm sample area, as well as to position either of two reference samples for measurement. This positioning system is mounted on a rotation stage used to rotate the sample with respect to the incident radiation. The relatively thin profile of the sample holder and positioning system gives this system its large working range of incident angles while maintaining rigidity. The receiver system is mounted on a light weight, rigid arm, which is mounted on a second rotation stage. This rotation stage is independent of and coaxial with the sample rotation stage. This allows the receiver to rotate around the sample holder at a constant radius of 672.6 mm (from the sample rotation axis to the receiver limiting aperture). These two rotation stages are precisely aligned. This is achieved through high precision machining of a heavy duty stainless steel chassis which was fabricated, along with most of the other custom components, in the NIST Fabrication Technology Division's main shop. All four stages are fitted with servo motors controlled by a four axis motion controller.

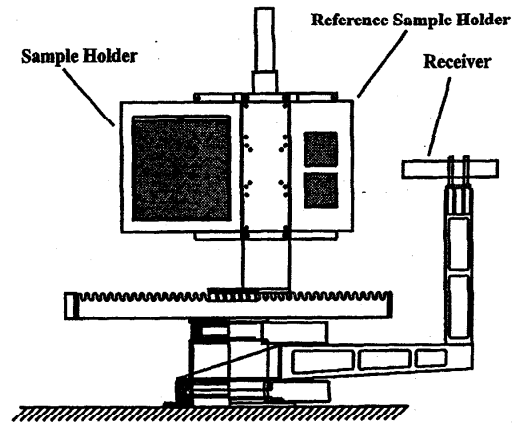

Fig. 2. Front view of the STARR goniometer.

To ensure adequate signal in the UV spectral region, the optical system was designed to minimize reflective losses. An optical system composed of n first surface reflective optics will have an overall effective reflectance (output flux divided by input flux, assuming no other loss mechanisms) of ρ_{eff} where

$$\rho_{\text{eff}} = \prod_{i=1}^{n} \rho_i$$

where ρ_1 is the reflectance of the first element, and ρ_n is the reflectance of the nth element. If we assume, for illustrative purposes, that all of the elements have the same reflectance ρ, then this simplifies to

$$\rho_{\text{eff}} = \rho^n .$$

Thus, if n is large, the overall effective reflectance of the optical system can be quite low, even for relatively high reflectance optics. The optical system for the RRI included 14 first surface reflective elements, while the STARR includes only 7 such elements. This provides a significant improvement in overall effective reflectance over the RRI.

3. Source System

The lamp housing (Oriel 7340 Monochromator Illuminator[1]) contains two sources. A 150 W ultraviolet enhanced xenon arc lamp is used for the 200 nm to 400 nm spectral range, and a 100 W quartz-tungsten-halogen (QTH) lamp is used for the 400 nm to 2500 nm spectral range. The xenon arc is monitored by a detector based light intensity controller (Oriel 68850 Light Intensity Controller) equipped with a UV bandpass filter to optimize the stability in this spectral region. This intensity controller provides feedback to the arc lamp power supply (Oriel model 68805) to stabilize the lamp intensity. The stability of the xenon arc was measured with and without the intensity controller. For this measurement, the receiver was positioned to measure the incident beam, and the beam and background were measured from 200 nm to 400 nm in 10 nm steps. This process was repeated ten times over a period of several hours. The intensity stabilizer improved the xenon arc stability by a factor of 5, reducing the relative experimental standard deviation of the measured intensity from 0.5 % to 0.1 %. The QTH lamp is operated by a high stability power supply (Oriel 68830 Radiometric Power Supply). The lamp housing has a collection mirror which focuses the radiation on the monochromator entrance slit, and matches the $f/\#$ of the monochromator. The collection mirror can be rotated to select either of the two lamps. The lamp housing is coupled to the 1/4 meter $f/3.9$ monochromator (Oriel 77700 Multispec 257) through a five position filter wheel. This filter wheel holds a series of cut-on (long-pass) filters, used to eliminate higher order wavelengths (order sorting). The monochromator has a four-grating turret equipped with three 600 lines per millimeter ruled gratings blazed at 200 nm, 400 nm, and 1000 nm, respectively, and a 150 lines per millimeter ruled grating blazed at 4000 nm (included for possible extension of the working range beyond 2500 nm). The filter wheel and the grating turret are controlled by the monochromator microprocessor. The filter and grating selection information, after being optimized experimentally, is stored in the monochromator nonvolatile memory. The proper filter and grating are automatically selected for any given wavelength. As the radiation exits the monochromator through a 1 mm circular aperture, it is collimated by a 51 mm diameter off-axis parabolic mirror. The radiation is then directed by a 51 mm diameter flat mirror through a series of baffles, an optical chopper, a Glan-Taylor polarizer, and a final baffle before exiting the source system along the optical axis of the instrument.

A 1 mm monochromator entrance slit is used for UV and visible (Vis) measurements. The spectral bandpass was evaluated using emission line measurements and found to be approximately 7 nm at 550 nm. A 2 mm entrance slit is used for near-infrared (NIR) measurements to improve signal to noise ratio, resulting in a slightly larger spectral bandpass in this region. A 1 mm diameter circular exit aperture is used for all measurements.

4. Receiver System

The STARR receiver system consists of a precision circular aperture with an area of 796.84 mm^2 [3], a fused silica lens, and several baffles mounted in a 51 mm diameter cylindrical housing. The precision aperture is the limiting aperture of the receiver and defines the collection solid angle for BRDF measurements. The lens has two functions in this system. First, it condenses the nearly collimated 14 mm diameter beam onto the detector such that the detector is underfilled. Second, the lens images the sample plane of the goniometer onto the detector, giving the STARR receiver a well-defined field of view.

Two detectors are utilized in the STARR receiver. A 10 mm by 10 mm silicon photodiode is used for the spectral range of 200 nm to 1100 nm. A 1 mm diameter thermoelectrically cooled photovoltaic indium arsenide photodiode coupled to an averaging sphere is used for the spectral range of 900 nm to 2500 nm. The receiver system was constructed in such a way that the baffles, limiting aperture, and fused silica focusing lens remain fixed on the detector arm, while the detectors are interchangeable. This design permits the interchanging of detectors without the need to realign the system. A low noise transimpedance amplifier (TIA) is used with both detectors. When using the silicon photodiode, the output of the TIA is measured with a seven and one-half digit digital voltmeter (DVM). When using the indium arsenide photodiode, an optical chopper is used in conjunction with a lock-in amplifier. The output of the lock-in amplifier is measured with the DVM.

The linearity of the detectors was measured using a combination of multiple apertures and neutral density filters. A double aperture mechanism consisting of two adjacent semicircular apertures, each with its own shutter, was placed in the sample holder and positioned such that both apertures were overfilled by the incident beam. The signal due to light passing through aperture "A" was measured and designated V_A. The signal due to light

[1] Certain commercial equipment, instruments, or materials are identified in this paper to foster understanding. Such identification does not imply recommendation or endorsement by the National Institute of Standards and Technology, nor does it imply that the materials or equipment identified are necessarily the best available for the purpose.

passing through aperture "B" was measured and designated V_B. Finally, the signal due to light passing through both apertures simultaneously was measured and designated V_{AB}. A neutral density filter was then used to attenuate the beam, and the above measurement sequence was repeated. This process continued using successively higher density filters until the attenuated beam could no longer be measured. These measurements were repeated at several wavelengths. The data were analyzed to determine at what signal level the relationship $V_A + V_B = V_{AB}$ was no longer satisfied to within the uncertainty of the measurement. For both detectors, it was found that the above relationship was satisfied until the noise floor of the detector system was reached. That is, no measurable nonlinearity was found at signal levels above the noise floor.

Since the silicon photodiode is used without an averaging sphere, its response uniformity was measured in the NIST Detector Comparator Facility to determine if the detector was suitable for use in the STARR receiver. Table 1 shows the nonuniformity of this detector at four wavelengths. While the nonuniformity is as high as 1 % in the NIR and 0.6 % in the UV, because the detector is underfilled, and because these nonuniformity figures represent extreme values which are limited to very small portions of the detector active area, the effect of these nonuniformities is insignificant. Due to the imaging characteristics of the receiver system, this nonuniformity would only contribute significantly to the measurement error when measuring a sample with a significantly nonuniform spatial distribution of reflected energy, such as measuring near-specular *BRDF* of a mirror. This is not the type of measurement that this system was designed to perform. The nonuniformity of this detector will not contribute significantly to the measurement uncertainty for the types of measurements to be performed.

Table 1. Silicon photodiode response non-uniformity

Wavelength	Detector response non-uniformity
250 nm	0.6 %
500 nm	0.2 %
800 nm	0.4 %
1000 nm	1.0 %

5. Measurement Results

For the purpose of this work, four types of samples were selected to demonstrate the capabilities of the new instrument: (1) A first-surface-aluminum-coated mirror, representative of the Standard Reference Material (SRM) 2003 used in industry to calibrate the photometric scale of spectrophotometers; (2) a porcelain enamel on steel tile which is used for colorimetric measurements of chromatic British Ceramic (BCRA) tiles; (3) an NG-9 black glass, representative of SRM 2026, which is also used to calibrate the photometric scale of spectrophotometers; and (4) a GL-2 black glass which was used to expand the dynamic range of the photomultiplier tube detector system used in the previous generation instrument for low level measurements in the ultraviolet region. All of these samples were chosen for their long history of stable, repeatable measurements.

Additionally, a freshly pressed plaque of Polytetrafluoroethylene (PTFE) resin was measured using an angle of incidence of 45° and angle of observation of 0° with respect to the sample normal (customarily denoted as 45°/0° geometry). This type of sample is currently being developed as a working standard for 45°/0° *BRDF* [4].

Measurements results given herein represent two types of measurement geometries: specular reflectance factor (*SRF*) using 6°/6° geometry, and bidirectional reflectance distribution function (*BRDF*) using 45°/0° geometry.

The *SRF* is measured by setting the angle of incidence (the angle between the incident radiation and the sample normal) to 6° and measuring the specularly reflected flux at 6° on the other side of the sample normal. The incident flux (Φ_i) and the reflected flux (Φ_r) are measured, and the ratio of these measurements gives the specular reflectance factor.

$$SRF = \Phi_r / \Phi_i \ .$$

BRDF is defined as the differential ratio of the reflected radiance (L_r) to the incident irradiance (E_i) and can be expressed as

$$BRDF = \mathrm{d}L_r / \mathrm{d}E_i$$

For practical measurements conditions [5], this can be expressed as

$$BRDF = \Phi_r / (\Phi_i \, \omega_r \cos\theta_r) \ ,$$

where Φ_r is the reflected flux collected by the receiver, Φ_i is the flux incident on the sample, θ_r is the angle of observation, and ω_r is the solid angle subtended by the limiting aperture of the receiver where, to a good approximation

$$\omega_r = \pi r^2 / R^2$$

where r is the radius of the receiver limiting aperture and R is the distance from the sample to the receiver limiting aperture.

Table 2 lists the components of relative standard uncertainty, the relative combined standard uncertainties, and the expanded uncertainties for these measurements [6]. The incident and reflected flux measurements each have a relative standard uncertainty of 0.10 %. These values arise from statistical variations in repeated flux measurements made over a period of approximately 5 h using the xenon arc lamp and light intensity controller, and are due to lamp drift, amplifier noise and drift, voltage measurement noise, and other contributions. The receiver limiting aperture area was determined using the NIST High Accuracy Aperture Comparator, and its uncertainty was assigned based on the uncertainty budget of the comparator. The distance from the sample plane to the receiver limiting aperture was measured using a precision inside-micrometer. This distance was measured at five different detector arm angles at 45° intervals. This measured distance varied by 0.05 mm. The inside micrometer had a standard uncertainty of 0.05 mm. These values are small compared to the overall distance, so for simplicity these were added together and treated as a standard uncertainty of 0.10 mm, or 0.02 % of the distance. The uncertainty in the solid angle of detection was calculated by combining in quadrature the uncertainties in the receiver limiting aperture area and the distance from the sample plane to the receiver limiting aperture (with appropriate weighting factors). This yielded a relative standard uncertainty in the solid angle of detection of 0.075 %. To check the angular accuracy of the goniometer system, the receiver was centered on the incident beam and the receiver angle counter was set to 0°. A first surface mirror was then mounted in the sample holder and positioned so as to retro-reflect the incident beam. The sample angle counter was then set to 0°. The sample holder was rotated in 10° steps and the receiver was positioned to the appropriate (theoretical) angle to intercept the specular reflection of the beam. The distance from the center of the receiver to the center of the reflected beam was measured for each angular setting. This procedure was repeated several times. The largest measured displacement of the beam from the receiver center was 0.5 mm. Because the center of the beam could be estimated to 0.5 mm, this was added to the measured displacement for a maximum displacement of 1.0 mm. At a distance from sample to receiver of 672.6 mm, this corresponds to a relative standard uncertainty in the receiver angle of 0.09°. The rotary stages used in the STARR goniometer have an angular resolution of 0.001° and an angular standard uncertainty and

Table 2. Relative combined standard uncertainties, expanded uncertainties, and their components

Components of the relative standard uncertainties.		
Source of uncertainty		Relative standard uncertainty
Incident flux measurement, Φ_i		0.10 %
Reflected flux measurement, Φ_r		0.10 %
Receiver limiting aperture area, A		0.05 %
Distance from sample to receiver, R		0.02 % [a]
Solid angle of detection, ω_r		0.075 %
Angle of observation, θ_r		0.09°
$\cos\theta_r$	$\theta_r = 0°$	<<0.001 %
	$\theta_r = 15°$	0.042 %
	$\theta_r = 30°$	0.091 %
	$\theta_r = 45°$	0.157 %
	$\theta_r = 60°$	0.272 %
	$\theta_r = 75°$	0.586 %

Relative combined standard uncertainties and expanded uncertainties for coverage factor $k = 2$			
		$u_c(SRF)$	$U(SRF)$
SRF measurements		0.14 %	0.28 %
		$u_c(BRDF)$	$U(BRDF)$
BRDF measurements	$\theta_r = 0°$	0.160 %	0.320 %
	$\theta_r = 15°$	0.165 %	0.330 %
	$\theta_r = 30°$	0.184 %	0.368 %
	$\theta_r = 45°$	0.224 %	0.448 %
	$\theta_r = 60°$	0.316 %	0.632 %
	$\theta_r = 75°$	0.607 %	1.214 %

[a] This is the only type B component of the combined standard uncertainty. All other components are type A.

repeatability of 0.01°. These are small compared to the measured receiver angular relative standard uncertainty of 0.09 %, and in fact, such stage-induced errors are included in the measurement of the receiver angular relative standard uncertainty.

Figure 3 shows the specular reflectance of an SRM 2003 first-surface-aluminum-coated mirror at 6°/6° geometry. Measurements made on the STARR and RRI agree to within their respective measurement uncertainties.

Figure 4 shows the *BRDF* of a white porcelain enamel on steel plaque at 45°/0° geometry. It is interesting to note that the RRI data for this sample were obtained in 1977 while the STARR data were obtained in 1995. Measurements made on the two instruments agree to within their respective measurement uncertainties over most of the spectral range measured. Considering that nearly 20 years elapsed between these measurements, the agreement is remarkable, and demonstrates the excellent long term stability of this sample. The

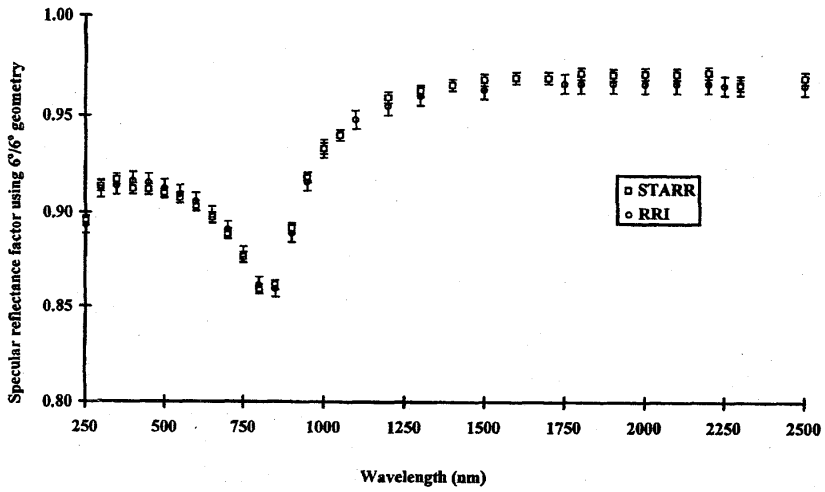

Fig. 3. Specular reflectance factor of a first-surface-aluminum-coated mirror using a 6° angle of incidence and a 6° angle of observation (6°/6° geometry) as measured by the STARR and the Reference Reflectance Instrument (RRI).

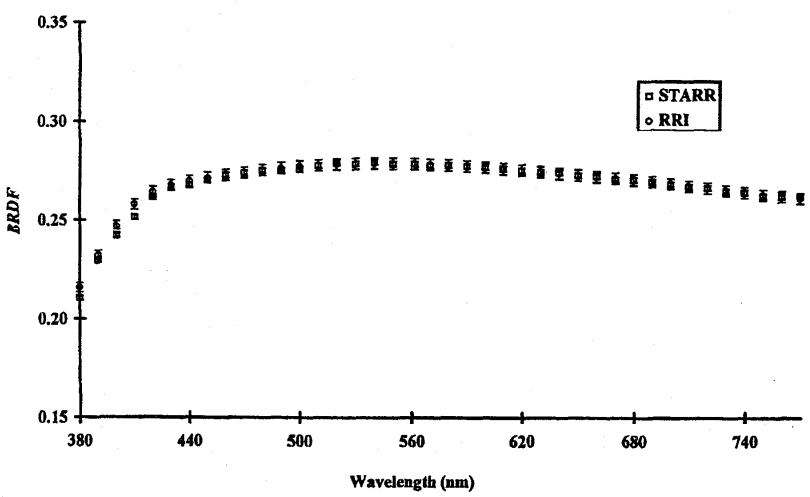

Fig. 4. BRDF of a porcelain enamel on steel tile using a 45° angle of incidence and a 0° angle of observation (45°/0° geometry) as measured by STARR and by RRI.

slight differences in the UV data could easily be due to aging of the sample or differences in cleaning techniques.

Figure 5 shows the *SRF* of NG-9 black glass (SRM 2026) at 6°/6° geometry. At some wavelengths the agreement between the instruments is excellent, while at other wavelengths they differ by several percent. Other types of black glass samples, such as GL-2, show much better agreement. A period of approximately 2 years elapsed between the RRI and STARR measurements, so further studies of NG-9 stability and the effects of cleaning procedures should be performed.

Figure 6 shows the *SRF* of GL-2 black glass at 6°/6° geometry. This sample was used in the RRI as a reference sample for low level reflectance measurements in the UV spectral region, and was chosen for its long

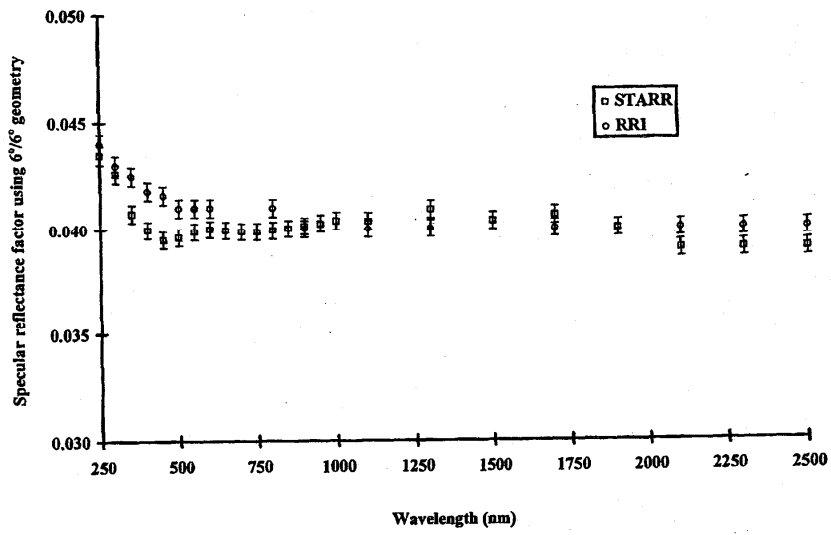

Fig. 5. Specular reflectance factor of NG-9 black glass using 6°/6° geometry as measured by STARR and by RRI.

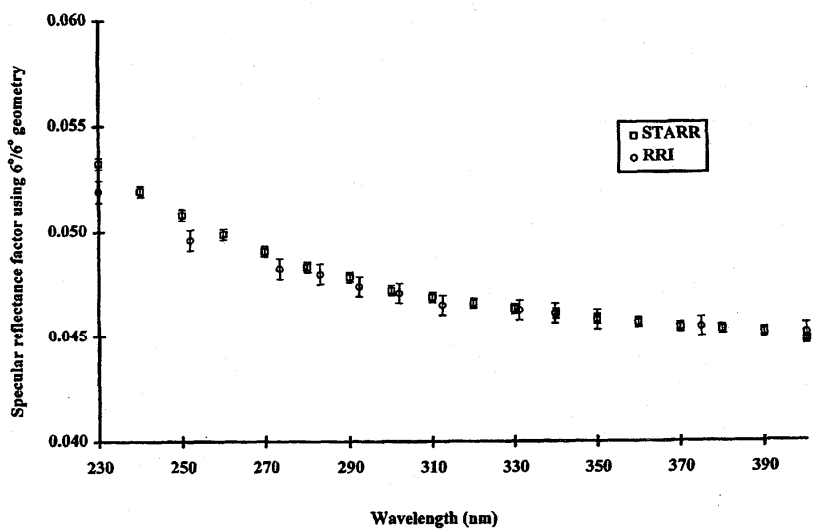

Fig. 6. Specular reflectance factor of GL-2 black glass using 6°/6° geometry as measured by STARR and by RRI.

measurement history and demonstrated long term stability. The agreement between the two instruments is excellent except for the 230 nm and 250 nm data. The RRI was known to have marginal low-level measurement performance at 250 nm. The RRI was not designed to operate at 230 nm, and at this wavelength, measurement performance was very poor.

Figure 7 shows the *BRDF* of pressed PTFE as measured by the STARR. Because this sample was freshly pressed for measurement on the STARR, no direct comparison can be made with the RRI. However, the results of the STARR measurements are in agreement with RRI measurements of similar samples.

6. Conclusion

The Reference Reflectance Instrument (RRI) had been in service at NIST for nearly 2 decades, performing specular reflectance and BRDF measurement services, as well as calibration of numerous SRMs. The Spectral Tri-function Automated Reference Reflectometer (STARR) was designed to replace the aged RRI, and to enhance the range of measurements that could be performed to include larger samples, raster-scanning of samples for uniformity, and spectral transmittance. The new instrument has been designed to provide these capabilities, as well as to provide greater speed of measurement, and more stable and accurate positioning.

The STARR source system was designed to deliver higher flux to the sample and more reliable alignment than the previous system. Care was taken in the optical layout to minimize the number of optical elements in the source system. The STARR source system (including the lamp housing, monochromator, and beam steering optics) has 7 first surface reflective elements versus 14 for the RRI. This allows the STARR source system to maintain optical performance longer in the presence of degradation of optical elements. As an example, if the reflectance of the elements degrades to 0.8, the effective reflectance of the seven elements would be $0.8^7 = 0.202$, while the same degradation in the RRI would result in an effective reflectance of $0.8^{14} = 0.044$.

During a 1 year testing period of the STARR, the mechanical stability of the system was shown to be excellent. During this period, frequent checks of the optical alignment demonstrated that the instrument maintained proper alignment for extended periods. The system required re-alignment only as a direct result of making changes to the optical components to improve performance. The longest period between optical system changes was 6 months, and during this time, no alignment adjustments were needed.

The STARR receiver system was designed to give better detector performance over a broader spectral range than that of the RRI. The STARR can measure reliably at 200 nm, while the RRI could not perform below 250 nm. Even at 250 nm, the measurement performance of the RRI was marginal.

Two limitations of the STARR were found during testing. First, the Glan-Taylor polarizer has fairly low transmittance in the 200 nm to 350 nm spectral region. A UV grade polarizer will be evaluated for use in this

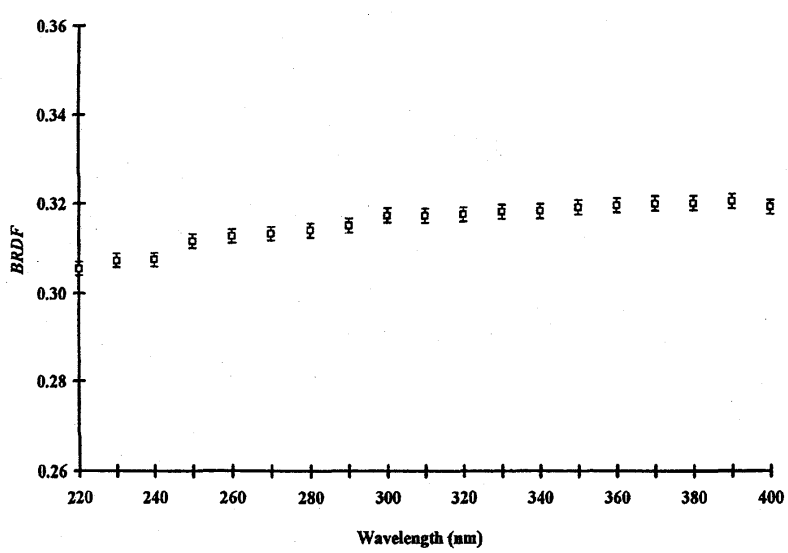

Figure 7. *BRDF* of pressed Polytetrafluoroethylene (PTFE) using 45°/0° geometry as measured by STARR.

spectral region. Second, while the indium arsenide phododiode has excellent responsivity and linearity, it is only available in sizes which are too small for use in the STARR receiver without some diffuser or light gathering mechanism. Several approaches to improve NIR performance are being considered. A 2 mm diameter InAs detector can be fabricated, but due to the relatively low shunt impedance of these detectors, it is not clear that the larger area will result in better performance. A nonimaging concentrator may be used to collect more flux from the averaging sphere and concentrate it onto the detector. Additional optical elements may be used to refocus the receiver at reduced image size directly onto the InAs photodiode, eliminating the need for the averaging sphere. Other detector technologies may also be evaluated.

The design goals for the STARR were to build an instrument which would perform all of the measurements of the former RRI, to perform these measurements with higher accuracy and greater speed, and to handle much larger samples. The STARR performs all of the measurements of the RRI, with additional capabilities, such as raster scanning of large samples, and transmittance measurements. Improvements in the detector system have reduced the radiometric uncertainties of these measurements. The accuracy of positioning and mechanical stability of the new system provide reduced geometrical uncertainties. High accuracy measurement of the receiver limiting aperture reduce both radiometric and geometric uncertainties. Many measurements which took several days on the RRI can be performed in a matter of hours on the STARR.

Acknowledgments

The authors wish to express special thanks to Albert C. Parr for initiating this project, for the support and encouragement needed to achieve our goals, and for many valuable suggestions; Robert D. Saunders and Christopher L. Cromer for their support and technical guidance; Jack J. Hsia for many useful discussions; and Sally Bruce, Thomas Larason, Joel Fowler, Clara Asmail, and Thomas Germer for calibrations and other contributions to this effort.

7. References

[1] Victor R. Weidner and Jack J. Hsia, NBS Measurement Services: Spectral Reflectance, NIST Special Publication 250-8, (1987).

[2] F. E. Nicodemus, J. C. Richmond, J. J. Hsia, I. W. Ginsburg, and T. Limperis, Geometrical Considerations and Nomenclature for Reflectance, NIST Monograph 160 (1977).

[3] Joel B. Fowler, High Accuracy Measurement of Aperture Area Relative to a Standard Known Aperture, J. Res. Natl. Inst. Stand. Technol. **100** (3), 277-283 (1995).

[4] P. Yvonne Barnes and Jack J. Hsia, 45°/0° Reflectance Factors of Pressed Polytetraflouroethylene (PTFE) Powder, NIST Technical Note 1413 (1995).

[5] John C. Stover, Optical Scattering: Measurement and Analysis—2nd edition, SPIE Press (1995) pp. 19-22.

[6] Barry N. Taylor and Chris E. Kuyatt, Guidelines for Evaluating and Expressing the Uncertainty of NIST Measurement Results, NIST Technical Note 1297 (1994).

About the authors: *James E. Proctor is an Electronics Engineer and P. Yvonne Barnes is a Physical Scientist in the Optical Technology Division of the NIST Physics Laboratory. The National Institute of Standards and Technology is an agency of the Technology Administration, U.S. Department of Commerce.*

Appendix F

JOURNAL OF RESEARCH of the National Bureau of Standards
Volume 82, No. 1, July–August 1977

Establishing a Scale of Directional-Hemispherical Reflectance Factor I: The Van den Akker Method

William H. Venable, Jr., Jack J. Hsia, and Victor R. Weidner

Institute for Basic Standards, National Bureau of Standards, Washington, D.C. 20234

(May 22, 1977)

A thorough study and error analysis was made of the Van den Akker or "auxiliary sphere" method of determining a scale of directional-hemispherical reflectance factor. The effects of a non-Lambertian distribution of the reflected radiation, including retroreflection, were included in this study. Three working standards were measured to an uncertainty in reflectance of less than ±0.0015 and these will be used as a basis for a new, more accurate NBS scale of 6°-hemispherical reflectance factor. The new scale and the NBS scale established in 1965 are in agreement to within the uncertainty of ±0.005 assigned to the 1965 scale.

Key words: Absolute reflectance; diffuse reflectance; error analysis; reflectance; reflectance factor; spectrophotometry.

Foreword

We have arranged this paper in a way which should accomodate readers who have an interest in this work from three quite different points of view:

1. Those who must make decisions based upon the results of the measurements are addressed principally in the Summary which directly follows this foreword. The material in parts I. and V.B. would also be of interest to such readers.

2. Those who wish to use the Van den Akker auxiliary sphere method for determining absolute reflectance should find the material in parts II, III, and V.A. to be of particular interest, and part IV can be read superficially, if at all, in order to glean a few technological ideas.

3. Those who are interested in a detailed understanding of the way in which these measurements are carried out at NBS and in a detailed discussion of the error analysis should, after a careful reading of parts II and III, place their emphasis on part IV.

Summary

Of the light or other optical radiation incident upon a surface in a given direction and at a given wavelength, a fraction is reflected from the surface. This fraction is called the spectral directional-hemispherical reflectance of the surface, and measuring it accurately is important in two different classes of applications:

1. Applications in which the value of the reflectance is of direct importance. Such applications include radiative energy transfer as in solar energy devices, lighting system engineering, calibrating radiometers in remote sensing satellites, and formulating the pigmentation in paints and other finishes.

2. Applications in which the actual value of the reflectance is of secondary importance, but for which the basis of measurement must be extremely stable in time. These applications include quality control in automated production and specifications involving color or appearance of finished products. For such applications, the instruments which are used are calibrated with material standards, and the laboratories supplying these standards must be able to measure reflectance directly in order to measure the standards and verify their stability.

The economic benefits derived from having this portion of the measurement system under control are very large, coming in the form of an accumulation of modest benefits over a very large base of application [1].[1] In order to realize these advantages, it is important that the uncertainty in the measurements be commensurate with the uniformity and stability of the reflectance of the surfaces encountered in practice.

For a number of applications, it is important to measure directional-hemispherical reflectance factors near 1 with an uncertainty in the neighborhood of ±0.001. The present extensive work on spectral directional-hemispherical reflectance was undertaken at NBS for two reasons. First, the stated uncertainty of ±0.005 for the NBS reflectance factor scale established in 1965 [2][1] was too large for many of the applications for which we were called upon to standardize the measurements. Second, and even more disturbing, intercomparisons between the scales of national standardizing laboratories in connection with the work of the International Standardization Organization (ISO) revealed differences as great as 0.015 between the measured value of reflectance of the same samples. Such a large difference can have serious economic consequences in international trade in finished goods such as paper.

As a first step in this work, we have investigated in great detail the Van den Akker auxiliary sphere method of determining spectral directional-hemispherical reflectance which

[1] Figures in brackets indicate the literature references on page 49.

has been used in the past at NBS, improving upon the techniques and providing the necessary corrections to make the measurements precise and accurate to within ±0.0015 to the best of our knowledge. This step has been completed and is reported in this paper. The new and former NBS scales of measurement agree to well within the combined measurement uncertainties.

As a second step, we plan to investigate the techniques used by the other major national laboratories and to work with our colleagues in these laboratories to determine the cause of the discrepencies which have been encountered internationally. As part of this step, we have already completed a set of measurements using a second method of determination, the Sharp-Little method. The results obtained with that method are in good agreement with those reported in this paper and are to be published soon in another paper in this same series. We have visited the National Research Council Laboratories in Canada (NRC) for detailed discussions of these results. We also plan to conduct experiments with the Korte method currently used by the Physikalisch-Technische Bundesanstaldt (PTB) in Germany and possibly with one or two other approaches less commonly used.

The scale of directional-hemispherical reflectance as currently established will be disseminated through standards supplied through the NBS Office of Standard Reference Materials and through commercial secondary standards laboratories in the United States. The improvements in techniques which have been developed as a result of this work will be submitted to the appropriate committees of ASTM, ANSI, and TAPPI for possible incorporation in standard procedures. When the international discrepancies have been eliminated, we will be working with NRC, PTB, and possibly other laboratories as standardizing laboratories for ISO reflectance measurements.

I. Introduction

Directional-hemispherical (d/h) reflectance factor measurements are important in a wide variety of applications. If the results of these measurements are to be a useful tool for technical communication, the measurements must be made accurately. Most reflectometers are not capable of measuring d/h reflectance factor directly, but can only compare the reflectance factors of two objects. The calibration of such instruments is accomplished by measuring a standard object which has a known reflectance factor. To see that accurately measured reflectance standards are available to the measurement community is one of the primary responsibilities of the spectrophotometry group of the Radiometric Physics Section of the Institute for Basic Standards.

In the development and production quality control of finished products in which appearance is an important factor, the measurement of reflectance should be accurate to within ±0.002. This level of accuracy or better is also important to rapidly evaluating the stability of reflecting materials under weathering and ageing. These two types of applications are the ones which commonly call for the lowest measurement uncertainty. It is difficult to produce highly reflecting surfaces for which the reflectance is reproduced to better than ±0.001 and the reflectance of most surfaces is not even uniform to this degree. Therefore, a reflectance measuring capability for which the uncertainty is less than ±0.001 is both necessary and sufficient for a national standardizing laboratory. The work described in this technical note is part of an effort to reduce the uncertainty in diffuse reflectance factor measurements at NBS from an estimated ±0.005, which it has been in the recent past, to ±0.001.

The National Bureau of Standards (NBS) has established its scale of d/h reflectance factor in 1965 through an extensive series of measurements by Goebel, Caldwell, and Hammond [2]. At that time, Vitrolite [3] glass standards [4] to calibrate the General Electric Recording Spectrophotometer (GERS) [5] (Cat. 5962004 G28 No. 732986) were measured. Until recently, that instrument has been used for most reflectance measurements made at NBS. The reflectance of the Vitrolite standards has been shown to be very stable by measurements made over a period of thirty years relative to freshly prepared MgO surfaces [6]. In 1974, the scale of measurement was rechecked using the same apparatus used in the 1965 experiments and the agreement was within the experimental error associated with the measurements.

In April of 1974 and through the following year, it was determined from measurements made on a number of samples that there was a systematic difference between the scales of measurement being used by NBS and the National Research Council Laboratories of Canada (NRC). This difference was approximately 0.015 at the short wavelength end of the visible spectrum and decreased more or less regularly to approximately 0.01 at the long wavelength end of the spectrum (table I). A similar intercomparison between NRC and Physikalisch-Technische Bundesanstalt of Germany (PTB) [7] revealed only slight differences between the measurements being made by these laboratories (table II). Since the NBS uncertainty at that time is conservatively estimated to be ±0.005 and the NRC uncertainty is conservatively estimated to be ±0.003, the difference is clearly significant.

TABLE I

Data from an intercomparison between NRC and NBS of reflectance measurements on a sprayed $BaSO_4$ coating*. (June 1975) (Spectral directional (6°)-hemispherical reflectance).

Wavelength	Reflectance		
	NRC	NBS†	Difference (NRC-NBS)
400	0.961	0.975	0.014
420	.963	.975	.012
440	.966	.978	.012
460	.970	.980	.010
480	.970	.981	.011
500	.972	.981	.012
520	.972	.985	.013
540	.972	.985	.013
560	.974	.984	.010
580	.975	.985	.010
600	.975	.985	.010
620	.976	.982	.006
640	.975	.986	.011
660	.976	.985	.009
680	.976	.985	.009
700	.977	.985	.008
720	.978	.985	.008
740	.979	.985	.007

* Samples prepared at NRC.
† Data from NBS test 232.14/49D.

The methods used by NBS, NRC, and PTB are all different. In any such case of disagreement between measurements, all measurements and methods are logically suspect

TABLE II

Data from an intercomparison between NRC and PTB of reflectance measurements on a pressed $BaSO_4$ tablet [7] (Spectral Hemispherical-directional (0°) reflectance factor).

Wavelength	Reflectance		
	NRC	PTB	Difference (PTB-NRC)
370	0.961	0.965	0.004
380	.969	.971	.002
390	.974	.976	.002
400	.977	.979	.002
420	.982	.983	.001
440	.985	.984	−0.001
460	.986	.985	−0.001
480	.987	.986	−0.001
500	.987	.987	0
550	.988	.988	0
600	.988	.988	0
650	.987	.988	0.001
700	.987	.989	.002
750	.987	.988	.001

until the cause of the difference is located. However, since the NRC and PTB measurements were in close agreement, it seemed reasonable to investigate the method used by NBS first. A Diffuse Transmittance and Reflectance Reference Spectrophotometer [8], which will be referred to by the acronym DRS for convenience, was completed at NBS in October 1975. This has been used to make detailed measurements of all aspects of the Van den Akker auxiliary sphere method for realizing an absolute scale of d/h reflectance factor [9], which was the method used to establish the NBS scale. The results of this investigation are reported in this paper.

As a result of this investigation a new NBS scale of diffuse reflectance factor measurements for 6° incidence and hemispherical collection has been established which is believed to be accurate to within ±0.0015. The new scale of reflectance factor differs by less than 0.002 from the scale formerly used by NBS. Since this investigation revealed no cause for the discrepancy between national laboratories, we are undertaking a thorough examination of the methods used by the other laboratories. The results of that work are to be reported in future papers.

II. Definitions

A. Directional-Hemispherical Reflectance

One quantity to be measured is the spectral d/h reflectance, ρ (U, P, λ) at a point on a plane surface. Using the notation described in NBS Technical Note 594-9 [10], this quantity can be expressed in terms of a generalized scattering function S as:

$$\rho\,(\mathbf{U}, \mathbf{P}, \lambda) = \iint S\,(\mathbf{U}, \mathbf{P}; \mathbf{u}, \mathbf{p}, \lambda)\,\mathbf{u}\cdot d\mathbf{a}\,d\omega \qquad (1)$$

where $S(\mathbf{U}, \mathbf{P}; \mathbf{u}, \mathbf{p}, \lambda)$ is the radiance emerging from the sample surface at point $\mathbf{p}$ in direction $\mathbf{u}$ due to a unit flux striking the sample at point $\mathbf{P}$ in direction $\mathbf{U}$. It is assumed that the sample is non-fluorescent so that all of the radiation can be confined to a very narrow band at wavelength λ. The integral with respect to the solid angle, ω, in which the radiation emerges is taken over the entire hemisphere of directions and the integral with respect to the area a from which the radiance emerges is taken over the entire area from which the flux emerges. For the uniform, isotropic samples to be discussed in this paper, the d/h reflectance can be represented by $\rho(\Gamma, \lambda)$, where Γ is the angle between the direction of incidence $\mathbf{u}$ and the surface normal.

B. Directional-Hemispherical Reflectance Factor

A typical d/h reflectometer has an entrance port which subtends at the sample a circularly shaped solid angle ω' which in magnitude is on the order of 10^{-3} steradians. None of the flux falling into ω' reaches the detector, and therefore the instrument does not compare d/h reflectances of the samples as just defined but rather compares "directional-hemispherical" reflectance factors [11] $F(\Gamma, \lambda)$ for collection over the entire solid angle except for ω'. That is to say, the retroreflected flux is excluded from the measurement. To a very good approximation,

$$F(\Gamma, \lambda) = \frac{\iint' S(\mathbf{U}, \mathbf{P}; \mathbf{u}, \mathbf{p}, \lambda)\mathbf{u}\cdot d\mathbf{a}d\omega}{\iint'[\delta(\mathbf{P} - \mathbf{p})/\pi]\mathbf{u}\cdot d\mathbf{a}d\omega} \qquad (2)$$

where the prime on the integral indicates integration over the entire hemisphere except for ω' and $\delta(\mathbf{P} - \mathbf{p})/\pi$ is the idealized scattering function S for an ideal diffuse reflector.

It is the quantity $F(\Gamma, \lambda)$ in which we are most interested when calibrating a reflectometer, and determining this quantity for several working standards is the object of the work reported in this paper.

III. An Overview of the Method

The method to be described for determining d/h reflectance factor is more complex than the method for measuring d/h reflectance originally proposed by Van den Akker. In the original method, it was assumed that d/h reflectance is independent of the direction of incidence. Since this is not sufficiently correct for many surfaces, additional measurements are needed in order to accurately determine the d/h reflectance using this approach. Also, the relationship between d/h reflectance and the reflectance factor as measured by an instrument must be determined. However, for simplicity, we will continue to call the entire process the Van den Akker method.

Although this method is simple in principle and is potentially one of the most accurate methods, the descriptions of it in the literature are usually given in terms of involved summations of infinite series. These descriptions tend to cloud the simplicity of the method and to lead to a misunderstanding of it. Therefore, before describing the details of the measurements as performed at NBS, we will first provide a brief overview of the method in terms of four main steps. The first and last steps were used in the original Van den Akker method, and we have added the additional steps to take into account the variation of $\rho(\Gamma, \lambda)$ with Γ and the difference between $\rho(\Gamma, \lambda)$ and $F(\Gamma, \lambda)$.

The primary measurement in the Van den Akker method is a measurement of the reflectance of the wall of an integrating sphere (fig 1) under the irradiation it receives in the sphere. We will call this reflectance the Van den Akker reflectance $\rho_v(\lambda)$. A flux is introduced into the sphere by reflecting a collimated beam of radiation from the back of the sphere.

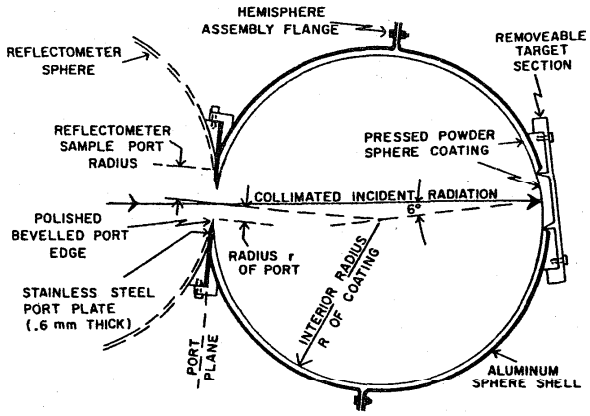

FIGURE 1. *Sphere used for measuring Van den Akker reflectance.*

Most of the radiation which strikes a given area of the sphere wall has undergone many reflections. In a sphere of this type, the average number of times a photon will have passed into the sphere wall and been reflected before it is absorbed or escapes would be between fifty and one-hundred. Because the reflection from the sphere wall is very diffuse, any asymmetry in the way the photons are introduced is dispelled in one or two reflections and the distribution of radiance, L_s, striking the wall has two characteristics properties. First, the irradiance is very nearly uniform over the sphere wall. This follows from the fact that a perfectly Lambertian (radiance constant with respect to direction) reflected flux would produce a uniform irradiance over the sphere wall. Since the distribution of the reflected flux is very nearly Lambertian, the distributon over the sphere wall of incident photons which have been reflected more than two or three times is for all practical purposes uniform. This phenomenon is well-known and forms the basis for the many applications of integrating spheres in which the sphere is used as a flux averaging device. Another property of the spherical geometry which is less often noticed is that a photon which leaves the sphere wall at an angle θ will next strike the sphere wall at the same angle. Thus, after one or two reflections, an angular distribution of radiance L_s (Γ), will be set up which represents, to within a proportionality constant, the incident and emerging radiance at any point on the sphere wall. Unlike the distribution of irradiance over the wall area, the distribution of the radiance with respect to the angle *does not become uniform with angle* but takes on a distribution determined by the bidirectional reflectance properties of the wall coating.

The remaining steps in the method relate the Van den Akker reflectance to the d/h reflectance factor and provide a method of using this reflectance data to calibrate an instrument. The four steps in the Van den Akker method can be outlined as follows:

A. Determining the Van den Akker Reflectance $\rho_v(\lambda)$

A sphere with a single port (see fig. 1) is lined with a highly reflecting white coating, radiation is introduced into the port in a collimated beam, and, from measurements made of the flux re-emerging from the port and of the flux reflected from the target area, the Van den Akker reflectance ρ_v[2] determined. A flux ϕ_0 (λ) is introduced into the sphere ir collimated beam which strikes the target area of reflectan ρ_t (Γ, λ), providing a nearly Lambertian source of radiati which emits a flux $\phi_0\rho_t$. A fraction f of this flux passes c through the port as a nearly collimated beam, and the r maining portion falls on the sphere wall and is reflected wi reflectance ρ'_v, the average reflectance of the sphere wa excluding the port. This flux, the strength of which is giv by $\phi_0\rho_t(1-f)\rho'_v$, acts as a radiation source which is ur formly distributed over the sphere wall. This flux is tl source of radiant energy for the total flux $\phi_i(\lambda)$ striking tl sphere boundary. A fraction f of λ_i passes out through tl port, and a fraction $(1-\rho'_v)$ of the remaining $(1-f)$ is a sorbed in the sphere wall or otherwise lost and is not returne to the sphere. In equilibrium, the flux lost from ϕ_i out tl port and into the walls is replaced by the uniformly di tributed source, from which an equilibrium flux balan equation can be obtained:

$$\phi_0\rho_t(1-f)\rho'_v = \phi_i[f + (1-f)(1-\rho'_v)]. \quad ($$

If the flux ϕ_0 is the sample beam flux from a dual bea reflectometer, a signal $Q_s(\lambda)$ is obtained with the sphere the sample position:

$$Q_s = k[\phi_i f(1-f') + \phi_0\rho_t f(1-f'')] \quad ($$

where f' is the fraction of the lambertian flux which escap from the ports of the reflectometer sphere and f'' is tl corresponding fraction of the nearly collimated beam whi emerges from the sphere as a result of the first reflection fro the back of the Van den Akker sphere. With the target ar from the back of the sphere placed directly on the reflectom ter sample port as a sample, a signal $Q_t(\lambda)$ is obtained:

$$Q_t = k\phi_0\rho_t(1-f'). \quad ($$

It is arranged that the angle of incidence Γ at which strikes the target when Q_t is measured is the same as when is measured. Equations (3), (4), and (5) can be solved obtain an expression for ρ'_v in terms of Q_t, Q_s, f, f' and f'

$$\rho'_v = \frac{1-(fQ_t/Q_s)(1/(1-\alpha))}{1-f} \quad ($$

where

$$\alpha = \frac{f(f'-f'')}{(1-f')}\frac{Q_t}{Q_s}. \quad (6$$

If α were 0, this would be the usual form cited for the Va den Akker reflectance. The factor $1/(1-\alpha)$ takes in account that the first reflection of the incident beam from tl target in the sphere emerges nearly collimated whereas tl remaining flux emerging from the sphere is nearly Lambe tian. If the reflectometer handled both fluxes in the sam way, i.e., if f' and f'' were equal, this term would be zer However, it is usually the cause that f'' is very much larg than f' and this contribution must be included.

[2] To keep the writing uncluttered, the functional dependence of each quantity is shown only wh it is introduced and at key points in the development.

An additional modification must be made in the original Van den Akker equation to take into account the effect on ρ_v' of the retroreflectance of the sphere wall. This modification, which results in only a small adjustment ρ_v' but which greatly complicates the form of eq (6), is discussed in detail in appendix A.

Since $(1 - f)(1 - \rho_v')$ in eq (3) represents the portion of ϕ_i which is lost everywhere but out of the port, it follows that the reflectance ρ_v' is the average reflectance over the sphere area excluding the port. To relate ρ_v' to a property of the sphere coating, it is important that the sphere coating be uniform and completely cover all of the sphere area except for the entrance port. If it is necessary to have cracks or other gross imperfections in the coating, the losses in such imperfections must be estimated and ρ_v' must be suitably corrected in order to obtain the Van den Akker reflectance ρ_v of the sphere coating.

B. Adjustment from Van den Akker Reflectance $\rho_v(\lambda)$ to d/h Reflectance $\rho(\Gamma, \lambda)$

In order that the need for the next steps be more readily understood, ρ_v will be interpreted in terms of the directional-hemispherical reflectance, ρ, as defined in eq (1).

$$\rho_v = \frac{2\pi \int_0^{\pi/2} L_s(\Gamma)\, \rho(\Gamma) \cos(\Gamma) \sin(\Gamma)\, d\Gamma}{2\pi \int_0^{\pi/2} L_s(\Gamma) \cos(\Gamma) \sin(\Gamma)\, d\Gamma} \tag{7}$$

where $L_s(\Gamma)$ is the radiance associated with ϕ_i at the incident angle Γ and explicit indication of the dependence on wavelength has been omitted for clarity. As we have indicated, ρ_v is just the weighted average over all directions of incidence Γ of the d/h reflectance. The weighting function $L_s(\Gamma) \cos\Gamma \sin\Gamma$ is proportional to the irradiance of the sphere wall per unit angle at the angle Γ. If the d/h reflectance were independent of angle of incidence, one can see from equation (7) that ρ_v and $\rho(\Gamma)$ would be identical. However, in any real sphere coating, $\rho(\Gamma)$ is not quite constant and this variation must be taken into account if d/h reflectance is to be determined from ρ_v.

The flux, ϕ_i, striking the sphere wall is composed of radiation most of which has undergone many reflections. As has already indicated, the radiance $L_s(\Gamma)$ striking the wall in one location emerged from the wall at the same angle at some other location. When the irradiance of the wall is uniform and if the generalized scattering function S of the coating were known, the function L_s could be determined by solving the integral equation

$$\rho_v L_s(\gamma) = 2\pi \int_0^{\pi/2} L_s(\Gamma)\, S(\Gamma, \gamma) \cos\Gamma \sin\Gamma\, d\Gamma. \tag{8}$$

Because the irradiance of the sphere wall is uniform, the self radiance distribution, L_s, can be determined to within a constant by measuring the radiance, $L_s(\gamma)$, emerging from the sphere coating through the port with an uncalibrated gonioreflectometer. The relative signal N_g from the gonioreflectometer as a function of the angle of observation γ can be related to $L_s(\gamma)$ as

$$L_s(\gamma, \lambda) = k_1(\lambda)\, N_g(\gamma, \lambda) / \cos(\gamma) \tag{9}$$

where k_1 is a constant of proportionality.

To complete the adjustment, information about the form of $\rho(\Gamma, \lambda)$ is obtained. A flat sample of the sphere wall coating is prepared in the same way as the sphere wall coating and its relative d/h reflectance is measured. The corrected reflectometer signal [12] N_G is proportional to the d/h reflectance.

$$\rho(\Gamma, \lambda) = k_2(\lambda)\, N_G(\Gamma, \lambda). \tag{10}$$

The constant k_2 can be expressed in terms of measured quantities by simultaneous solution of eqs (7), (9), and (10).

$$k_2(\lambda) = \frac{\rho_v(\lambda) \int N_g(\Gamma, \lambda) \sin\Gamma\, d\Gamma}{\int N_G(\Gamma, \lambda)\, N_g(\Gamma, \lambda) \sin\Gamma\, d\Gamma} \equiv \frac{\rho_v(\lambda)}{\bar{N}_G(\lambda)} \tag{11}$$

where $\bar{N}_G$ is the weighted average of $N_G(\Gamma, \lambda)$ with weighting function $N_g(\Gamma, \lambda) \sin\Gamma$. With the value of k_2 determined, the d/h reflectance for any wavelength and angle of incidence can be calculated from the relative d/h reflectance data by using eq (10). However, we prefer to use an expression for $\rho(\Gamma, \lambda)$ which takes the form of a small adjustment of the Van den Akker reflectance. By substituting the expression for k_2 from eq (11) into eq (10) and using some algebraic manipulation, one can put eq (10) into the form

$$\rho(\Gamma, \lambda) = \rho_v(\lambda)\, [1 + C(\Gamma, \lambda)] \tag{12}$$

where

$$C(\Gamma, \lambda) = \frac{N_G(\Gamma, \lambda)}{\bar{N}_G(\lambda)} - 1.$$

C. From d/h Reflectance $\rho(\Gamma, \lambda)$ to d/h Reflectance Factor $F(\Gamma, \lambda)$

If the generalized scattering function S for directions of incidence and reflectance both falling within the reflectometer entrance port (retroreflectance at entrance angle Γ) were equal to the average of S over all directions of viewing, then the reflectance $\rho(\Gamma, \lambda)$ and the reflectance factor $F(\Gamma, \lambda)$ will be equal. However, for the usual type of sphere coating, S in the retroreflective direction has been observed to be as much as 50 percent above the average at small angles of observation [13]. Therefore, the bidirectional reflectance factor $F(\mathbf{U}, \mathbf{u}\, \lambda)$ must be determined over the extent of the solid angle ω' surrounding the incident direction $\mathbf{U}$ and the relationship between $F(\Gamma, \lambda)$ and $\rho(\Gamma, \lambda)$ determined from eqs (1) and (2) as

$$F(\Gamma, \lambda) = \frac{\rho(\Gamma, \lambda) - \frac{1}{\pi} \int \mathbf{F}(\mathbf{U}, \mathbf{u}) \cos\gamma\, d\omega}{\left(1 - \frac{1}{\pi}\, \omega' \cos\gamma\right)} \tag{13}$$

where the integral in ω is taken over ω'. (Note that $F(\mathbf{U}, \mathbf{u}) = \pi \int S\, (\mathbf{U}, \mathbf{u})\, da$.)

D. Determining the Directional-Hemispherical Reflectance Factor of Standards and Other Samples

The d/h reflectance factor $F(\Gamma, \lambda)$ as determined in the preceding four steps is the d/h reflectance factor of the sphere wall coating. The final step is to use this information to measure a stable standard reflector which can then be used to calibrate a d/h reflectometer. One of the methods used by Van den Akker [9] was to compare the standard directly with sections of the sphere wall which were hoped to be representative. Another method is to prepare a large number of samples using the same materials and preparation techniques that were used in coating the sphere itself and comparing these to the standard. In either case, the d/h reflectance factor $F_c(\Gamma, \lambda)$ of the standard is calculated from the previously determined d/h reflectance factor $F(\Gamma, \lambda)$ of the sphere wall as

$$F_c(\Gamma, \lambda) = F(\Gamma, \lambda) \frac{n\, Q_c(\Gamma, \lambda)}{\sum_{i=1}^{n} Q_i(\Gamma, \lambda)} \tag{14}$$

where Q_c is the reflectometer signal for the standard and Q_i is the reflectometer signal for the ith one of the n samples which are taken to represent the sphere wall. In day-to-day use, the d/h reflectance factor $F_x(\Gamma, \lambda)$ of a sample can be measured by comparison to the stable standard.

$$F_x(\Gamma, \lambda) = F_c(\Gamma, \lambda) \frac{Q_x(\Gamma, \lambda)}{Q_c(\Gamma, \lambda)} \tag{15}$$

where the reflectometer readings Q_x and Q_c are taken close together in time in order to minimize the effects of instrument drift.

IV. The Measurements as Currently Made at NBS

The overview in the preceding section describes in general the way that d/h reflectance can be determined by the Van den Akker method. Three determinations of the d/h reflectance of a set of standards has been made using the DRS. Through the experience gained in these determinations, a procedure for making the measurements with this instrument has been worked out. That procedure is described in this section to give a documented starting point for future improvements in the method and the data from these three determinations provide the basis for the current NBS scale of $6°/h$ reflectance factor.

Three different materials were used as sphere coatings for the determinations. In the first determination, the sphere was coated with $BaSO_4$ powder [3, 14] from a stock which had been on our laboratory shelf for some time and had been opened on previous occasions. This was used to obtain experience with the method and to obtain an idea of some of the difficulties which might be encountered with a material which was slightly contaminated and which had a slightly lower reflectance than the best quality coatings. In the second determination, the sphere was coated with Halon [3, 15] powder, and in the third determination a fresh lot of reagent grade $BaSO_4$ powder [3, 16] was used. The advantages and disadvantages of each coating will be brought out in the discussion of the measurement errors in the description of each of the three main measurement steps.

A. Determining the Van den Akker Reflectance $\rho_v(\lambda)$

The design of the spheres used to determine the Van den Akker reflectance of the sphere coating material is shown in figure 1. In some of his earlier work using this method, Van den Akker used a sphere with many removable sections in order to sample at many points the actual sphere coating being measured. However, the presence of many removable sections provides an uneven substructure for the sphere coating, creating a potential for dark rings and even cracks in the coating at the border of each removable section. Therefore, we decided to have only the target area removable and to rely on reproducing the coating for a representative sampling.

The sphere coating is made by packing the powder into the aluminum sphere shell with an electrically driven hammer which has a Teflon [3] head (fig. 2). The hammer is mounted on a stand and each hemisphere of the sphere is mounted in turn on a gimbal which allows it to be rotated about a point a fixed distance behind the hammer. In this way, a hemisphere of constant interior radius R is packed uniformly in a mechanical way. A plastic ring attached to the flange of each hemisphere as it is being packed allows the packing jig to be aligned the same for both hemispheres and allows the coating to be built up to full thickness at the edge of the hemisphere. In this way, when the plastic ring is removed and the sphere is joined, a uniform sphere coating of interior radius R results which has no crack at the plane where the hemispheres join.

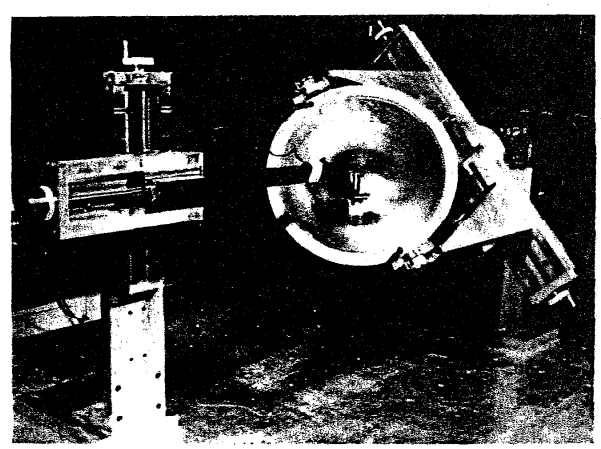

FIGURE 2. *Apparatus used to produce the sphere coating.*

1. Determining the Uncorrected Van den Akker Reflectance ρ_v'

The fraction f introduced in eq (6) is taken as that portion of the area of the sphere of radius R which is occupied by the port of radius r, i.e.,

$$f = (1 - (1 - (r/R)^2)^{1/2})/2. \tag{16}$$

Associated with each determinaton of f there is an estimated random error, as defined in appendix B. A random error δR arises from our inability to pack the sphere to the same radius

R from one determination of reflectance to the next and from the inability to measure the average R exactly. This gives rise to a random error δf which is given by:

$$\delta f = \frac{(r^2/R^3)}{2(1 - (r/R)^2)^{1/2}} \delta R. \tag{17}$$

A systematic error arises from any error in measuring r and from assuming that the measured r is the effective r. Both of these can be taken into account in terms of an uncertainty Δr in the effective port radius. The estimated systematic error Δf is given by

$$\Delta f = \frac{(r/R^2)}{2(1 - (r/R)^2)^{1/2}} \Delta r. \tag{18}$$

The reflectance of the sphere was measured using the DRS with the $6°/h$ (specular included) general purpose integrating sphere [17]. In this mode of operation, the instrument is a dual beam reflectometer with a capability of highly accurate measurements of relative $6°/h$ reflectance factor, i.e., the instrument measures a quantity Q which is proportional to the $6°/h$ reflectance factor of the sample appearing in the plane of its sample port. With the sphere in place as a sample, a reflectance value which will be called Q'_s is measured. As is described in detail in the Technical Note on the DRS [18], a correction must be made for the small amount of radiation which does not enter the sphere port but instead is reflected from that portion of the sphere port plate which shows in the reflectometer sample port or is reflected from the sphere wall of the reflectometer itself. In order to correct for this scattered radiation, a second reflectance measurement is made with the auxiliary sphere port plate in place without the sphere behind it, i.e., with most of the sample beam of the reflectometer passing out into the room and being lost. The reflectance value Q_p obtained in this manner must be subtracted from Q'_s in order to obtain a reflectance value proportional to the radiation being returned from inside the sphere. Most of the radiation emerging from the sphere passes freely back through the port into the reflectometer sphere. A small fraction of it, however, will strike the polished beveled edge of the auxiliary sphere port and will, thereby, suffer a slight loss as it returns to the reflectometer sphere. To correct for this loss, we measured the relative reflectance Q_f of a flat plate of the same stainless steel from which the auxiliary sphere port plate was made. Since Q_f in the reflectometer is approximately the reflectance of the sample relative to the sphere wall which in turn has a reflectance nearly 1, Q_f was approximately the reflectance of the stainless steel plate for 6° incidence. The radiation coming from the sphere which strikes the beveled edge strikes it at near grazing incidence. Since the reflectance from a metal surface near grazing incidence is higher than the near-normal reflectance, we chose to represent the reflectance from the beveled edge by $(1 + 2Q_f)/3$. This estimate is based on the general shape of the reflectance curves for metals [19] and on the port dimensions (fig. 3) [20]. Under this assumption, if the projected solid angle subtended by the beveled edge of the port averaged over the port area is ω_e, an expression for the corrected sphere reflectance Q_s can be written as

$$Q_s = (Q'_s - Q_p)\Big/\left[1 - \frac{\omega_e}{\pi}\frac{2(1 - Q_f)}{3}\right]. \tag{19}$$

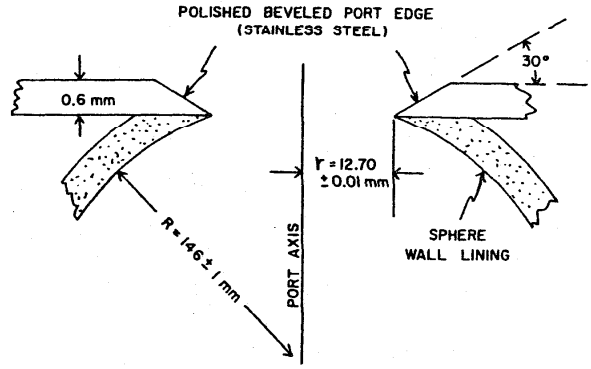

FIGURE 3. *Cross section detail of polished beveled port edge.*

Associated with this determination of Q_s, there is a random error δQ_s arising from the random errors in measuring Q'_s, Q_p, and Q_f. Because of the smallness of ω_e, the denominator in eq (19) is approximately 1 and the small random error in Q_f has little effect on the total random error. Therefore

$$\delta Q_s \simeq (\delta Q'^2_s + \delta Q^2_p)^{1/2}. \tag{20}$$

Also associated with the determination of Q_s is a systematic error ΔQ_s which arises from the uncertainty in ω_e and from the approximation used in estimating the effective reflectance of the beveled edge of the port. The systematic uncertainty in the beveled edge correction is estimated to be one-half as large as the correction itself, so that

$$\Delta Q_s \simeq Q_s \frac{2(1 - Q_f)}{3\pi}\left(\Delta\omega_e^2 + \left(\frac{\omega_e}{2}\right)^2\right)^{1/2} \tag{21}$$

The reflectance of the removable target was measured using the same instrument. In this case a value Q'_t was obtained which also included a small contribution due to stray radiation from the sample beam which is reflected from the reflectometer sphere wall and from that portion of the target which is outside the region occupied by the auxiliary sphere port. A correction for this contribution was obtained by measuring Q_e with a sample in the port made of the same material as the target but which has a hole in it the size of the port in the auxiliary sphere. Note that in this measurement, the beveled edge is not present, since the stainless steel port structure depicted in figure 3 is part of the auxiliary sphere. The corrected relative reflectance of the target Q_t is obtained as

$$Q_t = Q'_t - Q_e. \tag{22}$$

An expression for the random error associated with this determination of Q_t is determined in a straightforward fashion and resembles eq (20).

$$\delta Q_t = [\delta Q'^2_t + \delta Q^2_e]^{1/2}. \tag{23}$$

The values of f, Q_s, and Q_t obtained above were used in eq (6) (more specifically, eq (A7)) to calculate values of $\rho'_b(\lambda)$,

the Van den Akker reflectance of the sphere wall in its entirety. The random error in ρ_v' is obtained from eq (6) as

$$\delta\rho_v' = [((1 - Q_d/Q_s)/(1 - f)^2)^2\delta f^2 + ((f/Q_s)/(1 - f))^2\ \delta Q_t^2 + ((fQ_d/Q_s^2)/(1 - f))^2\ \delta Q_s^2]^{1/2}. \quad (24)$$

The systematic error in ρ_v' is given similarly by:

$$\Delta\rho_v' = [((1 - Q_d/Q_s)/(1 - f)^2)^2\Delta f^2 + ((fQ_d/Q_s^2)/(1 - f))^2\Delta Q_s^2]^{1/2} \quad (25)$$

where ΔQ_s is only that portion of the systematic uncertainty in Q_s given by eq (21). Note that the contribution to the systematic error in Q_s and Q_t due to systematic errors in the DRS are omitted because these errors are very small [21] and because they tend to cancel when the ratio Q_d/Q_s is taken in determining ρ_v' from eq (6). Therefore there is no ΔQ_t term in eq (25).

2. From Uncorrected Van den Akker Reflectance ρ_v' to Corrected Van den Akker Reflectance ρ_v

The quantity ρ_v' as determined in the preceding section is the average Van den Akker reflectance of the sphere wall. In order to obtain the Van den Akker reflectance of a thick coating of the sphere wall material, it is necessary to correct ρ_v' for the effect of the crack around the removable target section and for translucency in the sphere wall coating.

a. The Gap Around the Target

Since the target portion of the sphere is removable, there is a narrow gap in the sphere wall around the target. The gap acts as a light pipe between two aluminum surfaces, so that the effective reflectance of the gap is essentially zero. Therefore, in order to relate the measured Van den Akker reflectance ρ_v' to the Van den Akker reflectance ρ_v of the wall coating, the loss in the gap must be accounted for:

$$\rho_v = \frac{\rho_v'}{k_t\,[1 - 2r_tW/(4R^2 - r^2)]} \quad (26)$$

where r_t is the radius of the target, W is the width of the gap, r is the radius of the entrance port, and k_t is a transluency correction factor as determined in section IV. A.2.b. below. The systematic error associated with the crack correction is estimated to be one-half the magnitude of the correction. The total systematic error in ρ_v is given by

$$\Delta\rho_v = \rho_v\left[\left(\frac{\Delta\rho_v'}{\rho_v'}\right)^2 + \left(\frac{\Delta k_t}{k_t}\right)^2 + \left(\frac{r_tW}{4R^2 - r^2}\right)^2\right]^{1/2}. \quad (27)$$

b. Translucency of the Wall Coating

The relative reflectance as a function of thickness was measured at each of three wavelengths on samples of each type of coating material. The results of these measurements are depicted in figure 4. The coating in the sphere is, on t average, about 4 mm thick, so that the reflectance of barium sulfate sphere wall is equal to the reflectance in t limit of a very thick wall, ρ_∞ [22]. Therefore, for the coatings $k_t = 1$. However, in the case of Halon, the wall not thick enough and a correction was made based on the d in figure 4. In this correction, the thickness of the coating any point was taken to be the distance from the surface to t aluminum substrate at that point, and a translucence corr tion factor k_t was obtained by a calculation having the follo ing form:

$$k_t = \frac{\int \frac{\rho_x}{\rho_{10}}\,dA}{\int dA} \quad (2$$

where ρ_x is the relative reflectance for the coating thickne at a given point,

ρ_{10} is the relative reflectance for a 10 mm thick coati (assumed equal to ρ_∞),

dA is an element of the sphere wall area,

and the integral is taken over the entire area of the sphe wall.

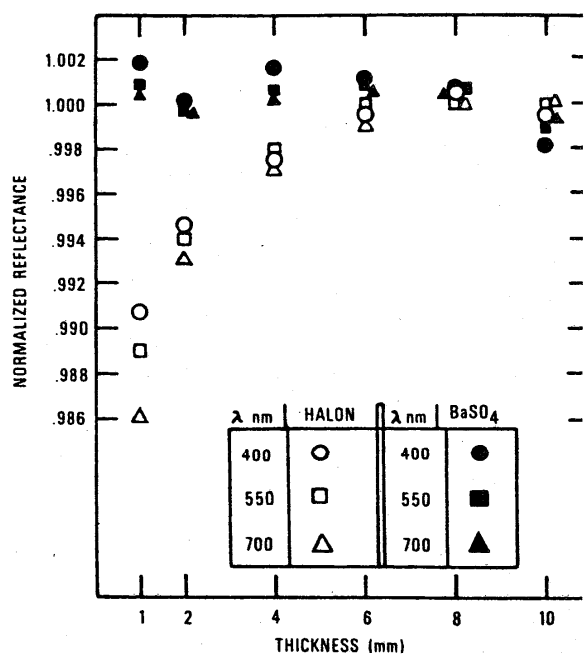

FIGURE 4. *Reflectance of wall coatings as function of thickness.*
(Normalized to give a reflectance of approximately 1 for thick samples.)

It is estimated that the coating thickness measuremer might have been in error by as much as 1/2 mm for the 4 m thickness. Therefore the calculation of eq (28) was redo using 3.5 and 4.5 mm for the average coating thickness ov the main sphere wall in order to obtain an estimate of t random uncertainty δk_t of this correction. An expression f

the random error in ρ_v as given by eq (26) is

$$\delta\rho_v = \rho_v\left[\left(\frac{\delta\rho_v'}{\rho_v'}\right)^2 + \left(\frac{\delta k_t}{k_t}\right)^2\right]^{1/2} \tag{29}$$

Since using the distance from the coating surface to the aluminum substrate as its thickness is only a rough approximation in the regions of the port and of the target boundary, a systematic error will be introduced by that approximation. An estimation of this uncertainty was obtained by calculating $k_t' = \rho_4/\rho_{10}$, and estimating the systematic error as $(k_t' - k_t)/2$. We assumed the translucency correction to be approximately independent of wavelength. The data in figure 4, for 1 mm thickness indicates that this may not be exactly correct. Therefore, there may be a wavelength dependent systematic error of approximately ± 0.0005 in k_t, with the positive error associated with short wavelengths and the negative error with long wavelengths.

The Halon coatings used in our apparatus had a density of 0.8 g cm^{-3}. Grum [23] refers to a coating of Halon which is opaque at 2 mm thickness. However, from the description of the pressure under which the coating was formed, his coatings are probably much denser than ours.

3. Sample Curvature and Sphere Size

Questions have been raised concerning the effect of the size of the sphere upon the Van den Akker reflectance. Possible errors may arise due to the inability of the measuring instrument to properly compare the reflectance of curved and flat surfaces, either due to the difference in the relative areas of the port and the remainder of the sphere wall or due to a change in the reflectance of the wall coating with curvature. This question has been addressed experimentally in two different ways. The relative $6°/h$ reflectance of curved and flat samples was measured directly. The average relative reflectance at 550 nm of four concave $BaSO_4$[14] samples from the first determination was 0.9826 ± 0.0027 and the average reflectance of two flat samples of the same material was found to be 0.9834, and the uncertainty is probably of the same order of magnitude. The difference of 0.0008 is probably not significant.

In the second test, the Van den Akker reflectance was determined using two different sized spheres, one with a 95 mm interior radius and the other with a 146 mm interior radius. Both spheres were coated with the type of $BaSO_4$ [6] used in the third determination. The Van den Akker reflectances for these two determinations are given in table III. It can be seen that there is no significant difference between the results from the two spheres.

4. Results and Error Analysis

The Van den Akker reflectances ρ_v determined for each coating at twenty-five nanometer intervals over the wavelength range 400 nm to 750 nm are given in tables IV, V and VI, and are pictured in figure 5. A listing of typical values used in the calculations for the Van den Akker reflectance is shown in table VII, and representative calculations of the random and systematic uncertainties in ρ_v are presented in tables VIII and IX respectively. The only known wavelength dependency of these uncertainties is in the random errors.

TABLE III

Comparison of the Van den Akker reflectance of ρ_v of the walls of two different size spheres coated with $BaSO_4$ [16].

Wavelength (nm)	Sphere radius R		Difference in ρ_v
	14.6 cm	9.5 cm	
400	0.9744	0.9744	0
425	.9771	.9769	0.0002
450	.9789	.9788	.0001
475	.9802	.9801	.0001
500	.9813	.9812	.0001
525	.9823	.9821	.0002
550	.9829*	.9828	.0001
575	.9834	.9832	.0002
600	.9836	.9835	.0001
625	.9838	.9836	.0002
650	.9838	.9836	.0002
675	.9837	.9836	.0001
700	.9836	.9835	.0001
725	.9835	.9833	.0002
750	.9832	.9831	.0001

* For this value, $\epsilon\rho_v = 2.1 \times 10^{-4}$.

TABLE IV

First Determination $BaSO_4$ [14]

Wavelength (nm)	Van den Akker Reflectance ρ_v	$\rho(6°, \lambda)$	$F(6°, \lambda)$
400	0.9661	0.9606	0.9599
425	.9688	.9638	.9631
450	.9721	.9675	.9668
475	.9744	.9703	.9696
500	.9767	.9728	.9721
525	.9788	.9752	.9745
550	.9806†	.9774*	.9767@
575	.9823	.9793	.9786
600	.9835	.9807	.9800
625	.9845	.9818	.9811
650	.9852	.9826	.9819
675	.9858	.9834	.9827
700	.9864	.9840	.9833
725	.9869	.9846	.9839
750	.9873	.9850	.9843

† $\epsilon\rho_v$ is 2.3×10^{-4} ($\delta\rho_v = 2.1 \times 10^{-4}$ and $\Delta\rho_v = 1.1 \times 10^{-4}$).
* $\epsilon\rho$ is 9.8×10^{-4} ($\delta\rho = 9.5 \times 10^{-4}$ and $\Delta\rho = 2.3 \times 10^{-4}$).
@ $\epsilon\delta$ is 1.01×10^{-3} ($\delta F = 9.5 \times 10^{-4}$ and $\Delta F = 3.3 \times 10^{-4}$).

TABLE V

Second Determination Halon [15]

Wavelength (nm)	Van den Akker Reflectance ρ_v	$\rho(6°, \lambda)$	$F(6°, \lambda)$
400	0.9961	0.9930	0.9927
425	.9961	.9932	.9929
450	.9961	.9933	.9930
475	.9960	.9934	.9931
500	.9959	.9935	.9932
525	.9958	.9935	.9932
550	.9957†	.9935*	.9932@
575	.9956	.9935	.9932
600	.9955	.9935	.9932
625	.9954	.9935	.9932
650	.9952	.9934	.9931
675	.9951	.9934	.9931
700	.9950	.9933	.9930
725	.9949	.9932	.9929
750	.9948	.9931	.9928

† $\epsilon\rho_v$ is 9.0×10^{-4} ($\delta\rho_v = 7.3 \times 10^{-4}$ and $\Delta\rho_v = 5.1 \times 10^{-4}$).
* $\epsilon\rho$ is 9.6×10^{-4} ($\delta\rho = 7.9 \times 10^{-4}$ and $\Delta\rho = 5.5 \times 10^{-4}$).
@ ϵF is 9.7×10^{-4} ($\delta F = 7.9 \times 10^{-4}$ and $\Delta F = 5.6 \times 10^{-4}$).

TABLE VI

Third Determination $BaSO_4$ [16]

Wavelength (nm)	Van den Akker Reflectance ρ_v	$\rho(6°, \lambda)$	$F(6°, \lambda)$
400	0.9744	0.9695	0.9688
425	.9771	.9732	.9725
450	.9789	.9757	.9750
475	.9802	.9775	.9768
500	.9813	.9791	.9784
525	.9823	.9804	.9797
550	.9829†	.9813*	.9806@
575	.9834	.9819	.9812
600	.9836	.9822	.9815
625	.9838	.9824	.9817
650	.9838	.9824	.9817
675	.9837	.9822	.9815
700	.9836	.9819	.9812
725	.9835	.9815	.9808
750	.9832	.9808	.9801

† $\epsilon\rho_v$ is 2.3×10^{-4} ($\delta\rho_v = 2.1 \times 10^{-4}$ and $\Delta\rho_v = 1.1 \times 10^{-4}$).
* $\epsilon\rho_v$ is 2.1×10^{-3} ($\delta\rho = 2.1 \times 10^{-3}$ and $\Delta\rho = 2.3 \times 10^{-4}$).
@ ϵF is 2.1×10^{-3} ($\delta F = 2.1 \times 10^{-3}$ and $\Delta F = 3.3 \times 10^{-4}$).

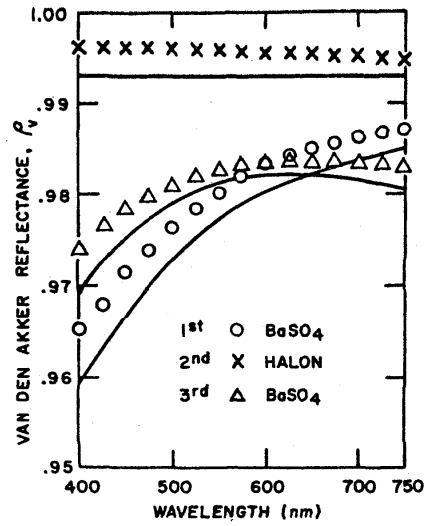

FIGURE 5. *Van den Akker reflectance of three coatings.*
(The height of the symbols × represent the total uncertainty. Height of the symbols 0 and Δ represents approximately 4 times the total uncertainty.) The associated solid curves show $\rho(6°, \lambda)$ for each coating.

The smallest random error is in the central region of the spectrum, where the product of the source intensity and the receiver sensitivity is maximum. At the short wavelength end of the spectrum, there is an increase in uncertainty in Q_t and Q_s associated with a decrease in source intensity, while at the long wavelength end of the spectrum there is an increase in uncertainty associated with a decrease in receiver sensitivity. However, because the random error associated with f dominates the overall uncertainty, we will cite only error figures at 550 nm for ρ_v as representing the entire spectrum.

The total uncertainty in determining the Van den Akker reflectance is obtained by adding the random and systematic uncertainties in quadrature. The total uncertainty in the Van den Akker reflectance is 0.0002 for the $BaSO_4$ coating. It can be seen that this uncertainty is very small, confirming the results of the error analysis by Goebel, et al., [2]. The larger uncertainty for the Halon coating is due to the transluscence of the coating and is introduced in the extrapolation to the reflectance of a thick enough layer rather than being caused by an uncertainty in the measurement. This additional uncertainty would not exist if the Halon coating were twice as thick.

B. Adjustment from Van den Akker Reflectance $\rho_v(\lambda)$ to 6°/h Reflectance $\rho(6°, \lambda)$

The second main step is the transition from $\rho_v(\lambda)$ to $\rho(6°, \lambda)$. As was pointed out in section III, this step is an intrinsic part of the determination which is needed because the sphere coating is a real material and not an ideal Lambertian reflector. For this reason it is not proper to regard this step as a correction. However, for the type of sphere coatings being examined, the departure from Lambertian reflection is small and the difference between ρ_v and ρ is small. For this reason, we will refer to the transition step from ρ_v to ρ as an adjustment in order to emphasize the small size of the change with respect to the quantity being changed.

TABLE VII

Typical Values Used in Calculating the Van den Akker Reflectance ρ_v (λ = 550 nm) for $BaSO_4$ [14].

Symbol	Reference Equation	Value	Comments
(a) r	(16)	12.70 mm	measured with inside caliper and micrometer.
(b) R	(16)	146 mm	measured with steel rule.
(c) f	(16)	1.90×10^{-3}	calculated using r and R above.
(d) Q'_s	(19)	8.731×10^{-2}	measured reflectance of auxiliary sphere.
(e) Q_p	(19)	1.24×10^{-3}	measured with stainless port open to dark room.
(f) Q_f	(19)	7.0×10^{-1}	measured reflectance of stainless steel port plate.
(g) ω_e	(19)	3.78×10^{-2} radians	calculated from dimensions of port structure [17].
(h) Q_s	(19)	8.630×10^{-2}	calculated using Q'_s, Q_p, Q_f, and ω_e above.
(i) Q'_t	(21)	9.832×10^{-1}	measured reflectance of target.
(j) Q_e	(21)	1.36×10^{-4}	measured with reflectometer port open into dark room.
(k) Q_t	(21)	9.831×10^{-1}	calculated using Q'_t and Q_e above.
(l) ρ_v	(6) and (A7)	9.805×10^{-1}	calculated using f, Q_s and Q_t from lines (c), (h) and (k) above respectively.
(m) r_t	(26)	25.4 mm	measured with micrometer caliper.
(n) W	(26)	0.17 mm	measured with traveling microscope.
(o) k_t	(26)	1	$BaSO_4$
		(0.9974)	(Halon determination only).
(p) ρ_v	(26)	9.806×10^{-1}	calculated using ρ'_v, r_t, W, and k_t above.

TABLE VIII

Calculation of the Random Error in the Van den Akker Reflectance

Symbol	Reference Equation	Value	Comments
(a) δR	(17)	.8 mm	Uncertainty in packing sphere coating to constant radius.
(b) δf	(17)	2×10^{-5}	Calculated from δR above.
(c) $\delta Q'_s$	(20)	7×10^{-5}	Uncertainty from 3 measurements.
(d) δQ_p	(20)	7×10^{-5}	Roundoff uncertainty.
(e) δQ_s	(20)	1×10^{-4}	Calculated from $\delta Q'_s$ and δQ_p as given above.
(f) $\delta Q'_t$	(23)	2×10^{-4}	See comment on (d) above.
(g) δQ_e	(23)	7×10^{-5}	See comment on (d) above.
(h) δQ_t	(23)	2.1×10^{-4}	Calculated from $\delta Q'_t$ and δQ_e above.
(i) $\delta \rho'_v$	(25)	2.1×10^{-4}	Calculated from δf, δQ_s, and ΔQ_t from (c), (g) and (j) above.
(j) δk_t	(27)	(7×10^{-4})*	Corresponds to an uncertainty in coating thickness of 0.5 mm.
(k) $\delta \rho_v$	(27)	2.1×10^{-4} (7.3×10^{-4})*	Calculated from $\delta \rho'_v$ and δk_t above.

* Halon coating only.

TABLE IX

Calculation of the Systematic Error in the Van den Akker Reflectance

Symbol	Applicable Equation	Value	Comments
(a) Δr	(18)	0.03 mm	Uncertainty in measuring port ±.01 mm. Another contribution is uncertainty in amount scattered back from port lip, which is estimated.
(b) Δf	(18)	9×10^{-6}	Calculated from Δr above.
(c) $\Delta \omega_e$	(21)	2×10^{-3} rad	
(d) ΔQ_s	(21)	1.1×10^{-4}	Calculated from $\Delta \omega_e$ above and from Q_f, ω_e, and Q_s from entries (f), (g) and (h) in table VII.
(e) $\Delta \rho'_v$	(25)	9.7×10^{-5}	Calculated from Δf and ΔQ_s from (b) and (d) above.
(f) Δk_t	(27)	(5×10^{-4})*	Wavelength dependent error ±.0005 estimated from fig. 4; uncertainty due to tapered edges of coating ±0.0001.
(g) $\frac{r_t W}{(R^2 + r^2)}$	(27)	5×10^{-5}	Calculated using R, r, r_t, W from (a), (b), (m), and (n) in table VII.
(h) $\Delta \rho_v$	(27)	1.1×10^{-4} (5.1×10^{-4})*	Calculated using $\Delta \rho'_v$, Δk_t, and the gap uncertainty as given in (e), (f) and (g) above respectively.

* Halon coating only.

1. Determining the Relative Self-Radiance $N_g(\gamma)/\cos\gamma$

For each type of sphere coating, the relative self-radiance $N_g(\gamma)/\cos\gamma$ was determined as a function of angle of emergence. A 75 mm radius sphere was coated using the same procedure as was used when coating the spheres for the Van den Akker reflectance determinations. This sphere was irradiated through its single port and the flux emitted from the port past a knife-edge was observed at a number of angles. The geometry of this measurement is illustrated in figure 6. The instrument used was the NBS-Gaertner goniophotometer illustrated in figure 7. The source aperture permitted collimation to within 0.25° of the optical axis, and the receiver was collimated to within 0.6° of the optic axis. All three coatings were measured with a V_λ-illuminant C [24] spectral weighting, the centroid of which falls at approximately 550 nm. In addition, the coatings from the second and third determinations were measured using a 550 nm low pass interference filter, which resulted in a centroid of spectral weighting at 450 nm, and using a 600 nm high pass filter which resulted in a centroid spectral weighting at approxi-

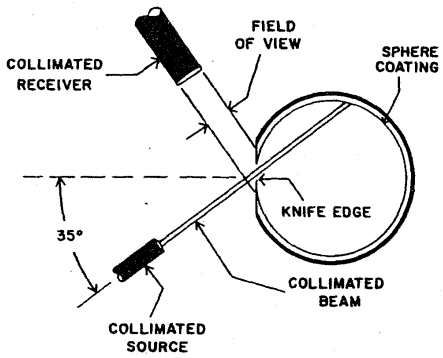

FIGURE 6. *Arrangement of knife-edge apparatus for measuring $N_g(\gamma)$.*

mately 700 nm. No distinction between the measurements under different spectral weightings were observed, indicating that $L_s(\gamma)$ depends principally on the geometrical nature of the surface. The relative magnitude of the observed flux divided by the cosine of the observation angle is shown in figure 8. Also shown in figure 8 are measurements made by scanning, with a telescopic detector, the interior of a 20 cm radius sphere coated with Halon. These latter measurements, believed to be much more accurate (± 0.001) than the knife-edge measurements, extend only to 45°. Because of the method used to produce the coating by hammering, there is reason to expect an increase in $N_g(\gamma)/\cos(\gamma)$ as γ approaches 90° because of a slight glossiness in the surface. However, it appears that this effect is not nearly as great as the measurements using the knife-edge indicate. Two possible sources for the difficulties at large γ are reflections from the corner of the knife-edge and scattered light from the receiver optics. At large γ, the flux to be measured is small, so that small amounts of stray radiation can cause large errors. Fortunately, this uncertainty in $N_g(\gamma)/\cos\gamma$ results in only a small uncertainty in determining $C(\Gamma, \lambda)$. A discussion of our

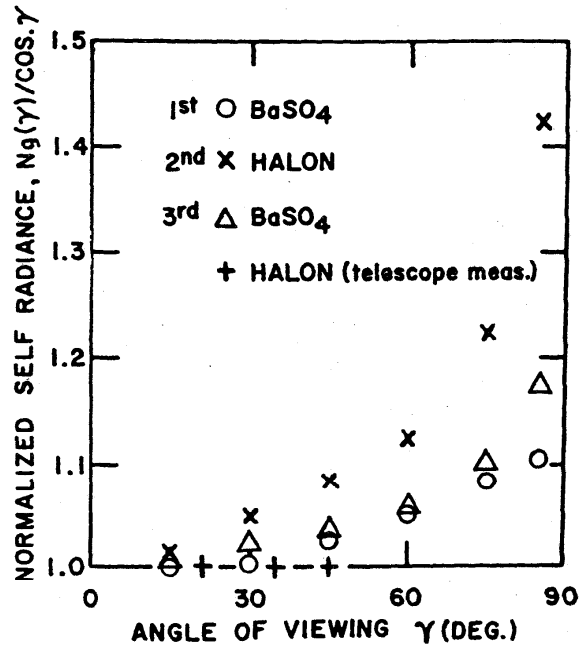

FIGURE 8. *Normalized self-radiance at 550 nm for each of three coating materials.*

choice of function to represent $N_g(\gamma)$ will be deferred to part IV.B.3 in which $C(\Gamma, \lambda)$ is calculated.

2. Determining the Relative Directional-Hemispherical Reflectance $N_G(\Gamma)$

The relative directional-hemispherical reflectance of a sample of each of the three coatings was measured with the

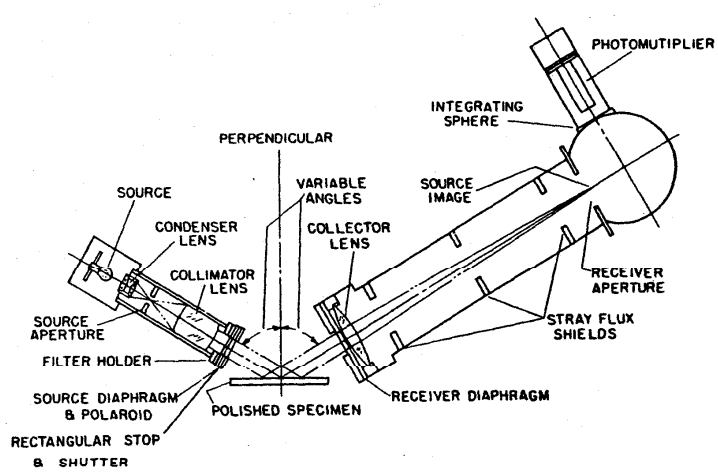

FIGURE 7. *NBS-Gaertner goniophotometer.*

DRS using the special measurement accessory apparatus for this purpose [12]. A diagram of this measurement accessory is reproduced from that reference in figure 9. The reflectance values were measured for radiation polarized with the electric vector in the plane of incidence and perpendicular to the plane of incidence. The average of the relative reflectance for the two polarizations was determined as a function of angle of incidence for each material for each of three wavelengths, 450 nm, 550 nm, and 750 nm. The data were fitted with a quadratic function, using a least-squares fitting program, to obtain the $N_G(\Gamma, \lambda)$ shown in figure 10. These curves were used to determine the adjustment function $C(\Gamma, \lambda)$ of eq (12). The general trend is for the reflectance to increase as the angle of incidence approaches grazing. The amount of the increase is greater for the materials with lower reflectance.

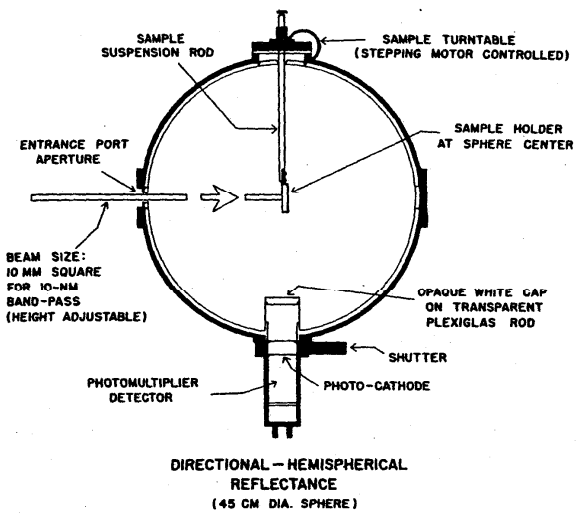

FIGURE 9. *Integrating sphere for measuring relative directional-hemispherical reflectance as a function of angle of incidence.*

3. Determining $C(\Gamma, \lambda)$

For each type of coating, the function C was evaluated using in eq (13) the $N_g(\gamma)$ and $N_G(\Gamma, \lambda)$ data from parts 1. and 2. above for each of the three wavelengths 450, 550, and 750 nm. Actually three sets of C were calculated for each of three interpretations of the highly uncertain data for $N_g(\gamma)$ in figure 8 above in order to evaluate the effect of that uncertainty. We wish to distinguish between the data taken from measurements of the radiance from the sphere wall and the interpretations of this data which are used as incident radiance values in calculating $C(\Gamma, \lambda)$. We will do this by using a lower case γ in $N_g(\gamma)/\cos\gamma$ to indicate the data obtained directly from the measurements and by using an uppercase Γ in $N_g(\Gamma)/\cos\Gamma$ to indicate the processed data used as the relative radiance distribution incident on the sphere wall when we calculate $C(\Gamma, \lambda)$. The first set of $C(\Gamma, \lambda)$ was calculated assuming that

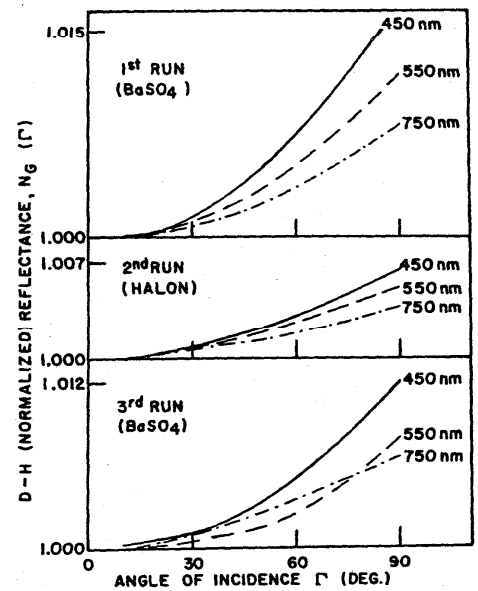

FIGURE 10. *Relative directional-hemispherical reflectance $N_g(\Gamma, \lambda)$ as a function of angle of incidence Γ for each of three coatings at three wavelengths.*

$N_g(\gamma)/\cos\gamma$ is independent of γ. This provides a lower limit on C. The second was calculated by using 1 for $N_g(\gamma)/\cos\gamma$ between 0 and 45°. To obtain the $N_g(\gamma)/\cos\gamma$ above 45° in this approximation, a straight line was drawn through the knife-edge experiment data from 0 to 45° and the amount by which the experimental data for greater than 45° fell above this line was added to 1 to obtain $N_g(\gamma)$. (See fig. 11 for a diagram illustrating this procedure for the Halon data in fig. 8.) The set of $N_g(\gamma)$ obtained in this way were consistent with the more accurate data from the telescopic detector scan and the $C(\Gamma, \lambda)$ calculated with these $N_g(\gamma)$ are used as the accepted values. Finally, as an upper limit, C's are calculated using the unmodified knife-edge experiment data given in figure 8. The functions $C(\Gamma, \lambda)$ corresponding to the accepted values, are plotted against Γ for each of the three materials at each of three wavelengths in figure 12. (See appendix C for details of the calculations leading to this figure.)

Since the goal of this section is to determine $\rho(6°, \lambda)$ at 25 nm intervals over the wavelength range 400 nm $\leq \lambda \leq$ 750 nm, we need values of $C(6°, \lambda)$ at these wavelengths. Since the large amount of data required would make impractical determining all of these values of $C(6°, \lambda)$ in the way described above, we choose to determine $C(6°, \lambda)$ from the data at the three wavelengths 450, 550, and 750 nm by interpolation and extrapolation. This determination is based on the definition of $C(6°, \lambda)$ which comes from eq (12)

$$C(6°, \lambda) = \frac{N_G(6°, \lambda)}{\bar{N}_G} - 1. \tag{30}$$

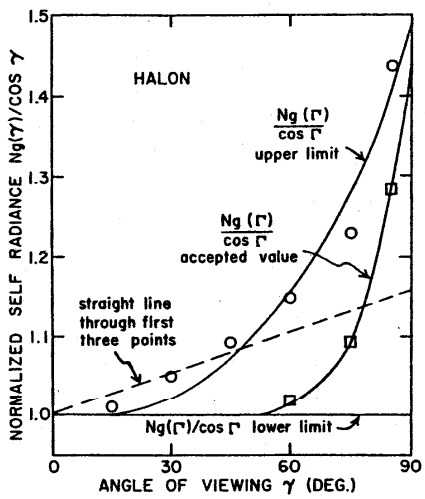

FIGURE 11. *An illustration of the three assumptions used in interpreting the $N_g(\gamma)$ data from the knife-edge determinations.*

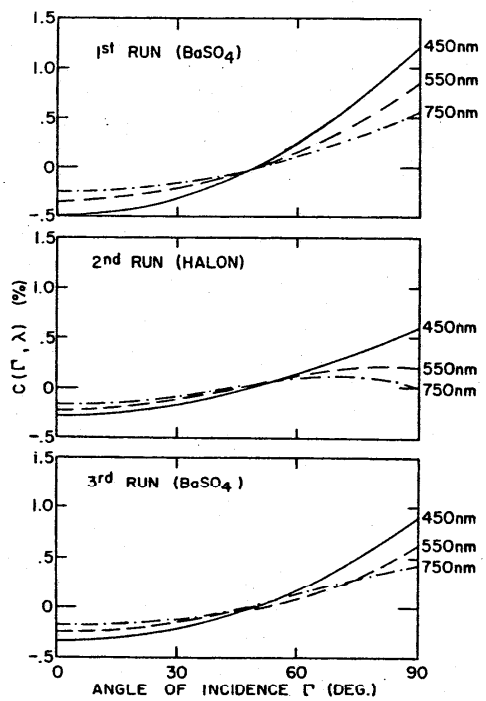

FIGURE 12. *$C(\Gamma, \lambda)$ as a function of Γ at three wavelengths for each of three coatings.*

Since the weighing to determine $\bar{N}_G(\lambda)$ is heaviest at 45°, it follows that

$$\bar{N}_G(\lambda) \simeq N_G(45°, \lambda). \tag{31}$$

Making use of this, we can write a correction factor $C'(6°, \lambda)$ which is a rough approximation to $C(6°, \lambda)$ as:

$$C'(6°, \lambda) = \frac{N_G(6°, \lambda)}{N_G(45°, \lambda)} - 1. \tag{32}$$

Since C and C' are approximately equal, their ratio is a smoothly varying function of wavelength. Therefore, we determined $J(\lambda)$ as

$$J(\lambda) = d_0 + d_1\lambda + d_2\lambda^2 \tag{33}$$

such that

$$J(\lambda) = \frac{C(6°, \lambda)}{C'(6°, \lambda)} \tag{34}$$

at the wavelengths 450 nm, 550 nm and 750 nm. We then determined $C(6°, \lambda)$ at other wavelengths as

$$C(6°, \lambda) = J(\lambda)C'(6°, \lambda) \tag{35}$$

where $C'(6°, \lambda)$ is calculated from expression (32) using values of $N_G(6°, \lambda)$ and $N_G(45°, \lambda)$ measured with the relative d/h reflectance instrument [12]. The values of $C(6°, \lambda)$ so determined are plotted in fig. 13.

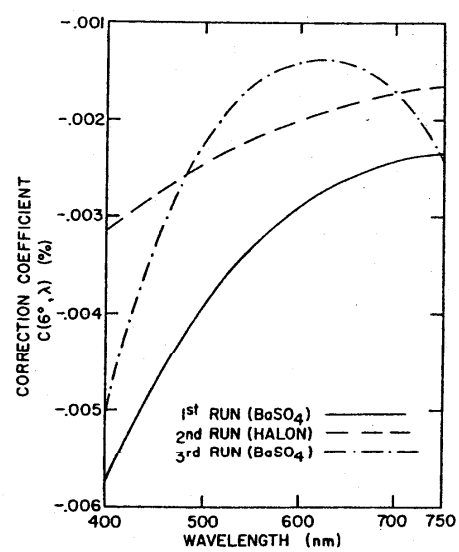

FIGURE 13. *$C(6°, \lambda)$ as a function of wavelength for each of three coatings.*

4. Results and Error Analysis

The three sets of values for $C(6°, \lambda)$ determined above were used in eq (12) to calculate $\rho(6°, \lambda)$ for the three wall materials. The results of this calculation are shown in the third columns of tables IV, V and VI and by the line curves in fig. 5.

From eq (12) one can determine a propagation of error formula for the random error $\delta\rho(6°, \lambda)$ as:

$$\delta\rho(6°, \lambda) = [\delta\rho_v(\lambda)^2 + \delta N_G(6°, \lambda)^2 + \delta\bar{N}_G(\lambda)^2]^{1/2}. \quad (36)$$

In this form ρ_v, N_G and $\bar{N}_G$ are each assumed to be 1, and errors common to N_G and $\bar{N}_G$ are ignored, since these will effectively cancel when the ratio is taken. Therefore the only errors to be included in eq (36) are the independent errors in the various quantities. The principal independent uncertainty in $\bar{N}_G$ is that due to the uncertainty in the self-radiance measurements as shown in appendix C. The principal random uncertainty in N_G is due to the noise in the d/h data. Since the value of $N_G(6°, \lambda)$ was obtained through a rather indirect procedure involving curve fitting, it is difficult to establish a good theoretical basis for the error estimate. Therefore, we sought a reproducible way of estimating the error which depended as little as possible on arbitrary judgment. Since most of the curves involved fitting through ten to fifteen points with a quadratic function with two independent parameters, there is almost no likelihood that a point taken from the curve will depart from the most probable value by more than the root mean square deviation of the individual points with respect to the curve. Therefore, we will use this deviation as the estimated random uncertainty. In determining N_G, two such fittings are involved, one to the original data as a function of angle and one to the $C(\lambda)$ data used in the interpolation. A summary of the random error analysis for the $\rho_v(\lambda)$ to $\rho(6°, \lambda)$ adjustment is given in table X.

The only source of systematic error which we have identified for this adjustment step is an uncertainty in the measurement of N_G due to the correction which is made for the entrance port of the reflectometer. This results in an uncertainty in $C(\Gamma, \lambda)$ of 2×10^{-4} independent of wavelength.

The total uncertainty in $\rho(6°, \lambda)$ for a given determination is obtained by adding $\delta\rho(6°, \lambda)$ and $\Delta\rho(6°, \lambda)$ in quadrature. The additional uncertainty introduced in making the adjustment from $\rho_v(\lambda)$ to $\rho(6°, \lambda)$ is of the same order of magnitude as the uncertainty in $\rho_v(\lambda)$ itself. Particularly noteworthy is the large increase in uncertainty in the third determination. The barium sulfate used in this determination had a rather "sticky" consistency which made it difficult to pack it into a uniform smooth surface, and this may have had an effect upon the noise in the $N_G(\Gamma, \lambda)$ data from this surface.

C. Adjustment from d/h Reflectance $\rho(6°, \lambda)$ to d/h Reflectance Factor $F(6°, \lambda)$

In order to determine the bidirectional reflectance factor in the retroreflective direction, apparatus was set up as customarily used for measuring the coefficient of luminous intensity of retroreflective sheeting (See fig. 14). Since the retroreflectance of the sphere coatings is essentially spectrally nonselective over the visible wavelength range [13] we measured the luminous reflectance factor for CIE illuminant A as being representative of the entire spectrum to within the uncertainty of the retroreflectance measurements.

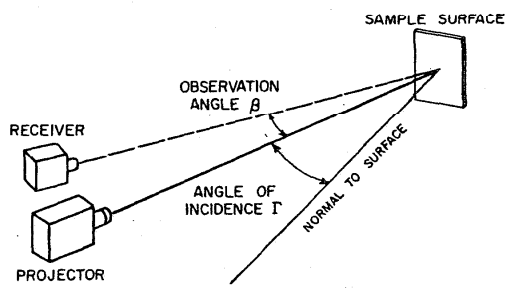

FIGURE 14. *Diagram of apparatus used in retroreflectance measurements.*

TABLE X

Calculation of the errors in the $\rho_v(\lambda)$ to $\rho(6°, \lambda)$ adjustment (See equation (36) and the accompanying discussion).

Symbol	$BaSO_4$ [14]	Halon [15]	$BaSO_4$ [16]	Comments
(a) $\delta\rho_v$	2.1×10^{-4}	7.3×10^{-4}	2.1×10^{-4}	See Table VIII.
(b) $\delta\bar{N}_G(\lambda)$	0.5×10^{-4}	0.5×10^{-4}	0.5×10^{-4}	See Appendix C.
(c) $\delta N_g(6°, \lambda)$	7×10^{-4}	3×10^{-4}	20×10^{-4}	Component due to fitting angular data for $N_G(\Gamma, \lambda)$.
(d) $\delta N_g(6°, \lambda)$	6×10^{-4}	3×10^{-4}	5×10^{-4}	Component due to fitting wavelength data to $C'(\lambda)$.
(e) $\delta N_g(6°, \lambda)$	9.2×10^{-4}	4.3×10^{-4}	21×10^{-4}	Quadrature combination of (c) and (d) above.
(f) $\delta\rho(6°, \lambda)$	9.5×10^{-4}	7.9×10^{-4}	21×10^{-4}	Quadrature combination of (a), (b) and (c) above.
(g) $\Delta\rho_v$	1.1×10^{-4}	5.1×10^{-4}	1.1×10^{-4}	See Table IX.
(h) ΔC	2×10^{-4}	2×10^{-4}	2×10^{-4}	Associated with d-h reflectometer port correction.
(i) $\Delta\rho(6°, \lambda)$	2.3×10^{-4}	5.5×10^{-4}	2.3×10^{-4}	Quadrature combination of (g) and (h) above.

To make the measurements, the receiver was placed in the sample position and a signal N_R proportional to the normal illuminance I_R on the sample was measured.

$$N_R = k_R I_R. \tag{37}$$

The receiver was then moved to a position a distance d away from the sample and, on the same scale of measurement and using the same receiver aperture, signals $N_r(\beta)$, which is in the same way proportional to the illuminance $I(\beta)$ on the receiver due to the radiation reflected from the sample, was measured with the entire sample area A in view. From the basic definition for reflectance factor, it follows that the reflectance factor $F_\Gamma(\beta)$ can be determined from

$$F_\Gamma(\beta) = \frac{N_r(\beta)}{N_R} \frac{A}{d^2 \cos(\Gamma) \cos(\Gamma + \beta)}. \tag{38}$$

The value of $F_{6°}(\beta)$ so determined as a function of observation angle β is given for $BaSO_4$ and for Halon in fig 15. (See appendix A, sec. A.2 for further discussion of these data and the evaluation of the integrals.) The retroreflectance factor $F_{6°}(\beta)$ was found to be essentially independent of the angle which the plane of observation makes with respect to the plane of incidence. Therefore, the integral in eq (13) becomes

$$\int^{\omega'} F(\mathbf{U}, \mathbf{u}) \cos\gamma \, d\omega = 2\pi \cos 6° \int_0^{r/d'} F_{6°}(\beta) \beta \, d\beta \tag{39}$$

and ω' in (13) becomes

$$\omega' = 2\pi \int_0^{r/d'} \beta \, d\beta \tag{40}$$

where r is the radius of the reflectometer entrance port and d' is the distance in the reflectometer sphere from the sample to the plane of the entrance port. The $\rho(6°, \lambda)$ data were adjusted to $F(6°, \lambda)$ using eq (13). In general, the difference $\rho(6°, \lambda) - F(6°, \lambda)$ is 0.0007 for $BaSO_4$ and 0.0003 for Halon. The estimated systematic uncertainty in this adjustment is approximately one-third of its value in each case. These uncertainties, added in quadrature with the uncertainties in $\rho(6°, \lambda)$ yield the total systematic uncertainty in $F(6°, \lambda)$. The values of $F(6°, \lambda)$ for the three coatings are given in the third columns of tables IV, V, and VI.

D. Determining the d/h Reflectance Factor of Working Standards

The d/h reflectance factor $F(6°, \lambda)$ determined in IV.C. above is the average for the wall coating used in the Van den Akker sphere. Since this coating is neither permanent nor readily accessible, the reflectance factor $F_c(6°, \lambda)$ is determined for working standards made of glass, ceramic, or some other permanent material. The value of F_c is assigned as indicated in eq (14) and the accompanying text. Specifically, we will denote by $F_{c,j}(6°, \lambda)$ the reflectance factor for standard c as obtained from the jth determination. Equation (14) takes the form:

$$F_{c,j} = \frac{Q_c}{\bar{Q}_j} F_j \tag{41}$$

where

$F_j \equiv F_j(6°, \lambda)$ is the reflectance factor for the jth wall coating,

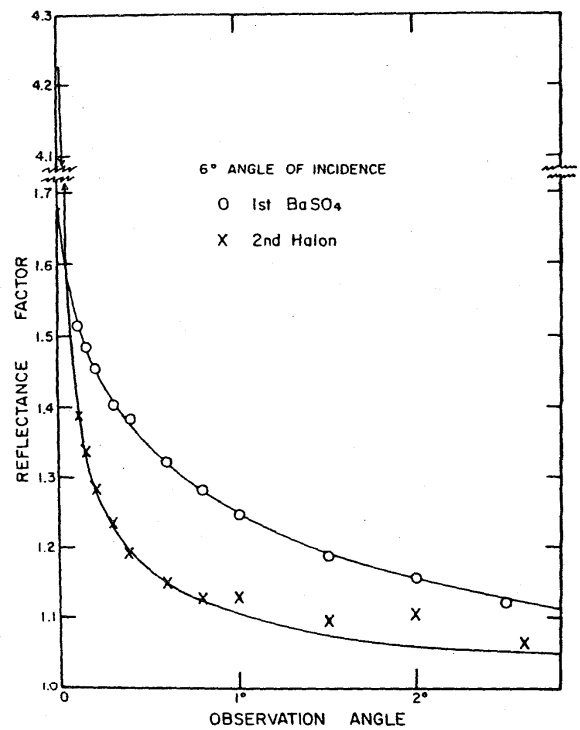

FIGURE 15. *Retroreflective bidirectional reflectance factor for 6° incidence as a function of observation angle.*

Q_c is the measured relative reflectance of working standard c, and

$\bar{Q}_j$ is the average of the measured relative reflectance for several representative samples of the jth wall coating.

The relative reflectances Q_c and $\bar{Q}_j$ were found by experiment to be independent of the polarization of the incident radiation for the working standards and sphere coatings used. It follows that the random error in $F_{c,j}$ is given by:

$$\delta F_{c,j} = F_{c,j}\left[\left(\frac{\delta Q_c}{Q_c}\right)^2 + \left(\frac{\delta \bar{Q}_j}{\bar{Q}_j}\right)^2 + \left(\frac{\delta F_j}{F_j}\right)^2\right]^{1/2}. \tag{42}$$

The largest new contribution to the uncertainty which is introduced in this step is $\delta \bar{Q}_j$. This is due to the variability between the representative samples and the resulting uncertainty in whether these samples properly represent the sphere coating. If the values of Q_c and $\bar{Q}_j$ differ significantly a small correction for instrument non-linearity must be made in the ratio $Q_c/\bar{Q}_j$. With this non-linearity is associated a small contribution to the systematic uncertainty.

$$\Delta F_{c,j} = F_{c,j}\left[\left(\frac{\Delta(Q_c/\bar{Q}_j)}{(Q_c/\bar{Q}_j)}\right)^2 + \left(\frac{\Delta F_j}{F_j}\right)^2\right]^{1/2}. \tag{43}$$

Three different working standards are currently used. These are identified and described in appendix D. The values of $F_{c,j}$ for each of these standards for each of three determinations are given in tables XI, XII and XIII, and sample calculations for the uncertainties appear in table XIV.

TABLE XI

Reflectance Factor of Working Standard 1
(Russian Opal Glass, Polished)

Wavelength (nm)	$F_{1,1}$	$F_{1,2}$	$F_{1,3}$	$\bar{F}_{1,2}$	$\bar{F}_{1,3}$
400	0.9793	0.9734	0.9738	0.9759	0.9753
425	0.9781	0.9739	0.9743	0.9756	0.9753
450	0.9803	0.9765	0.9779	0.9781	0.9781
475	0.9841	0.9807	0.9812	0.9822	0.9819
500	0.9854	0.9823	0.9846	0.9836	0.9838
525	0.9856	0.9821	0.9845	0.9836	0.9838
550	0.9837	0.9813	0.9830	0.9823	0.9835
575	0.9810	0.9785	0.9805	0.9796	0.9798
600	0.9792	0.9761	0.9785	0.9775	0.9777
625	0.9777	0.9742	0.9769	0.9757	0.9760
650	0.9770	0.9745	0.9774	0.9756	0.9761
675	0.9771	0.9751	0.9772	0.9759	0.9763
700	0.9761	0.9736	0.9761	0.9747	0.9750
725	0.9742	0.9718	0.9741	0.9728	0.9732
750	0.9716	0.9687	0.9711	0.9699	0.9702
δ	2.2×10^{-3}	1.6×10^{-3}	2.7×10^{-3}	1.3×10^{-3}	1.2×10^{-3}
Δ	3.3×10^{-4}	5.5×10^{-4}	3.3×10^{-4}	5.5×10^{-4}	5.5×10^{-4}
ϵ	2.2×10^{-3}	1.7×10^{-3}	2.7×10^{-3}	1.4×10^{-3}	1.3×10^{-3}
w	4.5	6.0	3.7	—	—
W	—	—	—	10.5	14.2

TABLE XII

Reflectance Factor of Working Standard 2
(Vitrolite)

Wavelength (nm)	$F_{2,1}$	$F_{2,2}$	$F_{2,3}$	$\bar{F}_{2,2}$	$\bar{F}_{2,3}$
400	0.9100	0.9049	0.9049	0.9071	0.9065
425	.8944	.8901	.8907	.8920	.8916
450	.9006	.8977	.8981	.8990	.8987
475	.9140	.9116	.9083	.9126	.9114
500	.9192	.9169	.9178	.9179	.9179
525	.9242	.9204	.9226	.9221	.9222
550	.9245	.9222	.9243	.9232	.9235
575	.9215	.9190	.9213	.9201	.9204
600	.9160	.9125	.9155	.9140	.9145
625	.9099	.9066	.9085	.9080	.9082
650	.9050	.9027	.9043	.9037	.9039
675	.9035	.9013	.9040	.9023	.9028
700	.9010	.8991	.8999	.8999	.8999
725	.8959	.8939	.8953	.8948	.8949
750	.8893	.8867	.8882	.8878	.8879
δ	2.2×10^{-3}	1.6×10^{-3}	2.3×10^{-3}	1.3×10^{-3}	9.8×10^{-4}
Δ	3.2×10^{-4}	5.3×10^{-4}	3.2×10^{-4}	5.3×10^{-4}	5.3×10^{-4}
ϵ	2.2×10^{-3}	1.7×10^{-3}	2.4×10^{-3}	1.4×10^{-3}	1.1×10^{-3}
w	4.5	5.9	4.2	—	—
W	—	—	—	10.4	14.6

The systematic uncertainty associated with the F_c for a particular standard is, by definition, independent of the number of determinations which are made. However, the random uncertainty associated with a given F_c can be reduced by taking the average of the F_c's from a number of determinations. We maintain a running weighted average $\bar{F}_{c,j}$ of the results of all determinations from 1 through j by means of the calculation

$$\bar{F}_{c,j} = \frac{W_{c,j-1}\bar{F}_{c,j-1} + w_{c,j}F_{c,j}}{W_{c,j}} \tag{44}$$

where the weighting factor $w_{c,j}$ for the jth determination of F_c is

$$w_{c,j} = 1/100\ \epsilon F_{c,j} \tag{45}$$

where $\epsilon F_{c,j}$ is the total uncertainty in $F_{c,j}$ as is given in appendix B. The weighting factor $W_{c,j}$ for the average of the j determinations is

$$W_{c,j} = \sum_{i=1}^{j} w_{c,i}\,. \tag{46}$$

TABLE XIII

Reflectance Factor of Working Standard 3
(Porcelain Enamel 80-1)

Wavelength (nm)	$F_{3,1}$	$F_{3,2}$	$F_{3,3}$	$\bar{F}_{3,2}$	$\bar{F}_{3,3}$
400	0.7615	0.7573	0.7571	0.7591	0.7585
425	.7936	.7911	.7915	.7922	.7920
450	.8042	.8019	.8034	.8029	.8030
475	.8093	.8072	.8073	.8081	.8079
500	.8105	.8078	.8101	.8090	.8093
525	.8104	.8091	.8096	.8096	.8096
550	.8090	.8083	.8094	.8086	.8088
575	.8063	.8045	.8071	.8053	.8058
600	.8030	.8017	.8032	.8022	.8025
625	.7990	.7969	.7994	.7978	.7983
650	.7949	.7937	.7960	.7942	.7947
675	.7926	.7911	.7925	.7917	.7919
700	.7909	.7900	.7927	.7904	.7910
725	.7885	.7869	.7886	.7875	.7878
750	.7855	.7839	.7860	.7846	.7850
δ	2.1×10^{-3}	1.5×10^{-3}	2.3×10^{-3}	1.3×10^{-3}	1.1×10^{-3}
Δ	3.0×10^{-4}	4.7×10^{-4}	3.0×10^{-4}	4.7×10^{-4}	4.7×10^{-4}
ϵ	2.2×10^{-3}	1.6×10^{-3}	2.3×10^{-3}	1.4×10^{-3}	1.2×10^{-3}
w	4.6	6.2	4.2	–	–
W	–	–	–	10.8	15.0

TABLE XIV

Calculation of the Uncertainties in the $\rho(6°,\lambda)$ to $F(6°,\lambda)$ and $F(6°,\lambda)$ to $F_{c,j}(6°, \lambda)$ steps as determined for Working Standard No. 2.

	Symbol	Value			Comments
		$BaSO_4$ [14]	Halon [15]	$BaSO_4$ [16]	
(a)	$\delta F(6°, \lambda)$ $(=\delta\rho(6°, \lambda))$	9.5×10^{-4}	7.9×10^{-4}	2.1×10^{-3}	See table X, entry (f).
(b)	F_j	0.9767	0.9932	0.9806	See tables IV, V, and VI.
(c)	δQ_c	2.7×10^{-4}	8.7×10^{-4}	3×10^{-4}	From three measurements in each determination.
(d)	Q_c	0.929833	0.931036	0.92922	Measured.
(e)	$\delta\bar{Q}_j$	2×10^{-3}	1.2×10^{-3}	1.2×10^{-3}	From measurements on a number of samples.
(f)	$\bar{Q}_j$	0.985022	1.00283	0.985982	Measured.
(g)	$\bar{F}_{2,j}$	.9245	0.9222	0.9243	Calculated from (b), (d) and (f) above in equation (41).
(h)	$\delta F_{2,j}$	2.2×10^{-3}	1.6×10^{-3}	2.3×10^{-3}	Calculated from equation (42) and (a) through (g) above.
(i)	$\Delta(Q_c/\bar{Q}_j)$ $(=-\Delta\bar{Q}_j)$	-1×10^{-4}	-1×10^{-4}	-1×10^{-4}	From reference [17].
(j)	ΔF_j	3.3×10^{-4}	5.6×10^{-4}	3.3×10^{-4}	From tables IV, V, and VI.
(k)	$\Delta F_{2,j}$	3.2×10^{-4}	5.3×10^{-4}	3.2×10^{-4}	Calculate from equation (43) and (b), (d), (f), (i) and (j) above.
(l)	$\epsilon F_{2,j}$	2.2×10^{-3}	1.7×10^{-3}	2.4×10^{-3}	Quadrature combination of (i) and (k) above.
(m)	$w_{c,j}$	4.5	5.9	4.2	Calculate from equation (45) using (l) above.
(n)	$W_{c,j-1}$	–	10.4	14.6	Calculate from equation (46) using (m) above.
(o)	$\bar{F}_{c,j}$	–	0.9232	0.9235	Calculate from equation (44) using (g) and (m) above.
(p)	$\delta\bar{F}_{c,j}$	–	1.3×10^{-3}	9.8×10^{-4}	Calculate from equation (47) using (g), (m), (n), and (o) above.
(q)	$\Delta\bar{F}_{c,j}$	–	5.3×10^{-4}	5.3×10^{-4}	Largest entry from (k) above.
(r)	$\epsilon\bar{F}_{c,j}$	–	1.4×10^{-3}	1.1×10^{-3}	Quadrature combination of (p) and (q) above.

The random uncertainty in the $\bar{F}_{c,j}$ is given by

$$\delta \bar{F}_{c,j} = \frac{[(W_{c,j-1}\delta \bar{F}_{c,j-1})^2 + (w_{c,j}\delta F_{c,j})^2]^{1/2}}{W_{c,j}}. \quad (47)$$

The values of $\bar{F}_{c,2}$ and $\bar{F}_{c,3}$ appear in tables XI, XII, and XIII along with the $\bar{F}_{c,j}$. The results of these three determinations are also displayed by way of summary in figure 16.

V. Conclusions

A. Precautions and Pertinent Parameters

In the work reported in this paper, a large number of potential sources of error in determining reflectance factor using the Van den Akker method were investigated in order to evaluate the magnitude of their importance. Many of these sources of uncertainty were of little importance in themselves and even cumulatively were of importance only to a laboratory seeking the highest accuracy possible. For a laboratory for which a total uncertainty on the order of ±0.005 is tolerable, a number of the detailed steps described in section IV are not necessary. In this section we will briefly describe precautions which should still be taken in the case of such truncated measurement procedures and make suggestions for possible improvements in the overall procedure.

1. Determining the Van den Akker Reflectance $\rho_v(\lambda)$

In an experiment designed and carried out with reasonable care, the Van den Akker reflectance ρ_v can be determined very accurately. The principal strong point in this method is the insensitivity of the basic measurement accuracy to uncertainties in any of the measured parameters such as the port diameter, the sphere diameter, or the ratio of the reflectance of the sphere to the reflectance of the wall sample. The sensitivity to such parameters is kept lowest by using a large sphere with a small port (low f) and by using a highly reflecting coating in the sphere so that the sphere reflectance is still reasonably high.

Considerable care should be taken however to make the sphere coating in such a way that the Van den Akker reflectance can be related meaningfully to the reflectance of a sample of the coating. This means that a coating should be chosen the reflectance of which is uniform and very reproducible. It is especially important that no cracks appear in the finished coatings and that the coating should be thick enough to be opaque. In this regard, it is probably best not to incorporate a removable port in the Van den Akker sphere at all, but rather to rely upon the reproducibility of the coating and use the average Q from several separate samples of coating for Q_ℓ in eq (6).

2. Adjustment from the Van den Akker Reflectance ρ_v to the d/h Reflectance $\rho(6°, \lambda)$

As can be seen from figure 13, the magnitude of this adjustment was in no case greater than −0.006. Since $\rho(\Gamma, \lambda)$ can never be greater than 1, it follows that this adjustment will be smaller for samples for which ρ_v closer to 1. It also is clear that the need for this adjustment comes about from the rise in reflectance at near-grazing incidence. This rise is due to the specular reflectance of the slightly glossy surface which is produced in pressing. For this reason, a coating technique which produces a rougher or more matted coating is to be preferred if no adjustment is to be made. It is probably the roughness of the coating that Goebel, et al., [2] produced by scraping which led to the rather remarkably good agreement between their results, which are the basis of the earlier NBS scale of $F(6°, \lambda)$, and the present adjusted results. (See fig. 17 and the discussion in section V.C. which follows.) An error of as much as 0.01 in the upward direction can result from assuming ρ_v and ρ to be equal, and an adjustment based on relative d/h reflectance measurements $N_G(\Gamma, \lambda)$ should be made if an uncertainty of less than ±.01 is desired. In all but the highest accuracy work, it is safe to assume the self-radiance is Lambertian, i.e., $N_g(\gamma, \lambda)/\cos\gamma$ is constant.

It should be pointed out that in every case ρ_v and $\rho_{45°/h}$ are very nearly equal, as can be determined from the $C(\Gamma, \lambda)$ curves in figure 12. Therefore the Van den Akker method is especially well adapted for calibrating measurements of directional-hemispherical reflectance at 45° incidence.

3. Adjustment from d/h Reflectance $\rho(6°, \lambda)$ to d/h Reflectance Factor $F(6°, \lambda)$

Since most reflectometers compare reflectance factor $F(6°, \lambda)$ rather than reflectance $\rho(6°, \lambda)$, it is in principle necessary to make an adjustment. However, since the solid angle subtended at the sample is small compared to the total hemisphere, any departure from Lambertian reflectance by the sphere coating would have to be large if the difference between ρ and F is to be significant. In the sphere coating materials ordinarily in use, the reflectance factor departs greatly from 1 only for small solid angles of collection at very small observation angles β (fig. 14). Therefore in general ρ is less than 0.001 higher than F and this adjustment can be ignored or estimated from data in the literature [13].

Note that if the object of the measurement is to determine the radiative transfer properties of the sphere coating itself, then ρ is the quantity of interest and the adjustment to F should not be made. This would be the case, for example, if the coating were being studied in order to determine the radiative heat transfer to the coating material.

4. Determining the d/h Reflectance Factor $F(6°, \lambda)$ of Working Standards

Next to the adjustment from ρ_v to ρ, it is this step which contains the highest potential for error. These measurements are meaningful only to the extent that the samples of coating with which the working standards are compared are representative of the sphere wall coating. It is for this reason that the sphere coating and the samples should be prepared in precisely the same way and that reproducibility of reflectance is an important requirement of the coating. It is also this reason that favors Van den Akker's original technique of having many removable sections in the sphere wall itself, provided that the presence of such removable sections does not give rise to irregularities in the sphere coating.

B. The Present NBS Scale of d/h Reflectance Factor $F(6°, \lambda)$

The present NBS scale of spectral d/h reflectance factor is maintained by means of three carefully preserved working standards which have been evaluated at 25 nm intervals. The reflectance factor data for the first three determinations are given in tables XI, XII and XIII. Figure 16 provides a

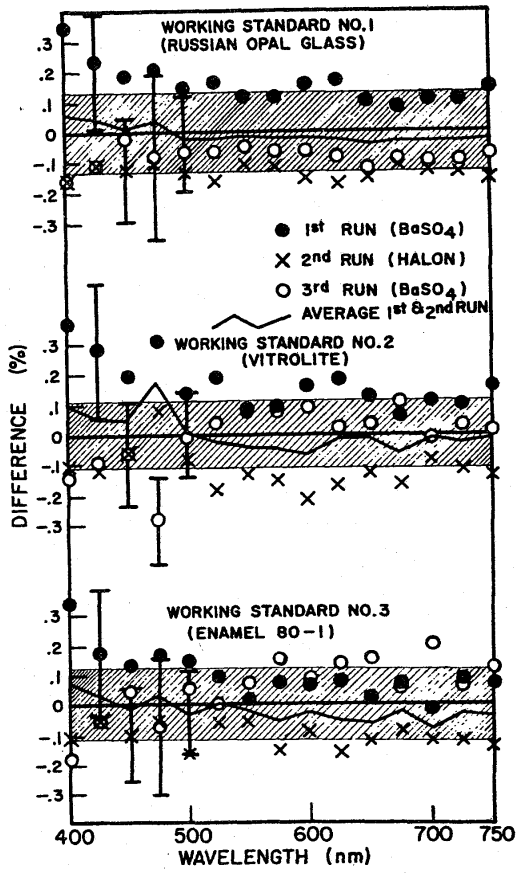

FIGURE 16. *Reflectance factor differences for the measurement of three working standards in three reflectance scale determinations.*

graphical record of the establishment of the average value for the three determinations. The representative error bars given to the left of the diagram actually were derived for 550 nm, but are fairly representative of the entire spectral range. The zero line in each case represents the average for the three determinations, and the shaded area represents the range of the total uncertainty of that average. Although the distribution of the points in general is consistent with the uncertainty levels which have been assigned, there is a lack of consistency from standard to standard between the relative values from pairs of determinations. For example, for working standard No. 1 (Russian opal glass), the third determination reflectance values are consistently lower than those of the first determination, whereas, for the other two working standards the first and third determinations yielded values which were more nearly equal (fig. 16). This difference in general behavior is too large to be explained by the uncertainties in the measured values of Q_c in expression (41). The most straightforward explanation for this difference is a slight drop in the reflectance of the working standard No. 1 during the interval between the second and third determinations. A better knowledge of the stability of the working standards will be obtained as more data are gathered from additional determinations.

The results of the work reported in this paper document the establishment of a scale of *d/h* reflectance factor at 25 nm intervals over the wavelength range 400 to 750 nm. The error analysis indicates that for high quality, uniform samples with reflectance greater than 0.5 there is only a very small probability that our measured reflectance factor values will be in error by more than 0.0015.

C. Relationship to Other Scales

In order to determine the relationship between the newly established NBS scale of *d/h* reflectance factor and the former one, we measured the three working standards on the NBS scale established in 1965. The results of this comparison are summarized in figure 17. In this figure, the data points indicate the departure of the old scale from the new for each working standard. The departure of the average value of the spectral 6°/*h* reflectance factors for the three standards on the 1965 scale from the same average on the new scale is shown by the light continuous line (GE average). The shaded area in the figure represents the uncertainty of the new scale, and the error bar on a central point indicates the uncertainty attributed to the 1965 scale. On the average, the old scale appears to depart from the new by about 0.002 at the short wavelength end of the range with the magnitude of the departure diminishing as the wavelength increases.

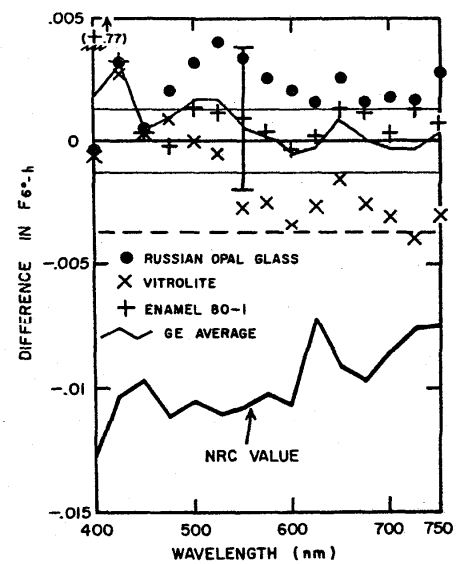

FIGURE 17. *Comparison of present NBS scale of $F_{6°-h}$ (taken as zero line) to previous NBS scale and to Results of an intercomparison with NRC.*

In 1974, measurements were made of several samples of pressed $BaSO_4$ and matte ground Russian opal glass at the National Research Council Laboratories (NRC) in Canada and at NBS on the 1965 NBS scale. The heavy line in figure 17 (NRC value) departs from the light line (GE average) by the difference between the averages of the reflectance values determined in the intercomparison. In this way, the present NBS scale and the NRC scale of 1974 are compared indirectly. The rather noisy appearance of the difference can very

probably be attributed to the imprecision of the NBS GE spectrophotometer.

The dashed line at approximately −0.004 indicates the combined error for this comparison. Since the NRC value differs from the present NBS value by over twice that amount, it is clear that at least one of these scales is in error by an amount greater than that claimed for it. At the time of this writing, work is under way on a new direct intercomparison between the present NRC and NBS scales of directional-hemispherical reflectance factor and on joint efforts to determine the cause of any differences.

D. Looking Ahead

We have already begun work on a determination of d/h reflectance factor by the Sharp-Little method [25, 26]. Most of the data have been obtained, and detailed analysis will be begun soon. Preliminary results indicate that the reflectance factors of the three working standards obtained by that method agree with those obtained by the Van den Akker method to well within the uncertainty of 0.0015. Therefore, it appears that the present NBS scale is accurate to within the uncertainty reported in this paper.

Mainly because of the slight instability and non-uniformity of the working standards, it is doubtful that an uncertainty in $F(6°, \lambda)$ of less than 0.1 percent of its value can be achieved on a practical, routine basis by any technique which relies on such standards. However, these working standards are more stable and more uniform than most samples encountered in practice. For this reason, we believe the newly established NBS scale of d/h reflectance factor to be sufficiently accurate and precise to serve the current needs for such measurements in science and industry.

VI. References

[1] Venable, William H. Jr., The National Measurement System for Spectrophotometry (Part of NBS Special Publication series 445, currently being prepared for publication.)

[2] Goebel, David G., Caldwell, B. Patrick, Hammond, Harry K., III, Use of an auxiliary sphere with a spectrophotometer to obtain absolute reflectance, J. Opt. Soc. Amer. **56**, 783 (1966).

[3] Certain products are mentioned in this paper by brand name or manufacturer for purposes of identification. This in no way implies recommendation or endorsement by the National Bureau of Standards.

[4] Keegan, Harry J., and Gibson, Kasson S., On the use of working standards of didymium and Vitrolite glasses for spectrophotometric measurements. J. Opt. Soc. Amer. **34**, 770 (Dec. 1944). (abstract).

[5] J. Opt. Soc. Amer. **28** (Oct. 1938). (Issue devoted to early development of recording spectrophotometer).

[6] NBS Letter Circular 1050 (June 1970). Preparation and Colorimetric Properties of a Magnesium-Oxide Relectance Standard.

[7] Private communication from W. Erb., Physikalisch-Technische Bundesanstalt.

[8] Venable, William H. Jr., Hsia, Jack J., and Weidner, Victor R., Development of an NBS reference spectrophotometer for diffuse reflectance and transmitance, Nat. Bur. Stand. (U.S.), Tech. Note 594-11, 47 pages (Oct. 1976).

[9] Van den Akker, J. A., Dearth, L. R., and Shillcox, W. M., Evaluation of absolute reflectance for standardization purposes, J. Opt. Soc. Am. **56**, 250 (1966).

[10] Venable, William H. Jr., and Hsia, Jack J., Describing spectrophotometric measurements, Nat. Bur. Stand. (U.S.), Tech. Note 594-9, 50 pages (Nov. 1974).

[11] International Lighting Vocabulary, Publication CIE No. 17 (E-1.1) 1970, section 45-20-201.

[12] Section III.B. of reference [8] above.

[13] Egan, W. G., and Hilgeman, T., Retroreflectance measurements of photometric standards and coatings, Applied Optics **15**, 1845 (1976).

[14] $BaSO_4$ manufactured by Mallincrodt Chemical Works (Reagent powder for X-ray diagnosis) #3808. [3]

[15] Halon tetrafluoroethylene powder manufactured by Allied Chemical Co. Type G-80, Lot 463169 Drum 31. [3]

[16] $BaSO_4$ manufactured by J. T. Baker Chemical Co. #5-1030 (553-1011) (analytical Reagent) [3].

[17] See section III. A. of reference [8] above.

[18] See Appendix C of Reference [8] above.

[19] Jenkins, F. A., and White, H. E., Fundamentals of Optics, 3rd edition (McGraw-Hill, N. Y., 1957) pg. 521, figure 25M.

[20] Jakob, Max, Heat Transfer, Volume II, p. 14 (John Wiley and Sons, N. Y., 1963), ($\omega_e/\pi = 1 - f_{12}$).

[21] See section III.A.4 of reference [8] above.

[22] Kubelka, Paul, New contributions to the Optics of Intensely Light Scattering Materials. Part I, J. Opt. Soc. Amer. **38**, 448 (1948).

[23] Grum, F. and Saltzman, M.; P-75-77 New White Standard of Reflectance. Compte Rendu 18^e Session, Londres 1975, CIE Publication No. 36, 91 (1976).

[24] Colorimetry, Publication CIE No. 15 (E13.1) 1971, pages 81 and 93.

[25] Sharp, C. H. and Little, W. F., Measurement of Reflection Factors, Transactions I.E.S. **15**, 802 (1920).

[26] Budde, Wolfgang, and Dodd, C. X., Absolute reflectance measurements in the $D/0°$ Geometry, Die Farbe **19**, 94 (1970).

[27] Hapke, Bruce W., A theoretical photometric function for the lunar surface, Journal of Geophysical Research **68**, 4571 (1963).

[28] Born, M., and Wolf, E., Principles of Optics, 3rd Edition, (Pergamon Press, New York, 1964), p. 399.

VII. Appendix A. Accounting for Retroreflectance

Retroreflectance refers to the tendency of objects to preferentially reflect radiation back in the direction from which it is incident. This can arise from several causes. If a focussing element such as a small dielectric sphere directs radiation onto a reflecting surface at or near its focal point, the reflected radiation will be returned back into the direction from which it came. This type of retroreflectance can be very directional, i.e., most of the radiation returns within a few tenths of a degree of the angle from which it came. A second, much less directional retroreflectance effect, results from the fact that shadows are not visible from the direction of incidence. This mechanism is important only for surfaces which are not highly reflecting, so that the radiation is not re-reflected out of the shadows. In the case of the highly reflecting coatings being used in the spheres in this experiment, the highly directional retroreflectance dominates.

1. The Effect of Retroreflectance

In order to obtain an estimate of how the presence of retroreflectance will affect a determination of the Van den Akker reflectance ρ_v, we will use a simple model in which most of the radiation is reflected in a Lambertian distribution but a small retroreflected fraction f_r appears above the Lambertain background. The effect which the retroreflectance has upon the flux $\phi_i(\lambda)$ (see III.A.) striking the sphere boundary can be seen by going one step backwards in determining the source of ϕ_i. The flux ϕ_i comes from the walls by reflection, and the incident radiation for this reflection is from the sphere walls, but *not from the port*. Therefore, in the presence of retroreflection the irradiance on the sphere boundary is higher on the wall coating than in the port. The makeup of ϕ_i can be determined by noting that, in this model, the flux incident upon the walls (which also comes from the walls) is either absorbed or reflected. The total reflected flux, which is ϕ_i, is made up of two parts

$$\phi_i = \phi_r + \phi_i' \tag{A1}$$

where ϕ_r is the retroreflected fraction of the reflected flux

$$\phi_r = f_r \phi_i \tag{A2}$$

and ϕ_i' is the diffusely reflected fraction

$$\phi_i' = (1 - f_r)\phi_i. \tag{A3}$$

With this model, the power balance equation, equation (3) of part III.A., takes on the following form.

$$\begin{aligned} \rho_v'(1 + f_r\rho_v')(1 - f)\rho_t\phi_0 \\ = \phi_i' f + [(1 - f)\phi_i' + \phi_r](1 - \rho_v') \end{aligned} \tag{A4}$$

where ρ_t is reflectance of the target exclusive of the augmented reflection in the retro direction, which is lost through the port of the measuring instrument in every case. The relative reflectance Q_s of the sphere is

$$Q_s = k[\phi_i' f(1 - f') + \phi_0(1 + f_r\rho_v')\rho_t f(1 - f'')] \tag{A5}$$

and the relative reflectance of the target is, as before

$$Q_t = k\phi_0\rho_t(1 - f'). \tag{A6}$$

Equations (A2), (A3), (A4), (A5), and (A6) can be solved to obtain an expression for ρ_v' in the following form:

$$\rho_v' = \frac{1 - f(1 - f_r)\dfrac{Q_t}{Q_s}}{1 - f(1 - f_r)} \quad \frac{1}{1 - \alpha} \tag{A7}$$

where

$$\alpha = \left\{\frac{f(1 + \rho_v' f_r)[f' - f'']}{(1 - f')} + \frac{ff_r(1 - f_r\rho_v'^2)}{1 - \rho_v'[1 - f(1 - f_r)]}\right\}\frac{Q_t}{Q_s} \tag{A7a}$$

Comparing (A7) with (6), it is seen that f in the dominant first term is replaced by $f(1 - f_r)$. This in essence states that the fraction the flux escaping from the port has been reduced relative to the flux lost to the walls by an amount proportional to the retroreflected fraction. The correction term α for the singular treatment of the first target reflection when the target is in the auxiliary sphere is also modified by the retroreflectance, making the form of this term so complicated that a closed solution in terms of the measurement parameters is not practical. We solve the equation iteratively, using as a first approximation for ρ_v' the value obtained from (A7) with $\alpha = 0$. Taking the retroreflectance into account has a very small effect on the calculated value of ρ_v'. For example, if $f_r = 0.001$, the effect of not ignoring this in the case of a sample for which $\rho_v' \approx 0.98$ is to reduce the calculated ρ_v' by approximately 10^{-6}. Note that ρ_v' must be the total reflectance, including retroreflectance, since $1 - \rho_v'$ represents loss of radiation by absorption.

2. *Models for Retroreflective Mechanisms*

Our measurements of retroreflective bidirectional reflectance factor, the data for which are shown in figure 15, were limited to observation angles greater than 0.1°. Therefore we sought a model which could be used to interpolate our data to 0° observation angle so that we could evaluate the integral in eq (39).

A model based on shadowing was developed by Hapke [27] to explain the retroreflective phenomena observed from the lunar surface. This model, which was quite successful in Hapke's application, was used by Egan and Hilgeman [13] in an effort to quantitatively evaluate the retroreflectance which they observed from barium sulfate paint and other highly reflective white coatings. Other possible mechanisms for producing retroreflectance include cube corner reflectors formed from broken cubic crystals and retroreflectance by focussing, as occurs in glass beaded retroreflecting sheeting. In the following paragraphs we will treat special cases of each mechanism.

a. Shadowing

The Hapke model includes as one of its basic assumptions that the absorbance of the scattering particles is very high. In this way, there will be a considerable contrast between the radiance coming from shadowed areas in which the radiation undergoes several reflections and the radiance reflected from an unshadowed area. Although there is relatively little loss in highly reflecting materials such as barium sulfate or Halon, it is still possible for an initial first surface reflection to add to the background of multiply reflected radiation in a preferential manner. In order to estimate the order of magnitude of the non-diffuse reflection, one can use layers of close-packed spheres as a model for the many randomly oriented particles in the coating. Referring to one such sphere as shown in figure 18a, one can calculate the reflectance factor for such an array as follows. The bidirectional reflectance factor is given by

$$F(\mathbf{U}, \mathbf{u}) = \frac{\pi L(\mathbf{u})}{E(\mathbf{U})} \tag{A8}$$

where $E(\mathbf{U})$ is collimated irradiance incident in the direction $\mathbf{U}$ and $L(\mathbf{u})$ is the reflected radiance in the direction $\mathbf{u}$, both averaged over a sufficiently large area of the sample. In the case of retroreflectance, we set the unit vectors $\mathbf{U}$ and $\mathbf{u}$ equal. The average reflected radiance is given by definition as

$$L(\mathbf{u}) = \frac{\Phi(\omega, A)}{\omega(\mathbf{u})A\cos\gamma}. \tag{A9}$$

where $\omega(\mathbf{u})$ is an element of solid angle oriented in the direction $(\mathbf{u})$, A is the area of the surface over which the average is being taken, and $\Phi(\omega, A)$ is the flux reflected from area S into solid angle ω. Collimated incident radiation will come to a virtual focus at a point I which is $r/2$ from the outer surface of the sphere. The solid angle ω is defined in terms of a small arbitrary area a on the sphere

$$\omega = \frac{4a}{r^2}. \tag{A10}$$

The flux reflected from this area into ω is given by

$$\Phi = \rho E a/\cos\gamma \tag{A11}$$

where ρ is the reflectance of the sphere surface. (Note that since we are treating retroreflectance, a is chosen so that it is centered on a radius in the direction of E, and therefore the direction of incidence is normal to a.) The area A occupied by this sphere in a hexagonal close-packed array is

$$A = \frac{6r^2}{\sqrt{3}}. \tag{A12}$$

Using expressions (A9), (A10), (A11), and (A12) above in (A8) one obtains under conditions of retroreflectance:

$$F\ (\dot{\mathbf{U}}, \mathbf{u}) = \frac{\pi\sqrt{3}}{24}\rho/\cos^2\gamma = 0.227\rho/\cos^2\gamma. \tag{A13}$$

This would be roughly the maximum amount of additional bidirectional reflectance factor which might occur in the retro-direction under ideal conditions of shading by surrounding particles. The $\cos^2\gamma$ term in the denominator is an artifact of the "array of spheres" model we are using. In the continuous surface being represented by the array of spheres model, the projected surface area goes as $\cos^2\gamma$ so that the $\cos^2\gamma$ term should be omitted.

b. Cube corners

In the ideal case, the bidirectional reflectance factor for a cube corner reflector would be infinite at zero observation angle and zero at all other observation angles. However, imperfections in the cube corners and diffraction tend to spread the reflected radiation out so that bidirectional reflectance factor has meaning in describing reflection by cube corners. For the model for maximum reflectance, we will assume that the cubes are perfect and that diffraction is the limiting factor. For near normal incidence the total retroreflectance from a close-packed array of cube corner reflectors is

$$\rho_t = \rho_1^3(1 - \rho_2)^2 \tag{A14}$$

where ρ_1 is the reflectance of the cube faces and ρ_2 is the reflectance of the entrance surface. For a perfect internal corner ρ_1 is 1 and ρ_2 is roughly 0.05, so that ρ_t is roughly 0.9. For an external corner (cube corner "hole"), $\rho_2 = 0$ and ρ_1 is roughly 0.05 so that ρ_t is roughly 1.25×10^{-4} in that case. The reflected radiance is distributed in the diffraction pattern associated with the reflecting faces treated as apertures. For this order of magnitude calculation, we will assume the pattern to be that of a circular aperture of effective radius $r = \sqrt{\frac{A}{\pi}}$ where A is the area of the entrance surface. The radiance in such a pattern would be given by [28].

$$L(\beta) = \frac{EA}{\lambda^2}\left[\frac{2J_1(x)}{x}\right]^2 \tag{A15}$$

where

$$x = 2\pi r \sin(\beta)/\lambda,$$

from which it follows that the reflectance factor is given by

$$F(\beta) = \frac{\pi A}{\lambda^2}\left[\frac{2J_1(x)}{x}\right]^2\rho_t. \tag{A16}$$

The data in figure 15 suggest that the particle sizes are such that the central bright spot would subtend an angle of about 1° for $BaSO_4$. The edge of the central bright spot falls at $x = 3.8$. For an effective wavelength of approximately 550 nm, it follows that the particle size would have to be such that $r \simeq 20\ \mu$m. Thus, the reflectance factor at $\beta \ll 1°$ would be roughly

$$F(\beta) \simeq 10^4\rho_t. \tag{A17}$$

c. Focussing retroreflectors

If the index of refraction of a bead is such that the radiation passing through it comes to a focus behind it, a suitable reflector may be placed at the focal point (I in fig. 18c.) and the radiation will be reflected back through the bead into a collimated retroreflected beam. Here, the spreading of the reflected radiance can be brought about either by diffraction, poor focussing, or both. The diffraction limiting case in the previous paragraph can be applied to the Halon data in figure 15. In this case, the central bright spot appears to subtend an angle of about 0.5° which corresponds to an effective lens radius of $r \simeq 40\ \mu$m. If one assumes a refractive index of 1.5 so that the radiation will come to a focus on the back of the bead and from experience with cheap cameras assumes that

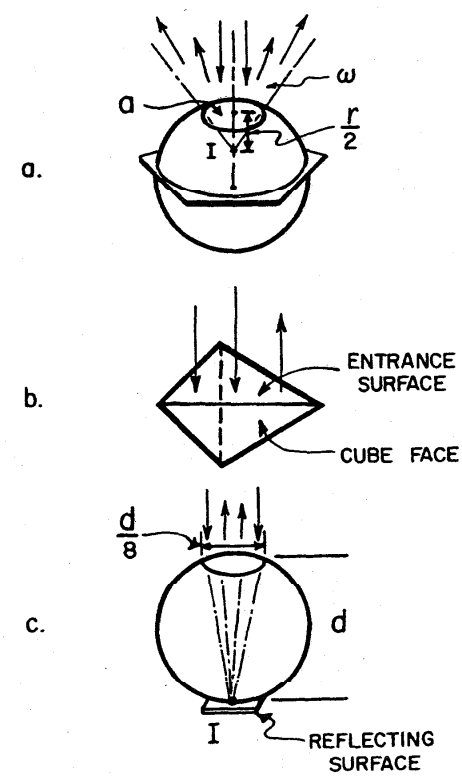

FIGURE 18. *Diagrams for estimating magnitude of retroreflectance by various means.*

the diameter of the effective lens area is roughly one-eighth of the diameter of the bead, it follows from expressions (A12) and (A16) that a closely packed array of such spheres would have a reflectance factor for $\beta \ll 1$ of

$$F(\beta) \simeq 6 \times 10^2 \rho_t \tag{A18}$$

for a specular reflector of reflectance ρ_t located at I and

$$F(\beta) \simeq 10 \rho_t \tag{A19}$$

for a diffuse reflector of reflectance ρ_t at I.

3. Interpolating the retroreflectance data

From the foregoing analysis, one can make the following deductions, assuming that the 0.5 excess reflectance factor is caused by only one mechanism:

a. Shadowing cannot by itself account for the observed retroreflectance.
b. At least 6×10^{-5} of the area is effectively taken up with inside corner cube retroreflectors.
c. At least 0.4 of the area is effectively taken up with outside corner cube retroreflectors.
d. At least 1.6×10^{-2} of the area is effectively taken up with focusing sphere retroreflectors backed by specular reflectors of reflectance 0.05.
e. At least 5×10^{-2} of the area is effectively taken up with sphere retroreflectors backed by diffuse reflectors of reflectance 1.

Since the mechanisms are not mutually exclusive, it is expected that all will operate to some extent in pressed powder samples. However it is highly unlikely that cube corner reflectors will be formed in Halon, so it would be expected that the mechanism in d. or e. above would predominate. Even though the cleavage of a crystal in such a way that it forms an inside corner cube reflector is not very likely, mechanism b. probably predominates in the $BaSO_4$ powder. Shadowing will contribute some effective retroreflectance in both cases.

The predominate mechanisms appear to depend on the sum of the diffraction patterns associated with a number of reflectors, each with a different effective aperture, and the statistical distribution of the aperture sizes is unknown. Therefore we chose to use an emperical fitting function. The function

$$F(\beta) = 1 + \exp(a + b\beta^c) \tag{A20}$$

was found to fit the data adequately. Fitting all $BaSO_4$ data, we obtained

$a = -0.393$
$b = -0.966$
$c = 0.57$

and fitting the first seven points of the Halon data we obtained

$a = 1.18$
$b = -3.41$
$c = 0.21$

These fitting functions are shown as solid curves in figure 15. The average of the function $F(\beta)$ for $BaSO_4$ over the range $0 \leq \beta \leq 0.5°$ is 1.42 which is in good agreement with the data of Egan and Hilgeman [13]. The difference values for $\rho(6°, \lambda) - F(6°, \lambda)$ were obtained by using the fitted functions in eqs (39) and (40) with $r = 1.9$ cm and $d' = 29.4$ cm. In each case, the contribution from the region of extrapolation ($|\beta| < 0.1°$) was only a small part of the total flux in the retroreflected component, so the choice of fitting functions was not critical. A crude measurement of $BaSO_4$ using a beam splitter yielded $\rho(6°, \lambda) - F(6°, \lambda) = 0.0006$ which is in good agreement with the value of 0.0007 obtained from the data in figure 15.

VIII. Appendix B. Interpretation of Error Statements

The error analysis in this paper involves three distinct classes of errors. The first class of error is the measured random error. This type of error appears as noise in the measurements and is evaluated by making each measurement several times and performing the usual error analysis on the results. For this type of error, we will cite three times the standard deviation of the mean.

The second class of error is the estimated random error. This class of error contributes to the outcome in the same way as the measured random error, but, either because of the inconsequential effects of the error or because of experimental difficulties which would be involved in evaluating it, we choose to estimate the size of the error instead of determining it by making several measurements. In making such an estimate, we choose to estimate the smallest range of uncertainty within which the correct value will fall with a very high probability, i.e., an intuitive ninety-five times out of a hundred. For this type of error, we will cite the size of the estimated error itself. The estimation process is carried out in such a way that the sign of the error is indeterminant. If it is known that a particular cause of error will result in an error which is always of one sign, we will correct the measured value to a most probable value and reduce the magnitude of the estimated random error appropriately. The estimated random error is combined in quadrature with the measured random error to obtain the total random error. All random errors, whether measured or estimated, will be denoted by the symbol δ.

The third type of error is the estimated systematic error, indicated by the symbol Δ. This error is like the estimated random error in all respectes except one, namely it is not independent from determination to determination, i.e., it will affect all determinations in the same way. It should be pointed out that this does not mean that the sign of the measurement is known, but only that the sign of the effect is known to be fixed from determination to determination. For example, in correcting for the reflection of radiation from the beveled lip of the sphere, we estimate that the radiation will be reflected with an average reflectance intermediate between one and the normal reflectance of the stainless steel. (See discussion preceding (19).) If the actual reflectance is less than our estimated value, determinations of reflectance made using this estimate will result in ρ_v values which are all slightly higher than if the estimates were correctly made. In the course of many determinations, the total random error will be reduced, but the systematic error will remain. Since the

sign of the systematic errors is not known, systematic errors from independent causes will be added in quadrature, and at each point in the analysis at which it is desirable to estimate a total uncertainty, the systematic error and the total random error will be added in quadrature. However, when proceeding to combine the results of several determinations, we will first combine the random errors in the ordinary way and add the largest systematic error in quadrature at the end. In this way, the calculated systematic error is not reduced by repeating the measurements. The total uncertainties so calculated are to be regarded as determining a range within which we expect the correct value to fall with a probability of approximately 0.95. This total uncertainty will be indicated by the symbol ϵ.

IX. Appendix C. Calculating $C(\Gamma, \lambda)$

The integrals in (11) are evaluated in closed form after fitting the experimental data for N_g and N_G.

1. *Fitting $N_G(\Gamma, \lambda)$*

The data for N_G were fitted by an expression of the form:

$$N_G(\Gamma, \lambda) = a_0(\lambda) + a_1(\lambda)\Gamma^2 + a_2(\lambda)\Gamma^4. \qquad \text{(C1)}$$

An even function of Γ was used, since we have assumed the directional-hemispherical reflectance of the coatings does not depend on the angle of azimuth of the incident direction, but depends only on the angle of elevation. The coefficients in (C1), as determined by a least squares fitting of the experimental data are given in table C1.

2. *Fitting $N_g(\Gamma, \lambda)$*

Since the experimental data for $N_g(\gamma, \lambda)/\cos(\gamma)$ were found to be nearly independent of wavelength, only one function $N_g(\Gamma)$ is needed for each type of coating. However, since there was such a large uncertainty in the $N_g(\Gamma)$ data, three sets of $N_g(\Gamma)$ were fitted as described in part IV.B.3. in the main text. The form used for the fitting the data was:

$$N_g(\Gamma)/\cos\Gamma = \sum_{i=0}^{4} b_i\Gamma^i. \qquad \text{(C2)}$$

TABLE CI

Coefficients for the expansion of $N_G(\Gamma, \lambda)$ in even powers of the angle of incidence Γ in radians at three different wavelengths for three sphere wall coatings.

Coating	Wave-length	a_0	a_1* $\times 10^3$	a_2* $\times 10^3$
$BaSO_4$ [14]	450	0.999942	5.99	0.438
	550	.99978	4.40	0.159
	750	1.00011	3.27	−0.00814
Halon [15]	450	0.999875	3.97	−0.172
	550	1.00004	4.17	−0.985
	750	1.00027	3.68	−1.20
$BaSO_4$ [16]	450	0.999829	4.08	0.405
	550	1.00047	1.43	0.741
	750	1.00012	3.91	−0.471

* The second and third digits are not significant but are kept to avoid round-off error in further calculations.

In the case of the original knife-edge data, the values of the coefficients, as obtained by least squares fitting, are given in table CII as describing the "upper limit" curve. In the original data, the least uncertainty was associated with the $\Gamma = 0$ reading. Therefore, all data were normalized to the $\Gamma = 0$ reading and b_0 was taken to be 1 when the data were fitted. Because of the symmetry in azimuth, b_1 and b_3 are taken to be zero.

In the accepted data, $N_g(\Gamma)/\cos\Gamma$ was taken as 1 up to $\Gamma = \pi/4$. To obtain the remaining part of this curve we obtained $N_g(\gamma)$ according to the expression

$$N_g'(\gamma)/\cos\gamma = 1 + C_1\gamma. \qquad \text{(C3)}$$

The difference data $N_g(\gamma) - N_g'(\gamma)$ using the data for the angles $\pi/3$ (60°), $5\pi/12$(75°) and $17\pi/36$(85°) were fitted using the form

$$N_g(\gamma)/(\cos\gamma) = 1 + b_1'(\Gamma - \frac{\pi}{4})^2 + b_2'(\Gamma - \frac{\pi}{4})^4. \qquad \text{(C4)}$$

After b_1' and b_2' were determined, these were used to obtain the b_i in the expression (C2).

3. *Calculating $C(\Gamma, \lambda)$*

With the expressions (C1) for $N_G(\Gamma, \lambda)$ and (C2) for $N_g(\Gamma, \lambda)$ substituted into eq (11), the integrals in that equation can be evaluated in closed form in terms of integrals of the form

$$I_i = \int_0^{\pi/2} \Gamma^i \cos\Gamma \sin\Gamma d\Gamma \qquad \text{(C5)}$$

for the upper and lower limit functions, and

$$I_i' = \int_0^{\pi/4} \Gamma^i \cos\Gamma \sin\Gamma d\Gamma \qquad \text{(C6)}$$

and

$$I_i'' = \int_{\pi/4}^{\pi/2} \Gamma^i \cos\Gamma \sin\Gamma d\Gamma \qquad \text{(C7)}$$

for the accepted value functions. The values of these integrals are given in table CIII, and the resulting values of $\bar{N}_G(\lambda)$ are given in table CIV. It can be seen from table CIV that the difference between the various assumptions concerning the self-radiance has a very small effect on the value of $\bar{N}_G$ in all cases. Therefore only the accepted value of $\bar{N}_G$ will be used in each case to calculate $C(\Gamma, \lambda)$. The results of the scanning which has been done to date with the telescopic detector indicate that the real value probably lies toward the lower limit from the accepted value. On this belief, we will assign the largest difference between an accepted value and a lower limit value, 0.00005, as the magnitude of the uncertainty in $\bar{N}_G$ due to the uncertainty in evaluating the self-radiance by measuring N_g.

X. Appendix D. The Three Working Standards

The properties which standards for reflectance factor measurements should have is a subject over which there is much diversity of opinion. By definition, reflectance factor is reflectance relative to the reflectance of a totally reflecting Lambertian reflector, both measured on the same instrument. Based on this definition, the best standard for calibrating an

the diameter of the effective lens area is roughly one-eighth of the diameter of the bead, it follows from expressions (A12) and (A16) that a closely packed array of such spheres would have a reflectance factor for $\beta \ll 1$ of

$$F(\beta) \simeq 6 \times 10^2 \rho_t \tag{A18}$$

for a specular reflector of reflectance ρ_t located at I and

$$F(\beta) \simeq 10 \rho_t \tag{A19}$$

for a diffuse reflector of reflectance ρ_t at I.

3. Interpolating the retroreflectance data

From the foregoing analysis, one can make the following deductions, assuming that the 0.5 excess reflectance factor is caused by only one mechanism:

a. Shadowing cannot by itself account for the observed retroreflectance.
b. At least 6×10^{-5} of the area is effectively taken up with inside corner cube retroreflectors.
c. At least 0.4 of the area is effectively taken up with outside corner cube retroreflectors.
d. At least 1.6×10^{-2} of the area is effectively taken up with focusing sphere retroreflectors backed by specular reflectors of reflectance 0.05.
e. At least 5×10^{-2} of the area is effectively taken up with sphere retroreflectors backed by diffuse reflectors of reflectance 1.

Since the mechanisms are not mutually exclusive, it is expected that all will operate to some extent in pressed powder samples. However it is highly unlikely that cube corner reflectors will be formed in Halon, so it would be expected that the mechanism in d. or e. above would predominate. Even though the cleavage of a crystal in such a way that it forms an inside corner cube reflector is not very likely, mechanism b. probably predominates in the $BaSO_4$ powder. Shadowing will contribute some effective retroreflectance in both cases.

The predominate mechanisms appear to depend on the sum of the diffraction patterns associated with a number of reflectors, each with a different effective aperture, and the statistical distribution of the aperture sizes is unknown. Therefore we chose to use an emperical fitting function. The function

$$F(\beta) = 1 + \exp(a + b\beta^c) \tag{A20}$$

was found to fit the data adequately. Fitting all $BaSO_4$ data, we obtained

a = −0.393
b = −0.966
c = 0.57

and fitting the first seven points of the Halon data we obtained

a = 1.18
b = −3.41
c = 0.21

These fitting functions are shown as solid curves in figure 15. The average of the function $F(\beta)$ for $BaSO_4$ over the range $0 \leq \beta \leq 0.5°$ is 1.42 which is in good agreement with the data of Egan and Hilgeman [13]. The difference values for $\rho(6°, \lambda) - F(6°, \lambda)$ were obtained by using the fitted functions in eqs (39) and (40) with $r = 1.9$ cm and $d' = 29.4$ cm. In each case, the contribution from the region of extrapolation ($|\beta| < 0.1°$) was only a small part of the total flux in the retroreflected component, so the choice of fitting functions was not critical. A crude measurement of $BaSO_4$ using a beam splitter yielded $\rho(6°, \lambda) - F(6°, \lambda) = 0.0006$ which is in good agreement with the value of 0.0007 obtained from the data in figure 15.

VIII. Appendix B. Interpretation of Error Statements

The error analysis in this paper involves three distinct classes of errors. The first class of error is the measured random error. This type of error appears as noise in the measurements and is evaluated by making each measurement several times and performing the usual error analysis on the results. For this type of error, we will cite three times the standard deviation of the mean.

The second class of error is the estimated random error. This class of error contributes to the outcome in the same way as the measured random error, but, either because of the inconsequential effects of the error or because of experimental difficulties which would be involved in evaluating it, we choose to estimate the size of the error instead of determining it by making several measurements. In making such an estimate, we choose to estimate the smallest range of uncertainty within which the correct value will fall with a very high probability, i.e., an intuitive ninety-five times out of a hundred. For this type of error, we will cite the size of the estimated error itself. The estimation process is carried out in such a way that the sign of the error is indeterminant. If it is known that a particular cause of error will result in an error which is always of one sign, we will correct the measured value to a most probable value and reduce the magnitude of the estimated random error appropriately. The estimated random error is combined in quadrature with the measured random error to obtain the total random error. All random errors, whether measured or estimated, will be denoted by the symbol δ.

The third type of error is the estimated systematic error, indicated by the symbol Δ. This error is like the estimated random error in all respectes except one, namely it is not independent from determination to determination, i.e., it will affect all determinations in the same way. It should be pointed out that this does not mean that the sign of the measurement is known, but only that the sign of the effect is known to be fixed from determination to determination. For example, in correcting for the reflection of radiation from the beveled lip of the sphere, we estimate that the radiation will be reflected with an average reflectance intermediate between one and the normal reflectance of the stainless steel. (See discussion preceding (19).) If the actual reflectance is less than our estimated value, determinations of reflectance made using this estimate will result in ρ_v values which are all slightly higher than if the estimates were correctly made. In the course of many determinations, the total random error will be reduced, but the systematic error will remain. Since the

sign of the systematic errors is not known, systematic errors from independent causes will be added in quadrature, and at each point in the analysis at which it is desirable to estimate a total uncertainty, the systematic error and the total random error will be added in quadrature. However, when proceeding to combine the results of several determinations, we will first combine the random errors in the ordinary way and add the largest systematic error in quadrature at the end. In this way, the calculated systematic error is not reduced by repeating the measurements. The total uncertainties so calculated are to be regarded as determining a range within which we expect the correct value to fall with a probability of approximately 0.95. This total uncertainty will be indicated by the symbol ϵ.

IX. Appendix C. Calculating $C(\Gamma, \lambda)$

The integrals in (11) are evaluated in closed form after fitting the experimental data for N_g and N_G.

1. *Fitting $N_G(\Gamma, \lambda)$*

The data for N_G were fitted by an expression of the form:

$$N_G(\Gamma, \lambda) = a_0(\lambda) + a_1(\lambda)\Gamma^2 + a_2(\lambda)\Gamma^4. \quad \text{(C1)}$$

An even function of Γ was used, since we have assumed the directional-hemispherical reflectance of the coatings does not depend on the angle of azimuth of the incident direction, but depends only on the angle of elevation. The coefficients in (C1), as determined by a least squares fitting of the experimental data are given in table C1.

2. *Fitting $N_g(\Gamma, \lambda)$*

Since the experimental data for $N_g(\gamma, \lambda)/\cos(\gamma)$ were found to be nearly independent of wavelength, only one function $N_g(\Gamma)$ is needed for each type of coating. However, since there was such a large uncertainty in the $N_g(\Gamma)$ data, three sets of $N_g(\Gamma)$ were fitted as described in part IV.B.3. in the main text. The form used for the fitting the data was:

$$N_g(\Gamma)/\cos\Gamma = \sum_{i=0}^{4} b_i\Gamma^i. \quad \text{(C2)}$$

TABLE CI

Coefficients for the expansion of $N_G(\Gamma, \lambda)$ in even powers of the angle of incidence Γ in radians at three different wavelengths for three sphere wall coatings.

Coating	Wave-length	a_0	a_1* $\times 10^3$	a_2* $\times 10^3$
$BaSO_4$ [14]	450	0.999942	5.99	0.438
	550	.99978	4.40	0.159
	750	1.00011	3.27	−0.00814
Halon [15]	450	0.999875	3.97	−0.172
	550	1.00004	4.17	−0.985
	750	1.00027	3.68	−1.20
$BaSO_4$ [16]	450	0.999829	4.08	0.405
	550	1.00047	1.43	0.741
	750	1.00012	3.91	−0.471

* The second and third digits are not significant but are kept to avoid round-off error in further calculations.

In the case of the original knife-edge data, the values of the coefficients, as obtained by least squares fitting, are given in table CII as describing the "upper limit" curve. In the original data, the least uncertainty was associated with the $\Gamma = 0$ reading. Therefore, all data were normalized to the $\Gamma = 0$ reading and b_0 was taken to be 1 when the data were fitted. Because of the symmetry in azimuth, b_1 and b_3 are taken to be zero.

In the accepted data, $N_g(\Gamma)/\cos\Gamma$ was taken as 1 up to $\Gamma = \pi/4$. To obtain the remaining part of this curve we obtained $N_g(\gamma)$ according to the expression

$$N_g'(\gamma)/\cos\gamma = 1 + C_1\gamma. \quad \text{(C3)}$$

The difference data $N_g(\gamma) - N_g'(\gamma)$ using the data for the angles $\pi/3$ (60°), $5\pi/12$(75°) and $17\pi/36$(85°) were fitted using the form

$$N_g(\gamma)/(\cos\gamma) = 1 + b_1'(\Gamma - \frac{\pi}{4})^2 + b_2'(\Gamma - \frac{\pi}{4})^4. \quad \text{(C4)}$$

After b_1' and b_2' were determined, these were used to obtain the b_i in the expression (C2).

3. *Calculating $C(\Gamma, \lambda)$*

With the expressions (C1) for $N_G(\Gamma, \lambda)$ and (C2) for $N_g(\Gamma, \lambda)$ substituted into eq (11), the integrals in that equation can be evaluated in closed form in terms of integrals of the form

$$I_i = \int_0^{\pi/2} \Gamma^i \cos\Gamma \sin\Gamma d\Gamma \quad \text{(C5)}$$

for the upper and lower limit functions, and

$$I_i' = \int_0^{\pi/4} \Gamma^i \cos\Gamma \sin\Gamma d\Gamma \quad \text{(C6)}$$

and

$$I_i'' = \int_{\pi/4}^{\pi/2} \Gamma^i \cos\Gamma \sin\Gamma d\Gamma \quad \text{(C7)}$$

for the accepted value functions. The values of these integrals are given in table CIII, and the resulting values of $\bar{N}_G(\lambda)$ are given in table CIV. It can be seen from table CIV that the difference between the various assumptions concerning the self-radiance has a very small effect on the value of $\bar{N}_G$ in all cases. Therefore only the accepted value of $\bar{N}_G$ will be used in each case to calculate $C(\Gamma, \lambda)$. The results of the scanning which has been done to date with the telescopic detector indicate that the real value probably lies toward the lower limit from the accepted value. On this belief, we will assign the largest difference between an accepted value and a lower limit value, 0.00005, as the magnitude of the uncertainty in $\bar{N}_G$ due to the uncertainty in evaluating the self-radiance by measuring N_g.

X. Appendix D. The Three Working Standards

The properties which standards for reflectance factor measurements should have is a subject over which there is much diversity of opinion. By definition, reflectance factor is reflectance relative to the reflectance of a totally reflecting Lambertian reflector, both measured on the same instrument. Based on this definition, the best standard for calibrating an

TABLE CII

Coefficient for the expansion of $N_p(\Gamma)/\cos\Gamma$ in powers of the angle of incidence Γ in radians for three different sphere coatings and three different assumptions concerning the self-radiance distribution.

Coating	Curve Type	b_0	$b_1 \times 100$	$b_2 \times 100$	$b_3 \times 100$	$b_4 \times 100$
	upper limit	1	0	7.0	0	−1.1
$BaSO_4$ [14]	accepted; $\Gamma \leq \pi/4$	1	0	0	0	0
	accepted; $\Gamma > \pi/4$	1.03	−1.240	−12.4	16.7	−5.33
	lower limit	1	0	0	0	0
	upper limit	1	0	5.3	0	6.1
Halon [15]	accepted; $\Gamma \leq \pi/4$	1	0	0	0	0
	accepted; $\Gamma > \pi/4$	1.45	−219	405	−339	107
	lower limit	1	0	0	0	0
	upper limit	1	0	3.8	0	1.6
$BaSO_4$ [16]	accepted; $\Gamma \leq \pi/4$	1	0	0	0	0
	accepted; $\Gamma > \pi/4$	1.17	−120	271	−248	79
	lower limit	1	0	0	0	0

TABLE CIII

Values of the integrals in equations (C5), (C6), and (C7) for nine values of i.

i	I_i	I_i'	I_i''
0	0.50000	0.25000	0.25000
1	.39270	.12500	.26770
2	.36685	.07135	.29550
3	.37990	.04382	.33608
4	.42147	.02819	.39328
5	.49129	.01872	.47257
6	.59443	.01273	.58170
7	.74046	.00882	.73164
8	.94416	.00614	.93802

TABLE CIV

Values of the weighted averages $N_G(\lambda)$ for each of three coatings for three wavelengths and three different assumptions concerning the self-radiance distribution.

Determination number	Wave-length λ	Upper limit	Accepted value	Lower limit
$BaSO_4$ [14]	450	1.00486	1.00479	1.00476
	550	1.00343	1.00338	1.00336
	750	1.00244	1.00240	1.00239
Halon [15]	450	1.00294	1.00282	1.00277
	550	1.00233	1.00225	1.00223
	750	1.00175	1.00170	1.00169
$BaSO_4$ [16]	450	1.00343	1.00335	1.00333
	550	1.00173	1.00168	1.00167
	750	1.00253	1.00247	1.00247

instrument to measure reflectance factor would be a totally reflecting Lambertian reflector, or the closest thing to it which could be obtained. The Halon and barium sulfate sphere linings which were used in the work described in this paper were very close to this ideal.

However, if reflectance factor measurements are going to be of use in practical applications, the instrument must be defined as part of the specification of the measurement. It is for this reason that we have defined the measurements as carefully as possible in terms of integrals describing the incident radiation and the instrument response. We believe the properties of our reference reflectometer are very close to those specified in the definition for directional-hemispherical reflectance factor which we have used, and furthermore, we believe the geometrical properties of that instrument to be stable in time. In order to confirm this, however, we feel that it is important to have several working standards representing the gamut of the highly reflecting materials which we would be measuring with this instrument. It is also important that several different types of working standards be used in order to be able to detect changes in the optical properties of any one of them. As a means of retaining our scale of measurement in day-to-day measurements and as a means of comparing one determination with another, we are using the following working Standards:

Working Standard No. 1—This standard is a piece of MC-20 opal glass purchased in September 1970 from

Mashpriborintorg
Smolenskaja pl., 32/34
121200, Moscow, G-200
U.S.S.R.

The piece used is 99 mm by 99 mm and is 20 mm thick. It is marked MC-20-2 for identification and is usually referred to as the Russian Opal Glass. The side which is measured has a very flat, highly polished surface.

Working Standard No. 2—This standard is a piece of Vitrolite glass which was manufactured by

Libbey Owens Ford
1701 E. Broadway
Toledo, Ohio 43605

The exact date of manufacture of this particular piece of glass is unknown, but it has been at least twenty years since any glass of this type has been manufactured. The piece used is

100 mm by 100 mm and is 11 mm thick. It is marked V6-D1 for identification. The side which is measured is flat and highly polished.

Working Standard No. 3—This standard is a porcelain enamel on steel plaque which was made around 1946 by

The Harshaw Chemical Co.
Division of Kewanee Oil Company
1933 E. 97th St.
Cleveland, Ohio 44106

The plaque used is 108 mm by 108 mm and is marked 80-1 for identification. The surface which is measured is smooth and non-porous, but it has a slight ripple or "orange peel" texture.

These three working standards cover the range of reflectance factor from nearly 1 to approximately 0.8, which is the range generally used for standards to calibrate the gain setting of reflectometers. In addition, the Vitrolite standard is slightly translucent. Recent tests have shown our instrument to be insensitive to this amount of translucence, but if this should change the difference will be noticeable in the measurements obtained using this standard as compared to the others. Because of the rippled surface in the porcelain enamel standard, the surface reflection from this standard is spread out more than that from the other two standards which have flat surfaces. Therefore, differences in the way the instrument handles specular reflection may show up in the relative measurements of this standard with respect to the others. (The most sensitive test of the way the instrument treats specular reflectance is made by measuring a specular mirror. We intend to use this procedure as soon as we have the capability to measure the reflectance of a mirror with the necessary accuracy.)

The cleaning procedure used is an important part of maintaining working standards of reflectance. Our present approach is to use a procedure which will disturb as little as possible the layers of oxides and other surface films characteristic of the materials. Therefore, we store the standards in dessicators and before each measurement we wash them with a mild nonfluorescing soap, rinse them thoroughly with hot water, rinse them with distilled water, and blot them dry with soft tissue paper. Any lint which remains on the surface is removed by gently brushing with a soft brush.

Reflection properties of pressed polytetrafluoroethylene powder

Victor R. Weidner and Jack J. Hsia

Radiometric Physics Division, National Bureau of Standards, Washington, D.C.

Received December 18, 1980; revised manuscript received February 12, 1981

The reflection properties of pressed polytetrafluoroethylene powder have been under investigation by the Radiometric Physics Division at the National Bureau of Standards for the past five years. This material has a great potential use, both as a standard of diffuse reflectance and as a coating for integrating spheres for applications in reflectance spectrophotometry and other signal-averaging devices. It possesses certain physical and optical properties that make it ideal for use in these applications. Techniques are given for preparing reflection standards and coating integrating spheres with the pressed powder. The effects of powder density and thickness on its reflectance are reported, and observations of possible problems with fluorescence that are due to the presence of contaminants in the powder are discussed. The absolute reflectance (6°/hemispherical reflectance factor relative to a perfect diffuser) is reported for the spectral range of 200–2500 nm. The directional/hemispherical reflectance factor relative to 6°/hemispherical reflectance is given for several wavelengths in the ultraviolet and visible spectrum and for angles of incidence between 5 and 75°. The bidirectional reflectance factor is reported for 300, 600, and 1500 nm at angles of incidence of −10, −30, −50, and −70° and at viewing angles at 10° intervals from −80 to +80°.

INTRODUCTION

The reflection properties of pressed polytetrafluoroethylene (PTFE) powder[1] in the ultraviolet, visible, and near-infrared spectral regions, combined with certain desirable physical characteristics, make this material exceptionally useful when there is a need for a good white diffuser or a standard of diffuse reflectance. The diffuse reflectance of pressed PTFE powder is remarkably high over the spectral range of 200–2500 nm and is probably higher than that of any other known material, its reflectance being 99% or higher over the spectral range of 350–1800 nm. It is particularly useful as a coating for integrating spheres commonly used in diffuse reflectance spectrophotometry. Historically, the most commonly used materials for this purpose have been magnesium oxide and barium sulfate powders or barium sulfate paint.[2] Much has been written on the optical properties of these materials, and the advantages and disadvantages of their use in spectrophotometric applications have been experienced by nearly everyone involved with reflectance spectrophotometry. Certainly, there is no longer any advantage in coating integrating spheres by the old method of burning magnesium and collecting the magnesium oxide smoke. The standards that still specify that reflectance measurements be reported on a photometric scale relative to smoked magnesium oxide should be rewritten to specify that reflectance measurements be reported on an absolute reflectance scale (relative to a perfect diffuser[3]). A review of publications on properties and reflection values of material reflection standards is given in Ref. 2.

The purpose of this paper is to make available the technical findings of several years of research on the optical properties of pressed PTFE powder. Other authors[4] have reported on the potential usefulness of this material as a reflection standard. The spectrophotometry group of the Radiometric Physics Division at the National Bureau of Standards (NBS) began studies of the reflection properties of pressed PTFE powder in 1975. At that time, this group was engaged in constructing a new reference spectrophotometer for diffuse reflectance[5] along with a number of accessory devices for measuring diffuse reflectance. These accessory devices include integrating spheres for measuring 6°/hemispherical reflectance factor, 45°/0° reflectance factor, and directional/hemispherical reflectance factor and a specular reflectometer.[6] At the same time, a more accurate absolute diffuse reflectance scale was being established by the auxiliary sphere or Van den Akker method.[7] A technique was developed for coating integrating spheres with the PTFE powder, and extensive measurements of the optical properties of this material were carried out over a five-year period. The results of these studies are reported here along with some descriptive details of the techniques used in preparing reflection standards from PTFE powder and its application to integrating spheres.

PREPARATION

The PTFE powder is somewhat lumpy as it comes in a shipping drum. It can be prepared for optical-coating purposes by reducing it to a uniform low-density powder. This can be accomplished with a blender or other chopping device, preferably one with stainless-steel blades and a glass container. The powder should be kept in glass containers and handled with tools made of materials such as stainless steel that are less likely to contaminate the material. The powder will adhere to itself on pressing, but it does not adhere well to metal, glass, or plastic. One technique for making it adhere to metal (or other materials) is first to coat the metal with a thin film of high-vacuum silicone grease. Once this is done, the powder can be pressed into place in thicknesses varying from 1 to 10 mm without much difficulty. The silicone grease has a low volatility and does not affect the reflection properties of the

Reprinted from **Journal of the Optical Society of America,**
Vol. *71*, page 856, July, 1981
Copyright © 1981 by the Optical Society of America and reprinted by permission of the copyright owner

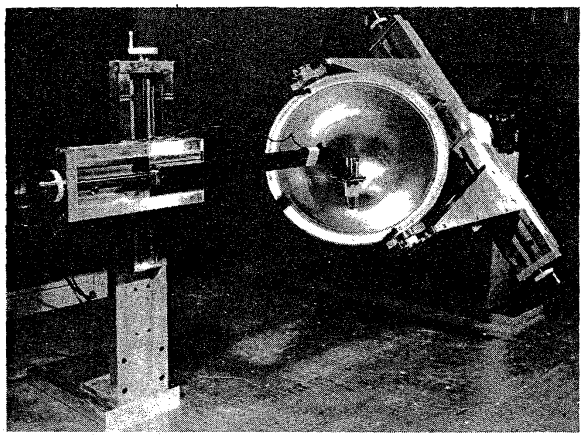

Fig. 1. The NBS integrating-sphere-coating apparatus showing the hemisphere manipulator with the electronically controlled tamping head used to press the PTFE powder into the hemisphere with a uniform radius.

PTFE powder because it contacts only a thin layer at the powder–metal interface.

PTFE powder has been successfully applied to integrating spheres ranging in diameter from a few centimeters to 45 cm and to large, flat surfaces used as reflection standards. The coatings are not affected by conditions of high humidity because the pressed powder repels water. Exposure to high-intensity ultraviolet radiation,[4] such as that encountered near a xenon arc, will slightly degrade the reflection properties of the coatings in the ultraviolet spectral region. The reflectance will be degraded as a result of contamination from smoke, dust, or other contaminants that may be present.

The time required for coating an integrating sphere of 20-cm diameter with a 6-mm-thick coating is typically about 4 h. This includes preparing the PTFE powder with a blender, trimming up the finished coating around the ports, and assembly of the usual two hemispheres. At NBS, spheres up to 45-cm diameter are coated with the aid of a special hemisphere manipulator (Fig. 1) that enables the technician to rotate and pivot the hemisphere about the center point of the sphere and pack the PTFE powder into the curvature of the hemisphere with a light pressure, using hand tools such as a stainless steel spoon or a round-bottom glass flask. In some special applications, such as in the preparation of an auxiliary sphere for determining the absolute reflectance of the sphere coating, the radius of curvature of the coating surface is carefully controlled by tamping the PTFE powder under an electronic tamping head before it is rolled to a final finish. A retainer ring is attached to the hemisphere flange during the coating procedure to retain the powder at the open edge of the hemisphere. When the coating is completed, this retaining ring is removed, and the two completed hemispheres are attached to each other by means of the flanges. The PTFE coating expands slightly at the hemisphere edge when the retaining ring is removed. This is an advantage because it results in the formation of a tight fit when the two hemispheres are combined to form the sphere.

As with any sphere-coating material, PTFE powder has its advantages and disadvantages. Some practice is required in order to master the coating techniques. The powder should be packed in lightly at first, to a depth of approximately 2–3 times the desired final thickness before it is pressed to a finish. The application of added powder to an already hard-pressed coating may result in a peeling and separation of the material into layers. The best results are obtained with a sand-blasted or ground-glass pressing tool, such as a round-bottom flask of small diameter. The coating should be done in a relatively clean, dust-free environment because the PTFE coating usually becomes electrostatically charged during the pressing and will hold small specks of dirt or lint. These can be picked up or removed with a small, clean artist's brush.

PTFE powder is very fine and easily mixes in the air about the working area. Although the powder is believed to be nontoxic, it is a good practice to use a dust mask to avoid unnecessary breathing of the material.

PTFE may form toxic gases at thermal decomposition temperatures above 400°C. These toxic products may be produced inadvertently by contact of the fine powder with a flame or other high-temperature source. For further information on the safe handling of fluorocarbon resins, refer to Ref. 8.

It should be noted that there are U.S. patents dealing with the use of fluorocarbons as coatings for integrating spheres. These U.S. patents are given in Ref. 9.

DENSITY

The reflectance of PTFE powder is influenced by the density to which the powder is pressed. This relationship is illustrated in Fig. 2, in which the results of a number of measurements of reflectance versus powder density are plotted. The reflectance scale in this illustration is a relative one with the data normalized at a density of 1.0 g/cm^3, because this is the density at which the powder reflectance is the highest. There seem to be no noticeable wavelength-related effects for wavelengths less than 2000 nm. The vertical bars in Fig. 2 show the spread in reflectance values at the 10 selected

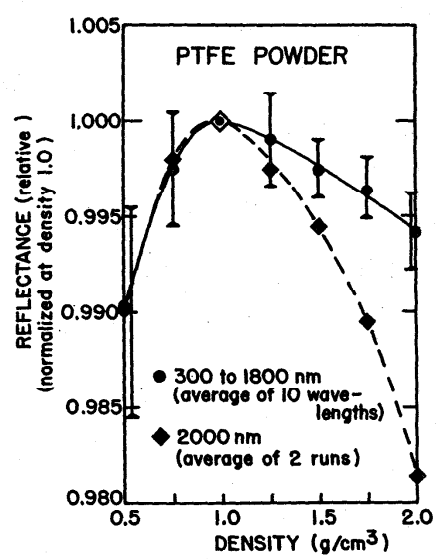

Fig. 2. Pressed PTFE powder reflectance as a function of powd density (10-mm thickness).

Table 1. Reflectance of Pressed PTFE Powder (0.8 g/cm³) Relative to That of a 10-mm-Thick Layer at Each Wavelength

Thickness (mm)	Relative Reflectance 400 nm	550 nm	700 nm
1	0.991	0.989	0.986
2	0.995	0.994	0.993
4	0.998	0.998	0.997
6	1.000	1.000	0.999
8	1.000	1.000	1.000
10	1.000	1.000	1.000

wavelengths. The maximum reflectance is obtained by compressing the powder to a density of from 0.8 to 1.2 g/cm³. The loose powder has a density of approximately 0.5 g/cm³. A sample of the pressed powder having the maximum reflectance can easily be prepared by compressing 2–2.5 volumes of loose powder into 1 volume. This results in a pressed sample that is rather soft. A sample compressed to a density of 2 g/cm³ will have a much harder surface and slightly lower reflectance. Higher densities require higher pressures, and a mechanical press must be used. As is shown in Fig. 2, the reflectance does not vary much with change in powder density for the density range of 0.8–1.2 g/cm³. Repeated preparation of pressed samples having reflectances that are the same to within a few tenths of a percent can easily be achieved, and a fresh sample can be prepared in minutes. At wavelengths greater than 2000 nm the reflectance drops more rapidly with increasing powder density.

THICKNESS

The diffuse reflectance of pressed PTFE powder is influenced by the thickness of the powder layer. Its translucency is such that at least a 6-mm thickness at a density of approximately 1 g/cm³ is required to obtain maximum reflectance. Table 1 shows the influence of thickness on the reflectance of PTFE powder at 400, 550, and 700 nm. These measurements were made with an aluminum backing having a reflectance of approximately 60%. Later measurements in the infrared out to 2500 nm indicate that 6- to 8-mm thicknesses and a density of 1 g/cm³ are adequate in order to achieve maximum diffuse reflectance values for the pressed powder. Coatings this thick are not required in applications where the coating is used in a signal-averaging sphere. However, when the PTFE powder is used as a reflection standard, a 10-mm thickness will be certain to give the maximum reflectance at all wavelengths.

FLUORESCENCE

There has been no clear evidence to show that the PTFE powder itself fluoresces. However, coatings made from PTFE powder show a very weak fluorescence. This fluorescence may be associated with a slight contamination from the plastic bag used to contain the PTFE powder in its shipping drum. As a test of the contribution of fluorescence to the reflectance of PTFE powder, a specimen was first measured on a double-beam reflectance spectrophotometer with the use of monochromatic illumination of the PTFE powder and then with polychromatic illumination. In Table 2 the normalized difference D between the reflectances obtained by these two modes of illumination is given as $D = (R_m - R_p)/R_p$, where R_m is proportional to the reflectance of the PTFE powder sample relative to that of an aluminum mirror with monochromatic irradiation and R_p is the same relative reflectance with polychromatic irradiation. There appeared to be a slight amount of fluorescence with excitation at wavelengths less than 290 nm and emission in the wavelength range of 310–350 nm. Subsequent measurements with a spectrofluorometer[10] confirmed these conclusions.

The levels of fluorescence observed may be negligible for most radiometric and spectrophotometric applications. However, in applications in which a small amount of fluorescence can cause a significant error, it would be wise not to use any kind of pressed-powder coating without first checking for the presence of fluorescence that is due to contaminants, especially when ultraviolet radiation below 300 nm is involved.[11]

REFLECTION PROPERTIES

The 6°/hemispherical reflectance factor of a diffuse reflectance standard is probably the most important calibration. The term 6°/hemispherical reflectance refers to a measurement geometry in which the sample is illuminated by a collimated source incident upon the sample at 6° from the normal

Table 2. Data from Fluorescence Check

Wavelength (nm)	D	Wavelength (nm)	D
250	0.019	500	0.000
260	0.016	510	−0.002
270	0.022	520	0.000
280	0.018	530	0.000
290	0.005	540	0.002
300	−0.004	550	0.000
310	−0.018	560	0.000
320	−0.011	570	0.000
330	−0.021	580	0.005
340	−0.015	590	0.001
350	−0.009	600	0.006
360	−0.007	610	0.004
370	−0.006	620	0.001
380	−0.003	630	0.001
390	−0.002	640	0.000
400	−0.006	650	−0.002
410	−0.002	660	0.000
420	−0.002	670	−0.002
430	0.002	680	−0.002
440	0.002	690	−0.006
450	0.000	700	−0.003
460	0.002	710	−0.004
470	−0.002	720	−0.003
480	0.002	730	0.002
490	0.002	740	−0.008
		750	−0.007

Table 3. 6°/Hemispherical Reflectance Factor of a 10-mm-Thick Pressed PTFE Powder Relative to a Perfect Diffuser

λ (nm)	ρ	λ (nm)	ρ	λ (nm)	ρ
200	0.962[a]	950	0.994	2140	0.964
210	0.964[a]	1000	0.994	2150	0.965
220	0.967	1050	0.994	2160	0.967
225	0.968	1100	0.994	2170	0.970
230	0.969	1150	0.994	2180	0.973
240	0.971	1200	0.993	2190	0.975
250	0.973	1250	0.993	2200	0.977
260	0.976	1300	0.992	2210	0.977
270	0.978	1350	0.991	2220	0.978
275	0.979	1400	0.991	2230	0.978
280	0.980	1450	0.992	2240	0.977
290	0.982	1500	0.992	2250	0.977
300	0.984	1550	0.992	2260	0.976
310	0.985	1600	0.992	2270	0.976
320	0.987	1650	0.991	2280	0.975
325	0.988	1700	0.990	2290	0.974
330	0.988	1750	0.990	2300	0.972
340	0.989	1800	0.990	2310	0.971
350	0.990	1850	0.986	2320	0.970
360	0.990	1900	0.985	2330	0.968
370	0.991	1950	0.984	2340	0.966
375	0.991	2000	0.981	2350	0.965
380	0.991	2010	0.979	2360	0.964
390	0.992	2020	0.978	2370	0.963
400	0.993	2030	0.976	2380	0.963
450	0.993	2040	0.975	2390	0.962
500	0.994	2050	0.973	2400	0.962
550	0.994	2060	0.972	2450	0.961
600	0.994	2070	0.971	2500	0.960
650	0.994	2080	0.970		
700	0.994	2090	0.969		
750	0.994	2100	0.968		
800	0.994	2110	0.967		
850	0.994	2120	0.966		
900	0.994	2130	0.964		

[a] Extrapolated.

and in which the reflected flux is averaged by an integrating sphere-detector system. An angle of 6° off the normal is commonly used to allow for including the specular component in the measurement.

The 6°/hemispherical reflectance factor of samples of PTFE powder pressed to a thickness of 6 mm or more with a density of 0.8–1.2 g/cm^3 is very reproducible. For a set of samples made at different times from different lots of PTFE powder, a standard deviation of less than 0.001 in measured reflectance was found for the wavelength range of 400–750 nm. Further measurements will have to be made in order to establish what this deviation will be in the ultraviolet and infrared regions. The 6°/hemispherical reflectance factor of pressed PTFE powder is given in Table 3 for a PTFE coating 10 mm in thickness and having a density in the range of 0.8–1.2 g/cm^3. The data listed in Table 3 are plotted in Fig. 3. These data are reported on an absolute reflectance scale (relative to a perfect diffuser) and were obtained by the auxiliary sphere

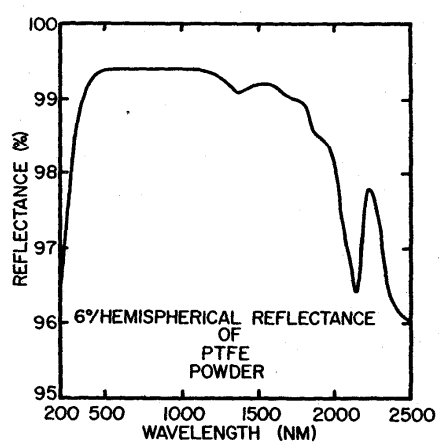

Fig. 3. The 6°/hemispherical reflectance factor (relative to a perfect diffuser) of 10-mm-thick, 1-g/cm^3-density pressed PTFE powder.

Table 4. Directional/Hemispherical Reflectance Factor of Pressed PTFE Powder for a 10-mm-Thick Coating (Relative to Hemispherical Reflectance at 6° Incidence)

Angle of Incidence	Reflectance					
	250 nm	300 nm	350 nm	450 nm	600 nm	750 nm
6°	1.0000	1.0000	1.0000	1.0000	1.0000	1.0000
10°	1.0003	1.0002	1.0001	1.0001	1.0001	1.0001
15°	1.0009	1.0005	1.0004	1.0002	1.0002	1.0002
20°	1.0017	1.0010	1.0007	1.0004	1.0004	1.0004
25°	1.0026	1.0015	1.0011	1.0007	1.0006	1.0006
30°	1.0038	1.0022	1.0015	1.0010	1.0008	1.0008
35°	1.0052	1.0030	1.0021	1.0013	1.0011	1.0011
40°	1.0066	1.0038	1.0026	1.0016	1.0014	1.0014
45°	1.0082	1.0047	1.0032	1.0020	1.0017	1.0017
50°	1.0099	1.0056	1.0038	1.0023	1.0020	1.0020
55°	1.0117	1.0065	1.0044	1.0026	1.0023	1.0023
60°	1.0134	1.0074	1.0049	1.0029	1.0025	1.0025
65°	1.0153	1.0083	1.0054	1.0031	1.0027	1.0027
70°	1.0170	1.0090	1.0058	1.0032	1.0028	1.0029
75°	1.0186	1.0097	1.0061	1.0032	1.0029	1.0029

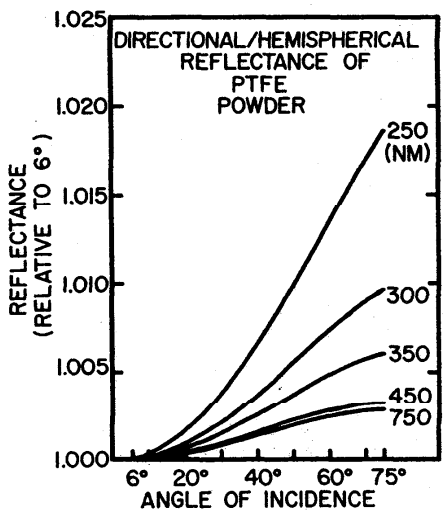

Fig. 4. The directional/hemispherical reflectance factor of pressed PTFE powder as a function of angle of incidence and wavelength.

method.[7] These absolute reflectance data are believed to be accurate to within ±0.002 on the basis of the analysis of the known sources of error as discussed in Ref. 7.

The directional/hemispherical reflectance factor of pressed PTFE powder given in Table 4 shows how the hemispherical reflectance of the material varies as a function of the angle of incidence. These measurements were made by means of an integrating sphere accessory to the NBS reference spectrophotometer for diffuse reflectance. This accessory consisted of a 45-cm-diameter sphere designed so that the sample can be mounted in the center of the sphere where it can be rotated to control the angle of incidence. The measurements were made at several wavelengths in the ultraviolet and visible spectra for both vertically and horizontally polarized sample beams. The results listed in Table 4 and illustrated in Fig. 4 are an average of the two polarizations. The values for either polarization did not vary by more than ±0.5% from the average. The most noticeable changes in reflectance as a function of angle of incidence occur in the ultraviolet spectral region. The data are relative to the 6°/hemispherical reflectance factor values.

The bidirectional reflectance factor of pressed PTFE powder listed in Table 5 shows how the reflectance varies over a wide range of viewing angles for four different angles of incidence. These measurements were made by means of the NBS specular reflectometer.[6] This instrument is ordinarily used for specular reflectance measurements as a function of angle of incidence. It can be used to measure the bidirectional reflectance of a diffuse sample in the plane of the incident sample beam. Measurements were made at 300, 600, and 1500 nm for angles of incidence of −10, −30, −50, and −70°. The angles of viewing were selected at 10° intervals from −80 to +80°. The bidirectional reflectance data reported in Table 5 are an average of the vertical and horizontal polarizations. The values for either polarization varied from this average by as little as ±0.2% to as much as ±20% depending on the combination of beam incidence and viewing angle. These data are relative to the reflectance values obtained at 0° (normal) viewing. The results listed in Table 5 are representative of the bidirectional reflectance of a "rough" surface prepared by pressing the PTFE powder with a coarsely ground glass plate. Samples pressed with a polished glass plate exhibit slightly higher values of reflectance, particularly at viewing angles greater than 75°. Figure 5 illustrates the bidirectional reflectance properties of pressed PTFE powder at 600 nm. Similar results are shown for barium sulfate powder in Fig. 6.

Further studies of the reflection properties of pressed PTFE powder are being made at NBS. Among these properties are the 45°/0° or 0°/45° reflectance factors for the visible spectral region. The results of these studies will be published at a future date.

Table 5. Directional/Directional Reflectance Factor (Bidirectional Reflectance) of 10-mm-Thick Pressed PTFE Powder

Angle of Viewing	Angle of Incidence											
	300 nm				600 nm				1500 nm			
	−10°	−30°	−50°	−70°	−10°	−30°	−50°	−70°	−10° gnhr	−30°	−50°	−70°
−80°	0.763	0.792	0.872	1.148	0.743	0.761	0.827	1.048	0.702	0.830	0.820	1.045
−70°	0.836	0.867	0.937	–	0.822	0.840	0.898	–	0.760	0.882	0.855	–
−60°	0.882	0.914	0.980	1.074	0.872	0.891	0.946	1.019	0.819	0.918	0.886	1.000
−50°	0.919	0.949	–	1.022	0.909	0.931	–	0.987	0.875	0.952	–	0.992
−40°	0.946	0.979	1.000	0.996	0.939	0.967	0.982	0.974	0.920	0.974	0.936	0.980
−30°	0.967	–	0.993	0.982	0.963	–	0.980	0.971	0.959	–	0.945	0.980
−20°	0.988	1.005	0.991	0.981	0.986	0.998	0.984	0.974	0.978	0.980	0.966	0.985
−10°	–	1.000	0.994	0.988	–	0.998	0.991	0.983	–	0.990	0.982	0.995
0°	1.000	1.000	1.000	1.000	1.000	1.000	1.000	1.000	1.000	1.000	1.000	1.000
10°	0.991	1.001	1.008	1.021	0.991	1.002	1.012	1.027	0.998	1.005	1.010	1.010
20°	0.982	1.001	1.022	1.052	0.983	1.003	1.027	1.067	0.986	1.012	1.018	1.060
30°	0.970	0.999	1.036	1.098	0.971	1.004	1.048	1.125	0.971	1.015	1.040	1.155
40°	0.960	0.997	1.056	1.163	0.957	1.004	1.076	1.212	0.942	1.018	1.066	1.270
50°	0.943	0.996	1.085	1.265	0.938	1.002	1.114	1.343	0.895	1.022	1.100	1.440
60°	0.921	0.992	1.125	1.426	0.914	1.000	1.168	1.549	0.832	1.030	1.155	1.695
70°	0.882	0.974	1.167	1.691	0.872	0.985	1.227	1.897	0.754	1.035	1.235	2.075
80°	0.817	0.937	1.214	2.190	0.802	0.946	1.291	2.551	0.660	1.040	1.340	3.090

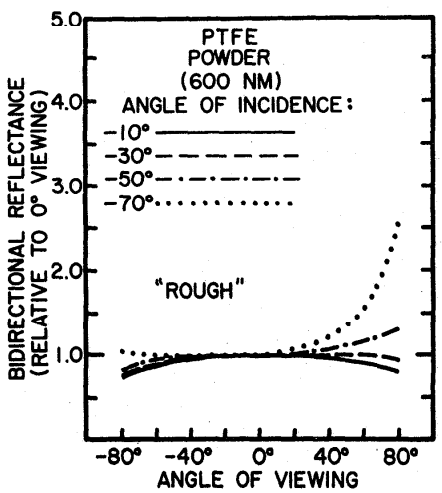

Fig. 5. The bidirectional reflectance factor at 600 nm of pressed PTFE powder having a rough surface finish.

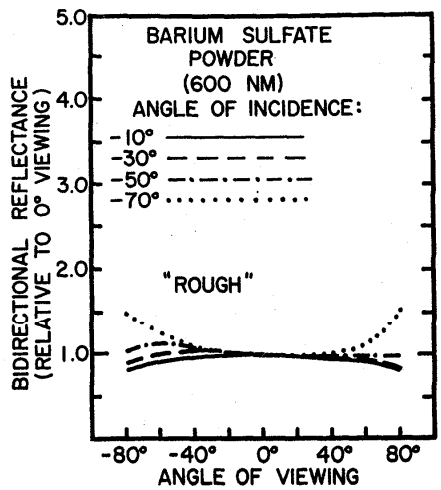

Fig. 6. The bidirectional reflectance factor at 600 nm of pressed barium sulfate powder having a rough surface finish.

REFERENCES

1. The polytetrafluoroethylene powder used in these investigations is manufactured by Allied Chemical Company. The material is commonly referred to by the trade name Halon and is further identified as type G-80 tetrafluoroethylene resin. The commercial name of this material is given here for purposes of identification only and in no way implies endorsement by the National Bureau of Standards.
2. Bureau Central de la Commission Internationale de l'Eclairage, *Review of Publications on Properties and Reflection Values of Material Reflection Standards* (Paris, 1979), CIE Publication 46 (TC-2.3), pp. 15–72.
3. The term "perfect diffuser" is defined in Bureau Central de la Commission Internationale de l'Eclairage, *International Lighting Vocabulary* (Paris, 1970), CIE Publication 17 (E-1.1), p. 95.
4. F. Grum and M. Saltzman, *P-75-77 New White Standard of Reflectance* (Paris, 1976), CIE Publication 36, 91.
5. W. H. Venable, J. J. Hsia, and V. R. Weidner, "Development of an NBS reference spectrophotometer for diffuse reflectance and transmittance," Nat. Bur. Stand. U.S. Tech. Note **594-11**, 47 pp. (1976).
6. V. R. Weidner and J. J. Hsia, "NBS specular reflectometer-spectrophotometer," Appl. Opt. **19**, 1268–1273 (1980).
7. W. H. Venable, J. J. Hsia, and V. R. Weidner, "Establishing a scale of directional-hemispherical reflectance factor I: the Van den Akker method," J. Res. Nat. Bur. Stand. **82**, 29–55, (1977).
8. E. I. Du Pont de Nemours and Company, Inc., Fluorocarbons Division, *Teflon Fluorocarbon Resins—Safety in Handling and Use* (Wilmington, Del., 1970), pp. 1–10. This publication references technical papers dealing with the thermal decomposition of fluorocarbons and associated safety problems.
9. The following U.S. patents are assigned to J. A. Seiner of PPG Industries, Inc., Pittsburgh, Pa.: U.S. Patent No. 3,956,201, May 11, 1976, and U.S. Patent No. 3,764,364, October 9, 1973.
10. From uncorrected emission spectra supplied by K. Mielenz and R. Velapoldi using the reference spectrofluorimeter in the NBS Center for Analytical Chemistry.
11. R. D. Saunders and W. R. Ott, "Spectral irradiance measurements: effect of UV produced fluorescence in integrating spheres," Appl. Opt. **15**, 827–828 (1976).

Appendix H

Reprinted from Applied Optics, Vol. 24, page 2225, July 15, 1985
Copyright © 1985 by the Optical Society of America and reprinted by permission of the copyright owner.

Laboratory intercomparison study of pressed polytetrafluoroethylene powder reflectance standards

V. R. Weidner, J. J. Hsia, and B. Adams

The object of this paper is to present results of several experiments relating to the preparation and use of pressed polytetrafluoroethylene (PTFE) powder as a diffuse reflectance standard for the 200–2500-nm spectral range. These experiments include two round-robin intercomparisons involving nine laboratories. These round-robin experiments provided data on the variability of the reflectance of pressed PTFE reflectance standards prepared in different laboratories. Results of these measurements provided insight into the problems associated with the PTFE standards and helped to establish what practices needed to be standardized to improve interlaboratory agreement for diffuse reflectance measurements.

I. Introduction

The object of this paper is to present the results of several experiments relating to preparation and use of pressed polytetrafluoroethylene (PTFE) powder as a diffuse reflectance standard for the 200–2500-nm spectral range. The usefulness of this material as a reflectance standard was first reported by Grum and Saltzman.[1] Further investigations into the reflection properties of pressed PTFE powder were reported by the authors.[2] As a result of the growing need for improved diffuse reflectance standards for the UV, visible, and near IR, and the interest shown in this material, the Inter Society Color Council (ISCC, Subcommittee 22) has suggested that a laboratory intercomparison be conducted to study the methods of preparation and uniformity of reflectance of pressed PTFE powder. In addition to these round-robin experiments, the results of some closely related PTFE investigations at the National Bureau of Standards (NBS) are also included.

II. Round-Robin Intercomparisons

Two round-robin experiments were conducted in spring 1984. The first experiment yielded results that established a need for further control over the experiment. Therefore, a second round robin was initiated. The design of the two experiments and the resulting data provided some insight into the problems associated with the use of PTFE reflectance standards and also helped to establish what practices needed to be standardized to improve the interlaboratory agreement for reflectance measurements.

A. Round-Robin Experiment 1

Six laboratories participated in this experiment. A quantity of PTFE powder sufficient to prepare two pressed plaques was sent to each laboratory. The PTFE powder was provided by NBS. It was mixed thoroughly by means of a glass blender and shipped in sealed glass jars. NBS also provided 50-mm diam by 10-mm depth holders with covers for the participating laboratories to use in preparation of the pressed PTFE specimens. The instructions requested that the laboratories weigh the powder holders before and after pressing the powder to be used in the pressing because the object was to determine what variations in reflectance would result if this part of the experiment were uncontrolled.

The participating laboratories were accustomed to using commercial powder presses and encountered some difficulty in using the holders provided by NBS. Because of this, some laboratories submitted additional pressed specimens in their own holders. As a result, more specimens were returned to NBS for analysis than had originally been planned on. However, this turned out to be useful because it provided a larger sampling for comparison.

Measurements of the spectral reflectance of the returned PTFE specimens were made at NBS and are reported in Table I. A white ceramic tile of known spectral reflectance was used to compare the PTFE specimens and place the measurements on an absolute scale for the 400–2500-nm wavelength range. For the

The authors are with U.S. National Bureau of Standards, Radiometric Physics Division, Gaithersburg, Maryland 20899.
Received 18 January 1985.

Table I. Round-Robin 1; Spectral Reflectance of Pressed PTFE Powder

Wavelength (nm)	Laboratory 1	1	2	2	2	2	2	3	3
250	0.973	0.973	0.931	0.935	0.962	0.967	0.922	0.983	0.984
300	0.984	0.984	0.963	0.963	0.974	0.975	0.956	0.988	0.988
350	0.990	0.990	0.984	0.984	0.983	0.983	0.977	0.992	0.992
400	0.993	0.993	0.991	0.991	0.985	0.986	0.984	0.993	0.993
500	0.992	0.992	0.992	0.991	0.988	0.987	0.989	0.993	0.993
600	0.993	0.993	0.993	0.993	0.990	0.990	0.992	0.994	0.994
700	0.993	0.993	0.993	0.993	0.987	0.988	0.991	0.993	0.993
800	0.993	0.993	0.993	0.993	0.988	0.988	0.992	0.993	0.993
1000	0.992	0.992	0.992	0.992	0.986	0.987	0.991	0.993	0.993
1200	0.989	0.989	0.989	0.989	0.983	0.984	0.988	0.991	0.991
1500	0.987	0.987	0.987	0.987	0.979	0.983	0.987	0.987	0.987
2000	0.978	0.978	0.978	0.978	0.960	0.962	0.976	0.979	0.980
2100	0.962	0.963	0.962	0.962	0.933	0.935	0.960	0.964	0.965
2200	0.967	0.967	0.965	0.966	0.946	0.948	0.963	0.967	0.967
2300	0.965	0.966	0.965	0.964	0.940	0.943	0.963	0.966	0.968
2400	0.960	0.960	0.959	0.959	0.923	0.926	0.956	0.961	0.960
2500	0.960	0.960	0.960	0.960	0.922	0.924	0.958	0.960	0.960
Density (g/cm^3)	(1.05)	(0.94)	(1.16)	(1.15)	(1.65)	(1.64)	(1.04)	(0.87)	(0.81)

Wavelength (nm)	Laboratory 3	3	4	4	5	5	6	Average of 16	Standard dev.
250	0.978	0.977	0.947	0.955	0.960	0.960	0.983	0.9619	0.0195
300	0.984	0.984	0.964	0.976	0.968	0.967	0.987	0.9753	0.0106
350	0.990	0.990	0.976	0.982	0.977	0.976	0.990	0.9847	0.0059
400	0.990	0.990	0.978	0.983	0.982	0.978	0.993	0.9877	0.0054
500	0.992	0.992	0.978	0.983	0.983	0.980	0.992	0.9886	0.0049
600	0.992	0.992	0.981	0.986	0.983	0.981	0.993	0.9900	0.0046
700	0.992	0.992	0.976	0.983	0.980	0.977	0.993	0.9886	0.0061
800	0.992	0.992	0.975	0.982	0.977	0.975	0.990	0.9881	0.0068
1000	0.990	0.990	0.974	0.981	0.974	0.971	0.988	0.9866	0.0075
1200	0.987	0.987	0.972	0.980	0.967	0.964	0.988	0.9836	0.0085
1500	0.985	0.985	0.966	0.976	0.957	0.954	0.986	0.9800	0.0111
2000	0.976	0.976	0.934	0.962	0.905	0.900	0.977	0.9824	0.0262
2100	0.960	0.960	0.893	0.937	0.845	0.832	0.962	0.9372	0.0430
2200	0.964	0.965	0.913	0.945	0.879	0.873	0.965	0.9475	0.0313
2300	0.964	0.964	0.903	0.945	0.860	0.848	0.964	0.9430	0.0386
2400	0.958	0.958	0.872	0.928	0.814	0.796	0.956	0.9279	0.0536
2500	0.957	0.957	0.862	0.923	0.795	0.781	0.948	0.9242	0.0592
Density (g/cm^2)	(1.18)	(1.23)	(1.77)	(1.67)	(2.05)	2.10	(1.15)	—	—

measurements at wavelengths of <400 nm the data were adjusted to an absolute scale by comparison of the specimens to a freshly prepared PTFE specimen. The absolute reflectance of this specimen was assumed to be that of the published data for the 6°/hemispherical reflectance of pressed PTFE powder (see Ref. 2). The average reflectance of the sixteen specimens and the standard deviations are listed in the last two columns of Table I. The approximate densities of the specimens are listed at the bottom of the table.

The densities of the pressed PTFE specimens listed in Table I varied from ~0.8 to 2 g/cm^3. The data indicate that the reflectances are less for the higher density specimens. Two specimens submitted by laboratories 2, 4, and 5 have densities that exceed 1.5 g/cm^3. At these higher densities the reflectance decreases at longer wavelengths in the 2000–2500-nm range. Similar effects have been reported for other compacted powders.[3] These specimens also have slightly lower reflectances at shorter wavelengths.

There are some larger variations in specimen reflectances at wavelengths <300 nm in the UV. These differences do not correlate with variations in specimen densities. This is a wavelength range in which the specimen reflectance may be easily altered by contamination. Since all the PTFE powder originated from the same source, it is assumed that these variations in the UV reflectance are the result of some change in the sample purity that took place during the round robin.

The variation in reflectance for the visible spectral range, shown in Table I, is small for all the specimens having densities of <1.5 g/cm^3. Because the PTFE reflectance is so reproducible in the visible spectrum, it is clear that the material can be used as a diffuse reflectance standard in this range. To improve the reproducibility of spectral reflectance measurements for pressed PTFE powder in the UV and near IR, the density of the pressed specimens must be controlled, and care must be taken to maintain material purity.

Table II. Round Robin 2; Spectral Reflectance of Presssed PTFE Powder

Wavelength (nm)	Laboratory 1	1	2	2	2	3	3	4	5	5
200	0.959	0.963	0.948	0.946	0.947	0.959	0.960	0.888	0.963	0.961
250	0.972	0.974	0.966	0.967	0.968	0.972	0.972	0.923	0.969	0.967
300	0.984	0.984	0.982	0.976	0.977	0.984	0.984	0.962	0.983	0.982
350	0.989	0.990	0.988	0.989	0.990	0.989	0.991	0.983	0.989	0.988
400	0.992	0.992	0.992	0.992	0.993	0.991	0.993	0.987	0.991	0.990
500	0.993	0.993	0.993	0.993	0.993	0.993	0.993	0.987	0.992	0.991
600	0.993	0.993	0.993	0.993	0.993	0.991	0.993	0.986	0.991	0.991
700	0.993	0.993	0.993	0.993	0.993	0.991	0.992	0.986	0.991	0.991
800	0.993	0.993	0.993	0.993	0.993	0.991	0.993	0.985	0.991	0.990
1000	0.994	0.993	0.993	0.993	0.993	0.990	0.991	0.986	0.991	0.988
1500	0.992	0.991	0.991	0.991	0.991	0.989	0.989	0.983	0.987	0.986
2000	0.981	0.981	0.981	0.980	0.980	0.980	0.979	0.974	0.978	0.975
2100	0.970	0.965	0.970	0.967	0.971	0.969	0.969	0.963	0.967	0.963
2200	0.976	0.973	0.981	0.976	0.982	0.974	0.977	0.968	0.971	0.976
2300	0.970	0.973	0.971	0.967	0.970	0.967	0.967	0.961	0.967	0.968
2400	0.968	0.962	0.962	0.964	0.964	0.962	0.960	0.953	0.952	0.951
2500	0.964	0.960	0.960	0.960	0.960	0.962	0.961	0.946	0.954	0.955
Density (g/cm^3)	(0.905)	(0.990)	(0.835)	(0.920)	(0.800)	(1.025)	(1.025)	(0.920)	(1.085)	(1.08)

Wavelength (mm)	Laboratory 6	7	7	8	8	9	9	Average of 17	Standard Dev.
200	0.898	0.823	0.905	0.905	0.911	0.954	0.949	0.9317	0.0382
250	0.968	0.920	0.950	0.921	0.929	0.971	0.970	0.9576	0.0204
300	0.985	0.968	0.975	0.977	0.979	0.983	0.982	0.9792	0.0063
350	0.990	0.984	0.986	0.988	0.989	0.989	0.989	0.9883	0.0021
400	0.993	0.988	0.988	0.991	0.992	0.992	0.992	0.9911	0.0018
500	0.993	0.988	0.989	0.992	0.993	0.993	0.993	0.9919	0.0020
600	0.993	0.987	0.988	0.992	0.993	0.993	0.993	0.9915	0.0023
700	0.992	0.987	0.988	0.992	0.993	0.993	0.993	0.9914	0.0023
800	0.992	0.987	0.988	0.991	0.993	0.992	0.993	0.9912	0.0024
1000	0.992	0.987	0.988	0.991	0.991	0.991	0.993	0.9910	0.0024
1500	0.989	0.985	0.984	0.988	0.988	0.990	0.990	0.9885	0.0027
2000	0.980	0.976	0.975	0.979	0.980	0.979	0.980	0.9787	0.0023
2100	0.965	0.962	0.962	0.972	0.973	0.972	0.971	0.9677	0.0038
2200	0.979	0.961	0.971	0.974	0.979	0.980	0.982	0.9753	0.0055
2300	0.965	0.967	0.974	0.965	0.972	0.967	0.968	0.9682	0.0032
2400	0.966	0.957	0.956	0.964	0.965	0.957	0.952	0.9597	0.0055
2500	0.959	0.948	0.953	0.957	0.962	0.961	0.962	0.9579	0.0051
Density (g/cm^3)	(0.900)	(0.845)	(0.830)	(0.900)	(0.890)	(0.900)	(0.895)	—	—

B. Round-Robin Experiment 2.

It was decided at the ISCC meeting in Apr. 1984 that a second round-robin experiment should be undertaken and that each participant would try to submit pressed PTFE specimens of 0.9 ± 0.05-g/cm^3 density in their own holders. All the participants received a new supply of PTFE powder from NBS. The six laboratories that participated in the first round robin also took part in the second, and three more laboratories joined in the experiment.

The returned specimens were measured relative to a freshly prepared PTFE specimen. The data were then adjusted to an absolute reflectance scale based on the 6°/hemispherical reflectance of PTFE previously published.[2] It was necessary to place all the measurements on an equal scale for comparison. The white ceramic tile used in round robin 1 to establish the absolute scale was not used since the same scale could be established with a fresh PTFE specimen. The freshly prepared PTFE specimen served to accomplish that purpose. Results of the spectral analysis of the pressed PTFE specimens for round-robin experiment 2 are shown in Table II.

The PTFE specimens ranged in density from ~0.80 to 1.08 g/cm^3 for the second round robin indicating that the density can be controlled at or near 0.9 ± 0.1 g/cm^3. This is a small spread in density, considering that most of the powder presses used to prepare these specimens are not well designed for controlling the density of the finished specimen.

Controlling the density of the specimens resulted in a smaller spread in the reflectance values than those reported in the first round robin. This is especially true for reflectance values in the wavelength range between 2000 and 2500 nm. The reflectance data at 250 nm show less variation than reported in the first round robin. However, the variation in the UV is still large and cannot be reduced by controlling the PTFE density.

Some of the variation in reflectance for the PTFE specimens listed in Tables I and II can be attributed to random noise. At wavelengths below 250 nm the noise level is approximately ±0.003. In the near-IR range of 2000 to 2500 nm, the noise is as high as ±0.010.

The data submitted by laboratories 4 and 7 for the second round robin show lower reflectances by ~0.5% than the other specimens. The reason for this is not clear. However, these specimen holders have a 0.2-mm raised metal ridge that causes a gap between the surface of the PTFE and the plane of the sample port of the reflectometer integrating sphere. This condition may contribute toward this observed lowering of the measured reflectance of the three PTFE specimens. However, 0.5% is a larger difference than would be expected for an 0.2-mm gap. Data will be presented in a later part of this paper that show how the reflectance of PTFE appears to decrease as the gap between the measured surface and port increases.

C. Conclusion of the Round-Robin Experiments

The round-robin experiments emphasize the need for some degree of standardization in the techniques used to prepare reflectance standards from PTFE powder. They also indicate that this material can be a useful and convenient diffuse reflectance standard if these techniques are followed.

NBS has found through experiment that pressed PTFE powder of ~1 g/cm^3 produces a reflectance standard with reflectance values that are reproducible to ±0.01 in the 200–300-nm wavelength range, ±0.005 for the 300–2000-nm wavelength range, and ±0.01 for the 2000–2500-nm wavelength range. Larger variations in the reflectance are possible, however, if the material is contaminated or if the specimen holders are not filled so that the measured surface is in contact with the plane of the sample port of the reflectometer. The data from these round-robin experiments confirm these findings.

III. Additional Experiments Relating the PTFE Reflectance

A. Influence of Specimen Positioning at the Reflectometer Sample Port

The influence of specimen positioning at the reflectometer sample port is demonstrated by the experimental results shown in Fig. 1. The data show how the diffuse reflectance of a specimen of pressed PTFE powder is influenced by controlling the spacing between the specimen plane and the plane of the sample port. The data are shown for measurements at 300, 550, and 1800 nm. Measurements with no spacing between the specimen and sample port are set equal to 100%, and measurements at increasing distance between the specimen and port are plotted relative to the zero spacing data. The sample beam illuminated an area of ~1-cm diameter in the center of a port of 2.3-cm diameter. The results plotted in Fig. 1 show that the effects are about the same at different wavelengths. The measured reflectance is ~1% lower if the spacing were

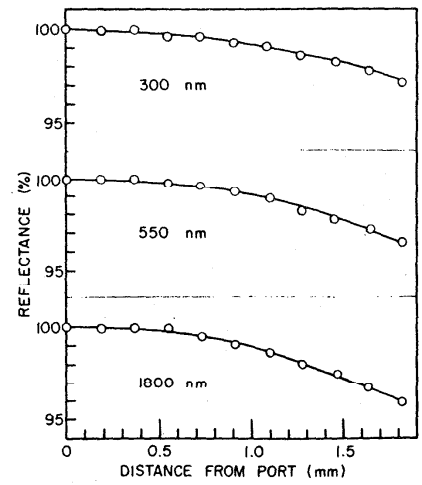

Figure 1. Measured diffuse reflectance of a pressed PTFE powder specimen is influenced by varying the spacing between the plane of the specimen and the plane of the integrating sphere port. The effect is shown for measurements at 300, 550, and 1800 nm.

1 mm. A spacing of 0.1 or 0.2 mm seems to have little effect on measured reflectance. However, an error of 0.5% could be introduced by a spacing as small as 0.7 mm. The results may vary for different instruments because the effect can be influenced by the ratio of the beam diameter to the port diameter and thickness of the port rim. One problem when the PTFE specimen is in contact with the sample port is of course that of damaging the standard. This occurs if the standard slips across the port during mounting and can only be avoided by allowing a small spacing between the specimen and port. The other solution is to prepare fresh samples when required and always allowing contact between the specimen and port.

B. Comparison of PTFE from Two Manufacturers

A comparison of the diffuse reflectance of pressed PTFE powder from two manufacturers was made to see if significant differences existed between them. The relative differences in the spectral reflectance of the two types of PTFE are shown in Table III. The differences reported are not significant since they fall within the random uncertainties associated with sample preparation and measurement.

C. Reproducibility of the Absolute Reflectance of Pressed PTFE Powder using the Double-Sphere Method

The best values of spectral reflectance of pressed PTFE powder as determined at NBS are reported in Ref. 2. The values are reported for the 6°/hemispherical reflectance factor (relative to a perfect diffuser). The reproducibility of the reflectance values for pressed PTFE powder as determined by the double-sphere technique was tested by repeating the experiment three times and computing the standard deviation for the three trials. Details of the double-sphere technique are reported in Refs. 2, 4, and 5. The standard deviations for three trial runs using this technique are reported in

Table III. Differences in Spectral Reflectance of PTFE Obtained from Manufacturers A and B

Wavelength (nm)	Reflectance differences	Measurement uncertainty
300	+0.004	±0.005
400	+0.003	±0.005
500	+0.002	±0.005
600	+0.002	±0.005
700	+0.001	±0.005
800	+0.001	±0.005
900	+0.001	±0.005
1000	0.000	±0.005
1100	0.000	±0.005
1200	+0.001	±0.005
1300	−0.002	±0.005
1400	+0.001	±0.005
1500	−0.002	±0.005
1600	−0.001	±0.005
1700	−0.001	±0.005
1800	−0.002	±0.005
1900	0.000	±0.005
2000	−0.003	±0.005
2100	−0.002	0.010
2200	−0.001	0.010
2300	−0.012	0.010
2400	−0.003	0.010
2500	−0.002	0.010

Table IV. Standard Deviation for Three Independent Determinations of the 6°/Hemispherical Reflectance Factor of Pressed PTFE Powder by the Double-Sphere Technique for Measuring Absolute Reflectance

Wavelength (nm)	Standard deviation of three determinations
200	0.0014
210	0.0014
220	0.0012
230	0.0008
240	0.0008
250	0.0011
300	0.0007
350	0.0003
400	0.0002
500	0.0003
600	0.0004
700	0.0005
800	0.0006
900	0.0006
1000	0.0006
1100	0.0006
1200	0.0006
1300	0.0006
1400	0.0008
1500	0.0007
1600	0.0007
1700	0.0008
1800	0.0007
1900	0.0006
2000	0.0004
2100	0.0005
2200	0.0005
2300	0.0007
2400	0.0007
2500	0.0006

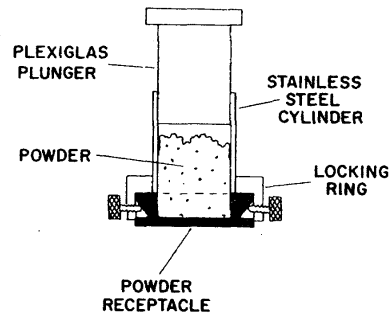

Fig. 2. Powder press is designed to provide a means for controlling the density of pressed PTFE diffuse reflectance standards. The preferred density is 1 g/cm^3.

Table IV. Each of the three trials represents independent determinations in which the auxiliary sphere was recoated with the pressed PTFE powder for each determination. The PTFE powder for two of the trial runs came from a drum of the powder that was the source of supply for the round-robin experiments described earlier. A third trial run was made with PTFE powder from a newer drum that had never been opened before. The resulting data indicated no differences in reflectance for the PTFE powder from these two drums.

IV. Recommended Procedures for Preparing and Using Pressed PTFE Powder as a Reflectance Standard

It is suggested that the following procedures and precautions be followed to improve the reproducibility of diffuse reflectance measurements and increase agreement among laboratories using pressed PTFE powder as a reflectance standard:

(1) Store the powder in sealed glass containers.

(2) Prepare the powder for use by pulverizing it into a uniform consistency in a glass blender with stainless steel blades.

(3) Use stainless steel spoons to transfer the powder.

(4) Press the powder into holders that have a depth of 10 mm.

(5) Press the powder to a density of $\sim 1 \pm 0.1$ g/cm^3. A 1-g/cm^3 density results in a firmer and less fragile specimen than lower densities. This can be done very conveniently with a powder press of the design shown in Fig. 2. This press is designed with a metal cavity of 10-mm depth. The diameter of this cavity will depend on the diameter of the sample port of the reflectometer integrating sphere. It should be made slightly larger than the diameter of the port. A stainless steel cylinder of the same inside diameter as the PTFE cavity is press fitted into a locking ring that can be locked onto this cavity with three thumbscrews. The PTFE powder is introduced into the stainless steel cylinder after it is locked onto the receiving cavity. To obtain a pressed PTFE reflectance standard of 1 g/cm^3, the volume of the receiving cavity must be determined in cubic centimeters. The pressing operation is done with a Plexiglas

plunger made for a sliding fit into the stainless steel cylinder. The plunger is designed so that when fully inserted into the cylinder, it just reaches the plane of the cavity opening. The plunger surface can be roughened by sandblasting if a coarser surface on the pressed PTFE is desired. However, this will not significantly affect the reflectance of the specimen. The pressure required to produce a standard of 1 g/cm^3 can easily be achieved by force of hand. A protective cover can be provided for storing the standard. This powder press and powder receptacle are not available commercially but can be made easily in a small machine shop.

(6) When measuring the PTFE reflectance standard, make sure it is pressed against the sample port of the integrating sphere so that no gap exists between the standard and port.

(7) Prepare fresh standards every day if necessary to avoid using soiled or damaged reflectance standards.

(8) Prepare at least three fresh standards when making reflectance measurement in the UV and use an average value of reflectance for these standards.

V. Remarks

The results of the round-robin experiments reported in Tables I and II should not be used as reference data for the absolute reflectance of pressed PTFE powder. Even the reported averages appearing in these tables are not considered good for reference purposes because some of the submitted specimens had significantly lower reflectances. Refer to the 6°/hemispherical reflectance data published in Ref. 2 for the absolute reflectance of PTFE powder.

The following laboratories participated in the round-robin experiments described in this paper: Burlington Industries, Corp. Research & Development, Greenboro, N.C.; E. I. Dupont Co., Troy, Mich.; Hunter Associates, Reston, Va.; Macbeth Division, Kollmorgen Corp., Newburgh, N.Y.; Munsell Color Science Laboratory, College of Graphic Arts and Photography, Rochester Institute of Technology, Rochester, N.Y.; National Research Council of Canada, Ottawa, Canada; Pacific Scientific, Gardner/Neotec, Silver Spring, Md.; The Sherwin-Williams Co., Chicago, Il., National Bureau of Standards, Radiometric Physics Division, Gaithersburg, Md.

References

1. F. Grum and M. Saltzman, P-75-77 New White Standard of Reflectance, CIE Publication 36, (Paris, 1976), p. 91.
2. V. R. Weidner and J. J. Hsia, "Reflection Properties of Pressed Polytetrafluoroethylene Powder," J. Opt. Soc. Am. **71**, 856 (1981).
3. E. Schatz, "Effects of Pressure on the Reflectance of Compacted Powders," J. Opt. Soc. Am. **56**, 389 (1966).
4. W. H. Venable, J. J. Hsia, and V. R. Weidner, "Establishing a Scale of Directional-Hemispherical Reflectance Factor I: The Van den Akker Method," J. Res. Natl. Bur. Stand. **82**, 29 (1977).
5. D. G. Goebel, B. P. Caldwell, and H. K. Hammond III, "Use of an Auxiliary Sphere with a Spectroreflectometer to Obtain Absolute Reflectance," J. Opt. Soc. Am. **56**, 783 (1966).

Appendix I

NIST Technical Note 1413

45°/0° Reflectance Factors of Pressed Polytetrafluoroethylene (PTFE) Powder

P. Yvonne Barnes and Jack J. Hsia

Radiometric Physics Division
Physics Laboratory
National Institute of Standards and Technology
Gaithersburg, MD 20899-0001

July 1995

U.S. Department of Commerce
Ronald H. Brown, Secretary

Technology Administration
Mary L. Good, Under Secretary for Technology

National Institute of Standards and Technology
Arati Prabhakar, Director

National Institute of Standards
and Technology
Technical Note 1413
Natl. Inst. Stand. Technol.
Tech. Note 1413
23 pages (July 1995)
CODEN: NTNOEF

U.S. Government Printing Office
Washington: 1995

For sale by the Superintendent of
Documents
U.S. Government Printing Office
Washington, DC 20402

Table of Contents

Abstract 1

1. Introduction 1

2. Sample Pressing Method 2

3. 45°/0° Reflectometer 3

4. Measurements 3

   4.1 Operator Variability 4

   4.2 Material Variability 4

   4.3 45°/0° Reflectance Factor and Uncertainty 4

5. Remarks 5

6. References 5

Tables and Figures 7

Appendix A. General and advance preparation information for pressing PTFE samples 12

Appendix B. Reprint, NBS 45°/normal reflectometer for absolute reflectance factors 13

List of Tables

1. Operator Variability : Each laboratory returned two pressed PTFE samples; alpha-numerics indicate the laboratory (A - J) or the sample (1 - 2). The quantity reflectance factor minus the average for the twenty samples is shown for each sample at the measurement wavelengths. The Type A uncertainty (k = 2) for the 20 measurements is shown in the last row. 7

2. Material Variability : Pressed PTFE samples from four drums; each drum was manufactured at a different time. The quantity reflectance factor is shown for each drum at the measurement wavelengths. The mean and Type A uncertainty (k = 2) for the measurements of the four drums are shown in the last two rows. 8

3. $45^\circ/0^\circ$ Reflectance Factors of Pressed PTFE Powder (1 g/cm^3) 9

List of Figures

1. PTFE powder presser designed to produce a sample with spatial uniformity in density and in appearance. 10

2. $45^\circ/0^\circ$ reflectometer system (Top view). 11

45°/0° Reflectance Factors of Pressed Polytetrafluoroethylene (PTFE) Powder

P. Yvonne Barnes and Jack J. Hsia

Radiometric Physics Division, National Institute of Standards and Technology, Gaithersburg, MD 20899, USA

Abstract

Pressed polytetrafluoroethylene (PTFE) powder is used for 45°/0° reflectance factor standards. The radiometric and spectrophotometric measurement community such as the Council for Optical Radiation Measurements (CORM) has demonstrated the need for such a standard and its application to quality control and quality assessment. This publication briefly describes the instrumentation used for the 45°/0° reflectance factor measurements of pressed PTFE powder from 380 nm to 770 nm. Also, the variations of 45°/0° reflectance factor with sample preparation and materials are discussed. The expanded uncertainty at a coverage factor of two for the 45°/0° reflectance factors of pressed PTFE powder ranges from 0.009 to 0.017.

Keywords

Diffuse Reflectance, 45°/0° Reflectance Factor, Polytetrafluoroethylene resins, Pressed PTFE powder, PTFE, Reflectance Factor

1. INTRODUCTION

Over the years, the Radiometric Physics Division at the National Institute of Standards and Technology (NIST) has investigated [1,2] the reflection properties of polytetrafluoroethylene (PTFE) resins, in a form of granular molding powder. NIST has established the 6°/hemispherical reflectance factor scale of pressed PTFE powder [3] and provided general preparation information on pressing PTFE powder (Appendix A). Recently, standards organizations, government agencies, national laboratories, optical material industries, and instrument manufacturers have expressed the need for a 45°/0° reflectance factor standard in a report on critical problems and projected national needs in optical radiation measurement by the Council for Optical Radiation

Measurements [4]. Although these requirements span the ultraviolet, visible and near infrared spectral regions, most of the requests for calibration are 45°/0° reflectance factors in the visible wavelength region.

The reflectance factor of a sample is defined [5] as "the ratio of the radiant flux reflected in the directions delimited by the cone to that reflected in the same directions by a perfect reflecting diffuser identically irradiated." This cone is formed by the receiver limiting aperture and with apex at the center of the sample surface. A perfect reflecting diffuser is an ideal (no loss) lambertian (uniform in all directions) diffuser. The 45°/0° reflectance factor is the reflectance factor measured at 45° incident angle and normal viewing angle. The governing equations and the description of how the reflectance factor is measured are given in Reference 6 and a reprint is included in Appendix B. The reflectance factor measurement method (see app. B) using a step-down technique and a view factor calls for the measurements of the ratio of two fluxes and, in addition, some linear dimensions.

In order to develop the pressed PTFE powder as an intrinsic standard, studies of the major factors that affect the measured values were performed. This publication describes the sample pressing method and briefly described the 45°/0° reflectometer for reflectance factor measurements of the samples from 380 nm to 770 nm. Also, the variations of 45°/0° reflectance factor with sample preparation and materials are discussed. Finally, a table is presented for 45°/0° reflectance factors and their associated uncertainties of pressed PTFE powder from 380 nm to 770 nm at every 10 nm.

2. SAMPLE PRESSING METHOD

This section describes the method used to prepare a diffuse PTFE sample that is uniform in both appearance and density (approximately 1 g/cm^3). After practice and familiarity with the presser (see fig. 1) [7], a sample can be made quickly, frequently, and with consistent results. For the best results and ease of processing, 25 g of PTFE powder is placed in a blender with sharp blades. The PTFE powder is pulverized until it appears light, airy and powder-like.

Referring to Figure 1, the diameter of the poly(methyl methacrylat) plunger is 51 mm; the height of the funnel is 75 mm; and the receptacle is 10 mm in depth. The end area of the plunger is pre-treated by pressing it on some amount of PTFE powder to reduce the influence of hydrocarbons in the plunger material. The following steps are followed to press a sample: 1) the funnel and the receptacle are assembled; 2) 25 g of pulverized PTFE powder is scooped into the funnel; 3) the pre-treated plunger is inserted into the funnel and manually pressed downward until it stops; 4) the plunger is withdrawn slowly to overcome the suction created by the close fit of the funnel and the plunger; 5) the receptacle is separated from the funnel by loosening the set screws; 6) the pressed sample is then imprinted with a sheet of pre-treated sandpaper by hand with minimum pressure. Some general information on PTFE powder and preparation

is provided in Appendix A. The safety aspects in handling and use of PTFE powder are listed in Reference 8.

3. 45°/0° REFLECTOMETER

The overall instrument consists of a source system and a 45°/0° reflectometer [6,9,10]. The source system consists of a tungsten ribbon-filament lamp, mirrors, polarizer, predisperser, monochromator, and other mirrors. The source system provides a nearly collimated, polarized output with 10 nm band pass. The configuration of the 45°/0° reflectometer is shown in figure 2. Details of the receiver system are shown in figure 2 of Appendix B.

Referring to figure 2a in Appendix B, the incident beam illuminates at 45° from the sample normal an area 21 mm by 21 mm at the center of the sample (S). Due to the change of the optical arrangement of the source system after the publication of the paper in Appendix B, the larger light beam still provides a 10 nm band pass. The receiver system views the entire sample at 0° from the sample normal. In figure 2b of Appendix B, two 15 cm diameter averaging spheres (AS) are mounted together vertically and the photomultiplier (D) is attached to the upper sphere. A precision circular limiting aperture (LA) on the lower sphere subtends a half angle of 2.8° from the center of the sample. This double-averaging sphere detection arrangement provides a uniform receiver system for both of the required measurement geometries: a small light beam reflected from a specular black glass plate and a larger diffusely reflected light beam from a diffuse sample.

4. MEASUREMENTS

Due to the low signal levels associated with this type of bidirectional reflectance factor measurement, a step-down technique is used to reduce the required dynamic range for measurements and to reduce measurement uncertainty. A specular black glass plate with a regular (specular) reflectance value of about 0.04 is employed. The 22.5°/22.5° regular reflectance of the black glass is measured, using a specular reflectometer [11], with light polarized parallel and perpendicular to the plane of incidence at each wavelength. The flux of the pressed PTFE sample is then measured relative to the flux of the black glass plate with the 45°/0° reflectometer for each polarization state. This relative value of the pressed PTFE sample, the specular reflectance of the black glass plate and the projected solid angle of the receiver limiting aperture are used to calculate the 45°/0° reflectance factor according to Eq (9) in Appendix B.

The 45°/0° reflectance factors of pressed PTFE powder were performed on ten freshly pressed samples. These samples were prepared by one operator, taken from one batch of PTFE powder, and measured over the visible spectral range. The standard deviation for these measurements for a coverage factor (k) of 2 was less than 0.001

indicating a good repeatability. There was no spectral dependence. The Type B uncertainty [12] for k = 2 was 0.0027 for the visible spectral region [6]. The contributors to Type B uncertainty were receiver system non-linearity and non-uniformity, scattered flux, and angular setting and view factor uncertainties.

4.1 Operator Variability

A study was conducted to investigate variability in the results when ten different laboratories prepared samples. Each laboratory received an instruction sheet, a presser, a container with pulverized PTFE powder, and a pre-labeled box with packing material to return the pressed PTFE samples to NIST. Each laboratory pressed two samples with the proper amount of PTFE powder needed to prepare a sample of 1 g/cm^3 in density, 51 mm in diameter and 10 mm in thickness. No measurements were required from the laboratories and all twenty samples were returned to NIST for measurements. Results of this study are reported in Table 1, which shows the difference of the reflectance factor for each sample from the mean value of 20 samples at each of the five wavelengths. The Type A uncertainty (k = 2) of these differences for the 20 samples range from 0.006 to 0.012 in the wavelength region from 380 nm to 770 nm.

4.2 Material Variability

The variability in the results due to the composition of the PTFE powder was studied by making samples from four different drums of PTFE powder. The Ausimont[1], type G-80 and type Algoflon F5 PTFE powder were used in this investigation. Each of these powders was produced at a different time with different lot numbers. The samples were made as described above and measured at seven wavelengths. The quantity reflectance factor for each drum at the measurement wavelengths is shown in Table 2. The Type A uncertainties (k = 2) for measurements of four drums range from 0.013 to 0.001 for the wavelength range from 380 nm to 770 nm.

4.3 45°/0° Reflectance factor and uncertainty

The 45°/0° reflectance factors of pressed PTFE powder of samples from four drums in Table 2 were averaged at each of the seven wavelengths and these values were

1. Certain commercial instrument or materials are identified in this paper in order to specify adequately the procedure. In no case does such identification imply endorsement or evaluation by the National Institute of Standards and Technology.

interpolated by spline fit for other wavelengths. These values are reported in Table 3 together with the expanded uncertainties for a coverage factor of 2. These uncertainties include the type B uncertainty, statistical measurement uncertainty, operator to operator variations, and material to material variations. The standard deviations (k = 2) range from 0.017 to 0.009 for wavelengths from 380 nm to 770 nm.

5. REMARKS

The results of this investigation show that the expanded uncertainties of the 45°/0° reflectance factors of pressed PTFE powder mainly due to two factors, one is the material variability which is larger at the shorter wavelengths and the other is the operator variability. Furthermore, these expanded uncertainties are about twice those of the 6°/hemispherical reflectance measurements [2].

The following laboratories participated in the PTFE powder pressing study described in this publication: Biospherical Instruments, San Diego, CA; Byk-Gardner, Silver Spring, MD; Datacolor, Lawrenceville, NJ; Hughes, Danbury, CT; Hunter Lab, Reston, VA; Jet Propulsion Laboratory, Pasadena, CA; Labsphere, North Sutton, NH; Miles Lab, Elkart, IN; Munsell Color Science Laboratory, Rochester Institute of Technology, Rochester, NY; University of Arizona, Tuscon, AZ.

Both the 45°/0° reflectometer and the specular reflectometer used in this investigation were replaced in 1995 by a new Spectral Tri-function Automated Reference Reflectometer (STARR) incorporating new detectors and electronics. Preliminary intercomparisons between the old and new instruments on 45°/0° reflectance factor show measurements agreeing to within 0.002.

6. REFERENCES

[1] V. R. Weidner and J. .J. Hsia, J. Opt. Soc. Am., **71**, 856 (1981).

[2] V. R. Weidner, J. J. Hsia and B. Adams, Appl. Opt., **24**, 2225 (1985).

[3] F. E Nicodemus, J. C. Richmond, J. J. Hsia, I. W. Ginsberg and T. Limperis, NBS Monograph No. 160 (1977) p. 9.

[4] Council for Optical Radiation Measurements: CORM Fifth Report on Pressing Problems and Projected National Needs in Optical Radiation Measurements (1989).

[5] Commission International de l'eclairage: International Lighting Vocabulary, CIE Publ. No. 17.4 (1987).

[6] J. J. Hsia and V. R. Weidner, Metrologia, **17**, 97 (1981). (A reprint is attached as Appendix B.)

[7] American Society for Testing and Materials: Standard Practice E259-93, ASTM Annual Book of ASTM Standards **06.01** (1994) p. 709

[8] E.I. Du Pont De Nemours and Company, Inc., Fluorocarbons Division, Teflon Fluorocarbon Resins - Safety in Handling and Use (1970)

[9] W. H. Venable, Jr., J. J. Hsia and V. R. Weidner, NBS Tech. Note 594-11 (1976).

[10] V. R. Weidner and J. .J. Hsia, NBS SP 250-8 (1987).

[11] V. R. Weidner and J. .J. Hsia, Appl. Opt., **19**, 1268 (1980).

[12] B. B. Taylor and C. E. Kuyatt, NIST Tech. Note 1297 (1994) p. 2.

Table 1. Operator Variability : Each laboratory returned two pressed PTFE samples; alpha-numerics indicate the laboratory (A - J) or the sample (1 - 2). The quantity reflectance factor minus the average for the twenty samples is shown for each sample at the measurement wavelengths. The Type A uncertainty (k = 2) for the 20 measurements is shown in the last row.

	Wavelength [nm]				
	380	450	600	700	770
A1	0.002	0.004	0.002	0.003	0.004
A2	0.004	0.006	0.003	0.001	0.003
B1	-0.001	0.001	0.000	0.000	-0.007
B2	-0.005	0.000	-0.001	0.000	-0.001
C1	0.009	0.006	0.004	0.004	0.005
C2	-0.005	-0.005	-0.004	-0.006	-0.005
D1	0.001	0.002	0.001	0.001	0.002
D2	0.007	0.004	0.003	0.002	0.002
E1	-0.003	0.002	0.002	0.003	0.004
E2	-0.004	-0.004	-0.005	-0.006	-0.006
F1	0.000	-0.011	-0.004	0.008	0.004
F2	-0.001	0.000	0.001	0.001	0.001
G1	-0.002	-0.004	-0.004	-0.004	-0.005
G2	0.009	0.005	0.002	0.002	0.004
H1	-0.012	-0.006	-0.006	-0.008	-0.007
H2	0.010	0.001	0.000	0.001	0.002
I1	-0.003	0.000	0.002	-0.001	0.000
I2	0.006	-0.002	0.002	0.002	0.005
J1	-0.010	-0.007	-0.005	-0.007	-0.004
J2	0.003	0.007	0.006	0.008	0.006
std dev (k = 2)	0.012	0.010	0.006	0.008	0.008

Table 2. Material Variability : Pressed PTFE samples from four drums, each drum was manufactured at a different time. The quantity reflectance factor is shown for each drum at the measurement wavelengths. The mean and Type A uncertainty (k = 2) for the measurements of the four drums are shown in the last two rows.

	Wavelength [nm]						
Drum #	380	420	470	550	630	700	770
1	1.005	1.008	1.011	1.013	1.012	1.013	1.016
2	1.001	1.006	1.009	1.011	1.012	1.012	1.017
3	0.993	0.999	1.003	1.007	1.010	1.011	1.016
4	1.007	1.010	1.011	1.012	1.013	1.013	1.017
mean	1.002	1.006	1.009	1.011	1.012	1.012	1.017
std dev (k=2)	0.013	0.010	0.008	0.005	0.002	0.002	0.001

Table 3. 45°/0° Reflectance Factors of Pressed PTFE Powder (1 g/cm^3)

Wavelength [nm]	Reflectance Factor	Uncertainty* k = 2
380	1.002	0.017
390	1.003	0.017
400	1.005	0.016
410	1.006	0.016
420	1.006	0.015
430	1.007	0.015
440	1.007	0.015
450	1.008	0.014
460	1.008	0.014
470	1.009	0.014
480	1.009	0.014
490	1.009	0.013
500	1.010	0.013
510	1.010	0.012
520	1.010	0.012
530	1.010	0.011
540	1.011	0.011
550	1.011	0.011
560	1.011	0.011
570	1.011	0.010
580	1.011	0.010
590	1.011	0.010
600	1.011	0.010
610	1.011	0.009
620	1.012	0.009
630	1.012	0.009
640	1.012	0.009
650	1.012	0.010
660	1.012	0.010
670	1.012	0.010
680	1.012	0.011
690	1.012	0.011
700	1.012	0.011
710	1.013	0.011
720	1.014	0.011
730	1.015	0.011
740	1.015	0.011
750	1.016	0.011
760	1.016	0.011
770	1.017	0.011

* The total uncertainty consists of the instrument uncertainty, material and operator variations.

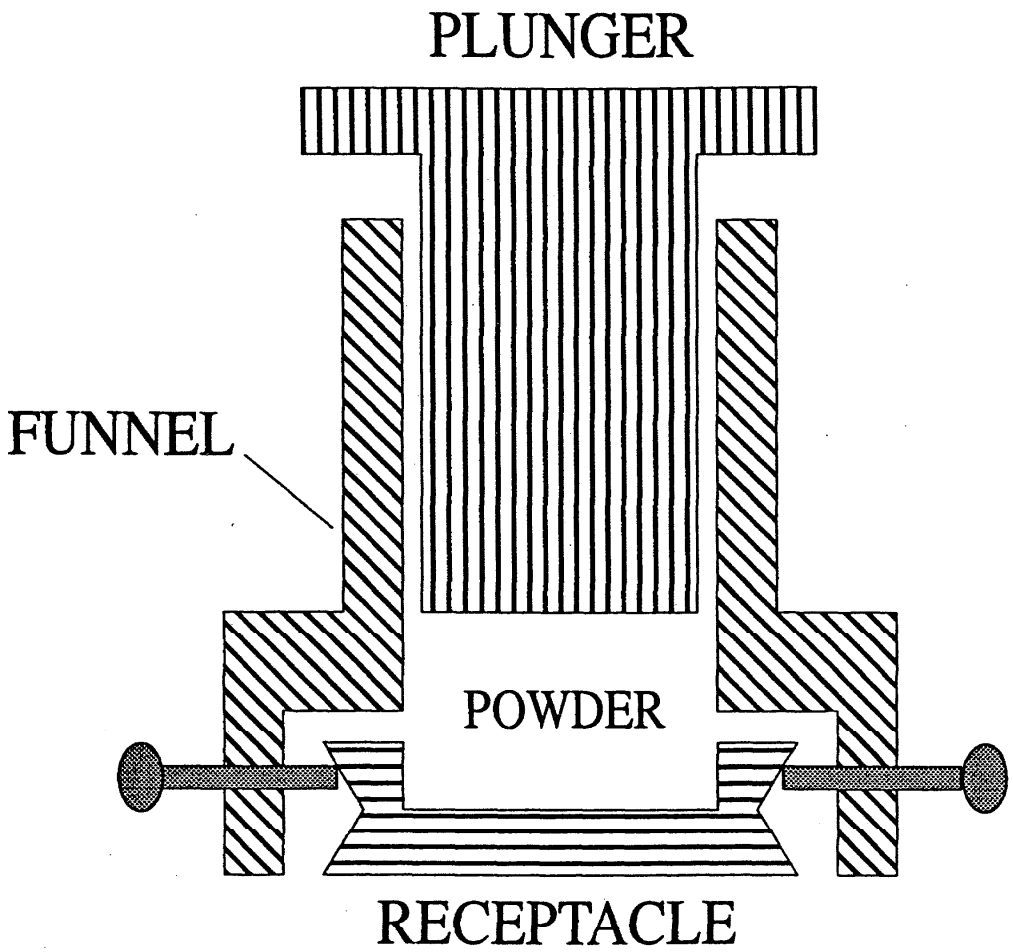

Figure 1. PTFE powder presser designed to produce a sample with spatial uniformity in density and in appearance.

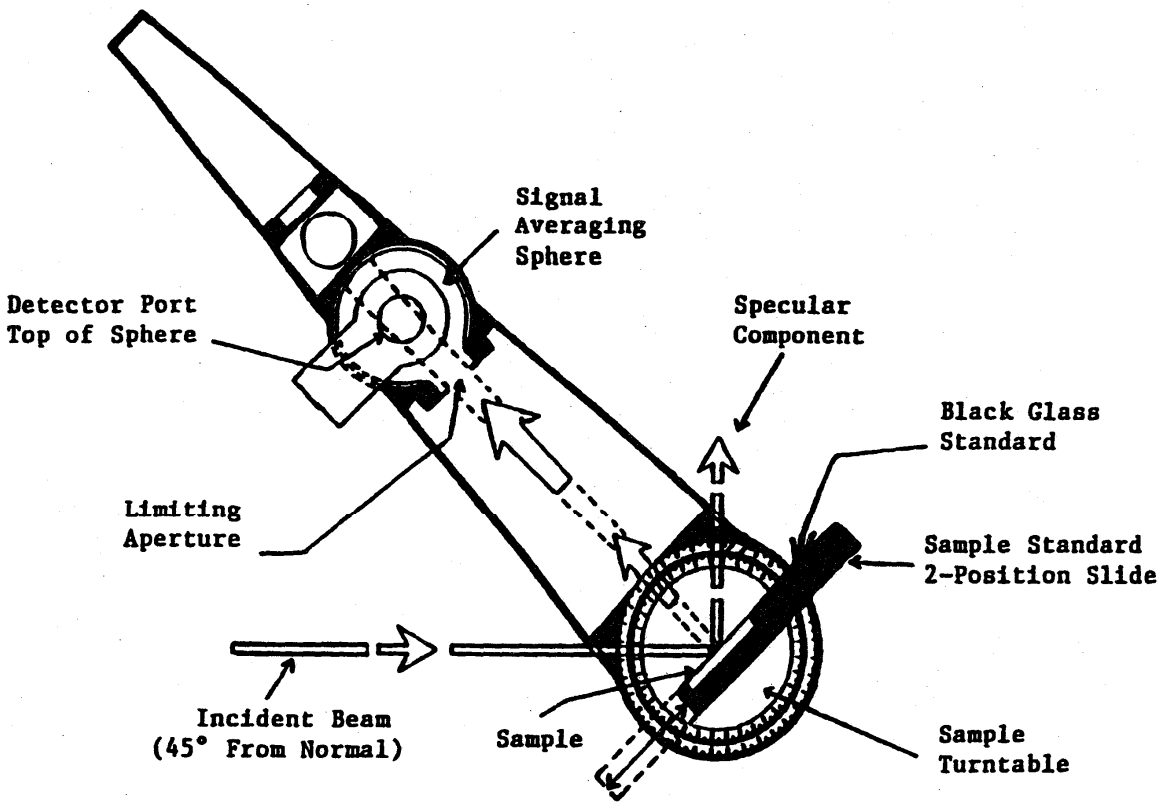

Figure 2. 45°/0° Reflectometer System
(Top View)

APPENDIX A. General and Advance Preparation Information for Pressing PTFE Samples

a. PTFE presser: Since there are no commercially available PTFE pressers that met our specifications, a simple PTFE presser was designed and fabricated at NIST (Refer to fig.1). The presser consists of three parts: a plunger that was constructed of poly(methyl methacrylate), a funnel of sufficient size to hold bulk PTFE powder before pressing, a receptacle designed to fit into the specimen holder of the 45°/0° reflectometer. This plunger was preconditioned by pressing against clean PTFE powder.

b. Commercial blender: PTFE powder naturally clumps together as aggregates. An Osterizer [13] blender was used to pulverize PTFE powder into a fluffy powder-like appearance. This type of commercial blender was chosen because it could be attached to glass jars and the blades could be sharpened in the machine shop.

c. Alternative devices: A stainless sifter or a flour sifter may be used instead of a commercial blender.

d. Static charge: PTFE powder acquires an electro-static charge throughout the pulverization process and will coat the glass blending jar and blades.

e. Utensils: Only stainless steel, glass, and porcelain materials or containers should be used to handle PTFE powder. The ultra-violet spectral reflectance factors of a pressed PTFE sample are affected by the hydrocarbons in plastic materials.

f. Containers of PTFE powder: PTFE powder is usually shipped by the manufacturer in drums of either 20 kg or 45.5 kg. The powder is packed in a plastic bag. Only the PTFE in the center portion of the drum is used, thus avoiding the powder that came in contact with the plastic bag.

g. Preconditioned sandpaper: A sheet of 150 grit size sandpaper was rubbed with a piece of sintered (in an electric furnace at 370 °C for 1 hour) PTFE, and shaken repeatedly so that the loose particles would fall off and not be embedded to the surface of the sample.

h. Ceramic tile: Use a ceramic tile or a similar type of object to evenly distribute the applied force over the preconditioned sandpaper on the sample area.

i. Laboratory conditions: PTFE powder is contaminated by airborne particles and smoke due to the electro-static charge (see sec. d above).

j. Safety: Obtain a Material Safety Data (MSD) sheet from the manufacturer of PTFE powder. Safety precautions and safety issues are the sole responsibility of users.

k. PTFE sample: A pressed sample of PTFE is durable and will not fall out of the receptacle. A sample may be positioned vertically, and if necessary it may also be inverted and tapped lightly so that the loose particles would fall off.

l. Cleaning. A clean camel-hair brush can be used to remove pieces of lint on the sample surface.

APPENDIX B. Reprint, NBS 45°/Normal Reflectometer for Absolute Reflectance Factors
(see next six pages)

Metrologia 17, 97–102 (1981)

metrologia
© by Springer-Verlag 1981

NBS 45°/Normal Reflectometer for Absolute Reflectance Factors

Jack J. Hsia and Victor R. Weidner

National Bureau of Standards, Washington, DC 20234, USA

Received: March 25, 1981

Abstract

A 45°/normal reflectometer has been constructed and tested for calibrating the absolute reflectance factor of diffuse samples over the 380–770 nm spectral range using polarized radiation. The measurement equations have been derived for the method used. The method using a step-down technique and view factor calls for the measurements of the ratio of two fluxes and, in addition, some linear dimensions. The uniformity of the receiver system is achieved by means of a double-sphere signal averager. Uncertainties of the absolute-reflectance-factor measurements obtained with this system are estimated to be ±0.3% of the measured value. For all the samples that have been tested, the 45°/normal reflectance factor was found to be higher than the 6°/hemispherical reflectance factor. The higher reflectance values for 45°/normal geometry were confirmed by additional gonioreflectometer measurements.

1. Introduction

Measurements of the diffuse reflecting characteristics of materials are of basic importance in radiometry, photometry and colorimetry as well as many other fields of science, technology and industry.

The International Commission on Illumination (Commission Internationale de l'Eclairage – CIE) recommended that starting in 1969, in colorimetric measurements of opaque materials, the perfect diffuser was to be taken as the primary reference standard. There is no existing material having diffuse reflection properties corresponding to the perfect diffuser with sufficient approximation. Therefore, the characteristics of all physical standards actually employed in comparison measurements must be established by techniques through which their absolute reflectance factors can be determined. The measurements involve not only the determination of the ratio of radiometric quantities but also the determination of linear dimensions.

The four geometries recommended by the CIE are 45°/normal, normal/45°, diffuse/normal, and normal/diffuse. The method and instrumentation to realize the NBS scale of directional-hemispherical reflectance factor has been described in [1].

For the 45°/normal and normal/45° reflectance factor measurements, there exists a large ratio of the incident flux to the reflected flux contained in a small solid angle. Various step-down techniques have been used by several National Laboratories [2–8] to insure sufficient accuracy over this wide dynamic range.

The purpose of this paper is to describe the method and the instrumentation used to establish the NBS scale of absolute reflectance factor in the 45°/normal geometry.

2. Measurement Equations

An absolute reflectance factor is defined [9, 10] as the ratio of the radiant flux reflected in the directions bounded by a given cone with the apex at a point of the surface under test to that reflected in the same directions by a perfect reflecting diffuser identically irradiated. The term "perfect reflecting diffuser" means the ideal (lossless) lambertian (uniform in all directions) diffuser. If the solid angle of the cone approaches zero, or 2π steradians, the reflectance factor approaches radiance factor or reflectance, respectively.

The reflectance factor of sample x, R_x, can be expressed as

$$R_x = \frac{\int^5 L(U,\lambda)\, S_x(U,u,\lambda)\, r(u,\lambda)\, U\cdot dA\, d\Omega\, u\cdot da\, d\omega\, d\lambda}{\int^5 L(U,\lambda)\, S_{id}\, r(u,\lambda)\, U\cdot dA\, d\Omega\, u\cdot da\, d\omega\, d\lambda} \qquad (1)$$

where L is the incident radiance; S_x and S_{id} are the scattering functions of the sample and of the ideal surface, r is the relative responsivity of the receiver; U and u are the direction vectors of travel of the incident and emergent radiation; $d\Omega$ and $d\omega$ are elements of solid angle oriented in the direction U and u; dA and da are elements of area through which the energy passes on to the sample and emerges from the sample; $d\lambda$ is the element of wavelength; and the symbol $\int^n$ indicates inte-

0026-1394/81/0017/0097/$01.20

gration with respect to n variables. In general, the nomenclature (especially the symbols) used here is that of reference [11]. There it is more completely defined and discussed.

If there is no interaction between the wavelength dependence and the geometrical dependence of the incident radiance and of the responsivity, the functions are separable. For any source function $C(\lambda)$ and luminous efficiency function $V(\lambda)$, Eq. (1) can be written as

$$R_x = \frac{\int C(\lambda)\, V(\lambda)}{\int C(\lambda)\, V(\lambda)} \tag{2}$$

$$\frac{[\int^4 L(U)\, S_x(U,u,\lambda)\, r(u)\, U\cdot dA\; d\Omega\; u\cdot da\; d\omega]\; d\lambda}{[S_{id} \int^4 L(U)\, r(u)\, U\cdot dA\; d\Omega\; u\cdot da\; d\omega]\; d\lambda}$$

$$R_x = \frac{\int C(\lambda)\, V(\lambda)\, R_x(\lambda)\, d\lambda}{\int C(\lambda)\, V(\lambda)\, d\lambda} \tag{3}$$

The spectral reflectance factor $R_x(\lambda)$ is expressed as

$$R_x(\lambda) = \frac{\int^4 L(U)\, S_x(U,u,\lambda)\, r(u)\, U\cdot dA\; d\Omega\; u\cdot da\; d\omega}{S_{id} \int L(U)\, r(u)\, U\cdot dA\; d\Omega\; u\cdot da\; d\omega} \tag{4}$$

For a receiver system with uniform responsivity within the cone,

$$r(u) = r \text{ within } \omega \text{ and } r(u) = 0 \text{ outside of } \omega. \tag{5}$$

The scattering function of a perfect diffuser could be written as

$$S_{id} = \delta(P - p)/\pi \tag{6}$$

where P and p are position vectors on the testing surface for incident space and the emergent space, respectively.

Thus (4) can be expressed as

$$R_x(\lambda) = \frac{\pi}{\omega_p} \frac{\Phi_x(\lambda)}{\Phi_i(\lambda)} \tag{7}$$

where $\omega_p = \int^2 u\cdot da\; d\omega$ is the projected solid angle of the cone onto the surface to be measured.

$\Phi_x = \int^4 L(U)\, S_x(U,u,\lambda)\, U\cdot dA\; d\Omega\, u\cdot da\; d\omega$ is the reflected radiant flux for the sample that enters the limiting receiver aperture, and

$\Phi_i = \int^2 L(U)\, \delta(P - p)\, U\cdot dA\; d\Omega$ is the incident radiant flux.

In radiation heat transfer [12, 13], ω_p/π (or f_{1-2}) is named the view factor (alternatively designated as the form factor, configuration factor, geometrical factor, or angle factor) representing the fraction of the radiant flux leaving a diffuse surface that is entering the limiting aperture. In other words, f_{1-2} is the fraction of the incident flux reflected from (1) a perfect diffuser that is entering the (2) limiting aperture. The spectral reflectance factor can now be expressed as

$$R_x(\lambda) = \frac{1}{f_{1-2}} \frac{\Phi_x(\lambda)}{\Phi_i(\lambda)} \tag{8}$$

Equation (8) clearly indicates that the reflectance factor is the ratio of the reflected flux (into the limiting aperture) to that of a perfect diffuser. If another sample S with known reflectance is used to step down[1] the incident flux, the reflectance factor of sample x can be calculated as

$$R_x(\lambda) = \frac{1}{f_{1-2}} \frac{\Phi_x(\lambda)}{\Phi_S(\lambda)} \cdot \rho_S \tag{9}$$

where Φ_S and ρ_S are the flux and the reflectance of the step-down sample S, respectively. The view factor will be expressed in detail below.

For a circular limiting aperture (diameter D) which is parallel to the sample surface at a distance d, and for $\Delta A1$, a small portion of the illuminated area, and the distance between a point in $\Delta A1$ and the central normal (on the sample surface) to the circular area of the limiting aperture being c, (see Fig. 1) the view factor can be expressed [14] as:

$$f_{\Delta A1-A2} = [1 - J/K]/2, \tag{10}$$

where $J = 1 + G^2 - B^2$

$K = [G^4 + 2G^2(1-B^2) + (1+B^2)^2]^{1/2}$

$B = D/2d$

$G = c/d$

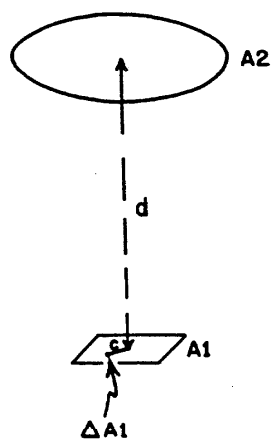

Fig. 1. Schematic for view factor (Eq. 10) Determination

When the illuminated area is very small and is at the central normal to the circular area of the limiting aperture, the view factor becomes

$$f_{1-2} = f_{\Delta A1-A2} = [1 + 4\, d^2/D^2]^{-1} \tag{11}$$

and when the illuminated area is finite, the view factor is

$$f_{1-2} = \frac{1}{A1} \int f_{\Delta A1-A2}\, dA1 \tag{12}$$

$$\text{or } f_{1-2} = \frac{\Delta A1}{A1} \sum_{A1} f_{\Delta A1-A2} \tag{13}$$

if $\Delta A1$ is selected to be sufficiently small.

[1] Procedure described in Sect. 5

3. NBS Reference Spectrophotometer

The 45°/normal reflectometer is an accessory to the NBS reference spectrophotometer for reflectance [15]. The light source, monochromator, electronics and other associated equipment are located in a system control room. The exit slit housing of the monochromator is attached to a light-tight diaphragm in a wall, which allows the exit light beam or sample beam to enter a second room where the various reflectance-measuring devices, such as the specular reflectometer or the 45°/normal reflectometer, are installed. The advantages of this arrangement are that the second room can be used as an experimental dark chamber, while the light source, electronics and control systems are isolated from the experimental area. The sample beam emerging from the exit slit of the monochromator can be controlled to provide a spectral bandpass of 2, 5, 10, or 20 nm. For a 10-nm bandpass, the light beam has a cross section 10 by 18 mm at the sample position.

To measure spectral reflectance factor over the visible wavelength range of the monochromator, the system employs a tungsten strip lamp and a photomultiplier detector. A complete description of the spectrophotometer is given in an earlier publication [15].

Data have been published [16, 17] on the large effect of polarization on the reflectance factor. Therefore, the NBS design includes a polarization-insensitive receiver system and the measurements are made with polarized incident light. The final result is the average of measurements made with light polarized perpendicular and parallel to the plane of incidence.

4. 45°/Normal Reflectometer

The light beam from the source system is incident on a sample at 45° from normal and the reflected flux at normal to the sample is collected and measured. The schematic of the instrument is shown in Fig. 2. The 45°/normal rather than the normal/45° geometry was chosen, because the distance between the limiting aperture and the sample surface and, in turn, the view factor could be determined more accurately.

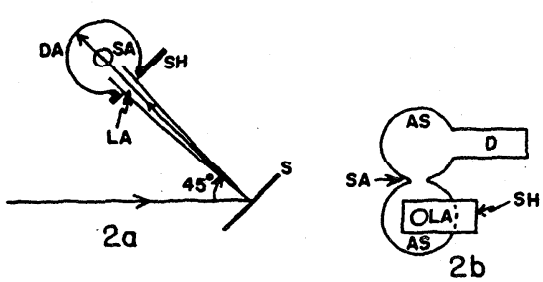

Fig. 2 a and b. Schematic of the 45°/normal Reflectometer. a Top view with top sphere not shown, for clarity. S: Sample, LA: Limiting Aperture, DA: Detector assembly, SA: Aperture between spheres; b Front view of the two-sphere Receiver Assembly, AS: Averaging Sphere, SH: Shutter, D: Detector, LA: Limiting Aperture, SA: Aperture between spheres

Because the step-down technique with a polished black glass is used to obtain the absolute reflectance factors of a diffuse sample, the instrument should be able to measure accurately both the specularly and the diffusely reflected light beams. This requires that the responsivity of the receiver system be uniform over its aperture area.

To fulfill the above requirement, the photomultiplier is equipped with a double-sphere signal averager. The spheres are approximately 15 cm in diameter. The sphere coating is a fluorocarbon powder, which is a nearly perfect diffuser of very high reflectivity. The two spheres are mounted together vertically and are designed to allow the inside curvature of the sphere coating to meet at the center of the port between the two spheres. The photomultiplier is mounted horizontally on the upper sphere. The spheres are attached to a stepping-motor-controlled vertical slide for alignment and scanning purposes. The lower sphere has a circular limiting aperture facing the sample. To prevent scattered radiation, other than that directly from the sample, reaching the limiting aperture, no component is placed between the surfaces of the sample and the limiting aperture. A black felt is placed on the top surface of the rotation arm to further reduce scattered radiation.

The sample holder, which can hold two samples, is mounted on a two-position slide that moves 12.5 cm between positions and is pneumatically driven. The slide is mounted on a stepping-motor-controlled turntable. The detector assembly is on an arm attached to another independently-controlled turntable having the same axis of rotation as that of the sample turntable.

The signal processing of the output from the photomultiplier utilizes a current-to-frequency converter that can integrate the detector output over a selected time interval, and a digital counter. The digital data from the counter are transferred to a computer for analysis.

5. Measurement Procedure

Before a measurement is performed, the instrument is first aligned. The sample holder can be adjusted normal to the incident light beam with the aid of a flat mirror in the sample position. The sample holder is then turned 22.5° from the normal position toward the limiting aperture. The limiting aperture is adjusted to center on the reflected light beam which is 45° from the incident light beam. A thin mirror, with the reflecting surface facing the limiting aperture, is held against the limiting aperture. The limiting aperture is aligned so that the light is reflected back to the exit slit of the monochromator. Thus the limiting aperture is aligned normal to the reflected light beam 45° from the incident beam.

The diameters of the limiting aperture were measured at eight places by using a shadow profile projector before the aperture was mounted on the lower sphere. The circularity has been checked by a deviation plotter. The average diameter is 38.238 mm. The distance be-

tween the surfaces of the limiting aperture and the sample is determined when the sample holder is turned 45° from the normal position. A thin glass plate is placed over the limiting aperture. The distance between this glass plate and a flat surface at the sample position is measured with an inside micrometer. The thickness of the glass plate is added to the micrometer measurement to give the total distance which in this case is 381.89 mm. The view factor can thus be calculated using (10) and (13).

The spectral 22.5° specular reflectances of a piece of polished black glass are first determined with the specular reflectometer [18] with light polarized perpendicular and parallel to the plane of incidence. This piece of black glass is then used to step down the incident flux to determine the 45°/0° reflectance factors of a sample. The flux of the sample in 45°/0° geometry is compared to the flux of the black glass in the 22.5°/22.5° geometry. The reflectance factor of the sample can thus be calculated using (9). The measurements are performed with polarized light, and the final result is the average of measurements made with light polarized perpendicular and parallel to the plane of incidence.

6. Performance

It is beyond the intent of this paper to describe in detail the various checks that were made on the performance of the monochromator, other components of the spectrophotometer, and the reflectometer, except to mention briefly the magnitudes of errors associated with this portion of the system, since they do influence the accuracy of measurements of reflectance factor. Information regarding some of these investigations is presented in [15].

Wavelength scale uncertainties, receiver linearity, receiver uniformity, scattered radiation, angular setting uncertainty, and view factor uncertainty are involved in checking the performance of the instrument.

The wavelength scale of the monochromator was checked by measuring the emission lines [18] of several line-source lamps and the instrument function, then determining the centroid wavelengths. Uncertainty in the wavelength scale is 1 nm or less for a 10 nm bandpass. Corrections for these errors are made by adjustment of the wavelength-scale setting to compensate for differences between the wavelength counter and the true wavelength.

The linearity of the receiver system was measured by the light addition method with a double aperture apparatus [20, 21]. The results indicate the receiver system is linear to better than ±0.1% and the nonlinearity is corrected for measured data.

Even though the receiver system utilizes double spheres as an averager device, there is still a slight nonuniformity causing 0.05% uncertainty in comparing the fluxes of specularly and diffusely reflected beams.

Radiation scattered off the components between the exit slit of the monochromator and the limiting aperture of the receiver system causes errors in a reflectometer. The room containing the reflectometer is lined with a black felt material to absorb scattered radiation. All mechanical components, including the sample holder and the limiting aperture, are black anodized to reduce the scattered radiation. Some interreflections between the limiting aperture and the sample and between the sphere coating and the sample are unavoidable. The scattered radiation caused by the interreflection is determined to be less than 0.05% of the reflected radiation.

The 0.05° uncertainty of the angular setting of the sample holder contributes to 0.15% uncertainty in determining the ratio of the reflected fluxes of the sample and the piece of black glass.

The uncertainties in determining the diameter of the limiting aperture, the distance between the sample surface and the limiting aperture, and the dimensions of the light image size on the sample surface result in an uncertainty of about 0.05% for the view factor.

An analysis of the various sources of error that may affect the accuracy of reflectance factor measurements on the NBS 45°/normal reflectometer indicates that the final uncertainty in these measurements will be of the order of ±0.3% of the measured value.

7. Ratio of R(45°/Normal) TO R(6°/Hemispherical) with Specular Component Excluded

The hemispherical reflectance factor R(0°/h) of a diffuser for normally incident light can be calculated from the angular variations of reflectance factors R(0°/θ) using the following expression:

$$R(0^\circ/h) = \frac{\int_0^{\pi/2} R(0^\circ/\theta)\cos\theta\sin\theta\, 2\pi d\theta}{\int_0^{\pi/2} \cos\theta\sin\theta\, 2\pi d\theta} \tag{14}$$

Divided by R(0°/45°), Eq. (14) can be written as:

$$\frac{R(0^\circ/h)}{R(0^\circ/45^\circ)} = 2\int_0^{\pi/2} \frac{R(0^\circ/\theta)}{R(0^\circ/45^\circ)}\sin\theta\cos\theta d\theta \tag{15}$$

In terms of measurable quantities, (15) can be rewritten as:

$$\frac{R(0^\circ/h)}{R(0^\circ/45^\circ)} = 2\int_0^{\pi/2} B(0^\circ/\theta)\sin\theta\cos\theta d\theta \tag{16}$$

where

$$B(0^\circ/\theta) = \frac{\Phi(0^\circ/\theta)/\cos\theta}{\Phi(0^\circ/45^\circ)/\cos 45^\circ} \tag{17}$$

with Φ as the reflected flux from the sample.

The two working standards, vitrolite glass and porcelain enamel plate, one pressed $BaSO_4$ sample, and one pressed fluorocarbon sample were measured on the gonioreflectometer at 550 nm with 10 nm bandpass. The incident angle was 0° and the angles of viewing were from 5° to 85° at 10° intervals. Measurements were

made with light polarized parallel and perpendicular to the plane of incidence. $B(0°/\theta)$'s were calculated for each polarization and the averages obtained.

Average $B(0°/\theta)$'s at the discrete intervals were fitted by the least-squares method. Individual data did not deviate from the fitted curve by more than ±0.001 and were typically within 0.0005 of the fitted curve. The curve fittings were done by using a six-parameter equation:

$$B(0°/\theta) = \sum_{i=0}^{5} b_i \theta^i \tag{18}$$

Inserting (18) into (16), we have

$$\frac{R(0°/h)}{R(0°/45°)} = 2 \sum_{i=0}^{5} b_i I_i \tag{19}$$

where

$$I_i = \int_0^{\pi/2} \theta^i \sin\theta \cos\theta \, d\theta \tag{20}$$

The values [1] of the integrals I_i are (from i = 0 to 5): 0.50000, 0.39270, 0.36685, 0.37990, 0.42147, and 0.49129. With the values of I_i and b_i, $R(0°/h)/R(0°/45°)$ can be predicted using (19).

Six deg.-hemispherical reflectance factors, $R(6°/h)$, with specular component excluded and 45°/normal reflectance factors, $R(45°/0°)$, were also measured for the four samples. $R(6°/h)$ will not be different significantly from $R(0°/h)$, and $R(45°/0°)$ is equal to $R(0°/45°)$ according to the Helmholtz reciprocity principle.

The measured values of $R(45°/0°)$, $R(6°/h)$ and the ratio of the measured values and integrated ratios are given in Table 1. The measured and integrated values of the ratios agree to 0.005. These ratios are consistent with references [4, 22, 23] in that the values of 45°/normal reflectance factors are higher than the values of the 6°/h reflectance factors. And in the cases of vitrolite and enamel samples the ratios are about four percent higher than unity.

Table 1. Comparison of $R(45°/0°)$ and $R(6°/h)$* (at 550 nm)

Sample	Measured Value $R(45°/0°)$ (b)	$R(6°/h)$* (a)	$R(45°/0°)/R(6°/h)$ (b)/(a)	Integrated**
$BaSO_4$	0.987	0.982	1.005	1.002
Fluorocarbon	1.009	0.994	1.015	1.011
Vitrolite	0.922	0.884	1.043	1.044
Enamel	0.875	0.839	1.043	1.040

* Specular component excluded
** Integration using normalized gonioreflectance data

8. Summary

A 45°/normal reflectometer spectrophotometer was constructed for calibrating the absolute reflectance factor of diffuse samples over the 380–770 nm spectral range. The measurement equations were derived and the measurements were made as a function of wavelength with a polarized light beam. The system performance was examined for such parameters as wavelength scale uncertainties, receiver system linearity and uniformity, scattered radiation, angular setting and view factor uncertainties. Uncertainty in the measurements of reflectance factor will be of the order of ±0.3% of the measured value. Measured ratios of the 45°/normal reflectance factor to the hemispherical reflectance factor with specular component excluded were found to be greater than one for all the samples that have been tested. The higher reflectance values for 45°/normal geometry were confirmed by additional gonioreflectometer measurements.

References

1. W.H. Venable Jr, J.J. Hsia, V.R. Weidner: Establishing a scale of directional-hemispherical reflectance factor. I: The Van den Akker method. National Bureau of Standards (US). J. Res. **82**, 29–55 (1977)
2. J.S. Preston, G.W. Gordon-Smith: A new determination of the luminance factor of magnesium oxide. Proc. Phys. Soc. **B65**, 76–80 (1952)
3. F.J.J. Clark, G.E.V. Lambert, J.M.B. Sparrock, F.A. Gargorth: Research on absolute reflectance standards at the National Physical Laboratory. Proc. Symp. Color Measur. Ind. 25–40, 1967 (The Color Group, London)
4. F.J.J. Clark, F.A. Garforth, D. Parry: Goniophotometric and polarization properties of the common white reflection standards. Nat. Phys. Lab. Rep. MOM 26 (1977)
5. W. Erb: Bestimmung des spektralen Leuchtdichte-Koeffizienten für die Messgeometrie 45°/Normal. Die Farbe **20**, 179–186 (1971)
6. L. Morren: Mesure absolute des facteurs de luminance et de réflection. LUX No. 45, 448–453 (1967)
7. V.E. Kartahevskaya, S.P. Skachkova: New method of the luminance factors and total reflectances for the standard plates of the Institute of Metrology. Svetsteknika **1**, 16–19 (1966); also available as translation NRC TT-1265
8. Commission internationale de l'éclairage: Absolute methods for reflection measurements. CIE Publication Nos. 44 and 46 (1979)
9. Commission internationale de l'éclairage: Colorimetry, official CIE recommendations. CIE Publication No 15 (1971)
10. F.E. Nicodemus, J.C. Richmond, J.J. Hsia, J.W. Ginsberg, T. Limperis: Geometrical considerations and nomenclature for reflectance. Nat. Bur. Stand. (US). Monogr. 160 (1977)
11. W.H. Venable, Jr, J.J. Hsia: Describing spectrophotometric measurements. Nat. Bur. Stand. (US). Tech. Note 594-9 (1976)

12. E.M. Sparrow, R.D. Cess: Radiation heat transfer (augmented edition) p. 121. New York: McGraw-Hill Book Company, 1978
13. F.E. Nicodemus (ed.): Self-study manual on optical radiation measurements: Part I – Concepts, Chap. 4 and 5 p. 97. Nat. Bur. Stand. (US). Tech. Note 910-2 (1978)
14. M. Jakob: Heat transfer. Vol. II p. 11. New York: John Wiley and Sons Inc., 1957
15. W.H. Venable, Jr, J.J. Hsia, V.R. Weidner: Development of an NBS reference spectrophotometer for diffuse transmittance and reflectance. Nat. Bur. Stand. (US). Tech. Note 594-11 (1976)
16. A.R. Robertson: Effect of polarization on reflectance factor measurements. Appl. Opt. **11**, 1936–1941 (1972)
17. D.C. Cramer, M.E. Bair: Some polarization characteristics of magnesium oxide and other diffuse reflectors. Appl. Opt. **8**, 1597–1605 (1969)
18. V.R. Weidner, J.J. Hsia: NBS specular reflectometer-spectrophotometer. Appl. Opt. **19**, 1268–1273 (1980)
19. C.E. Hodgman (ed.): Handbook of Chemistry and Physics, 44th. edn, pp. 2892, 2931, 2961. The Chemical Rubber Publishing Co. 1962–1963
20. K.D. Mielenz, K.L. Eckerle: Design, construction, and testing of a new high accuracy spectrophotometer. Nat. Bur. Stand. (US). Tech. Note 729 (1972)
21. K.D. Mielenz, K.L. Eckerle: Spectrophotometer linearity testing using the double-aperture method. Appl. Opt. **11** 2294 (1972)
22. V.E. Kartachevskaya, H. Korte, A.R. Robertson: International comparison of measurements of luminance factor and reflectance of white diffusing samples. Appl. Opt. **14**, 2694–2702 (1975)
23. A.R. Robertson, W.D. Wright: International comparison of working standards for colorimetry. J. Opt. Soc. Am. **55**, 694–706 (1965)

Journal of Research of the National Bureau of Standards

A Wavelength Standard for the Near Infrared Based on the Reflectance Of Rare-Earth Oxides

Volume 91 Number 5 September–October 1986

Victor R. Weidner, Patricia Y. Barnes, and Kenneth L. Eckerle

National Bureau of Standards
Gaithersburg, MD 20899

This work describes the techniques used to prepare and analyze a reflectance wavelength standard composed of three rare-earth oxides. A mixture of dysprosium oxide (Dy_2O_3), erbium oxide (Er_2O_3), and holmium oxide (Ho_2O_3) provides a pressed powder specimen exhibiting a near infrared reflectance spectrum characterized by many discrete absorption minima in the wavelength range 700 to 2000 nm. The object of this activity was to develop a wavelength standard for improving the accuracy of reflectance measurements in the near infrared. The reflectance minima of the rare-earth oxide mixture was analyzed for the effects of varying spectral resolution and temperature. The uncertainties associated with the various parameters affecting the measurements and the determination of the location of the reflectance minima have been analyzed. The overall uncertainty in the location of these reflectance minima is believed not to exceed ±1 nm.

Key words: dysprosium oxide; erbium oxide; holmium oxide; near infrared reflectance; rare-earth oxides; spectral bandwidths; wavelength calibration; wavelength standard.

Accepted: February 28, 1985

1. Introduction

This work describes the techniques used to prepare and characterize a reflectance wavelength standard composed of three rare-earth oxides. A mixture of dysprosium oxide (Dy_2O_3), erbium oxide (Er_2O_3), and holmium oxide (Ho_2O_3) provides a pressed powder specimen exhibiting a near infrared reflectance spectrum characterized by many discrete reflectance minima in the wavelength range 700 to 2000 nm. This wavelength standard is primarily intended for checking the wavelength accuracy of spectrophotometric instrumentation designed for measuring diffuse reflectance in the near infrared.

About the Authors: Victor R. Weidner, Patricia Y. Barnes, and Kenneth L. Eckerle are with the Radiometric Physics Division in NBS' National Measurement Laboratory.

2. Experimental

2.1 Instrumentation

Measurements of spectral reflectance of the rare-earth oxide mixture were made by means of a Varian Cary Model 2390 recording spectrophotometer [1][1]. The optical system of this double beam instrument consists of a filter predisperser and a double-pass monochromator with UV-VIS and near IR gratings. A deuterium lamp is used as a source for the ultraviolet spectral range. The visible and near infrared source is a tungsten-halogen lamp. The deuterium lamp also serves as a wavelength scale calibration source when the instrument is operated in a single beam mode, providing emission lines at 486.0 and 656.1 nm in the visible spec-

[1] Figures in brackets indicate literature references.

trum and 2nd, 3rd, and 4th order lines of the 656.1 nm line with the near infrared grating.

The spectrophotometer is equipped with an integrating sphere diffuse reflectance reflectometer. This device is capable of measuring total hemispherical reflectance over the wavelength range 200 to 2500 nm, using a photomultiplier detector for the ultraviolet and visible spectral range, and a lead sulfide detector for the near infrared. When operating with the lead sulfide detector, the reference mode (which determines the method used to control the reference signal level) operates at constant gain. The constant gain is maintained by varying the spectral bandwidth as a function of wavelength. The available range of spectral bandwidth settings is approximately 1 to 14 nm when using the diffuse reflectance attachment. The noise associated with the recording of a spectrum increases as the spectral bandwidth is narrowed and the spectral resolution must be sacrificed in order to maintain reasonable noise levels when recording spectra near the extreme short and long wavelength range of the lead sulfide detector. In order to record a spectrum over the full near infrared spectral range at approximately constant resolution, the gain must be reset every 25 to 50 nm. When constant resolution is not important, a complete scan of the near infrared range can be made at a fixed gain setting. For the measurements described in this work, the control of spectral resolution was of primary importance and gain settings were varied to provide a number of fixed spectral bandwidths for analysis of the effects of resolution on the location of the wavelengths of minimum reflectance of the rare-earth oxide mixture.

2.2 Materials

2.2.1 Rare-Earth Oxides. The rare-earth oxides of dysprosium, erbium, and holmium were selected for preparation of the reflectance wavelength studies after extensive measurements of the near infrared reflectance spectra of numerous rare-earth oxides. None of the single component rare-earth specimens analyzed exhibited enough absorption bands to serve as a wavelength standard for the full

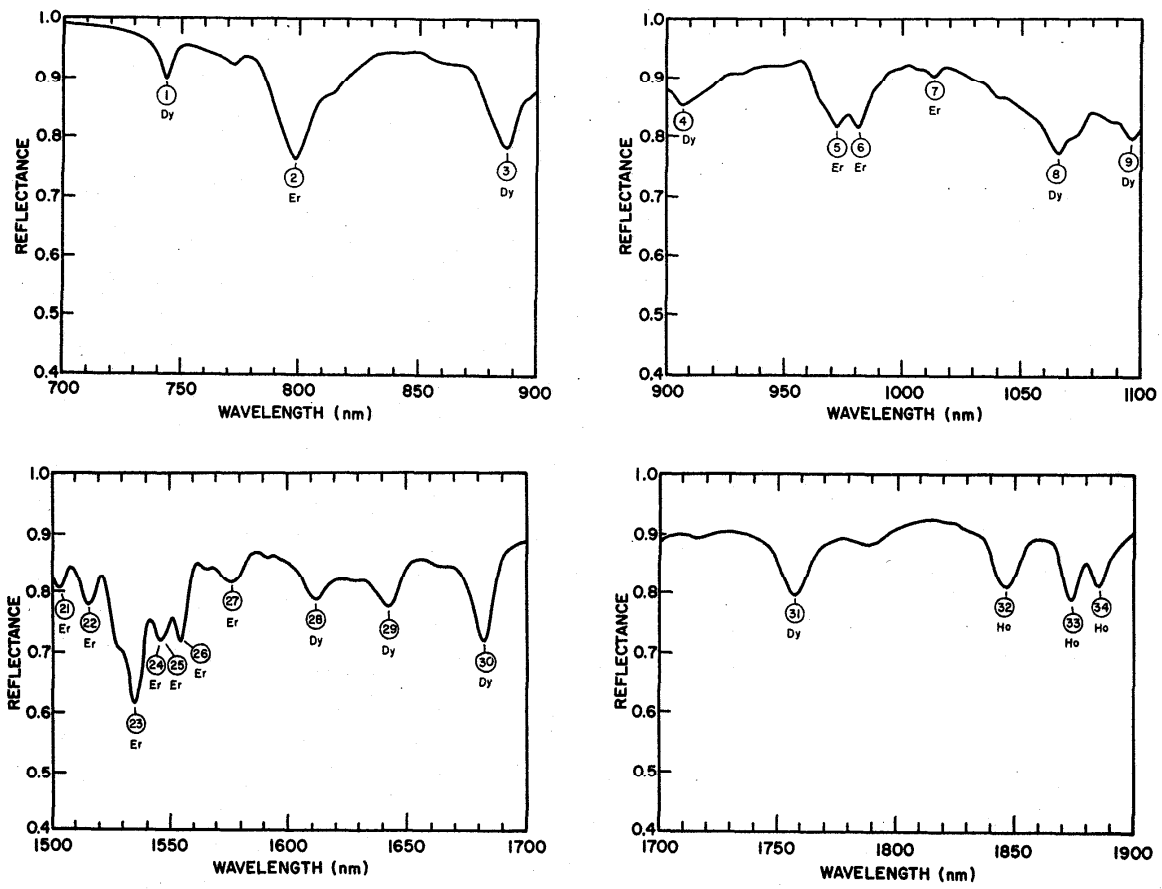

700 to 2500 nm spectral range and none showed any promise at wavelengths much beyond 2000 nm. The oxides of dysprosium, erbium, and holmium were selected because their infrared absorption bands occurred at various wavelengths throughout the 700 to 2000 nm spectral range with a minimum of overlapping of the bands attributed to each oxide. The disadvantage of mixing the three component rare-earth oxides was the loss of some intensity of depth of the individual absorption bands. The reflectance spectra of the three component rare-earth oxide mixture is illustrated in figures 1-1 through 1-7 for a nominal spectral bandwidth of 4 nm. The absorption features selected for analysis are numbered 1–37 and the rare-earth oxide attributed to each of these absorption features is identified by the elemental symbols Dy, Er, and Ho appearing with each band number.

The three rare-earth oxides were mixed in equal parts by weight. The purity of each rare-earth oxide was indicated by the manufacturer [2] to be 99.99 percent. The specimens are identified by lot numbers; (Dy: lot no. Dy-0-4-018), (Er: lot no. Er-0-4-028), and (Ho: lot no. Ho-0-4-007). Each rare-earth oxide was weighed in portions of 2 g ±0.01g. These were combined to form a total weight of 6 g. After throughly mixing the three components, the mixture was pressed into an aluminum cavity having a depth of 0.5 cm and diameter of 2.85 cm. This produced a specimen with a powder density of approximately 2 g/cm^3. The powder specimen was provided with a sapphire window of 1.5 mm thickness. This window retained the powder and protected it against damage and contamination. Sapphire was selected as a window material because it is essentially free of absorption features in the near infrared.

2.3 Measurement Techniques

2.3.1 Calibration of the Spectrophotometer Wavelength Scale. The spectrophotometer wavelength scale error was evaluated by measuring the emission lines of the following elements: neon at 703.24 nm, xenon at 881.94 and 979.97 nm, mercury at 1013.97 and 1529.58 nm, and krypton at 1816.73

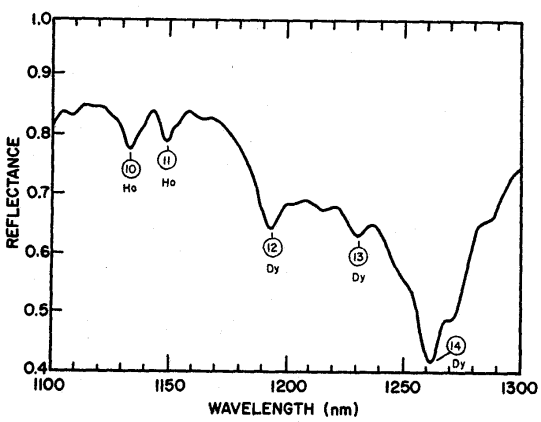

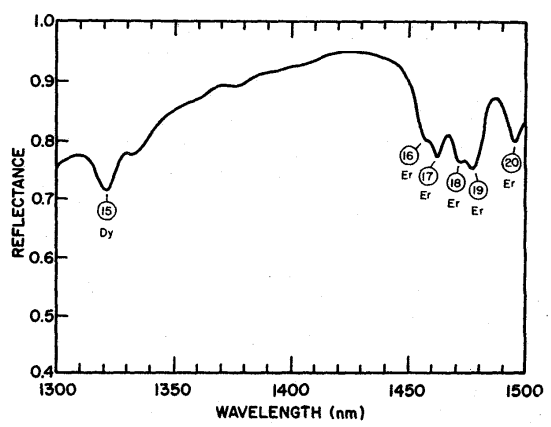

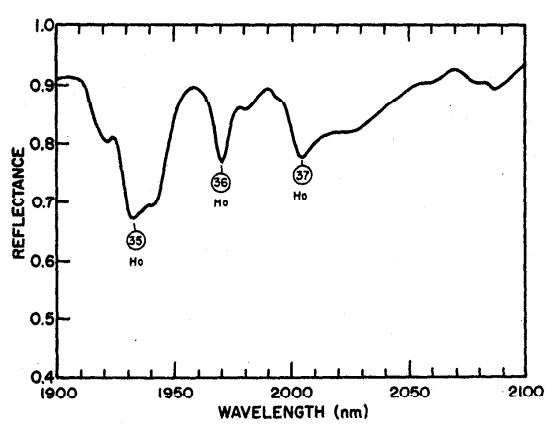

Figures 1-1 through 1-7–Beginning upper left at a wavelength 700 nm the near infrared spectral reflectance of a rare-earth oxide mixture composed of Dy_2O_3, Er_2O_3, and Ho_2O_3 in equal portions by weight compressed to a density of 1g/cm^3.

nm. [3] In addition to these, the absorption band of 1-2-4 trichlorobenzene at 2152.60 nm [4] was also measured.

The wavelength scale of the spectrophotometer was calibrated at the beginning of the study and again after completion of the spectral analysis of the rare-earth oxide spectra. The day-to-day stability of the instrument wavelength scale was monitored by recording the 2nd order emission of the 656.1 nm deuterium line at 1312.2 nm after a nominal warm-up time of 1 hour. The record of this day-to-day stability check is illustrated in figure 2 for the time period of November 13 to December 24. The data in figure 2 show that the wavelength scale was stable to ±0.2 nm during this time interval.

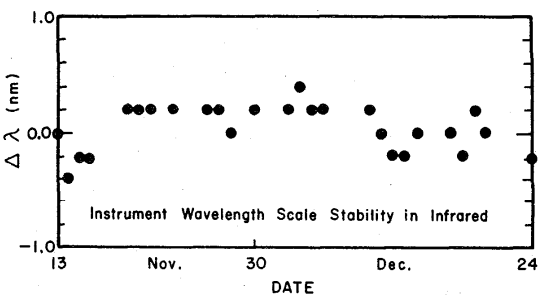

Figure 2–The day-to-day record of the stability of the spectrophotometer wavelength scale in the near-infrared.

The wavelength error was evaluated by scanning the emission lines at a rate of 0.01 nm/sec. and recording the resulting spectrum on a scale of 0.2 nm/cm. The recorded emission peaks were bisected, using a proportional divider, to determine the wavelengths at the center of the recorded triangular lines. Using this technique, the wavelength scale was read to the nearest 0.01 nm.

The wavelength errors were evaluated for spectral bandwidths of 2, 3, 4, 5, and 10 nm. The differences between the published or "true" wavelengths of the emission lines as determined from the measurements on the spectrophotometer, are plotted in figures 3-1 and 3-2 for analysis of the instrument wavelength error. The data points were found to be closely grouped for the measurements at spectral bandwidths of 2, 3, 4, and 5 nm. The data points for the 10 nm spectral bandwidth measurements were somewhat separated from the others. For this reason the analysis of the 2, 3, 4, and 5 nm bandwidth data are illustrated in figure 3-1 and the 10 nm bandwidth data in figure 3-2. Since the day-to-day wavelength scale stability check indicates a possible point spread of 0.4 nm, this grouping of the bandwidth data into one group for the 2, 3, 4, and 5 nm measurements seemed reasonable.

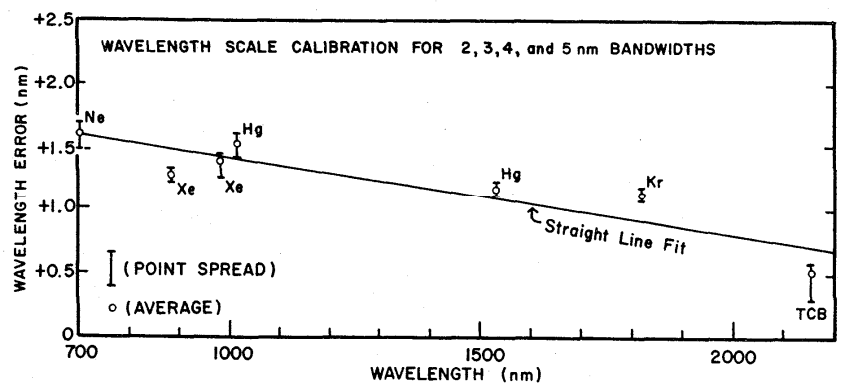

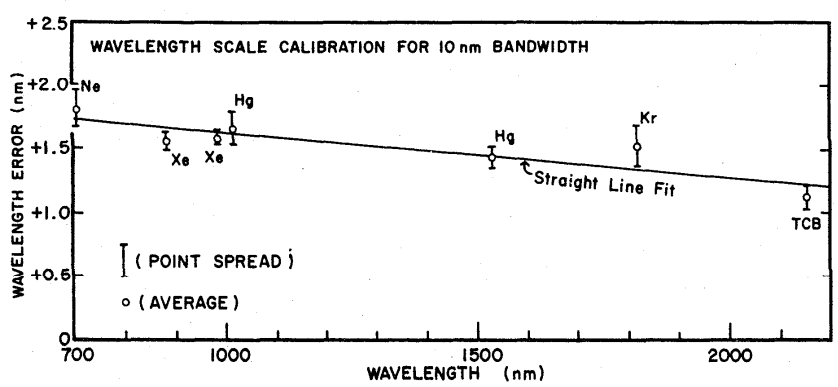

Figure 3-1 (upper) and **Figure 3-2**–The wavelength scale calibration results for the selected spectral bandwidths showing the data point spread (vertical bars), data point averages (open circles on the vertical bars), the linear least-squares fit to the data point averages (sloping solid straight line).

The spread of data points in figures 3-1 and 3-2 is indicated by the vertical bars. The average of the data points within the vertical bar is indicated by the open circle on the bar. A linear least-squares fit of the the average data points, (represented by the open circles), is shown as a straight line across the graph. This line was taken as a indication of the wavelength scale error of the spectrophotometer for these spectral bandwidths over the near infrared spectral range 700 to 2150 nm. This linear least-squares fit represents a nominal wavelength correction. The data spread bars shown in figures 3-1 and 3-2 are sometimes completely above or below the least-squares fit. Repeated measurements probably would not improve the fit because of hidden factors that influence where a particular emission line will appear.

A mathematical estimation of the uncertainty in the calibration of the instrument wavelength scale can be derived from the sum of the following observed uncertainties:

The wavelength scale uncertainty (a) is:

$$a = 2d + r + v$$

where:

$2d$ = twice the standard deviation of the linear least-squares fit for the emission line wavelengths,

$r = 1/2$ the range of the data point spread for the worst case for location of an emission line,

v = the day-to-day stability of the wavelength scale.

For the 2, 3, 4, and 5 nm spectral bandwidths:

$$a = \pm 0.57 \text{ nm}$$

For a 10 nm spectral bandwidth:

$$a = \pm 0.66 \text{ nm}.$$

Other uncertainties associated with the overall determination of the wavelengths of minimum reflectance of the rare-earth oxide mixture will add to these uncertainties. These uncertainties will be discussed in section 2.3.4.

2.3.2 Spectral Bandwidths. The spectral bandwidth settings used in the analysis of the rare-earth oxide mixture were selected to provide data on the effect of changing resolution on the location of the reflectance minima that are characteristic of this material in the near infrared. The spectral bandwidths in the near infrared are controlled by adjusting the reference signal gain. This adjustment involves the monochromator slit width mechanism which in effect controls the spectral bandwidth or resolution. The bandwidth is displayed on the instrument control panel. In order to check the validity of the spectral bandwidth readout on the display panel, a series of measurements were made of the half-band widths of the mercury emission line at 1014 nm for nominal bandwidth settings of 2, 3, 4, 5, and 10 nm. In the single beam mode of operation the gain can be adjusted without changing the selected bandwidth. The half-band width is determined by scanning the emission line with the gain adjusted until the peak of the emission is approximately 100 percent. The measured width of the recorded emission spectra at half the peak height is an indication of the spectral bandwidth. A comparison of the nominal spectral bandwidth, as indicated on the instrument display panel, and the measured half-band width of the mercury emission spectra is given in table 1. The comparison shows that the actual bandwidths are less than the nominal bandwidths for the 2, 3, 4, and 5 nm settings and the same for the 10 nm setting.

2.3.3 Determination of the Wavelength of Minimum Reflectance. The spectral reflectance of the rare-earth oxide mixture is shown in figures 1-1 through 1-7 for a nominal spectral bandwidth of 4 nm. The number of observed absorption bands varies as a function of the spectral bandwidth setting selected for recording the spectrum. There are 37 reflectance minima identified in the figures. Most can be observed at bandwidths less than 4 nm. Only a few can be observed at 10 nm spectral bandwidth.

The reflectance spectra of the mixture of rare-earth oxides was recorded on a chart with a wavelength display of 0.5 nm/cm and a wavelength scan range of 0.05 nm/sec. This speed is a relatively slow scan rate for these absorption bands so that the effect of recorder inertia error is essentially eliminated as a source of wavelength scale error.

The reflectance was measured with a sapphire window between the rare-earth oxide mixture and the sample port of the integrating sphere of the reflectometer. The 100 percent (baseline) calibration was set with a pressed powder Halon (polytetrafluoroethylene) specimen, also covered by a sapphire window. The near infrared spectral reflectance of a sapphire window covered Halon

Table 1. Comparison of the spectral bandwidths as indicated by the instrument readout (A) with the spectral bandwidths as derived from the half-height bandwidth measurements of the 1014 nm Hg emission line (B).

Spectral Bandwidths	
(A)	*(B)*
2 nm	1.4 nm
3	2.6
4	3.6
5	4.6
10	10.0

specimen versus an uncovered Halon Specimen (100 percent) is shown in figure 4. The spectral transmittance of the sapphire window is also shown in figure 4.

The determination of the wavelengths of minimum reflectance of the rare-earth mixture was accomplished through an analysis of the recorded spectral curves. The location of the wavelengths of minimum reflectance for a given absorption band was graphically determined by bisecting the absorption band. The technique is illustrated in figure 5. The horizontal grid lines of the chart paper that intersect the two slopes of the absorption band are bisected by means of a proportional divider. The points of bisection locate a line between the two slopes that intersects the minimum reflectance point, (usually at the lowest point of the curve). The wavelength at this point of intersection was taken as the measured wavelength of minimum reflectance for the absorption feature. The true wavelength of the minimum was determined by applying a wavelength correction to this measured value. This correction was discussed in section 2.3.1. Various uncertainties are associated with these assigned true wavelengths. These will be discussed in section 2.3.4.

2.3.4 Accuracy of the Wavelengths of Minimum Reflectance. The overall uncertainty in the location of the wavelengths of minimum reflectance is believed to be no greater than ±1 nm. This conclusion is based on the reproducibility of the following calibration parameters:

a) The uncertainty of the calibration of the spectrophotometer wavelength scale using the emission lines of Ne, Xe, Hg, and Kr, and the absorption band of 1-2-4 trichlorobenzene, and the day-to-day instabilities of the instrument; (±0.57 nm and ±0.66 nm depending on the spectral bandwidth).

b) The imprecision of the graphical technique for deriving the measured wavelengths of minimum reflectance; (±0.41 nm), (twice the largest standard deviation), (see table 2).

c) The maximum observed temperature effect; (±0.15 nm).

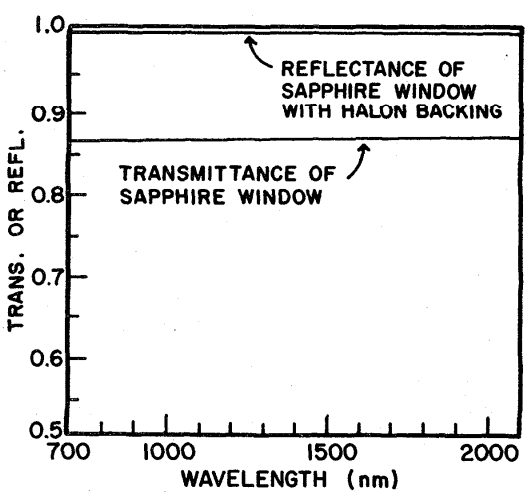

Figure 4–The spectral transmittance of the sapphire window used to cover the rare-earth oxide pressed powder specimen, and the spectral reflectance of a sapphire window covering the Halon diffuse reflectance standard.

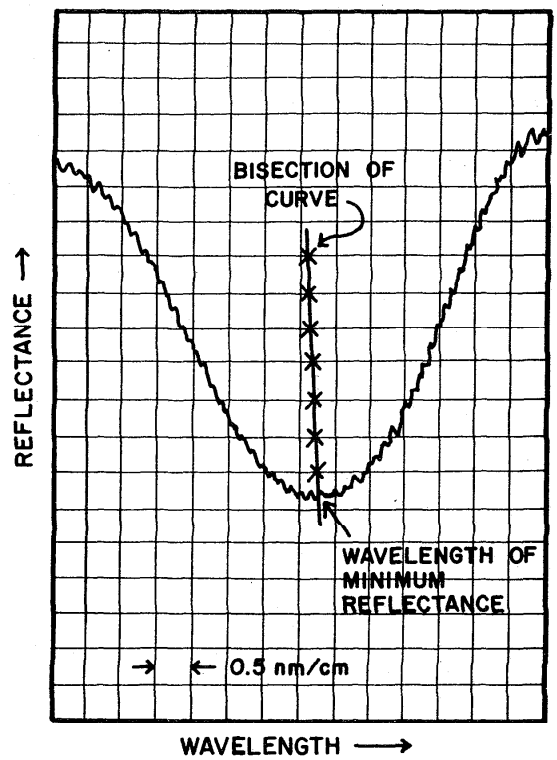

Figure 5–The wavelengths of minimum reflectance are determined by bisecting the recorded absorption feature as illustrated in this example.

A mathematical estimation of the overall uncertainty (T) in the location of the wavelengths of minimum reflectance can be derived from the square root of the sum of the independent errors squared:

$$T=\sqrt{a^2+b^2+c^2}$$

where:

a = uncertainty in the instrument wavelength scale,

Table 2. Ten measurements of the reflectance minima for each of three absorption bands at a spectral bandwidth of 4 nm, showing the spread of values obtained by the graphical location of the minima. The average, standard deviation, and standard error for the ten values are also given. These measurements are for 25 °C.

Measurement No.	Band No. 14 (Dy_2O_3)	Band No. 23 (Er_2O_3)	Band No. 32 (Ho_2O_3)
1	1261.00	1535.68	1847.09
2	1260.93	1535.65	1847.00
3	1261.15	1535.70	1846.77
4	1261.00	1535.70	1847.00
5	1261.03	1535.60	1846.73
6	1261.20	1535.65	1846.78
7	1261.08	1535.63	1846.50
8	1260.93	1535.60	1846.70
9	1260.93	1535.69	1846.73
10	1261.00	1535.70	1846.43
Average	1261.03	1535.66	1846.77
Standard Deviation	0.09	0.04	0.21
Standard Error	0.03	0.01	0.07

Note: The data in this table have not been corrected for the wavelength scale error of the spectrophotometer.

b = twice the standard deviation for the graphical determination of the minima,

c = the largest observed temperature effect.

For spectral bandwidths of 2, 3, 4, and 5 nm:

$T = \pm 0.72$ nm

For a spectral bandwidth of 10 nm:

$T = \pm 0.79$ nm.

These uncertainties are for a 95 percent confidence level. Some other possible uncertainties are discussed in the conclusion.

3. Measurements

3.1 Influence of the Sapphire Window and the Baseline Calibration

In measuring diffuse spectral reflectance, some reference must be used to establish a 100 percent level (baseline). In this double beam spectrophotometer, the reference beam enters the integrating sphere and is incident on a Halon target. The sample beam enters through another port and is incident on the sample. In order to establish a 100 percent level calibration curve, a sample of pressed Halon is placed at the sample port. The 100 percent level is established by the ratio of the sample (Halon) reflectance to the reference beam signal (also Halon). The instrument records this baseline in a computer memory. When the Halon sample is replaced by a test specimen, the reflectance of the specimen is recorded relative to this stored baseline or 100 percent level. This method is called the substitution method. The reflectance of the test specimen is a relative measurement. Halon is used to establish the 100 percent level because its absolute reflectance is very high and it has no significant absorption features that would introduce a distortion in the recorded spectra. The absolute reflectance of the test specimen can be obtained by adjusting the relative measurement to the absolute reflectance of the Halon [5].

In this study a sapphire window is placed over the rare-earth oxide test specimen. This window is 1.5 mm thick. A similar window is placed over the Halon sample during the recording of the 100 percent level. By using a sapphire window on both the Halon and the rare-earth oxide specimens, the effects of the window reflectance and absorbance are cancelled out in the baseline calibration.

The sapphire window has no absorption bands in the near infrared that would influence the determination of the wavelength of minima reflectance of the rare-earth oxide mixture. The absolute reflectance data for Halon [5] also show that it can be used as a baseline standard for purposes of this investigation.

3.2 Influence of Spectral Bandwidth

The effects of spectral bandwidth on the location of the rare-earth oxide reflectance minima are shown in table 3. The absorption bands are numbered from 1 at approximately 742 nm to 37 at approximately 2005 nm. Measurements were made at nominal spectral bandwidths based on the instrument display readout of this parameter. However, the data listed in table 1 indicate that the spectral bandwidths were less than the nominal values for all but the 10 nm setting.

The blank spaces in table 3 are blank for the following reasons: (1) The noise level was too large to make reliable measurements. This was the case for bands 1, 2, 36, and 37 at the 2 nm spectral bandwidth setting. (2) Two adjacent bands merged together because the selected spectral bandwidths did not resolve the two bands. This was the case for bands 24 and 25 at 3 nm spectral bandwidth. (3) The band became too shallow due to the large spectral bandwidth. This case occurs for many of the bands at 5 and 10 nm spectral bandwidths.

Table 3 does not give a clear picture of the exact effects of changing spectral bandwidth on the location of the the wavelengths of minimum reflec-

Table 3. The adopted wavelengths of minimum reflectance for the rare-earth oxide mixture at 25 °C and for spectral bandwidths (SBW) of 2, 3, 4, 5, and 10 nm.

Rare-earth oxide	Band No.	SBW 2 nm	SBW 3 nm	SBW 4 nm	SBW 5 nm	SBW 10 nm
Dy_2O_3	1	-----	743.0	743.4	743.4	-----
"	2*	-----	799.0	799.0	798.6	798.0
"	3*	887.2	886.9	886.7	886.7	886.5
"	4	906.3	906.8	907.5	907.3	-----
Er_2O_3	5	970.6	971.3	971.6	971.6	-----
"	6	979.6	980.8	980.8	980.8	-----
"	7	1012.9	1013.2	1012.9	1012.8	-----
Dy_2O_3	8	1064.7	1065.0	1065.0	1064.9	-----
"	9	1095.6	1096.0	1096.2	1096.4	-----
Ho_2O_3	10*	1132.2	1132.3	1132.4	1132.9	1132.9
"	11*	1148.1	1148.4	1148.5	1148.7	1148.6
Dy_2O_3	12	1192.9	1192.7	1192.9	1192.9	-----
"	13	1230.2	1230.2	1230.2	1230.3	-----
"	14*	1261.0	1260.9	1260.8	1260.8	1261.8
"	15	1320.7	1320.7	1320.8	1320.7	1320.2
Er_2O_3	16	1456.2	1456.4	1456.7	-----	-----
"	17	1461.7	1461.9	1462.2	-----	-----
"	18	1471.2	1471.6	1471.6	-----	-----
"	19	1477.4	1477.6	1477.5	-----	-----
"	20	1494.8	1494.9	1495.0	1495.0	-----
"	21	1503.4	1503.5	1503.5	-----	-----
"	22	1516.0	1516.0	1515.9	1515.7	-----
"	23*	1535.5	1535.6	1535.6	1535.4	1534.6
"	24	1544.7	-----	-----	-----	-----
"	25	1548.1	-----	-----	-----	-----
"	26	1555.1	1555.0	1554.8	-----	-----
"	27	1577.1	1577.2	1577.2	-----	-----
Dy_2O_3	28	1611.8	1611.7	1611.7	1611.9	-----
"	29	1642.7	1642.7	1642.5	1642.5	-----
"	30*	1682.6	1682.3	1682.2	1682.2	1681.4
"	31*	1757.6	1757.8	1757.9	1757.8	1757.6
Ho_2O_3	32*	1847.5	1847.3	1846.9	1847.0	1847.3
"	33	1874.3	1874.0	1873.8	1874.0	-----
"	34	1885.0	1885.3	1885.7	1885.5	-----
"	35*	1930.9	1931.6	1932.2	1932.5	1935.5
"	36*	-----	1970.6	1970.7	1970.8	1970.8
"	37	-----	2004.5	2005.9	2005.8	2006.3

The uncertainty in the wavelengths of minimum reflectance are believed to be no greater than ±1 nm.

* (preferential bands)

tance for the rare-earth oxide absorption bands because some of the uncertainties discussed in section 2.3.4 are large enough to mask the bandwidth effects. However, the apparent shift in the wavelengths of the minima are sometimes larger than the overall uncertainty. Therefore, all the results are listed in the table.

For purposes of checking the wavelength scale of a reflectance spectrophotometer there are many reflectance minima listed in table 3. A few of the minima might be considered as being preferable because the absorption bands are observed at bandwidths as large as 10 nm. These bands are marked with an asterisk after the band number in the table.

3.3 Influence of Temperature

All the data listed in table 3 was obtained at a temperature of 25 °C ±0.5 °C. The effects of temperature on the location of the wavelengths of minimum reflectance of the rare-earth oxide mixture were studied by analyzing one absorption band for each of the three rare-earth components. The results are shown in table 4 for bands 14, 23, and 32, at 20 °C, 25 °C, and 30 °C. These measurements were made with a spectral bandwidth of 4 nm. Because these measurements did not prove or disprove the effects of temperature, and effect was as-

Table 4. The observed effects of temperature on the wave lengths of minimum reflectance for 20 °C, 25 °C, and 30 °C. The temperature effects are not revealed by the observed differences because of larger uncertainties discussed in section 2.3.4.

	(spectral bandwidth=4 nm)		
Temperature	Band No. 14 (Dy_2O_3)	Band No. 23 (Er_2O_3)	Band No. 32 (Ho_2O_3)
20 °C	1260.8 nm	1535.7 nm	1847.0 nm
25 °C	1260.8	1535.6	1846.9
30 °C	1261.0	1535.5	1846.7

sumed based on the largest differences observed for the data in table 4 for purposes of estimating the overall uncertainty (see sec. 2.3.4).

3.4 Influence of Instrument Sensitivity Function

The instrument function is the relative sensitivity of the instrument as a function of wavelength as observed in the single beam mode of operation with no sample in the beam. The instrument sensitivity is influenced by a number of parameters such as the energy output of the source as a function of wavelength, grating efficiency, reflection of mirrors, transmission of windows, and spectral response of the detector. The near infrared instrument sensitivity of the Varian-Cary 2390 spectrophotometer, increases from 700 nm to approximately 1150 nm, then decreases with increasing wavelength. There are some local variations in this sensitivity curve due to absorption features associated with optics and atmospheric conditions. The effect of the instrument sensitivity function on the wavelengths at which absorption features appear for a specimen being scanned is to shift the scale to longer wavelength when the instrument sensitivity is increasing from shorter wavelength to longer wavelength (positive slope) and to shift the scale to shorter wavelength when the instrument sensitivity is decreasing from shorter wavelength to longer wavelength (negative slope). The amount of wavelength shift increases as the slope becomes steeper with changing wavelength.

The shift in wavelength due to the influence of the instrument sensitivity can be determined to a close approximation, using the following equation:

$$d\lambda = \frac{a\,w^2}{6}$$

where:

$d\lambda$ = the wavelength displacement,

a = the slope of the sensitivity curve normalized at the center of a triangle,

w = the width at the half-height of the geometrical passband.

The wavelength shift is greater for very wide spectral bandwidths and almost negligible for very narrow spectral bandwidths. The effect of instrument sensitivity function is not cancelled by operating the instrument in a double-beam mode. The measured location of emission lines such as those described in section 2.3.1 is not influenced by the instrument sensitivity function because the emission lines are relatively narrow with respect to the spectral bandwidth.

The data for the reflectance minima listed in table 3 and 1 have been adjusted for the influence of the instrument sensitivity function. The amount of adjustment varied from zero where the sensitivity slope was essentially flat to as much as 0.26 nm where the slope was steep and the spectral bandwidth was 10 nm. For all but 10 of the values listed in these tables, the wavelength shift due to the influence of the instrument sensitivity function was less than 0.1 nm.

4. Results

4.1 Reflectance of the Rare-Earth Oxide Mixture

The general reflectance spectrum of the rare-earth oxide mixture is illustrated in figures 1-1 through 1-7 for a nominal spectral bandwidth of 4 mm. The absorption bands are numbered in order to associate the data listed in the tables with the spectral features illustrated in the figures.

4.2 Numerical Results

Most of the absorption bands appearing in figures 1-1 through 1-7 were analyzed and the recommended values for the wavelengths of minimum reflectance are listed in table 3 for the indicated spectral bandwidths. Preferred bands are identified by asterisks after the band numbers in the table.

5. Other Measurements

A check of the reflectance of the Er_2O_3 absorption bands at approximately 1012 nm (Band No. 7) and 1535 nm (Band No. 23), and Dy_2O_3 band at approximately 1260 nm (Band No. 14) was made on the NBS Reference spectrophotometer for diffuse reflectance [6]. This spectrophotometer uses a 1-meter monochromator equipped with a prism predisperser. The spectral bandwidth was set at 5

nm or 10 nm. The reflectometer is a 30 cm diameter integrating sphere with a lead-sulfide detector. Measurements are recorded with the wavelength drive set at fixed wavelengths. At each wavelength setting the signal is processed by a current-to-frequency converter and integrated over a 4 second time interval. The reflectance of the sample is measured relative to the sphere wall which is coated with a spectrally neutral white diffuser [5].

The wavelength correction for the reference spectrophotometer was determined by measuring the emission lines of a Hg lamp at 1013.97 nm and 1529.58 nm. These measurements indicate that the reference instrument wavelength scale was reading too high by +0.82 nm at 1014 nm and +0.35 nm at 1530 nm for a 5 nm spectral bandwidth. The reflectance minima of the Er_2O_3 bands at approximately 1012 nm and 1535 nm are close to the Hg emission wavelengths. The sample reflectance was measured at 0.2 nm intervals. From these data, the reflectance minima for band numbers 7, 14, and 23 were determined to be 1012.9 nm, 1260.7 nm and 1535.5 nm respectively for a spectral bandwidth of 5 nm after correcting for the wavelength scale error. Band No. 23 was determined to be at 1534.5 nm for a 10 nm spectral bandwidth.

A comparison of reflectance minima results for bands 7, 14, and 23 as determined on the Varian-Cary and Reference spectrophotometers, indicates that a wavelength bias of approximately 1 nm exists between the two instruments after the wavelength scale has been corrected for all known sources of error (see table 5). Measurements of the reflectance minima made by the Instrumental Research Laboratory [7], of the U.S. Department of Agriculture (USDA) indicate a similar wavelength bias between their spectrophotometers and the Varian-Cary instrument used in this work. Repeated measurements on the Varian-Cary instrument after 1.5 years indicate that the bias remains constant. Because of the strong evidence for this wavelength bias and confidence in the wavelength accuracy of the NBS Reference spectrophotometer, and the supporting evidence from the USDA, the data in table 3 has been adjusted to correct for the Varian-Cary near infrared wavelength scale bias. The over-all uncertainty of ±1 nm given in section 2.3.4 remains the same for these adjusted reflectance minima.

Table 5. A comparison of the data for reflectance minima numbers 7, 14, and 23 as determined on the Varian-Cary spectrophotometer and the NBS Reference spectrophotometer.

Band No.	SBW (nm)	Reflectance Minima Varian-Cary Instrument (1)	Reference Instrument (2)	Difference (2)-(1)
7	5	1011.8	1012.9	−1.1
14	5	1259.8	1260.7	−0.9
23	5	1534.4	1535.5	−1.1
23	10	1533.6	1534.5	−0.9

6. Conclusion

In addition to those uncertainties discussed above there are also other factors that might introduce uncertainties affecting the results of this study. Although these have not been quantitatively investigated, they include: 1) purity of the rare-earth oxides. 2) variation in the ratios of the three rare-earths that are mixed to form the specimen, and 3) variation in the density of the pressed powder. All three of these factors can be controlled to a high degree of precision in the preparation of the three-component rare-earth mixture used in this study. The purity of the individual constituents is sufficiently high (99.99%) so that it is not likely that slight variations in this parameter will affect the location of the wavelengths of minimum reflectance. The ratios of the three rare-earth components was established by careful weighing. For a weighing of 2 g, an uncertainty of ±0.01 g is too small to have much effect on the location of the wavelengths of minimum reflectance. Mixing of the three components must be thorough, however, to avoid inhomogeneities.

Figures 1-1 through 1-7 should only be used as a key to the appearance of the reflectance spectra. Refer to table 3 for the numerical values. The reflectance data shown in the figures should not be used for purposes of a reflectance standard. The absolute reflectance of pressed Halon [5] has been established for this type of calibration.

A wavelength standard based on the diffuse reflectance of a mixture of three rare-earth oxides has been analyzed and calibrated for the near infrared spectral range 700 to 2000 nm. The reflectance minima obtained from a mixture of Dy_2O_3, Er_2O_3, and Ho_2O_3 have been determined for nominal spectral bandwidths of 2, 3, 4, 5, and 10 nm. The principal sources of error influencing the accuracy of the assigned wavelengths of the reflectance minima are the calibration of the spectrophotometer wavelength scale and the imprecision in the techniques used to record and estimate these minima.

This proposed wavelength standard should provide a useful means for checking the accuracy of the near infrared wavelength scale of spectrophotometers equipped with suitable accessories

for measuring diffuse reflectance if the required wavelength accuracy does not have to be better than ±1 nm.

An uncertainty of ±1 nm for this near infrared wavelength standard is less accurate than current wavelength standards for the ultraviolet and visible spectral ranges. A wavelength standard based on a solution of Ho_2O_3 in perchloric acid [8] provides 14 transmittance minima for wavelength scale calibration in the ultraviolet and visible spectrum. The overall uncertainty for this wavelength standard is ±0.1 nm for the location of the transmittance minima.

References

[1] *Certain commercial equipment or products are metioned* in this paper in order to adequately document the work. In no case does this imply that the equipment or product is being endorsed by the National Bureau of Standards or that it is necessarily the best equipment or product for the application.

[2] The rare-earth oxides were obtained from Research Chemicals, a division of Nucor Corp., Phoenix, Arizona.

[3] CRC Handbook of Chemistry and Physics, 63rd Edition, CRC Press Inc., (1982–1983).

[4] Acquista, N., and E. K. Plyler, Calibrating Wavelengths in the Region from 0.6 to 2.6 Microns, J. Res. Natl. Bur. Stand., Vol. 49, 13–16 (July 1952).

[5] Weidner, V. R., and J. J. Hsia, Reflection Properties of Pressed Polytetrafluoroethylene Powder, J. Opt. Soc. Am., Vol. 71, 856–861, (July 1981).

[6] Venable, W. H. Jr., J. J. Hsia, and V.R. Weidner, Development of an NBS Reference Spectrophotometer for Diffuse Transmittance and Reflectance, Natl. Bur. Stand., Tech. Note 594–11, October 1976.

[7] Memorandum from: Dr. Karl H. Norris and William R. Hruschka, Instrumentation Research Laboratory, USDA, BARC-W, Beltsville, MD 20912.

[8] Weidner, V. R.; R. Mavrodineanu, K. D. Mielenz, R. A. Velapoldi, K. L. Eckerle, and B. Adams, Spectral Transmittance Characteristics of Holmium Oxide in Perchloric Acid Solution, J. Res. Natl. Bur. Stand., **90–2** (1985).

☆U.S. GOVERNMENT PRINTING OFFICE:1998-433-235/93211